TECHNIQUES FOR HANDLING MULTILAYERED MEDIA IN THE FDTD METHOD

A Thesis
Presented to
The Academic Faculty

by

İlker R. Çapoğlu

In Partial Fulfillment
of the Requirements for the Degree
Doctor of Philosophy in the
School of Electrical and Computer Engineering

Georgia Institute of Technology
August 2007

TECHNIQUES FOR HANDLING MULTILAYERED MEDIA IN THE FDTD METHOD

Approved by:

Glenn S. Smith, Committee Chair
School of Electrical and Computer Engineering
Georgia Institute of Technology

Gregory D. Durgin
School of Electrical and Computer Engineering
Georgia Institute of Technology

Waymond R. Scott, Jr.
School of Electrical and Computer Engineering
Georgia Institute of Technology

Levent Degertekin
School of Mechanical Engineering
Georgia Institute of Technology

Andrew F. Peterson
School of Electrical and Computer Engineering
Georgia Institute of Technology

Date Approved: June 27, 2007

To my parents

Saffet and Ayser Çapoğlu,

and to my sister Nazan.

ACKNOWLEDGMENTS

I am indebted and eternally grateful to my advisor, Dr. Glenn S. Smith, for guiding me patiently and diligently through this long journey. I consider having worked under his supervision a great privilege; which I will cherish throughout the rest of my life.

I would like to express my gratitude to my dissertation committee members: Dr. Waymond R. Scott, Jr., Dr. Andrew F. Peterson, Dr. Gregory D. Durgin, and Dr. Levent Degertekin. I would especially like to thank Dr. Scott for his efforts in building and maintaining an excellent Beowulf cluster, without which most of my results would have taken much longer to produce.

Without the substantial help and guidance from my colleagues and friends, much of this work could not have been achieved. I wish to thank all these fascinating people for their friendship and support.

I would like to thank the Signature Technology Laboratory (STL) of the Georgia Institute of Technology Research Institute (GTRI) for the use of their measurement facilities. This work was supported in part by the John Pippin Chair in Electromagnetics within the School of Electrical and Computer Engineering, Georgia Institute of Technology.

TABLE OF CONTENTS

LIST OF TABLES

LIST OF FIGURES

SUMMARY

In this research, we introduce methods to be used in the finite-difference time-domain (FDTD) analysis of *planar multilayered media*, characterized by the invariance of material properties in planes perpendicular to an axis called the *axis of symmetry*. The invariance is allowed to be disturbed by any imperfection, provided that these imperfections are local and therefore can be contained within an FDTD simulation grid. A transmitting wire antenna over a dielectric half space, a straight or bent transmission line on a grounded dielectric slab, and a UWB antenna over an ungrounded dielectric slab are some of the examples that are considered in our study. Some other examples of imperfections in multilayered media are: scattering objects buried under ground, receiving or transmitting antennas over/under ground or water, and different cell types in multilayered skin tissue.[1]

We specifically investigate two FDTD methods that were not previously developed for general multilayered media: the *near-field-to-far-field transform* (NFFFT) and the *total-field/scattered-field* (TF/SF) *boundary* (or the plane-wave injector). The NFFFT (Chapter 2) uses the FDTD output on a virtual surface surrounding the local imperfections and calculates the radiated field (or the far field), defined as the $1/r$-dependent field that is the first term in the asymptotic expansion of the exact field. The plane wave injector (Chapter 3) builds an incident plane wave inside a certain boundary (TF/SF boundary) while allowing any scattered fields created by the imperfections inside the boundary to exit the boundary with complete transparency. The NFFFT is applicable for any *lossless* multilayered medium, while the plane-wave injector is applicable for any *lossy* multilayered medium.

After developing the respective theories and giving simple examples, we apply the

[1] We only consider *permittivity* variations. Results for permeability variations follow from duality.

NFFFT and the plane-wave injector to a series of problems in Chapter 4. These problems are divided into two main groups. In the first group, we consider plane-wave scattering problems involving perfectly-conducting objects buried in multilayered media. In the second group, we consider problems that involve radiating structures in multilayered media. Specifically, we investigate the reciprocity of antennas radiating in the presence of an ungrounded dielectric slab using the methods developed in this study.

In Chapter 5, we present our previous work on an entirely different subject, namely, the analysis of *prolate spheroidal monopoles*, which was completed between June 2004 and January 2005. At that time, this research subject was considered as a possible thesis topic. Although the focus of our research has changed since then, the originality of the work and the amount of effort spent on creating it prompted us to include it in our thesis.

CHAPTER I

INTRODUCTION

In this chapter, we provide background information on our research subject, and explain briefly the contributions made by our research. We start by giving a brief account of the basic equations of electromagnetics, and the basics of the *finite-difference time-domain method* (FDTD). Then, we present a historical overview of the literature on our research subject, and the contributions made to the literature by our research.

1.1 Maxwell's Equations

Electromagnetics (or precisely, classical electromagnetics) is the branch of classical physics that explains the behavior of an entity called *electrical charge*. Probably the first recorded account of observed electromagnetic phenomenon is due to Thales, an ancient Greek philosopher from the sixth century BC, who noted the attractive force exerted on some light particles by an amber rod rubbed with silk. Thales also observed the force of attraction between pieces of rock called lodestone, mined at a city called Magnesia. Although numerous great physicists and mathematicians (Gauss, Coulomb, Faraday, Ampére and many others) later contributed to their explanation and relationship, the two phenomena associated with amber and lodestone were largely treated separately, as *electric* and *magnetic*, until the 19th century.

Between 1861 and 1864, a Scottish physicist named James Clerk Maxwell published a series of groundbreaking papers, the most famous and decisive being "A Dynamical Theory of the Electromagnetic Field," presented to the Royal Society in 1864. In this paper, he presented the famous equations (now known as *Maxwell's equations*) explaining in a consistent fashion both electrical and magnetic phenomena in terms of the distribution and movement of electrical charge. His remarkable physical insight in constructing the equations led to the prediction that electromagnetic energy would *propagate* in vacuum almost exactly at the speed of light. This observation, in turn, led to the magnificent discovery that light,

the nature of which had been debated for centuries, is merely an electromagnetic wave in a certain frequency range.

Maxwell's equations are usually expressed in the following vector form [1]:

$$\nabla \times \boldsymbol{\mathcal{E}} = -\frac{\partial \boldsymbol{\mathcal{B}}}{\partial t} - \boldsymbol{\mathcal{M}} \tag{1}$$

$$\nabla \times \boldsymbol{\mathcal{H}} = \frac{\partial \boldsymbol{\mathcal{D}}}{\partial t} + \sigma \boldsymbol{\mathcal{E}} + \boldsymbol{\mathcal{J}} \ , \tag{2}$$

in which calligraphic font is used to denote time-varying field variables and boldface font is used to indicate their vector nature. The vectors $\boldsymbol{\mathcal{J}}$ and $\boldsymbol{\mathcal{M}}$ denote the electric and magnetic currents, which provide the excitation for the electromagnetic field. The vectors $\boldsymbol{\mathcal{E}}$, $\boldsymbol{\mathcal{B}}$ are the electric and magnetic field strengths and $\boldsymbol{\mathcal{D}}$, $\boldsymbol{\mathcal{H}}$ are the electric and magnetic excitations, respectively. The relationships between the excitations and the field strengths are strongly dependent on the properties of the surrounding medium. These relationships are called the *constitutive relations*, which, for a wide class of materials called *simple materials*, assume a simple linear form:

$$\boldsymbol{\mathcal{D}} = \epsilon \boldsymbol{\mathcal{E}} \tag{3}$$

$$\boldsymbol{\mathcal{H}} = \frac{1}{\mu} \boldsymbol{\mathcal{B}} \ . \tag{4}$$

Given the excitation $\boldsymbol{\mathcal{J}}$ and $\boldsymbol{\mathcal{M}}$ and certain information on the time history of the boundaries of the problem at hand, a solution to the combined equations (1)–(4) is guaranteed to be unique. Unless the problem at hand belongs to the tiny class of canonical problems for which exact closed-form solutions are known, approximate numerical methods are necessary to find the solution. One of these methods is the *finite-difference time-domain method* (FDTD), which is summarized in the next section.

1.2 FDTD Method

FDTD is a numerical method for solving Maxwell's equations (1)–(2) directly in the time domain [2, 3]. The method involves the *discretization* of the field variables $\boldsymbol{\mathcal{E}}$, $\boldsymbol{\mathcal{B}}$, $\boldsymbol{\mathcal{D}}$, $\boldsymbol{\mathcal{H}}$ in both space and time and converting the continuous space and time derivatives $(\nabla, \partial/\partial t)$ into finite differences in space and time. In our work, only simple materials are considered;

therefore $\boldsymbol{\mathcal{D}}$ and $\boldsymbol{\mathcal{H}}$ are simply proportional to $\boldsymbol{\mathcal{E}}$ and $\boldsymbol{\mathcal{B}}$, respectively. The constants of proportionality $(\epsilon, 1/\mu)$, however, may depend on position. A clear example of this non-uniformity is found in planar multilayered media, which we investigate in our study.

We first consider a simplification of Maxwell's equations to demonstrate the discretization process. We specifically assume that neither the geometry nor the excitation has any variation in the y and z directions and only the excitation components $\mathcal{M}_y$ and $\mathcal{J}_z$ are nonzero. In this case, Maxwell's equations in (1)–(2) determine the x-directed, z-polarized transverse electromagnetic (TEM) wave [2]:

$$\frac{\partial \mathcal{H}_y}{\partial t} = \frac{1}{\mu}\left[\frac{\partial \mathcal{E}_z}{\partial x} - \mathcal{M}_y\right] \tag{5}$$

$$\frac{\partial \mathcal{E}_z}{\partial t} = \frac{1}{\epsilon}\left[\frac{\partial \mathcal{H}_y}{\partial x} - \mathcal{J}_z\right] \ . \tag{6}$$

In the FDTD analysis of the above TEM problem, the computational space-time region is divided into square cells with dimensions $(\Delta x, \Delta t)$ and the derivatives in space and time are approximated by central differences evaluated at the center of each square. For example, the space and time derivatives of a function $\mathcal{A}(x,t)$ are approximated as

$$\left.\frac{\partial \mathcal{A}}{\partial t}\right|_{(x_0,t_0)} \approx \frac{\mathcal{A}(x_0, t_0 + \Delta t/2) - \mathcal{A}(x_0, t_0 - \Delta t/2)}{\Delta t} \tag{7}$$

$$\left.\frac{\partial \mathcal{A}}{\partial x}\right|_{(x_0,t_0)} \approx \frac{\mathcal{A}(x_0 + \Delta x/2, t_0) - \mathcal{A}(x_0 - \Delta x/2, t_0)}{\Delta x} \ , \tag{8}$$

in which (x_0, t_0) is at the center of one of the squares in the computational grid (see Fig. 1(a)). In this fashion, the TEM equations in (5)–(6) are approximated using central differences (see Fig. 1(b)):

$$\frac{\mathcal{H}_y|_{i+1/2}^{n+1/2} - \mathcal{H}_y|_{i+1/2}^{n-1/2}}{\Delta t} \approx \frac{1}{\mu}\left[\frac{\mathcal{E}_z|_{i+1}^{n} - \mathcal{E}_z|_{i}^{n}}{\Delta x} - \mathcal{M}_y|_{i+1/2}^{n}\right] \tag{9}$$

$$\frac{\mathcal{E}_z|_{i}^{n+1} - \mathcal{E}_z|_{i}^{n}}{\Delta t} \approx \frac{1}{\epsilon}\left[\frac{\mathcal{H}_y|_{i+1/2}^{n+1/2} - \mathcal{H}_y|_{i-1/2}^{n+1/2}}{\Delta x} - \mathcal{J}_z|_{i}^{n+1/2}\right] \ , \tag{10}$$

in which the common FDTD notation $\mathcal{A}|_i^n = \mathcal{A}(i\Delta x, n\Delta t)$ is used. It is observed from Fig. 1(b) that the field components $\mathcal{E}_z$ and $\mathcal{H}_y$ are staggered with respect to each other by $\Delta x/2$

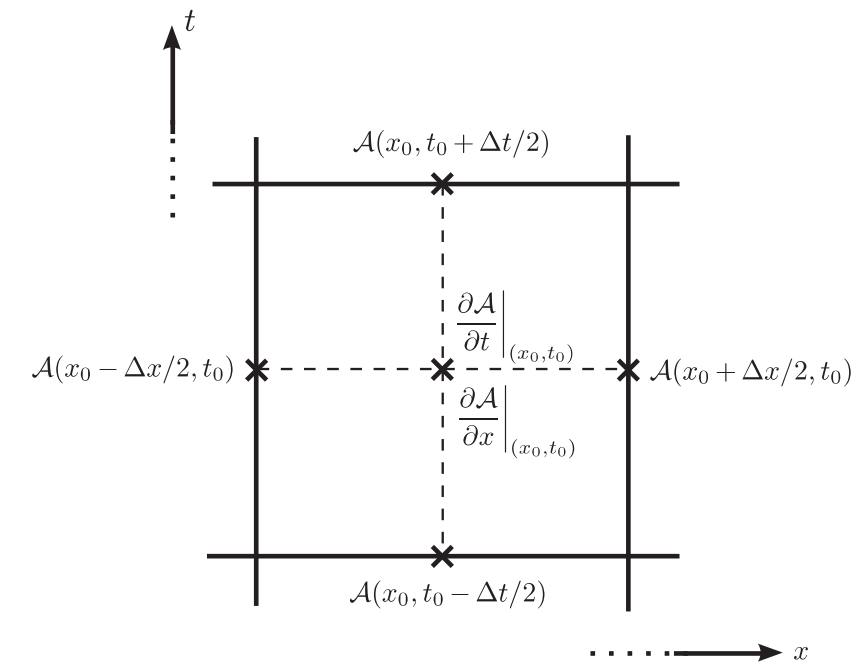

(a)

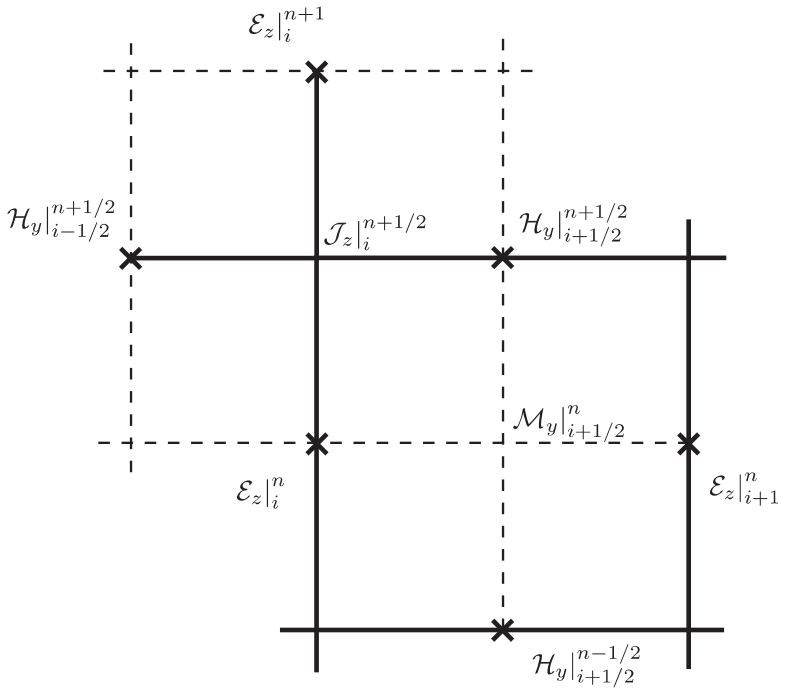

(b)

Figure 1: The central difference approximation in the FDTD method. (a) The space and time derivatives of the function $\mathcal{A}(x,t)$ are evaluated at the center of the square cell $(\Delta x, \Delta t)$ and approximated by central differences using the two adjacent values evaluated at the center of each edge. (b) Based on (a) and eq. (9)–(10), the TEM field components $\mathcal{E}_z$, $\mathcal{H}_y$ and the excitations $\mathcal{M}_y$, $\mathcal{J}_z$ are placed in the space-time grid as shown.

in space and by $\Delta t/2$ in time. Rewriting (9)–(10), we obtain the following *update equations*:

$$\mathcal{H}_y|_{i+1/2}^{n+1/2} \approx \mathcal{H}_y|_{i+1/2}^{n-1/2} + \frac{\Delta t}{\mu \Delta x}\left[\mathcal{E}_z|_{i+1}^{n} - \mathcal{E}_z|_{i}^{n} - \mathcal{M}_y|_{i+1/2}^{n}\,\Delta x\right] \tag{11}$$

$$\mathcal{E}_z|_{i}^{n+1} \approx \mathcal{E}_z|_{i}^{n} + \frac{\Delta t}{\epsilon \Delta x}\left[\mathcal{H}_y|_{i+1/2}^{n+1/2} - \mathcal{H}_y|_{i-1/2}^{n+1/2} - \mathcal{J}_z|_{i}^{n+1/2}\,\Delta x\right] \ . \tag{12}$$

As the name suggests, these equations are used to update the electric and magnetic field components at each time step. An update cycle consists of two updates according to (11)–(12). First, the value of the magnetic field component $\mathcal{H}_y$ at time $n+1/2$ is calculated using the previous value at time $n-1/2$ and the values of the nearby electric field component $\mathcal{E}_z$ at time n. Second, the value of the electric field component $\mathcal{E}_z$ at time $n+1$ is calculated using the previous value at time n and the values of the nearby magnetic field component $\mathcal{H}_y$ at time $n+1/2$. Since each field component "jumps" $1/2$ time step ahead of the other field component, the scheme is commonly called the *leapfrog algorithm*. With this algorithm, the values of the field variables are overwritten in each update cycle and it is not necessary to record the time history of any variable.

It can be shown [2] that stability requirements impose a limit on the choice of the grid spacing Δx and the time step Δt. The required relation between Δx and Δt in (11)–(12) is given by the *Courant stability criterion*:

$$\Delta t \leq \frac{\Delta x}{c} \ . \tag{13}$$

If this condition is not satisfied, the update equations (11)–(12) will support exponentially growing solutions for both $\mathcal{E}_z$ and $\mathcal{H}_y$. If these solutions exist, they will be inevitably triggered by any practical excitation. Therefore, if equations (11)–(12) are to be used, the criterion (13) must be strictly observed.

The FDTD method described above is applicable for time-varying fields that depend only on one spatial dimension (the x dimension for the TEM case given above). In two and three dimensions, the FDTD method is still applicable, with careful placement of the field components in space and time according the central difference scheme. Regardless of the number of dimensions in the problem, the electric and magnetic fields $\mathcal{E}$, $\mathcal{H}$ are centered in time in a leapfrog arrangement, as for the 1-D TEM problem described above. In space,

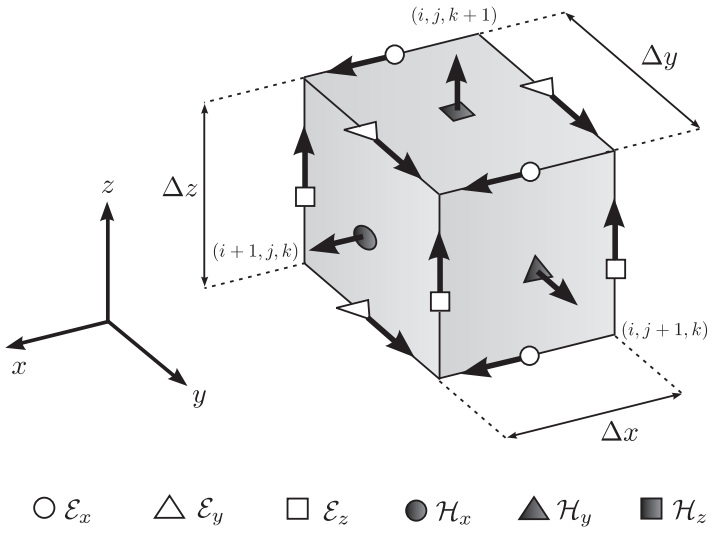

Figure 2: The spatial positioning of the six components of the electromagnetic field in a single cell in the Yee lattice. Identical field components are located at all edges and faces parallel to the ones shown here.

however, the staggered positioning of the field components for two and three dimensions requires extra attention. Therefore, we mainly concentrate on the spatial arrangement of the field components for two and three dimensions.

In three dimensions, the computational space is divided into cubic cells with dimensions $(\Delta x, \Delta y, \Delta z)$, forming a grid (called the *Yee lattice*, after Yee [3]). The six components of the electromagnetic field $\mathcal{E}_x$, $\mathcal{E}_y$, $\mathcal{E}_z$, $\mathcal{H}_x$, $\mathcal{H}_y$, $\mathcal{H}_z$ are positioned in space as shown in Fig. 2. Note that the electric field components $\mathcal{E}_x$, $\mathcal{E}_y$, $\mathcal{E}_z$ are placed at the centers of the *edges* of the grid cells and the magnetic field components $\mathcal{H}_x$, $\mathcal{H}_y$, $\mathcal{H}_z$ are placed at the centers of the *faces* of the grid cells. This spatial arrangement lends itself beautifully to the central difference approximation of the spatial derivatives of the field components. For example, the update equations for the field components $\mathcal{E}_y|^n_{i+1,j+1/2,k+1}$ and $\mathcal{H}_x|^{n-1/2}_{i+1,j+1/2,k+1/2}$ in Fig.

2 are given by

$$\mathcal{E}_y|^{n+1}_{i+1,j+1/2,k+1} = \mathcal{E}_y|^{n}_{i+1,j+1/2,k+1} + \frac{\Delta t}{\epsilon} \cdot \left[\frac{\mathcal{H}_x|^{n+1/2}_{i+1,j+1/2,k+3/2} - \mathcal{H}_x|^{n+1/2}_{i+1,j+1/2,k+1/2}}{\Delta z} - \frac{\mathcal{H}_z|^{n+1/2}_{i+3/2,j+1/2,k+1} - \mathcal{H}_z|^{n+1/2}_{i+1/2,j+1/2,k+1}}{\Delta x} - \mathcal{J}_y \right] \tag{14}$$

$$\mathcal{H}_x|^{n+1/2}_{i+1,j+1/2,k+1/2} = \mathcal{H}_x|^{n-1/2}_{i+1,j+1/2,k+1/2} + \frac{\Delta t}{\mu} \cdot \left[\frac{\mathcal{E}_y|^{n}_{i+1,j+1/2,k+1} - \mathcal{E}_y|^{n}_{i+1,j+1/2,k}}{\Delta z} - \frac{\mathcal{E}_z|^{n}_{i+1,j+1,k+1/2} - \mathcal{E}_z|^{n}_{i+1,j,k+1/2}}{\Delta y} - \mathcal{M}_x \right] . \tag{15}$$

The update equations for other field components can be written in a similar fashion [1, 2]. The key point to visualize is that each magnetic field component is surrounded by a square loop formed by four electric field components and vice versa. In (14)–(15), these four surrounding components are found in the central difference expressions within the square brackets.

FDTD applications almost invariably include *absorbing boundary conditions* (ABC) that absorb the incoming wave and thus emulate the extension of the finite geometry to infinity. Among the different approaches to ABCs, the *perfectly matched layer* (PML) [2, 4–6] has been the most popular. Another aspect of many FDTD applications is the extraction of radiated field (or far-field) information from near-field information obtained directly through FDTD simulation. For this purpose, *near-field-to-far-field transformers* (NFFFT) in free space have been proposed and successfully applied [2, 7]. In scattering problems, it is usually desirable to have a plane wave impinging on the scatterer under study. The incident wave can be efficiently introduced into the FDTD analysis of such problems by the use of *incident wave source conditions* [2]. The most widely used incident wave source condition method is the *total-field/scattered-field boundary* (TF/SF boundary), or the plane-wave injector method [2, 8, 9]. In this method, a special TF/SF boundary is formed and field corrections are applied on this boundary. Since we consider only *closed* TF/SF boundaries in our study, the terms *TF/SF boundary* and *TF/SF box* will be used interchangeably. In the case of a TF/SF box, the corrections serve to inject the desired incident fields into the box. The corrections are achieved by keeping track of the incident field values on the box at all times

and carefully adding these values to the field components on the box. In this manner, a perpetual contrast is maintained between the total fields (TF) inside the box and the scattered fields (SF) outside the box.

Historically, initial implementations of the techniques mentioned above (PML, NFFFT and TF/SF boundary) have been for free space. Some of these methods were later fully or partially generalized to planar multilayered media. The generalization of the PML to general multilayered media is quite straightforward [2]. However, full generalizations of the NFFFT and the TF/SF plane-wave injector to general multilayered media have not yet been documented. As mentioned before, the purpose of our work is achieving this generalization. A brief description of our research can be found in Sections 1.3–1.5. In Section 1.3, we present an introduction to the FDTD analysis of multilayered media. In Sections 1.4–1.5, we present the history of the application of the NFFFT and the TF/SF boundary to multilayered media, and briefly explain the contributions made by our research.

1.3 FDTD Analysis of Multilayered Media

One of the key advantages of the FDTD method is the simplicity of introducing material non-uniformities into the problem. For example, variations in the dielectric constant ϵ of the medium are simply introduced into the FDTD update equations by treating ϵ as a function of position: $\epsilon = \epsilon_{i,j,k}$. For a multilayered medium with the x axis as the symmetry axis, the electric field update equation (12) for the x-directed, z-polarized TEM wave becomes

$$\mathcal{E}_z|_i^{n+1} \approx \mathcal{E}_z|_i^n + \frac{\Delta t}{\epsilon_i \Delta x}\left[\mathcal{H}_y|_{i+1/2}^{n+1/2} - \mathcal{H}_y|_{i-1/2}^{n+1/2} - \mathcal{J}_z|_i^{n+1/2}\,\Delta x\right] . \tag{16}$$

The central difference scheme dictates that the dielectric constant ϵ_i be evaluated at the same space position (i) as the electric field, $\mathcal{E}_z|_i^n$. This is also true for three dimensions, an example of which can be given by reproducing (14) for non-uniform dielectric constant ϵ:

$$\mathcal{E}_y|_{i+1,j+1/2,k+1}^{n+1} = \mathcal{E}_y|_{i+1,j+1/2,k+1}^{n} + \frac{\Delta t}{\epsilon_{i+1,j+1/2,k+1}} \cdot \left[\frac{\mathcal{H}_x|_{i+1,j+1/2,k+3/2}^{n+1/2} - \mathcal{H}_x|_{i+1,j+1/2,k+1/2}^{n+1/2}}{\Delta z} - \frac{\mathcal{H}_z|_{i+3/2,j+1/2,k+1}^{n+1/2} - \mathcal{H}_z|_{i+1/2,j+1/2,k+1}^{n+1/2}}{\Delta x} - \mathcal{J}_y\right] . \tag{17}$$

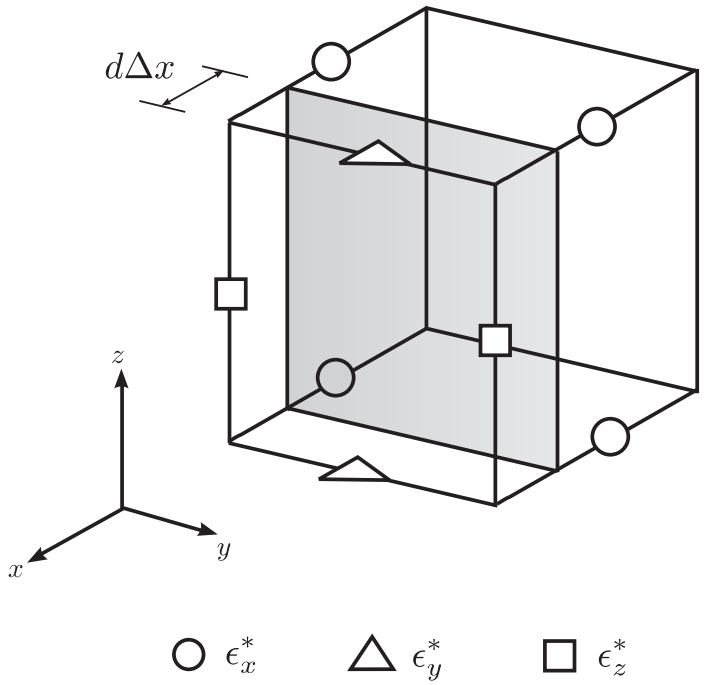

Figure 3: The FDTD modeling of a planar interface between two dielectric media. The locations of the effective permittivities ϵ_x^*, ϵ_y^*, ϵ_z^* in the grid cell are shown.

Note again that $\epsilon_{i+1,j+1/2,k+1}$ is evaluated at the same space position $(i+1, j+1/2, k+1)$ as the electric field, $\mathcal{E}_y|^n_{i+1,j+1/2,k+1}$.

Despite the simplicity of introducing non-uniformities in the dielectric constant into the FDTD update equations, appropriate placement of these non-uniformities into the Yee lattice requires care. The purpose is to model the dielectric discontinuity while maintaining second-order accuracy both in space and time. Even if the dielectric discontinuities coincide with the faces of the grid cells, it is no trivial task to determine the *effective permittivities* $\epsilon^*_{i,j,k}$ that must be placed at the cell edges in the vicinity of the discontinuity. For arbitrary variations of the dielectric constant, determining the values of these effective permittivities is a very difficult task. However, for planar multilayered media, exact values for the effective permittivities that are second-order accurate in space and time have been derived [10, 11]. The geometry of the grid associated with a planar interface between two media with permittivities ϵ_1 and ϵ_2 is shown in Fig. 3. It is assumed that the planar interface is parallel to the yz plane and at a distance $d\,\Delta x$ from the nearest tangential field component

in the positive x direction (without loss of generality, $d < 1/2$). The second-order accurate tangential and normal effective permittivities $\epsilon_{y,z}^*$, ϵ_x^* in Fig. 3 are given by

$$\begin{aligned} \epsilon_y^* = \epsilon_z^* &= \left(\frac{1}{2} + d\right)\epsilon_1 + \left(\frac{1}{2} - d\right)\epsilon_2 \\ \frac{1}{\epsilon_x^*} &= \frac{d}{\epsilon_1} + \frac{1-d}{\epsilon_2} \end{aligned} \tag{18}$$

It was mentioned in the previous sections that the near-field-to-far-field transform (NFFFT) method has not yet been generalized to general multilayered media. In this work, we present a generalization of this technique to *lossless* multilayered media. The other technique that we develop for use in the FDTD analysis of multilayered media is the total-field/scattered-field (TF/SF) boundary method, or the plane-wave injector. Our research provides a generalization of this technique to general (possibly lossy) multilayered media. A historical overview of the application of these techniques to the FDTD analysis of multilayered media is given in the following two sections. Our contributions to the literature in this area is given comparatively along with the overview.

1.4 NFFFT for Lossless Multilayered Media

The finite-difference time-domain (FDTD) method is frequently used to analyze the time-domain response of multilayered media. Although the FDTD method is inherently a near-field method, one is occasionally interested in the far-field response of the structure. As mentioned in Section 1.2, the near-field-to-far-field transform (NFFFT) method is used for this purpose. The geometry of the NFFFT for a *lossless* multilayered medium with $N+1$ layers is shown in Fig. 4. In Fig. 4(a), the structure A is radiating (or scattering) in the presence of a multilayered medium. The uppermost layer is free space and the lowermost layer is a dielectric half space with relative permittivity ϵ_{r_N}. The finite layers indexed by $i = 1, 2, \ldots, N-1$ are located between $z = -h_{i-1}$ and $z = -h_i$. For the NFFFT, there is a virtual closed surface S in the near field that encloses the structure A. The surface equivalence theorem [12] is invoked on the total tangential electric and magnetic near fields $\mathcal{E}_t$, $\mathcal{H}_t$ on S obtained through FDTD simulation. The resulting equivalent geometry is shown in Fig. 4(b). In the application of the equivalence theorem, the field-free volume inside S is filled to complete the multilayered structure. Then the equivalent electric and

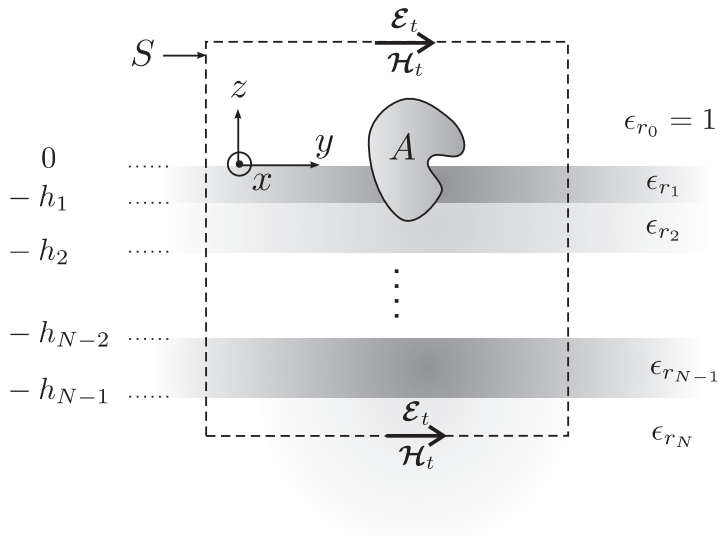

(a)

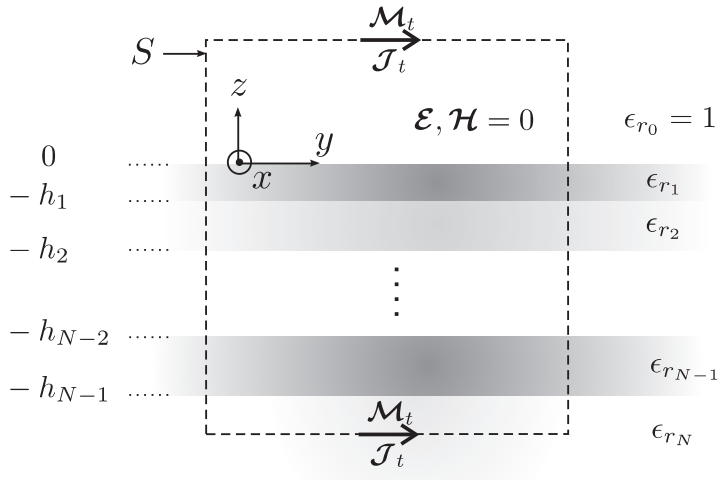

(b)

Figure 4: Geometry of the NFFFT for general lossless multilayered media. (a) The original geometry. (b) The equivalent geometry.

magnetic surface currents $\boldsymbol{\mathcal{J}}_t$, $\boldsymbol{\mathcal{M}}_t$ radiate in a perfect multilayered medium, for which the pertinent Green functions may be used [13]. These Green functions provide the very link between the *near field* and the *far field*, thereby constituting the basis of the *near-field*-to-*far-field* transformer. However, as explained next, obtaining these Green functions poses the greatest difficulty in deriving an efficient NFFFT for a general multilayered medium.

For radiation in free space, several frequency and time-domain near-field-to-far-field transforms (NFFFT) that obtain the far field using the available FDTD near-field data have been developed [2, 7]. The success of these methods is due to the simplicity of the free-space dyadic Green function for the vector potentials. However, the Green functions associated with multilayered geometries are much more complicated [13], which makes the NFFFT harder to implement and computationally more expensive. A frequency-domain NFFFT for a general lossy multilayered medium was introduced in [14]; and the method was applied to a half-space configuration. For the grounded dielectric slab, an approximate frequency-domain NFFFT has been reported in [15].

There has been very few attempts to develop a *direct time-domain* NFFFT for a multilayered medium ("direct time-domain" meaning that Fourier transforms are never used). The direct time-domain NFFFT for free space is well known [2, 7], however; to the authors' knowledge, the only direct time-domain NFFFT for a multilayered medium was given in [16] for the special case of a lossy dielectric half-space. However, this method involves the calculation of part of the far-field data by frequency-domain analysis followed by an inverse discrete Fourier transform (DFT). In this regard, the method does not follow a direct time-domain approach. Our research offers a direct time-domain NFFFT for lossless multilayered media, with *on-the-fly* calculation of the far-field waveform, as in [7].

Another advantage of the NFFFT introduced in our study is that it incorporates the *transmission-line* analogy into the far-field derivation. This analogy is commonly used in the derivation of Green functions for multilayered media [13, 17, 18]. Since the transmission-line Green functions are well-documented and relatively easy to derive [19], their incorporation into the method provides a common framework for successive generalization of the method to more general lossless multilayered media, as will be seen in Chapter 2.

An important point to be made is that our derivation considers only the *radiated* or far-zone field, which decays as $1/r$. Near the interfaces, cylindrical *surface waves* [13] may exist, which decay as $1/\sqrt{r}$. However, when the observation point is far away, the angular range in which the surface wave dominates is negligible.

1.5 TF/SF Boundary for General Multilayered Media

One of the most useful features of the FDTD method is the possibility of efficiently introducing an *incident plane wave* into the grid. It was mentioned in Section 1.2 that the most common technique used for this purpose is the total-field/scattered-field (TF/SF) boundary technique [2, 20, 21], which had been initially developed for free-space and awaits full generalization to multilayered media. In our work, we present an efficient TF/SF plane-wave source (or plane-wave injector) that is applicable for general lossy multilayered media. For this purpose, a generalization of the free-space TF/SF formulation is introduced. As in the free-space formulation, a special boundary, called the TF/SF boundary or the TF/SF box, is formed in the FDTD grid, and field corrections are applied on this boundary at each FDTD time step. The corrections serve the purpose of creating and isolating an incident plane wave inside the box, and they follow directly from the values of the incident plane wave on the TF/SF boundary. These field values are obtained numerically via an auxiliary FDTD simulation, which is carried out along with the main FDTD simulation. The procedure for achieving this will be described in Chapter 3.

The geometry for the TF/SF plane-wave injector is shown in Fig. 5 for a 5-layer medium. The TF/SF boundary is denoted by the rectangular prism that passes through the entire multilayered structure. The axis of symmetry is z, and the planar interfaces between the layers are represented by sheets with different shades of gray. The layers between the interfaces have relative permittivities ϵ_{r_n} and conductivities σ_n, for $n = 0 \ldots 4$. We restrict the uppermost and lowermost layers to half spaces with constant permittivity and conductivity (a perfectly-conducting half space is allowed for the lowermost layer). We also assume that the material properties ϵ_{r_n}, σ_n are independent of frequency, i.e., the only sources of dispersion are the frequency-independent conductivities of the layers. The uppermost layer is

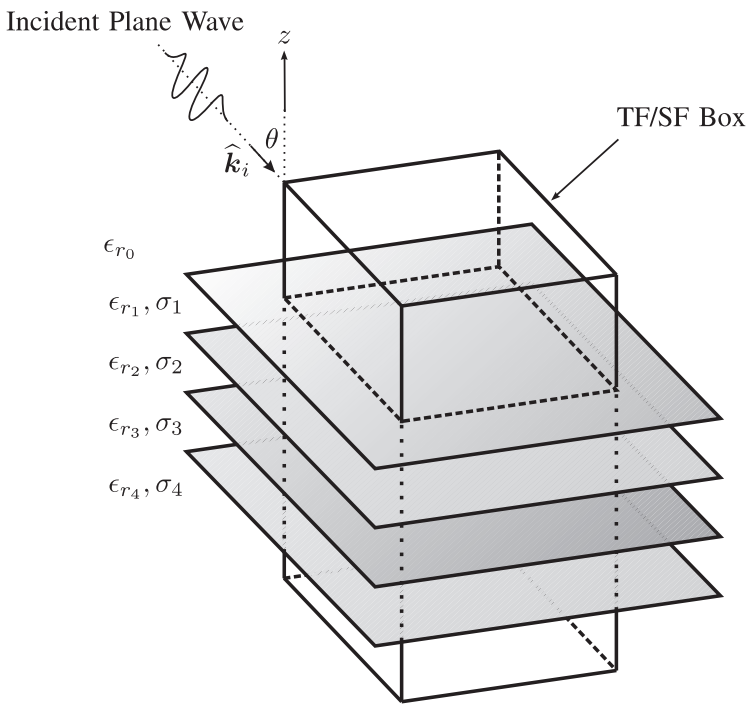

Figure 5: Geometry of the plane-wave injector for general lossy multilayered media.

assumed to be lossless ($\sigma_0 = 0$), which is justified by the need for a well-defined wavefront for the incoming plane wave that does not disperse until it makes contact with the dielectric layers. This wavefront is denoted by the wavy arrow in Fig. 5.

Being the central problem in any FDTD incident wave source, the a priori calculation of the incident field in the presence of the multilayered medium poses the main difficulty. Since the behavior of waves in a multilayered medium is much more complex than in free space, the exact calculation of the incident field is usually very complicated. This is true even for the simplest type of incident wave: the plane wave. The difficulty arises from the fact that, in a multilayered medium, the incident plane wave consists of not only the initial wavefront, but the numerous reflections from the boundaries of the layers as well.

A FDTD plane-wave injector for a simple multilayered medium such as a dielectric half space can be easily constructed using the exact theoretical formula for the reflected and transmitted fields, as done in [22]. The first FDTD plane-wave injector for a non-trivial multilayered medium appears to have been introduced by Hsu and Carin [23]. They developed a TF/SF boundary for injecting a plane wave on a 2-D scatterer (one that

is invariant in one spatial dimension) placed on an ungrounded infinite dielectric slab. In their implementation, they used the exact theoretical expression for the plane wave scattered from the ungrounded dielectric slab. In this regard, the method is strictly limited to this specific case. Furthermore, the method is only applicable when the direction of incidence is perpendicular to the axis of invariance, namely, when the incident plane wave has no variation along the axis of invariance. Recently, Yi et al. [24] introduced a generalization of this technique. They allowed oblique incidence with respect to the axis of invariance and removed the necessity of deriving theoretical formulas by obtaining the incident field via a 1-D auxiliary FDTD grid. Although their presentation was limited to a lossy ground, the technique is potentially applicable to any lossy multilayered medium. This potential had been partially recognized by Winton et al. [25]. They introduced a plane-wave injector for a general lossy multilayered medium using the aforementioned 1-D-auxiliary-grid technique. However, their analysis for lossy media includes a questionable step for the TE_z case, which will be discussed in further detail in Sec. 3.2. Furthermore, their TF/SF boundary extends into the upper and lower PML regions, which makes obtaining the far field with a near-field-to-far-field transform (NFFFT) impractical.

Neither of the above studies addresses vital issues such as the placement of the field variables, stability assessment, excitation techniques, etc. The issue of instability, which is encountered for large incidence angles, is an especially important one. In our work, we present a complete development of the plane-wave injector for general multilayered media by carefully assessing these issues. Our derivation also differs from that of Yi et al. [24] in that it lends itself naturally to generalization to other types of dispersive media.

Finally, neither of the techniques described above considers the presence of *inhomogeneous or evanescent plane waves* [1]. The plane-wave injector presented in this study has the capability of handling *narrowband* inhomogeneous plane waves as an extension of its traditional function of injecting homogeneous plane waves. The reasons for the assumption of a narrowband spectrum will be made clear in Chapter 3.

Compared to previous plane-wave injectors, the formulation introduced in our study provides another key advantage: the possibility of incorporating the NFFFT into the FDTD

analysis of scattering problems. This is because the developed TF/SF boundary does not penetrate into the PML layer (see Fig. 5), and therefore can be enclosed by a NFFFT surface. Hence, the plane-wave injector described here can be easily used together with the NFFFT, as will be seen in Chapter 4.

CHAPTER II

NFFFT FOR LOSSLESS MULTILAYERED MEDIA

2.1 General Considerations

The geometry used for the NFFFT in general multilayered media was given previously in Fig. 4(b), which is reproduced in Fig. 6 for convenience. The equivalent electric and magnetic surface currents $\boldsymbol{\mathcal{J}}_t$, $\boldsymbol{\mathcal{M}}_t$ radiate in the presence of the $(N+1)$-layered medium. For representing the direction of observation, we employ the usual spherical coordinates (r, θ, ϕ).

It is shown in Appendix A that the time-domain radiated electric field $\boldsymbol{\mathcal{E}}^r(\boldsymbol{r}, t)$ in air (uppermost half space with index 0) can be expressed as a superposition integral in terms of the time-domain surface currents $\boldsymbol{\mathcal{J}}_t$, $\boldsymbol{\mathcal{M}}_t$:

$$\boldsymbol{\mathcal{E}}^r(\boldsymbol{r}, t) = \frac{1}{2\pi c r} \frac{\partial}{\partial t} \Big[\mathcal{F}_\theta \left(\theta, \phi, t - r/c\right) \hat{\boldsymbol{\theta}} + \mathcal{F}_\phi \left(\theta, \phi, t - r/c\right) \hat{\boldsymbol{\phi}} \Big] \ , \tag{19}$$

in which $c = (\epsilon_0 \mu_0)^{-1/2}$ is the speed of light in free space, and

$$\mathcal{F}_{\theta,\phi}(\theta, \phi) = \iint_S \Big[\boldsymbol{\mathcal{G}}^{EJ}_{\theta,\phi}(\theta, \phi, t|z') \odot \boldsymbol{\mathcal{J}}_t(\boldsymbol{r}', t) + \boldsymbol{\mathcal{G}}^{EM}_{\theta,\phi}(\theta, \phi, t|z') \odot \boldsymbol{\mathcal{M}}_t(\boldsymbol{r}', t) \Big]_{t_r} dS' \ . \tag{20}$$

In these expressions, boldface script letter indicates a time varying vector. In the above integral, $t_r = t + (x' \cos\phi \sin\theta + y' \sin\phi \sin\theta)/c$ is the lateral retarded time, and the vector variables $\boldsymbol{\mathcal{G}}^{EJ,EM}_{\theta,\phi}$ are defined by

$$\boldsymbol{\mathcal{G}}^{EJ}_{\theta} = -\hat{\boldsymbol{x}} \mathcal{V}^e_i \cos\phi - \hat{\boldsymbol{y}} \mathcal{V}^e_i \sin\phi + \hat{\boldsymbol{z}} Z_0 \mathcal{V}^e_v \sin\theta / \epsilon'_r \tag{21}$$

$$\boldsymbol{\mathcal{G}}^{EM}_{\theta} = \hat{\boldsymbol{x}} \mathcal{V}^e_v \sin\phi - \hat{\boldsymbol{y}} \mathcal{V}^e_v \cos\phi \tag{22}$$

$$\boldsymbol{\mathcal{G}}^{EJ}_{\phi} = \hat{\boldsymbol{x}} \mathcal{V}^h_i \sin\phi \cos\theta - \hat{\boldsymbol{y}} \mathcal{V}^h_i \cos\phi \cos\theta \tag{23}$$

$$\boldsymbol{\mathcal{G}}^{EM}_{\phi} = \hat{\boldsymbol{x}} \mathcal{V}^h_v \cos\phi \cos\theta + \hat{\boldsymbol{y}} \mathcal{V}^h_v \sin\phi \cos\theta - \hat{\boldsymbol{z}} Y_0 \mathcal{V}^h_i \sin\theta \cos\theta \ . \tag{24}$$

In (20), the symbol $\odot$ denotes the convolutional dot product, defined by

$$\hat{\boldsymbol{a}} \mathcal{A}(t) \odot \hat{\boldsymbol{b}} \mathcal{B}(t) = (\hat{\boldsymbol{a}} \cdot \hat{\boldsymbol{b}})(\mathcal{A}(t) \star \mathcal{B}(t)) \ , \tag{25}$$

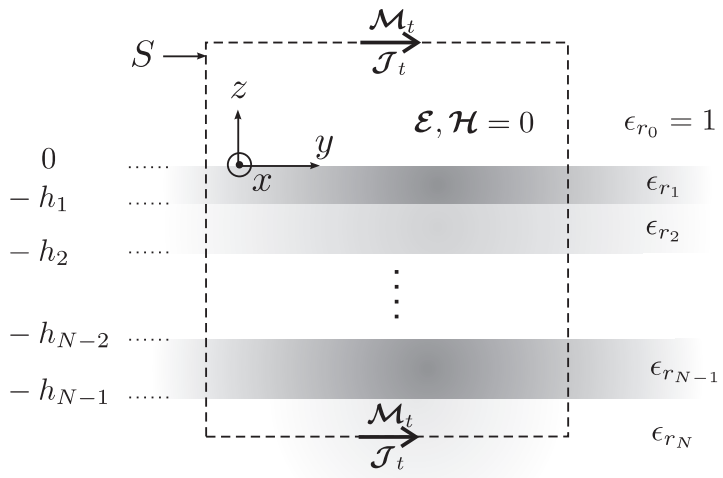

Figure 6: Equivalent geometry of the NFFFT for general lossless multilayered media.

in which $\mathcal{A}(t), \mathcal{B}(t)$ are time-dependent scalar variables, $\hat{\boldsymbol{a}}, \hat{\boldsymbol{b}}$ are time-independent vectors, and the symbol $\star$ denotes convolution in time. In (21)–(24), ϵ_r' denotes the relative permittivity at the source point, $Z_0 = 1/Y_0 = \sqrt{\mu_0/\epsilon_0}$ is the wave impedance of free space, and $\mathcal{V}_v^p(t|\, z'), \mathcal{V}_i^p(t|\, z')$ are quantities intimately related to *time-domain transmission-line* (TL) *Green functions* (polarization superscript p is e (TM) or h (TE)) [17]. They constitute the only part of the formulation in (19)–(24) that is dependent on the layering of the multilayered structure in Fig. 6. Detailed expressions for these functions for specific multilayered media (such as a dielectric half space, or a grounded dielectric slab) will be given in Section 2.2.

The results in (19)–(24) provide us with a direct link between the time-domain equivalent surface currents $\boldsymbol{\mathcal{J}}_t$, $\boldsymbol{\mathcal{M}}_t$ in Fig. 6, and the radiated electric field $\boldsymbol{\mathcal{E}}^r(\boldsymbol{r}, t)$ in the upper half space. This link is the theoretical basis for the direct FDTD NFFFT that eliminates any need for numerical inversion from frequency-domain to time-domain. The key aspect of these results is that the functions $\mathcal{V}_v^p(t|\, z')$, $\mathcal{V}_i^p(t|\, z')$ in (21)–(24) are in the form of an *impulse train* (see Section 2.2 for details). This is a direct result of the non-dispersion property of the multilayered medium. Owing to this phenomenon, the convolutions in (20) reduce to multiple shifting-and-delaying operations. Therefore, a direct time-domain NFFFT similar to the free-space NFFFT in [7] can be constructed for lossless multilayered

media, which is explained next.

The NFFFT for *free space* involves keeping track of *six* storage arrays that are updated after each FDTD time step. At the end of the simulation, these arrays are combined appropriately to yield the far-field waveforms. From (20) and (21)–(24), we see that a similar approach can be followed for the NFFFT for a *lossless multilayered medium* by keeping track of *ten* arrays. These arrays are for the following waveforms:

$$W_\alpha^p(\boldsymbol{r},t) = \iint_S \Big[\mathcal{V}_i^p(t|z') \star \mathcal{J}_\alpha(\boldsymbol{r}',t)\Big]_{t_r} dS' = \iint_S \sum_n a_n \mathcal{J}_\alpha(\boldsymbol{r}', t_r - \tau_n) dS' \tag{26}$$

$$W_z^e(\boldsymbol{r},t) = \iint_S \Big[\mathcal{V}_v^e(t|z') \star \mathcal{J}_z(\boldsymbol{r}',t)\Big]_{t_r} dS' = \iint_S \sum_n a_n \mathcal{J}_z(\boldsymbol{r}', t_r - \tau_n) dS' \tag{27}$$

$$U_\alpha^p(\boldsymbol{r},t) = \iint_S \Big[\mathcal{V}_v^p(t|z') \star \mathcal{M}_\alpha(\boldsymbol{r}',t)\Big]_{t_r} dS' = \iint_S \sum_n a_n \mathcal{M}_\alpha(\boldsymbol{r}', t_r - \tau_n) dS' \tag{28}$$

$$U_z^h(\boldsymbol{r},t) = \iint_S \Big[\mathcal{V}_i^h(t|z') \star \mathcal{M}_z(\boldsymbol{r}',t)\Big]_{t_r} dS' = \iint_S \sum_n a_n \mathcal{M}_z(\boldsymbol{r}', t_r - \tau_n) dS' \ , \tag{29}$$

in which α is x or y, p is e or h, $\mathcal{J}_{x,y,z}$, $\mathcal{M}_{x,y,z}$ refer to the x, y, z components of the surface currents $\boldsymbol{\mathcal{J}}_t$, $\boldsymbol{\mathcal{M}}_t$, and "$\star$" denotes convolution in time. Although the coefficients a_n and delays τ_n may be different for different arrays, a common notation has been used for the sake of clarity.

The discrete-time far-field storage arrays representing the waveforms in (26)–(29) are denoted as

$$W_\alpha^p|^n, \quad W_z^e|^n, \quad U_\alpha^p|^n, \quad U_z^h|^n \ . \tag{30}$$

After each FDTD time step, the above arrays are updated by numerical integration over the surface S, which is usually chosen to be the outer surface of a rectangular prism of FDTD cells. The surface S is therefore naturally divided into smaller patches that correspond to the faces of individual FDTD cells. The integrands in (26)–(29) are evaluated at the center of each patch. Note that the convolutions in these integrands reduce to summations of delayed replicas of the current waveforms, since $\mathcal{V}_v^p(t|\,z')$, $\mathcal{V}_i^p(t|\,z')$ are simply impulse trains. Remember that in the free space NFFFT, a single $\boldsymbol{\mathcal{J}}$ or $\boldsymbol{\mathcal{M}}$ value at a certain time is used to update only a *single* future position in the arrays for U or W. Inspection of (26)–(29) reveals that, in the NFFFT for lossless multilayered media, a single $\boldsymbol{\mathcal{J}}$ or $\boldsymbol{\mathcal{M}}$ value at a certain time is used to update *multiple* future positions in the arrays for U or

W. For example, the update for $W_z^e(\boldsymbol{r},t)$ after an FDTD time step consists of the following multiple recursive additions to the array $W_z^e|^n$:

$$W_z^e|^{n+f_k} = W_z^e|^{n+f_k} + \mathcal{J}_z|^n \cdot \Delta S, \qquad k = 1, 2, \dots \ , \tag{31}$$

in which $\mathcal{J}_z|^n$ denotes the current value $\mathcal{J}_z(\boldsymbol{r}', t_r)$ at the surface patch ΔS and lateral retarded time t_r, and $f_k = \tau_k/\Delta t$ is the k^{th} delay in terms of time steps. In the common case when f_k is not an integer, interpolation methods must be used to maintain second-order accuracy [2].

After the FDTD simulation is finished, the arrays in (30) are post-processed according to (19)–(24). The post-processing stage involves the interpolative time-alignment of the U and W arrays (due to the half-time-step difference between E and H), additive combination according to (21)–(24), and finally, time-differentiation according to (19).

2.2 Transmission-Line Green Functions

In this section, we provide expressions for the functions $\mathcal{V}_v^p(t|\, z')$, $\mathcal{V}_i^p(t|\, z')$ in the far-field formulation in (19)–(24). They are related (through a simple delay) to certain *transmission-line* (TL) *Green functions* associated with the geometry, hence the name of the current section. These TL Green functions, consequently $\mathcal{V}_v^p(t|\, z')$ and $\mathcal{V}_i^p(t|\, z')$, constitute the geometry-dependent part of the NFFFT described in the previous section. In other words, the implementation of the NFFFT for different multilayered media would differ only by the details regarding these functions.

The transmission lines mentioned above are defined by the transmission-line equations in Appendix A, (256)–(257), reproduced here for convenience:

$$\begin{aligned} \frac{\partial \mathcal{V}^e}{\partial z} &= -\left[\frac{\mu_0(\epsilon_r - \sin^2\theta)}{\epsilon_r}\right] \frac{\partial \mathcal{I}^e}{\partial t} \\ \frac{\partial \mathcal{I}^e}{\partial z} &= -\Big[\epsilon_0\epsilon_r\Big] \frac{\partial \mathcal{V}^e}{\partial t} \end{aligned} \qquad \text{(TM)} \tag{32}$$

$$\begin{aligned} \frac{\partial \mathcal{V}^h}{\partial z} &= -\Big[\mu_0\Big] \frac{\partial \mathcal{I}^h}{\partial t} \\ \frac{\partial \mathcal{I}^h}{\partial z} &= -\Big[\epsilon_0(\epsilon_r - \sin^2\theta)\Big] \frac{\partial \mathcal{V}^h}{\partial t} \end{aligned} \qquad \text{(TE)} \ . \tag{33}$$

These scalar transmission-line equations completely describe the behavior of the electromagnetic field in the multilayered medium. The "voltages" in the TL represent the tangential

(in the xy plane) components of the electric field, whereas the "currents" in the TL represent the tangential components of the magnetic field. The velocity of propagation v and the characteristic impedance Z^p of these transmission lines follow directly from Appendix A, (258)–(260):

$$v = c/\sqrt{\epsilon_r - \sin^2\theta} \tag{34}$$

$$Z^e = \frac{1}{Y^e} = Z_0\sqrt{\epsilon_r - \sin^2\theta}/\epsilon_r \tag{35}$$

$$Z^h = \frac{1}{Y^h} = Z_0/\sqrt{\epsilon_r - \sin^2\theta}\ , \tag{36}$$

in which $c = (\epsilon_0\mu_0)^{-1/2}$ is the velocity of propagation in free space, and $Z_0 = (\mu_0/\epsilon_0)^{1/2}$ is the wave impedance in free space. Because the velocity of propagation v and the characteristic impedances Z^p are independent of frequency, the transmission lines defined by (32)–(33) are *non-dispersive*, as is the underlying multilayered medium. Later in this section, this property will be of invaluable help in the derivation of the Green functions for the transmission lines.

It is shown in Appendix A that the functions $\mathcal{V}_v^p(t|\,z')$, $\mathcal{V}_i^p(t|\,z')$ in (21)–(24) are given by

$$\mathcal{V}_v^p(t|\,z') = \mathcal{V}_v^p(z_0, t + z_0\cos\theta/c|\,z') \tag{37}$$

$$\mathcal{V}_i^p(t|\,z') = \mathcal{V}_i^p(z_0, t + z_0\cos\theta/c|\,z')\ , \tag{38}$$

in which $\mathcal{V}_v^p(z_0, t|\,z')$, $\mathcal{V}_i^p(z_0, t|\,z')$ are the time-domain TL Green functions for the source coordinates $(z, t) = (z', 0)$ and observation coordinates $(z, t) = (z_0, t)$. They are defined as the voltage induced in the transmission line defined by (32) or (33) at the observation point z_0 at time t, created by an impulsive voltage/current at source point z' at time $t = 0$. The observation point z_0 is arbitrary, provided that it is above the uppermost material interface, i.e., $z_0 > 0$. Note that the notation implies that the time-advance $z_0\cos\theta/c$ cancels the z_0-dependence of $\mathcal{V}_v^p(z_0, t|\,z')$, $\mathcal{V}_i^p(z_0, t|\,z')$, and the final result $\mathcal{V}_v^p(t|\,z')$, $\mathcal{V}_i^p(t|\,z')$ becomes independent of z_0. This will be proven rigorously upon investigation of specific multilayered media in the following subsections.

It is now clear that the functions $\mathcal{V}_v^p(t|\,z')$, $\mathcal{V}_i^p(t|\,z')$, which constitute the basis of the far-field formulation in (19)–(24), are closely related to the transmission-line Green functions $\mathcal{V}_v^p(z_0,t|\,z')$, $\mathcal{V}_i^p(z_0,t|\,z')$ for the transmission lines defined by (32)–(33). The derivation of these TL Green functions is greatly aided by a schematic drawing of the transmission line associated with the geometry. In Fig. 7, we provide the schematic drawing of the transmission-line geometry associated with the general multilayered medium in Fig. 6. In Fig. 7(a), the TL setting used for obtaining the Green function $\mathcal{V}_v^p(z_0,t|\,z')$ is shown. The impulsive *voltage* source (both in space and time) is applied at position $z=z'$ and time $t=0$ within the n^{th} layer, and the voltage response $\mathcal{V}_v^p(z_0,t|\,z')$ is observed at $z=z_0$ in the the uppermost layer. In Fig. 7(b), the TL setting used for obtaining the Green function $\mathcal{V}_i^p(z_0,t|\,z')$ is shown. The impulsive *current* source (both in space and time) is applied at position $z=z'$ and time $t=0$ within the n^{th} layer, and the voltage response $\mathcal{V}_i^p(z_0,t|\,z')$ is observed at $z=z_0$ in the the uppermost layer.

It should be noted that the TL Green functions $\mathcal{V}_v^p(z_0,t|\,z')$, $\mathcal{V}_i^p(z_0,t|\,z')$ are defined in time domain. For the derivation of these functions, we shall use the well-known *frequency-domain* results for the TL Green functions [19]. We start by writing the simple frequency-domain TL Green functions $V_v^p(z_0|z')$, $V_i^p(z_0|z')$ for a uniform transmission line:

$$V_v^p(z_0|z') = \frac{\text{sgn}(z_0-z)}{2} e^{-jk^p|z_0-z|} \tag{39}$$

$$V_i^p(z_0|z') = \frac{Z^p}{2} e^{-jk^p|z_0-z|}\ , \tag{40}$$

in which k^p, Z^p are the propagation constant and the wave impedance of the uniform transmission line, respectively. Because the transmission line in Fig. 7 is non-dispersive, the inversion of the frequency-domain results in (39)–(40) to time domain can be performed quite easily. After this inversion, we arrive at the following result for the time-domain TL Green functions:

$$\mathcal{V}_v^p(z_0,t|z') = \frac{\text{sgn}(z_0-z)}{2}\,\delta\left(t-|z_0-z|/c\right) \tag{41}$$

$$\mathcal{V}_i^p(z_0,t|z') = \frac{Z^p}{2}\,\delta\left(t-|z_0-z|/c\right)\ , \tag{42}$$

in which $\delta(\cdot)$ denotes the impulse function, and $c=\omega/k^p$ is the velocity of propagation in

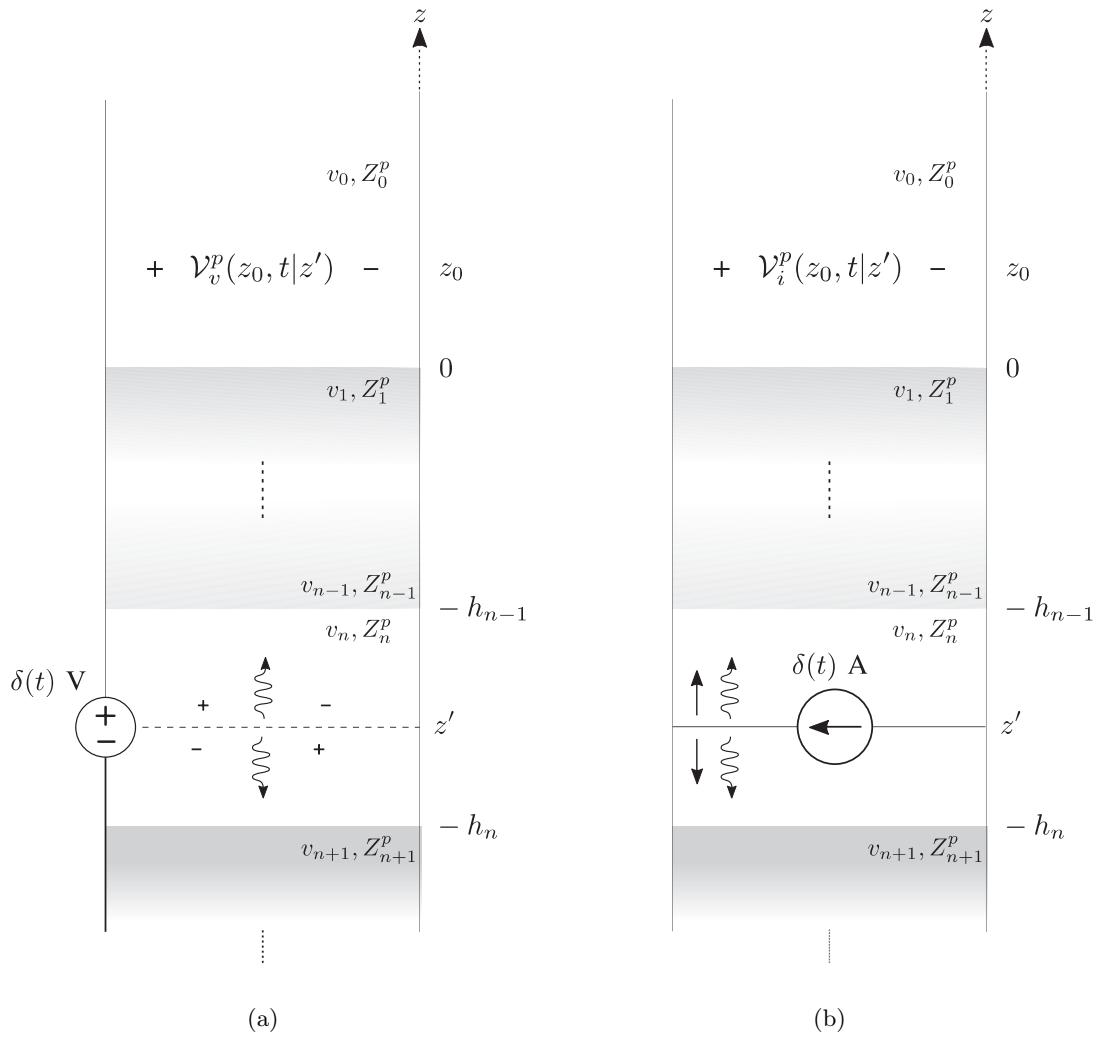

Figure 7: The transmission-line geometry associated with the multilayered medium in Fig. 6. (a) Voltage excitation. (b) Current excitation.

the uniform transmission line. The interpretation of (41)–(42) is quite intuitive: A time-domain voltage impulse applied to the TL as in Fig. 7(a) immediately creates two impulsive (in space) voltage waves traveling in opposite directions in the TL, with opposite signs and half the amplitude of the original voltage impulse. Similarly, a time-domain current impulse applied to the TL as in Fig. 7(b) immediately creates two impulsive current waves traveling in opposite directions in the TL, with opposite signs and half the amplitude of the original current impulse.

The TL Green functions (39)–(42) were derived for a uniform transmission line; however, our transmission line in Fig. 7 is piecewise-continuous. The effect of the discontinuities in the TL on the time-domain TL Green functions in (41)–(42) is the addition of *reflected* and *transmitted* impulses to the TL Green function, apart from the two impulses created right after the application of the impulsive voltage/current in Fig. 7(a)/7(b). The mechanism of reflection and transmission at the discontinuities in the TL is very simple, due to the non-dispersion of the TL. For example, when the upward-traveling impulsive voltage wave in Fig. 7(a) impinges on the boundary at $z = -h_{n-1}$, an impulsive wave of amplitude $\Gamma^p_{n,n-1}/2$ is reflected back into the n^{th} layer, and impulsive wave of amplitude $\Upsilon^p_{n,n-1}/2$ is transmitted into the $(n-1)^{\text{th}}$ layer. The coefficients $\Gamma^p_{n,n-1}$ and $\Upsilon^p_{n,n-1}$ are the *reflection* and *transmission* coefficients at the interface at $z = -h_{n-1}$, given simply by

$$\Gamma^p_{n,n-1} = \frac{Z^p_{n-1} - Z^p_n}{Z^p_{n-1} + Z^p_n} \tag{43}$$

$$\Upsilon^p_{n,n-1} = 1 + \Gamma^p_{n,n-1} = \frac{2Z^p_{n-1}}{Z^p_{n-1} + Z^p_n} \ . \tag{44}$$

It is seen from (35)–(36) that the characteristic impedances Z^p are independent of frequency. This also makes the reflection and transmission coefficients in (43)–(44) independent of frequency, which is the main reason for the preservation of the impulsive shape in the reflection/transmission process. As a side note, we mention the following interesting fact: Upon substitution of (35)–(36) into (43)–(44) quickly reveals that the coefficients in (43)–(44) are *Fresnel reflection and transmission coefficients* for plane-wave incidence with polarization p at a planar interface [12].

We now have all the information required for the derivation of the TL Green functions

$\mathcal{V}_v^p(z_0, t|\, z')$, $\mathcal{V}_i^p(z_0, t|\, z')$. We know that an impulsive excitation applied at $z = z'$ creates two impulses traveling in the opposite direction, and these impulsive waves obey very simple propagation and reflection rules dictated by (41)–(42) and (43)–(44). However, keeping track of the reflected and transmitted impulses is generally not a trivial task. In fact, the reflected and transmitted impulses can be written in closed form only for $N \leq 2$, where $N + 1$ is the number of layers in the multilayered medium in Fig. 6. For $N > 2$, recursive relations can be derived between the impulse trains observed at different positions in the TL. The recursive nature of these relations allows for easy translation to computer code, since recursive calls to functions are supported by almost every major programming language, including Fortran and C.

In the following subsections, we consider multilayered media of increasing complexity, and provide expressions for $\mathcal{V}_v^p(t|\, z'), \mathcal{V}_i^p(t|\, z')$ in each geometry. We describe only the derivation of $\mathcal{V}_v^p(t|\, z')$ in detail, since $\mathcal{V}_i^p(t|\, z')$ can be obtained from $\mathcal{V}_v^p(t|\, z')$ via multiplication by Z^p and a sign change for the downward-propagating impulse, see (41)–(42).

2.2.1 Dielectric Half-Space

The dielectric half space is a two-layered medium with air as the uppermost layer and lossless dielectric half space with relative permittivity ϵ_r as the lowermost layer. The geometry of the dielectric half space is shown in Fig. 8(a). The electric and magnetic surface currents $\boldsymbol{\mathcal{J}}_t$, $\boldsymbol{\mathcal{M}}_t$ on S are radiating in the presence of the dielectric half space. The radiated electric field due to these currents are given by (19) with (20)–(24). For obtaining the time-domain functions $\mathcal{V}_v^p(t|\, z'), \mathcal{V}_i^p(t|\, z')$, we consider the transmission-line geometry associated with the dielectric half space, shown in Fig. 8(b). We focus primarily on $\mathcal{V}_v^p(t|\, z')$, hence only the voltage-excitation case is shown in Fig. 8(b). The results for the current-excitation case can be obtained trivially from those for the voltage-excitation case, as mentioned in the previous section.

Using (34)–(36) and (43)–(44), the propagation velocities, characteristic impedances and

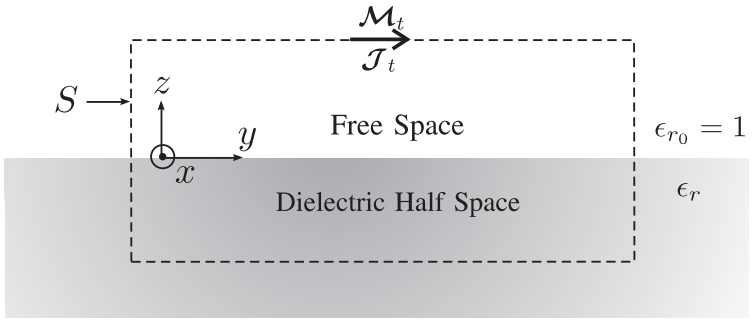

(a)

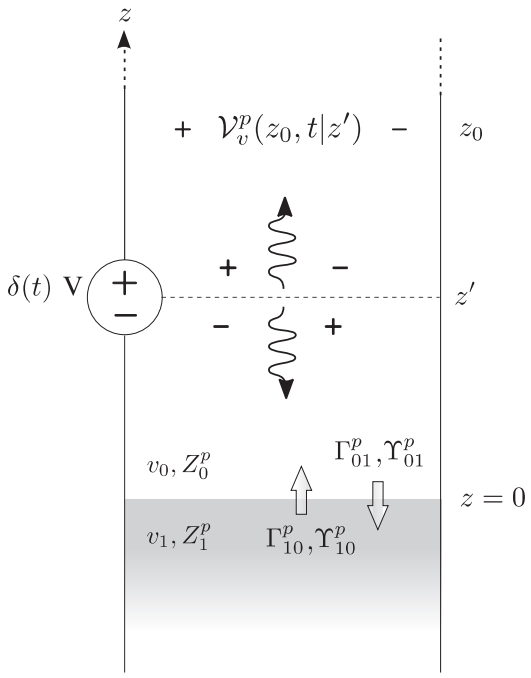

(b)

Figure 8: The geometry of the dielectric half space. (a) The geometry of the medium. (b) The associated transmission-line geometry (with voltage excitation.)

reflection/transmission coefficients for the TL in Fig. 8(b) are obtained as follows:

$$v = \begin{cases} v_0 = c/\cos\theta, & z > 0 \\ v_1 = c/\sqrt{\epsilon_r - \sin^2\theta}, & z < 0 \end{cases} \tag{45}$$

$$Z^e = \begin{cases} Z_0^e = Z_0 \cos\theta, & z > 0 \\ Z_1^e = Z_0\sqrt{\epsilon_r - \sin^2\theta}/\epsilon_r, & z < 0 \end{cases} \tag{46}$$

$$Z^h = \begin{cases} Z_0^h = Z_0/\cos\theta, & z > 0 \\ Z_1^h = Z_0/\sqrt{\epsilon_r - \sin^2\theta}, & z < 0 \end{cases} \tag{47}$$

$$\begin{aligned} \Gamma_{01}^p &= \Upsilon_{01}^p - 1 = \frac{Z_1^p - Z_0^p}{Z_1^p + Z_0^p} \\ \Gamma_{10}^p &= \Upsilon_{10}^p - 1 = -\Gamma_{01}^p \end{aligned} \tag{48}$$

In Fig. 8(b), a unit-amplitude impulsive voltage source is applied at the source point $z = z'$ above the interface. As shown previously in this section, this impulsive excitation creates two impulsive (in space) voltage waves traveling in opposite directions in the TL, with opposite signs and amplitude 1/2. These waves are shown by the two wavy arrows in Fig. 8(b). The upward-traveling wave propagates with velocity $v_0 = c/\cos\theta$ [from (45)] and makes the following contribution to the voltage at $z = z_0$:

$$\frac{1}{2}\ \delta\left(t - \frac{(z_0 - z')}{v_0}\right)\ . \tag{49}$$

The downward-traveling wave in Fig. 8(b) propagates in the $-z$ direction with with velocity v_0, until it comes in contact with the interface at $z = 0$. At this point, it splits into two impulsive waves: one being reflected back into the upper half space, and the other being transmitted into the lower half space. The reflected wave makes the following contribution to the voltage at $z = z_0$:

$$-\frac{\Gamma_{01}^p}{2}\ \delta\left(t - \frac{(z' + z_0)}{v_0}\right)\ , \tag{50}$$

whereas the downward-traveling component makes no contribution to the voltage at $z = z_0$, since the dielectric half space extends to infinity in the $-z$ direction, hence the impulsive wave does not reflect from any discontinuity. Combining (49)–(50), and applying the time-advance $z_0\cos\theta/c$ in (37), we obtain the following expression for $\mathcal{V}_v^p(t|\,z')$ when $z' > 0$:

$$\mathcal{V}_v^p(t|\,z') = \frac{1}{2}\ \delta\left(t + \frac{z'}{v_0}\right) - \frac{\Gamma_{01}^p}{2}\ \delta\left(t - \frac{z'}{v_0}\right), \qquad z' > 0 \tag{51}$$

If the source point in Fig. 8(b) is *below* the interface ($z' < 0$), the impulsive waves reaching the observation point $z = z_0$ follow a different route. After the application of the impulsive excitation, two impulsive waves are created in the lower half space. The downward-traveling wave goes into the lower half space and does not reflect from anything. The upward-traveling wave propagates in the lower half space with velocity $v_1 = c/\sqrt{\epsilon_r - \sin^2\theta}$ [from (45)] before reaching the interface at $z = 0$. At the interface, it splits into two impulsive waves: one being transmitted into the upper half space, and the other being reflected back into the lower half space. The transmitted wave makes the following contribution to the voltage at $z = z_0$:

$$\frac{\Upsilon_{10}^p}{2}\ \delta\left(t - \frac{z_0}{v_0} + \frac{z'}{v_1}\right)\ , \tag{52}$$

whereas the reflecting wave goes into the lower half space and makes no contribution to the voltage at $z = z_0$. Similar to the case for $z' > 0$, we apply the time-advance $z_0 \cos\theta/c$ in (37) to (52), and obtain the following expression for $\mathcal{V}_v^p(t|\,z')$ when $z' < 0$:

$$\mathcal{V}_v^p(t|\,z') = \frac{\Upsilon_{10}^p}{2}\ \delta\left(t + \frac{z'}{v_1}\right), \qquad z' < 0 \tag{53}$$

In summary, the function $\mathcal{V}_v^p(t|\,z')$ for the dielectric half space can be written as the combination of (51) and (53), covering every case for z':

$$\mathcal{V}_v^p(t|\,z') = \begin{cases} \dfrac{1}{2}\ \delta\left(t + \dfrac{z'}{v_0}\right) - \dfrac{\Gamma_{01}^p}{2}\ \delta\left(t - \dfrac{z'}{v_0}\right) & ,\quad z' > 0 \\ \dfrac{\Upsilon_{10}^p}{2}\ \delta\left(t + \dfrac{z'}{v_1}\right) & ,\quad z' < 0\ . \end{cases} \tag{54}$$

To obtain $\mathcal{V}_i^p(t|\,z')$, (54) is multiplied by Z^p and the sign of the second term for $z' > 0$ is reversed. This yields the following expression for $\mathcal{V}_i^p(t|\,z')$:

$$\mathcal{V}_i^p(t|\,z') = \begin{cases} \dfrac{Z_0^p}{2}\ \delta\left(t + \dfrac{z'}{v_0}\right) + \dfrac{Z_0^p\Gamma_{01}^p}{2}\ \delta\left(t - \dfrac{z'}{v_0}\right) & ,\quad z' > 0 \\ \dfrac{Z_1^p\Upsilon_{10}^p}{2}\ \delta\left(t + \dfrac{z'}{v_1}\right) & ,\quad z' < 0\ . \end{cases} \tag{55}$$

2.2.2 Grounded Dielectric Slab

The grounded dielectric slab is a three-layered medium with air as the uppermost layer, a lossless dielectric slab with relative permittivity ϵ_r as the middle layer, and a perfectly-conducting ground as the lowermost layer. The geometry of the grounded dielectric slab is

shown in Fig. 9. The electric and magnetic surface currents $\boldsymbol{\mathcal{J}}_t$, $\boldsymbol{\mathcal{M}}_t$ on S are radiating in the presence of the grounded dielectric slab. The radiated electric field due to these currents are given by (19) with (20)–(24). For obtaining the time-domain functions $\mathcal{V}_v^p(t|\,z')$, $\mathcal{V}_i^p(t|\,z')$, we consider the transmission-line geometry associated with the grounded dielectric slab, shown in Fig. 9(b). Again, we focus primarily on $\mathcal{V}_v^p(t|\,z')$, hence only the voltage-excitation case is shown in Fig. 9(b). The results for the current-excitation case can be obtained trivially from those for the voltage-excitation case.

We define the propagation velocities v_n, characteristic impedances Z_n^p and reflection/ transmission coefficients Γ_{mn}^p, Υ_{mn}^p in Fig. 9(b) in the exact same manner as in the previous section, (45)–(48). Using these definitions, we are now ready to derive the time-domain function $\mathcal{V}_v^p(t|\,z')$ by following a similar method as we did in the previous section, namely, by keeping track of the impulses reflected and transmitted at the material interfaces.

In Fig. 9(b), a unit impulsive excitation is applied at $z = z'$ above the grounded dielectric slab (the case in which the source is inside the slab will be considered later.) This excitation creates two impulses traveling in opposite directions, $+z$ and $-z$. The impulsive wave traveling in the $+z$ direction with amplitude 1/2 makes the following contribution to the voltage at $z = z_0$:

$$\frac{1}{2}\,\delta\left(t - \frac{(z_0 - z')}{v_0}\right)\ . \tag{56}$$

The first contribution of the impulsive wave traveling in the $-z$ direction is the impulse that is reflected at the interface $z = 0^+$:

$$-\,\frac{\Gamma_{01}^p}{2}\,\delta\left(t - \frac{(z_0 + z')}{v_0}\right)\ . \tag{57}$$

The remaining contribution comes from the impulse that is transmitted into the region $z < 0$. Reaching the interface $z = 0^-$ after being reflected from the short circuit at $z = -h$, this impulse makes the following contribution to the voltage at $z = z_0$:

$$\frac{\Upsilon_{01}^p}{2}\mathcal{V}^p\left(t - \frac{(z_0 + z')}{v_0} - \frac{2h}{v_1}\right)\ , \tag{58}$$

in which the function $\mathcal{V}^p(t)$ is given by

$$\mathcal{V}^p(t) = \sum_{n=0}^{\infty} \Upsilon_{10}^p(-\Gamma_{10}^p)^n \delta\left(t - 2nh/v_1\right)\ . \tag{59}$$

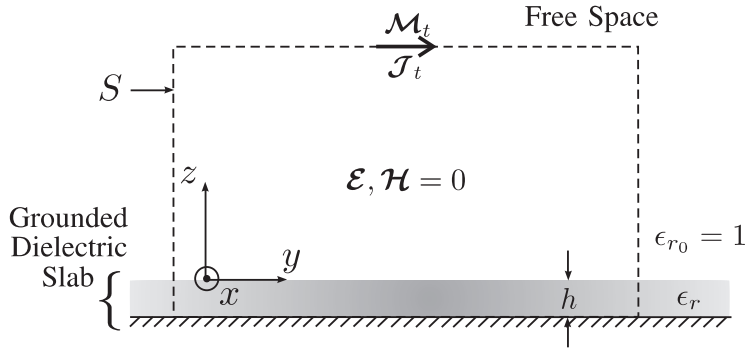

(a)

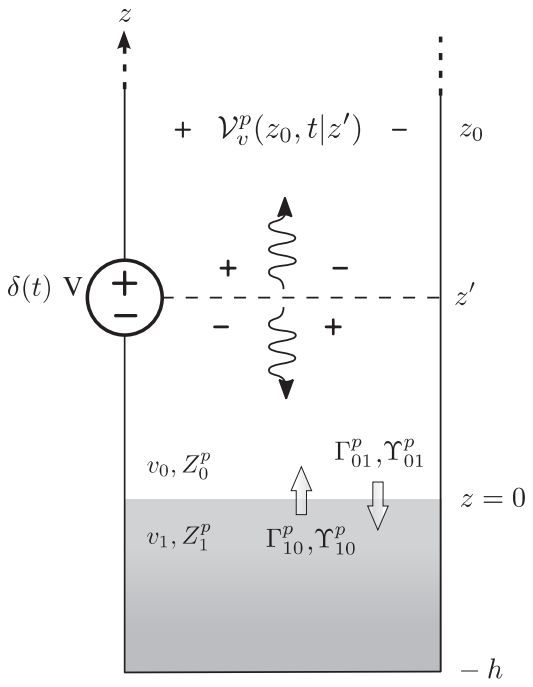

(b)

Figure 9: The geometry of the grounded dielectric slab. (a) The geometry of the medium. (b) The associated transmission-line geometry (with voltage excitation.)

This impulse train represents the voltage induced at $z = 0^+$ by an impulsive voltage wave at $z = 0^-$ traveling in the $+z$ direction. It should be noted that $\mathcal{V}^p(t)$ is an *infinite* impulse train, due to the infinite number of reflections within the slab. In practice, one has to truncate the impulse train at a certain point. Fortunately, the individual impulses decay exponentially in (59), since $|\Gamma^p_{10}| < 1$ unless $\theta = \pi/2$ (grazing angle). It therefore follows that for $\theta \approx \pi/2$, more impulses must be included in $\mathcal{V}^p(t)$, and the computational burden in (31) increases.

Adding the contributions (56)–(58) and applying the time-advance in (37), we obtain the following expression for $\mathcal{V}^p_v(t|\, z')$ when $z' > 0$:

$$\mathcal{V}^p_v(t|\, z') = \frac{1}{2}\,\delta\left(t + \frac{z'}{v_0}\right) - \frac{\Gamma^p_{01}}{2}\,\delta\left(t - \frac{z'}{v_0}\right) + \frac{\Upsilon^p_{01}}{2}\mathcal{V}^p\left(t - \frac{z'}{v_0} - \frac{2h}{v_1}\right)\ . \tag{60}$$

For $z' < 0$, the derivation of $\mathcal{V}^p_v(z_0, t|\, z')$ follows along the same lines. The contribution of the impulse wave traveling in the $+z$ direction is

$$\frac{1}{2}\mathcal{V}^p\left(t - \frac{z_0}{v_0} + \frac{z'}{v_1}\right)\ , \tag{61}$$

whereas the contribution of the wave traveling in the $-z$ direction is

$$\frac{1}{2}\mathcal{V}^p\left(t - \frac{z_0}{v_0} - \frac{(2h + z')}{v_1}\right)\ . \tag{62}$$

Adding the contributions (61)–(62) and applying the time-advance in (37), we obtain the following expression for $\mathcal{V}^p_v(t|\, z')$ when $-h < z' < 0$:

$$\mathcal{V}^p_v(t|\, z') = \frac{1}{2}\mathcal{V}^p\left(t + \frac{z'}{v_1}\right) + \frac{1}{2}\mathcal{V}^p\left(t - \frac{(2h + z')}{v_1}\right) \tag{63}$$

In summary, the function $\mathcal{V}^p_v(t|\, z')$ for the grounded dielectric slab can be written as the combination of (60) and (63), covering every case for z':

$$\mathcal{V}^p_v(t|\, z') = \begin{cases} \dfrac{1}{2}\,\delta\left(t + \dfrac{z'}{v_0}\right) - \dfrac{\Gamma^p_{01}}{2}\,\delta\left(t - \dfrac{z'}{v_0}\right) & \\ \qquad + \dfrac{\Upsilon^p_{01}}{2}\mathcal{V}^p\left(t - \dfrac{z'}{v_0} - \dfrac{2h}{v_1}\right) & ,\quad z' > 0 \\ \dfrac{1}{2}\,\mathcal{V}^p\left(t + \dfrac{z'}{v_1}\right) & \\ \qquad + \dfrac{1}{2}\mathcal{V}^p\left(t - \dfrac{(2h + z')}{v_1}\right) & ,\quad -h < z' < 0\ . \end{cases} \tag{64}$$

To obtain $\mathcal{V}_i^p(t|\,z')$, (64) is multiplied by Z^p, and the signs of all but the first terms are reversed. This yields the following expression for $\mathcal{V}_i^p(t|\,z')$:

$$\mathcal{V}_i^p(t|\,z') = \begin{cases} \dfrac{Z_0^p}{2}\,\delta\left(t+\dfrac{z'}{v_0}\right) + \dfrac{Z_0^p\Gamma_{01}^p}{2}\,\delta\left(t-\dfrac{z'}{v_0}\right) & \\ \qquad - \dfrac{Z_0^p\Upsilon_{01}^p}{2}\mathcal{V}^p\left(t-\dfrac{z'}{v_0}-\dfrac{2h}{v_1}\right) & , \quad z'>0 \\ \dfrac{Z_1^p}{2}\,\mathcal{V}^p\left(t+\dfrac{z'}{v_1}\right) & \\ \qquad - \dfrac{Z_1^p}{2}\mathcal{V}^p\left(t-\dfrac{(2h+z')}{v_1}\right) & , \quad -h<z'<0\ . \end{cases} \tag{65}$$

The difference between the functions $\mathcal{V}_v^p(t|\,z')$, $\mathcal{V}_i^p(t|\,z')$ for the dielectric half space [(54) and (55)] and those for the grounded dielectric slab [(64) and (65)], is a very crucial one: The functions $\mathcal{V}_v^p(t|\,z')$, $\mathcal{V}_i^p(t|\,z')$ for the grounded dielectric slab are *infinite impulse trains*, unlike those for the dielectric half space, which are finite in duration. The infinite nature of these functions is a result of the infinite number of reflections within the slab, and is quantified by the function $\mathcal{V}^p(t)$ given in (59). In the discussion following (59), it was noted that this infinite impulse train has to be truncated in practical applications, and this truncation is almost always possible since $|\Gamma_{10}^p| < 1$ (unless $\theta = \pi/2$). As the number of impulses taken for the truncated $\mathcal{V}^p(t)$ increases, the computational burden on the NFFFT increases. Specifically, the increased burden is manifested as an increased number of updates in the multiple-updating of the arrays U and W at each time step, as indicated in (31). The total number of impulses in $\mathcal{V}^p(t)$ is usually reasonable unless $\theta \approx 90^\circ$ (grazing angle), for which $|\Gamma_{10}^p| \approx 1$ in (59). In that case, the amplitudes of the delayed impulses decay slowly. As a measure of the mentioned computational burden, we can estimate the number of reflections that have amplitudes above a certain fixed threshold K. From the Taylor series expansions of (48) with (46)–(47) evaluated around $\theta = \pi/2$, it can be shown that the number of reflections with amplitude above K becomes, as $\theta \to \pi/2$,

$$n \approx \frac{\sqrt{\epsilon_r - 1}\ \ln K}{2}\ (\theta - \pi/2)^{-1}\ . \tag{66}$$

Hence, the overhead increases as the inverse of $(\theta - \pi/2)$ when θ is close to $\pi/2$.

Finally, note that the bottom face of the NFFFT box in Fig. 9 coincides with the ground plane. This is usually desirable because the ground plane cancels the effect of the equivalent

electric current $\boldsymbol{\mathcal{J}}_t$ and allows us to discard the bottom face in the transform process.

2.2.3 Ungrounded Dielectric Slab

The ungrounded dielectric slab is a three-layered medium with air as the uppermost layer, a lossless dielectric slab with relative permittivity ϵ_{r_1} as the middle layer, and a lossless dielectric half space with relative permittivity ϵ_{r_2} as the lowermost layer. The geometry of the ungrounded dielectric slab is shown in Fig. 10. The electric and magnetic surface currents $\boldsymbol{\mathcal{J}}_t$, $\boldsymbol{\mathcal{M}}_t$ on S are radiating in the presence of the ungrounded dielectric slab. The radiated electric field due to these currents are given by (19) with (20)–(24). For obtaining the time-domain functions $\mathcal{V}_v^p(t|\,z'), \mathcal{V}_i^p(t|\,z')$, we consider the transmission-line geometry associated with the ungrounded dielectric slab, shown in Fig. 10(b). Again, we focus primarily on $\mathcal{V}_v^p(t|\,z')$; the results for the current-excitation follow trivially from those for the voltage-excitation case.

In Fig. 10(b), the propagation velocities v_n, characteristic impedances Z_n^p, and reflection/transmission coefficients Γ_{mn}^p, Υ_{mn}^p are defined in accordance with the numbering for the layers in the piecewise-continuous medium:

$$v_n = c/\sqrt{\epsilon_{r_n} - \sin^2\theta} \qquad n = 0, 1, 2 \tag{67}$$

$$Z_n^e = Z_0\sqrt{\epsilon_{r_n} - \sin^2\theta}/\epsilon_{r_n} \qquad n = 0, 1, 2 \tag{68}$$

$$Z_n^h = Z_0/\sqrt{\epsilon_{r_n} - \sin^2\theta} \qquad n = 0, 1, 2 \tag{69}$$

$$\Gamma_{mn}^p = \Upsilon_{mn}^p - 1 = \frac{Z_m^p - Z_n^p}{Z_m^p + Z_n^p} \qquad n = 0, 1, 2 \tag{70}$$

The derivation of the function $\mathcal{V}_v^p(t|\,z')$ for the ungrounded dielectric slab is very similar to that for the grounded dielectric slab in the previous subsection. The major difference here is that *three* cases must be considered for the position of the source point z' instead of two. As we did for the previous cases, we start with the case with $z' > 0$. The impulsive voltage excitation at z' creates two impulsive voltage waves traveling in the $+z$ and $-z$ directions. The upward-traveling wave makes the following direct contribution to the observed voltage at $z = z_0$:

$$\frac{1}{2}\,\delta\left(t - \frac{(z_0 - z')}{v_0}\right)\,. \tag{71}$$

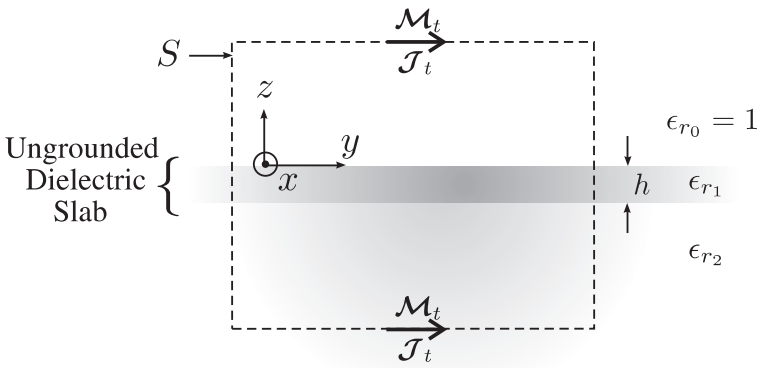

(a)

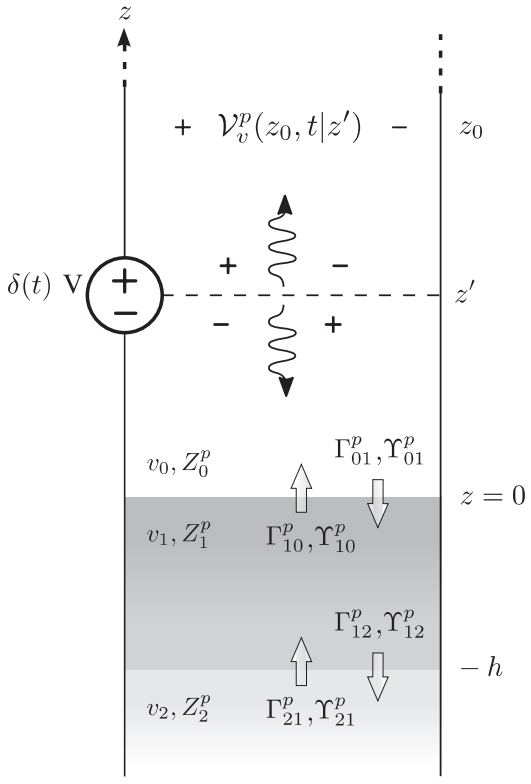

(b)

Figure 10: The geometry of the ungrounded dielectric slab. (a) The geometry of the medium. (b) The associated transmission-line geometry (with voltage excitation.)

The downward-traveling wave splits into two parts at the interface at $z = 0$. The reflected part makes the contribution

$$-\frac{\Gamma_{01}^p}{2}\,\delta\left(t-\frac{(z_0+z')}{v_0}\right)\,, \tag{72}$$

and the transmitted wave, after reflecting from the interface at $z = -h$, makes the contribution

$$-\frac{\Upsilon_{01}^p\Gamma_{12}^p}{2}\mathcal{V}^p\left(t-\frac{(z_0+z')}{v_0}-\frac{2h}{v_1}\right)\,. \tag{73}$$

The function $\mathcal{V}^p(t)$ in (73) is defined as

$$\mathcal{V}^p(t)=\sum_{n=0}^{\infty}\Upsilon_{10}^p(\Gamma_{10}^p\Gamma_{12}^p)^n\delta\left(t-2nh/v_1\right), \tag{74}$$

and represents the voltage induced at $z = 0^+$ by an impulsive voltage wave at $z = 0^-$ traveling in the $+z$ direction. This function is essentially a generalization of the similar one defined for the grounded dielectric slab in (59), in which $\Gamma_{12}^p = -1$ because of the total reflection from the perfectly-conducting ground plane.

Combining the contributions in (71)–(73) and applying the time advance $z_0\cos\theta/c$ in (37), we obtain the following expression for $\mathcal{V}_v^p(t|\,z')$ when $z' > 0$:

$$\mathcal{V}_v^p(t|\,z')=\frac{1}{2}\,\delta\left(t+\frac{z'}{v_0}\right)-\frac{\Gamma_{01}^p}{2}\,\delta\left(t-\frac{z'}{v_0}\right)-\frac{\Upsilon_{01}^p\Gamma_{12}^p}{2}\mathcal{V}^p\left(t-\frac{z'}{v_0}-\frac{2h}{v_1}\right)\,. \tag{75}$$

When the source point is inside the dielectric slab ($-h < z' < 0$), the impulsive excitation again creates two impulsive waves, one propagating toward the interface at $z = 0$, the other propagating toward the interface at $z = -h$. The upward-traveling wave makes the contribution

$$\frac{1}{2}\mathcal{V}^p\left(t-\frac{z_0}{v_0}+\frac{z'}{v_1}\right)\,, \tag{76}$$

and the downward-traveling wave makes the contribution

$$-\frac{\Gamma_{12}^p}{2}\mathcal{V}^p\left(t-\frac{z_0}{v_0}-\frac{(2h+z')}{v_1}\right)\,. \tag{77}$$

The function $\mathcal{V}^p(t)$ is again defined by (74). Combining the contributions in (76)–(77) and applying the time advance $z_0\cos\theta/c$ in (37), we obtain the following expression for $\mathcal{V}_v^p(t|\,z')$ when $-h < z' < 0$:

$$\mathcal{V}_v^p(t|\,z')=\frac{1}{2}\mathcal{V}^p\left(t+\frac{z'}{v_1}\right)-\frac{\Gamma_{12}^p}{2}\mathcal{V}^p\left(t-\frac{(2h+z')}{v_1}\right)\,. \tag{78}$$

The major difference between the the ungrounded and grounded dielectric slab is that the surface currents *below* $z' = -h$ contribute to the radiated field for in the presence of the ungrounded dielectric slab. Therefore, we consider a third case, in which $z' < -h$. The only contribution made by an impulsive excitation applied in this region comes from the upward-traveling wave:

$$\frac{\Upsilon_{21}^p}{2}\mathcal{V}^p\left(t - \frac{z_0}{v_0} + \frac{(z'+h)}{v_2} - \frac{h}{v_1}\right) \ . \tag{79}$$

Applying the time advance $z_0 \cos\theta/c$ in (37), the function $\mathcal{V}_v^p(t|\, z')$ for $z' < -h$ is given by

$$\mathcal{V}_v^p(t|\, z') = \frac{\Upsilon_{21}^p}{2}\mathcal{V}^p\left(t + \frac{(z'+h)}{v_2} - \frac{h}{v_1}\right) \ . \tag{80}$$

In summary, the function $\mathcal{V}_v^p(t|\, z')$ for the ungrounded dielectric slab can be written as the combination of (75), (78) and (80), covering every case for z':

$$\mathcal{V}_v^p(t|\, z') = \begin{cases} \dfrac{1}{2}\ \delta\left(t + \dfrac{z'}{v_0}\right) - \dfrac{\Gamma_{01}^p}{2}\ \delta\left(t - \dfrac{z'}{v_0}\right) & \\ \qquad - \dfrac{\Upsilon_{01}^p\Gamma_{12}^p}{2}\mathcal{V}^p\left(t - \dfrac{z'}{v_0} - \dfrac{2h}{v_1}\right) & , \quad z' > 0 \\ \dfrac{1}{2}\mathcal{V}^p\left(t + \dfrac{z'}{v_1}\right) - \dfrac{\Gamma_{12}^p}{2}\mathcal{V}^p\left(t - \dfrac{(2h+z')}{v_1}\right) & , \quad -h < z' < 0 \\ \dfrac{\Upsilon_{21}^p}{2}\mathcal{V}^p\left(t + \dfrac{(z'+h)}{v_2} - \dfrac{h}{v_1}\right) & , \quad z' < -h \ . \end{cases} \tag{81}$$

To obtain $\mathcal{V}_i^p(t|\, z')$, (81) is multiplied by Z^p, and the signs of all but the first terms are reversed. This yields the following expression for $\mathcal{V}_i^p(t|\, z')$:

$$\mathcal{V}_i^p(t|\, z') = \begin{cases} \dfrac{Z_0^p}{2}\ \delta\left(t + \dfrac{z'}{v_0}\right) + \dfrac{Z_0^p\Gamma_{01}^p}{2}\ \delta\left(t - \dfrac{z'}{v_0}\right) & \\ \qquad + \dfrac{Z_0^p\Upsilon_{01}^p\Gamma_{12}^p}{2}\mathcal{V}^p\left(t - \dfrac{z'}{v_0} - \dfrac{2h}{v_1}\right) & , \quad z' > 0 \\ \dfrac{Z_1^p}{2}\mathcal{V}^p\left(t + \dfrac{z'}{v_1}\right) + \dfrac{Z_1^p\Gamma_{12}^p}{2}\mathcal{V}^p\left(t - \dfrac{(2h+z')}{v_1}\right) & , \quad -h < z' < 0 \\ \dfrac{Z_2^p\Upsilon_{21}^p}{2}\mathcal{V}^p\left(t + \dfrac{(z'+h)}{v_2} - \dfrac{h}{v_1}\right) & , \quad z' < -h \ . \end{cases} \tag{82}$$

2.2.4 General Lossless Multilayered Media

The NFFFT geometry for a *general multilayered medium* with $N+1$ layers is as shown earlier in Fig. 6, and the associated transmission-line geometries are as shown in Fig. 7. The uppermost layer is free space and the lowermost layer is a dielectric half space with

relative permittivity ϵ_{r_N}. The finite layers indexed by $i = 1, 2, \ldots, N-1$ are located between $z = -h_{i-1}$ and $z = -h_i$.

In contrast to the simpler cases considered in the previous subsections, the functions $\mathcal{V}_v^p(t|\, z'), \mathcal{V}_i^p(t|\, z')$ for the general multilayered medium in Fig. 6 *cannot* be obtained in closed form. However, computer implementation offers the possibility of obtaining these functions *recursively*, as will be explained shortly. Almost all the information contained in these functions can be computed *off-line* using a recursive algorithm and the simple dependence on z' (vertical coordinate of the source current on the NFFFT box) can be easily accounted for during each cycle of the on-the-fly NFFFT.

In the TL geometry in Fig. 7, the impulsive voltage source is located in medium n, between $z = -h_{n-1}$ and $z = -h_n$. The propagation velocities v_n, characteristic impedances Z_n^p, and reflection/transmission coefficients Γ_{mn}^p, Υ_{mn}^p are defined in accordance with the numbering for the layers in the piecewise-continuous medium:

$$v_n = c/\sqrt{\epsilon_{r_n} - \sin^2\theta} \qquad n = 0, 1, \ldots \tag{83}$$

$$Z_n^e = Z_0\sqrt{\epsilon_{r_n} - \sin^2\theta}/\epsilon_{r_n} \qquad n = 0, 1, \ldots \tag{84}$$

$$Z_n^h = Z_0/\sqrt{\epsilon_{r_n} - \sin^2\theta} \qquad n = 0, 1, \ldots \tag{85}$$

$$\Gamma_{mn}^p = \Upsilon_{mn}^p - 1 = \frac{Z_m^p - Z_n^p}{Z_m^p + Z_n^p} \qquad n = 0, 1, \ldots, \quad m = n \pm 1 \tag{86}$$

The driving impulsive voltage in the n^{th} layer creates two impulsive (in space) voltage waves traveling in opposite opposite directions in the TL, with opposite signs and half the amplitude of the original voltage impulse, as shown in Fig. 7. We can write the following expression for $\mathcal{V}_v^p(t|\, z')$:

$$\mathcal{V}_v^p(t|\, z') = \begin{cases} \dfrac{1}{2}\,\delta\left(t + \dfrac{z'}{v_0}\right) - \dfrac{1}{2}\,\mathcal{V}_{0,1}^p\left(t - \dfrac{z'}{v_0}\right) & , \quad n = 0 \\ \dfrac{1}{2}\,\mathcal{V}_{n,n-1}^p\left(t + \dfrac{(z' + h_{n-1})}{v_n}\right) - \dfrac{1}{2}\,\mathcal{V}_{n,n+1}^p\left(t - \dfrac{(z' + h_n)}{v_n}\right) & , \quad 0 < n < N \\ \dfrac{1}{2}\,\mathcal{V}_{N,N-1}^p\left(t + \dfrac{(z' + h_{N-1})}{v_N}\right) & , \quad n = N\ . \end{cases} \tag{87}$$

As in the previous subsections, the function $\mathcal{V}_i^p(t|\, z')$ is obtained from $\mathcal{V}_v^p(t|\, z')$ via multiplication by Z_n^p, and a sign change for the downward-traveling component created after the

application of the impulsive current source. The resulting expression for $\mathcal{V}_i^p(t|\,z')$ is the following:

$$\mathcal{V}_i^p(t|\,z') = \begin{cases} \dfrac{Z_0^p}{2}\,\delta\left(t+\dfrac{z'}{v_0}\right) + \dfrac{Z_0^p}{2}\,\mathcal{V}_{0,1}^p\left(t-\dfrac{z'}{v_0}\right) & , \quad n=0 \\ \dfrac{Z_n^p}{2}\,\mathcal{V}_{n,n-1}^p\left(t+\dfrac{(z'+h_{n-1})}{v_n}\right) + \dfrac{Z_n^p}{2}\,\mathcal{V}_{n,n+1}^p\left(t-\dfrac{(z'+h_n)}{v_n}\right) & , \quad 0<n<N \\ \dfrac{Z_N^p}{2}\,\mathcal{V}_{N,N-1}^p\left(t+\dfrac{(z'+h_{N-1})}{v_N}\right) & , \quad n=N\ . \end{cases} \tag{88}$$

The definitions of $\mathcal{V}_v^p(t|\,z')$, $\mathcal{V}_i^p(t|\,z')$ in (87)–(88) are generalizations of those for the dielectric half space and the grounded/ungrounded dielectric slab in (54), (64),(81) and (55), (65),(82). Similarly, the function $\mathcal{V}_{i,j}^p(t)$ in (87)–(88) is a generalization of the functions $\mathcal{V}^p(t)$ in (59) and (74). It is defined as the voltage waveform created at position $z=0^+$ and time t by an impulsive voltage wave in medium i, infinitesimally close to the interface between interface between medium i and medium j and traveling toward medium j at time $t=0$. Although closed-form expressions exist for $\mathcal{V}^p(t)$ in (59) and (74), the generalized function $\mathcal{V}_{i,j}^p(t)$ usually cannot be expressed in closed form. However, the following *recursive* relations are valid for $\mathcal{V}_{i,j}^p(t)$:

$$\begin{aligned} \mathcal{V}_{n,n+1}^p(t) = {} & \Gamma_{n,n+1}\mathcal{V}_{n,n-1}^p\left(t-\frac{(h_n-h_{n-1})}{v_n}\right) \\ & + \Upsilon_{n,n+1}\mathcal{V}_{n+1,n+2}^p\left(t-\frac{(h_{n+1}-h_n)}{v_{n+1}}\right) \end{aligned} \tag{89}$$

$$\begin{aligned} \mathcal{V}_{n+1,n}^p(t) = {} & \Upsilon_{n+1,n}\mathcal{V}_{n,n-1}^p\left(t-\frac{(h_n-h_{n-1})}{v_n}\right) \\ & + \Gamma_{n+1,n}\mathcal{V}_{n+1,n+2}^p\left(t-\frac{(h_{n+1}-h_n)}{v_{n+1}}\right)\ . \end{aligned} \tag{90}$$

These relations simply describe the dispersionless transmission and reflection of an impulsive wave at the interface between media n and $n+1$. Since $|\Gamma^p|<1$, the amplitudes of the recursively called functions $\mathcal{V}_{i,j}^p$ eventually *decrease* as the recursion code moves higher in the stack. Therefore, a lower threshold for these amplitudes can be incorporated into the code as a legitimate stopping condition for the recursion. Another special condition is reached within the recursion when one of the indexes i,j corresponds to the *uppermost* or

lowermost half spaces. For these cases, (89)–(90) simplify to

$$\mathcal{V}_{0,1}^{p}(t) = \Gamma_{0,1}\delta(t) + \Upsilon_{0,1}\mathcal{V}_{1,2}^{p}\left(t - \frac{h_1}{v_1}\right) \tag{91}$$

$$\mathcal{V}_{1,0}^{p}(t) = \Upsilon_{1,0}\delta(t) + \Gamma_{1,0}\mathcal{V}_{1,2}^{p}\left(t - \frac{h_1}{v_1}\right) \tag{92}$$

for the upper half space and

$$\mathcal{V}_{N-1,N}^{p}(t) = \Gamma_{N-1,N}\mathcal{V}_{N-1,N-2}^{p}\left(t - \frac{(h_{N-1} - h_{N-2})}{v_{N-1}}\right) \tag{93}$$

$$\mathcal{V}_{N,N-1}^{p}(t) = \Upsilon_{N,N-1}\mathcal{V}_{N-1,N-2}^{p}\left(t - \frac{(h_{N-1} - h_{N-2})}{v_{N-1}}\right) \tag{94}$$

for the lower half space. These special conditions simply state that an impulsive waveform transmitted into medium 0 or medium N will not be reflected from any other discontinuity.

Once the functions $\mathcal{V}_{i,j}^{p}$ are determined recursively off-line, they can be used in (87)–(88) within the FDTD time stepping. The z' dependence in (87) can be simply accounted for by introducing a time delay $t \rightarrow t \pm z'/v_0$.

2.3 Radiated Electric Field in The Lowermost Half Space

Up to this point, we have only considered the radiated electric field in the *uppermost half space* with index 0 in Fig. 6. In some cases, one might be interested in the radiated electric field in the *lowermost half space* with index N. This corresponds to the range $\pi/2 < \theta \leq \pi$ for the angle variable θ. In this section, we will extend the results obtained in the previous sections to allow for this possibility. The corresponding geometry is given also by Fig. 6, with a minor change: The lowermost layer is air ($\epsilon_{r_2} = 1$), and the uppermost layer is arbitrary ($\epsilon_{r_0} \neq 1$).

It can be shown that the expressions for the radiated electric field given in (19)–(24) *change sign* for the lowermost half space, i.e., $\pi/2 < \theta \leq \pi$. Moreover, the expressions for the functions $\mathcal{V}_v^p(t|\, z')$, $\mathcal{V}_i^p(t|\, z')$ must be modified. We will not go into the same details for the derivation of these functions as we did in the previous section. Here, we will only present the results for a specific case, namely, the ungrounded dielectric slab. Note that the results for free space, dielectric half space and grounded dielectric slab are merely special cases of the result for the ungrounded dielectric slab. The general result for a general multilayered

medium can also be obtained by following the recursive method described in Section 2.2.4, but the details are not given here. The functions $\mathcal{V}_v^p(t|\,z')$, $\mathcal{V}_i^p(t|\,z')$ for the ungrounded dielectric slab are

$$\mathcal{V}_v^p(t|\,z') = \begin{cases} -\dfrac{\Upsilon_{01}^p}{2}\mathcal{V}^p\left(t - \dfrac{z'}{v_0} - \dfrac{h}{v_1} + \dfrac{h}{v_2}\right) & , \quad z' > 0 \\ \dfrac{-1}{2}\mathcal{V}^p\left(t - \dfrac{(z'+h)}{v_1} + \dfrac{h}{v_2}\right) & \\ \qquad + \dfrac{\Gamma_{10}^p}{2}\mathcal{V}^p\left(t - \dfrac{(-z'+h)}{v_1} + \dfrac{h}{v_2}\right) & , \quad -h < z' < 0 \\ \dfrac{-1}{2}\,\delta\left(t - \dfrac{z'}{v_2}\right) + \dfrac{\Gamma_{21}^p}{2}\,\delta\left(t + \dfrac{(z'+2h)}{v_2}\right) & \\ \qquad + \dfrac{\Upsilon_{21}^p\Gamma_{10}^p}{2}\mathcal{V}^p\left(t + \dfrac{(z'+2h)}{v_2} - \dfrac{2h}{v_1}\right) & , \quad z' < -h\ . \end{cases} \tag{95}$$

$$\mathcal{V}_i^p(t|\,z') = \begin{cases} \dfrac{Z_0^p\Upsilon_{01}^p}{2}\mathcal{V}^p\left(t - \dfrac{z'}{v_0} - \dfrac{h}{v_1} + \dfrac{h}{v_2}\right) & , \quad z' > 0 \\ \dfrac{Z_1^p}{2}\mathcal{V}^p\left(t - \dfrac{(z'+h)}{v_1} + \dfrac{h}{v_2}\right) & \\ \qquad + \dfrac{Z_1^p\Gamma_{10}^p}{2}\mathcal{V}^p\left(t - \dfrac{(-z'+h)}{v_1} + \dfrac{h}{v_2}\right) & , \quad -h < z' < 0 \\ \dfrac{Z_2^p}{2}\,\delta\left(t - \dfrac{z'}{v_2}\right) + \dfrac{Z_2^p\Gamma_{21}^p}{2}\,\delta\left(t + \dfrac{(z'+2h)}{v_2}\right) & \\ \qquad + \dfrac{Z_2^p\Upsilon_{21}^p\Gamma_{10}^p}{2}\mathcal{V}^p\left(t + \dfrac{(z'+2h)}{v_2} - \dfrac{2h}{v_1}\right) & , \quad z' < -h\ . \end{cases} \tag{96}$$

In the above expressions, the transmission-line velocities v_n are

$$v_n = c/\sqrt{\epsilon_{r_n} - \sin^2\theta}\ , \qquad n = 0, 1, 2 \tag{97}$$

and $\mathcal{V}^p(t)$ is

$$\mathcal{V}^p(t) = \sum_{n=0}^{\infty} \Upsilon_{12}^p(\Gamma_{12}^p\Gamma_{10}^p)^n\delta\left(t - 2nh/v_1\right)\ . \tag{98}$$

2.4 Comparison with Exact Results

In this section, we present a verification of the FDTD NFFFT method described in the previous sections by comparing the FDTD simulation results with exact theoretical formulas available in the literature [26–28]. Specifically, the concise formulation in [27] regarding the far field of an infinitesimal (Hertzian) electric dipole embedded in a grounded dielectric slab

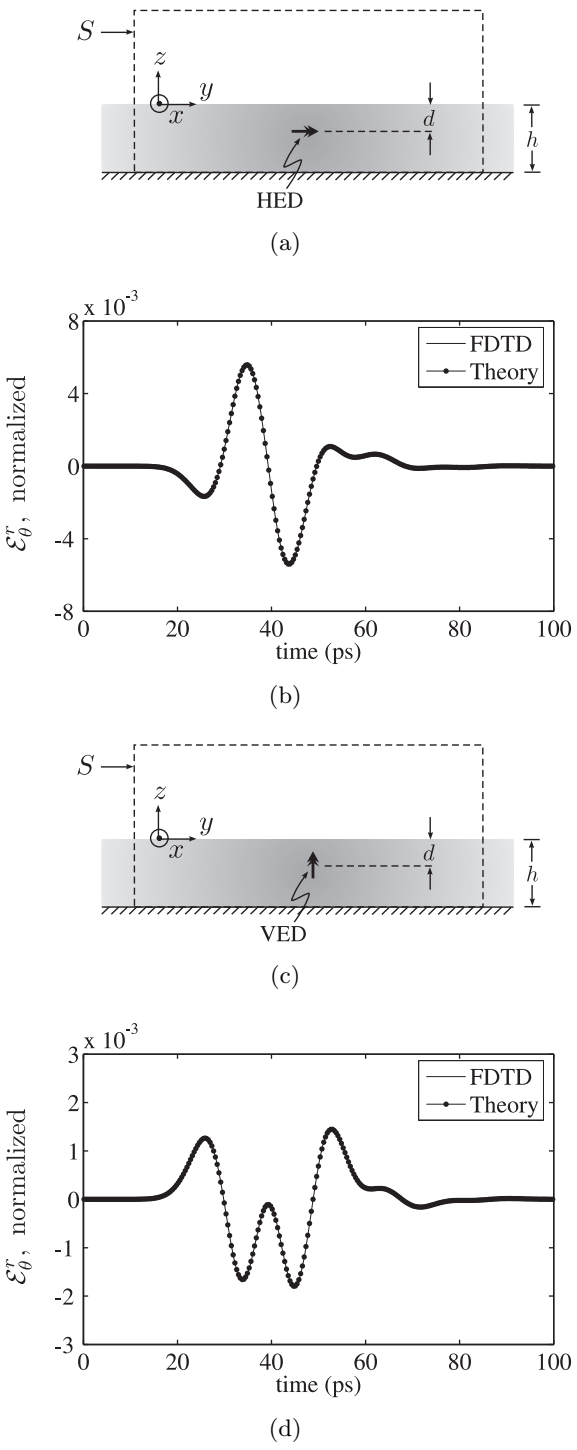

Figure 11: Time-domain radiation from infinitesimal (Hertzian) electric dipoles embedded in a grounded dielectric slab. (a) The geometry for the horizontal electric dipole (HED). (b) The $\hat{\boldsymbol{\theta}}$ component of the time-domain radiated electric field at $\theta = \phi = \pi/4$ created by the HED in (a). (c) The geometry for the vertical electric dipole (VED). (d) The $\hat{\boldsymbol{\theta}}$ component of the time-domain radiated electric field at $\theta = \phi = \pi/4$ created by the VED in (c).

will be considered. The geometry is shown in Fig. 11(a) for a horizontal electric dipole (HED), and in Fig. 11(c) for a vertical electric dipole (VED). The $\hat{\boldsymbol{y}}$ and $\hat{\boldsymbol{z}}$ oriented dipoles in Fig. 11(a) and Fig. 11(c) are both located at $z = -d$, $d = 1$ mm, in the dielectric slab with $\epsilon_r = 2.5$, and thickness $h = 2$ mm. Both dipoles are driven by a differentiated Gaussian current waveform:

$$\begin{aligned} \boldsymbol{\mathcal{J}}(\boldsymbol{r}, t) = \hat{\boldsymbol{a}} \mathcal{J}_0 \left[- \left(\frac{t - n\tau}{\tau} \right) e^{-(t-n\tau)^2/2\tau^2 + 1/2} \right] \\ \cdot \, \delta(x)\, \delta(y)\, \delta(z + d) \ , \end{aligned} \tag{99}$$

in which $\tau = 5$ ps, $n = 6$, and $\hat{\boldsymbol{a}} = \hat{\boldsymbol{y}}$ or $\hat{\boldsymbol{z}}$. The infinitesimal Hertzian dipoles are modeled in the FDTD method by a single current element on the edge of a grid cell. The $\hat{\boldsymbol{\theta}}$ component of the radiated electric field at $\theta = \phi = \pi/4$ is shown in Fig. 11(b) and Fig. 11(d) for the HED and VED, respectively. The field is advanced by r/c and normalized by $(\mathcal{J}_0/\Delta)Z_0/r$, where $\Delta = 0.1$ mm is the FDTD grid spacing. The solid lines denote the results obtained by the FDTD NFFFT method, and the dotted lines denote the theoretical results obtained using eq. (4)–(5) in [27]. For both the HED and VED, the FDTD results are in very good agreement with the theory.

2.5 Examples

In this section, we apply the NFFFT described in the previous sections to the FDTD analysis of radiation in different multilayered media. Specifically, we demonstrate examples for the dielectric half space and the grounded dielectric slab. Additional examples will be provided for the ungrounded dielectric slab in Chapter 4, where the NFFFT is used in conjunction with the plane-wave injector developed in Chapter 3.

As an example of the NFFFT for the dielectric half space, we consider a thin cylindrical dipole radiating on top of a dielectric ground. As examples of the NFFFT for the grounded dielectric slab, we consider the radiation from a length of microstrip line, and the radiation from a microstrip bend.

An example of time-domain radiation in the presence of a dielectric half space is shown in Fig. 12(a). A thin cylindrical dipole of length L is radiating at the interface between air and a dielectric half space with permittivity ϵ_r. The dipole is excited at its center by a

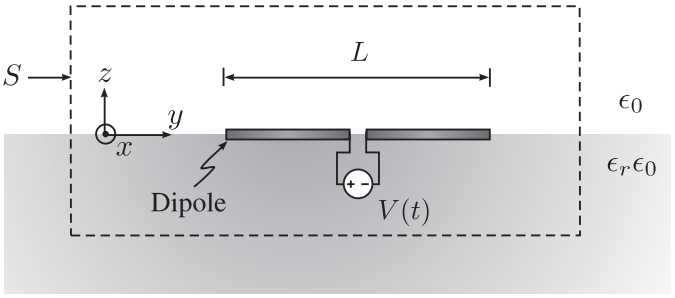

(a)

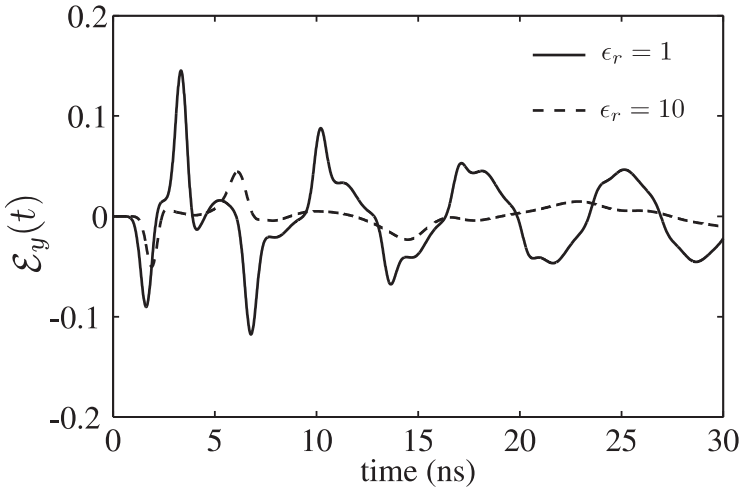

(b)

Figure 12: Dipole radiation in the presence of a dielectric half space with relative permittivity ϵ_r. (a) The geometry of the problem. (b) The radiated electric field $\mathcal{E}_y(t)$ at $\theta = 0$ (along the z-axis) for $\epsilon_r = 1$ (solid line) and $\epsilon_r = 10$ (dashed line).

Gaussian voltage:

$$V(t) = V_0 e^{-((t-n\tau)/\tau)^2/2} \ . \tag{100}$$

In Fig. 12(b), the time-domain radiated electric field (normalized by V_0/r) at $\theta = 0$ (along the z axis) is given for the following parameters: $L = 1$ m, $\tau = 0.283$ ns, $n = 3$. The solid line represents the radiated field in free space, while the dashed line represents the radiated field in the presence of the dielectric half space with $\epsilon_r = 10$. The difference between the propagation velocity of the signal on the dipole in the free space case ($\epsilon_r = 1$) and the dielectric half-space case ($\epsilon_r = 10$) can be compared to numerical formulas obtained in [29]. In fact, inspection of the signal peaks in Fig. 12(b) reveals a velocity ratio of $v_{\text{free}}/v_{\text{diel}} \approx 2.35$, which is in accordance with the results given in [29].

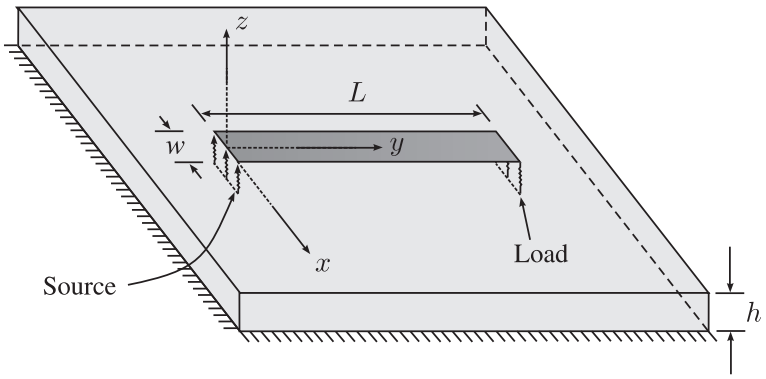

Figure 13: The geometry of the microstrip line.

Now, we consider the usage of the NFFFT described in the previous sections in the presence of a grounded dielectric slab. Specifically, we analyze the radiation from a *microstrip line* and a *microstrip bend*. This should be of interest in problems involving pulsed signals transmitted on microstrip circuits, which is a practical issue encountered in contemporary digital computer circuit design.

First, we consider the radiation from a finite length of microstrip line on an infinite substrate. The geometry considered in this example is shown in Fig. 13. The physical parameters for the line are $w = h = 2$ mm, $L = 570$ mm, and $\epsilon_r = 2.5$. The characteristic resistance of the line is determined from the empirical formulas given in [30], and matched terminations with this resistance are placed at the source and load ends of the line using the method described in [2]. The driving voltage is the Gaussian pulse $V_0 e^{-t^2/2\tau^2}$ with the characteristic time $\tau = 240$ ps. This corresponds to a 1%-amplitude (-40 dB) bandwidth of 2 GHz, which is approximately the maximum frequency that allows the quasi-TEM assumption for propagation on this line [31].

After analyzing this structure with the FDTD method, the NFFFT is used on the surface of a rectangular box containing the line to obtain the time-domain radiated electric field in different planes orthogonal to the ground plane. The results, scaled by V_0/r and advanced in time by r/c, are shown in Figs. 14(a)–(c). Each graph gives the time history of the field at a particular angle ψ in the yz plane (Fig. 14(a)), or xz plane (Fig. 14(b) and Fig. 14(c)).

The time axis is normalized by $\tau_L = \sqrt{\epsilon_{re}}L/c$, which is the time for the quasi-TEM wave to travel the length of the line. Here, ϵ_{re} is the relative effective permittivity for propagation of the quasi-TEM wave on the microstrip line [30]. The electric field in each graph is positive on the side of the time axis for which $\hat{\boldsymbol{\psi}}$ points away from the axis (clockwise direction).

The dashed curves W_1 and W_2 represent spherical wavefronts centered at the source and termination, respectively. These results clearly support the well-known fact that radiation occurs at the feed and the termination [1]. The fact that there are only two wavefronts present strongly suggests that there is very little reflection from the load; which has indeed been verified by the observation of the electric field normal to the surface of the microstrip line.

The $\hat{\boldsymbol{\phi}}$ component of the radiated electric field (where $\hat{\boldsymbol{\phi}}$ is the unit vector pointing in the y direction) in the yz plane is zero (which is expected due to symmetry), so only the $\hat{\boldsymbol{\psi}}$ component is shown in Fig. 14(a). In the xz plane, however, both $\hat{\boldsymbol{\psi}}$ and $\hat{\boldsymbol{\phi}}$ components are present. These components are shown in Fig. 14(b) and Fig. 14(c), respectively. It is apparent from Fig. 14(b) that the electric field radiated by the traveling-wave antenna formed by the microstrip line does *not* merely reside on planes passing through the axis of the microstrip line (y axis in our example), as would be expected for a thin traveling-wave antenna in free-space [1]. The cross-polarized component in Fig. 14(b) results from the upward and downward currents (along the z axis) in the source and load regions, respectively. Furthermore, Fig. 14(c) indicates that the component of the radiated electric field that is tangential to the ground plane diminishes at the grazing angle, which is expected since the tangential electric field must vanish on the ground plane.

Note the differentiated Gaussian shape of the radiation, which is unlike the Gaussian shape of the radiation from a similar traveling-wave antenna in free space. This difference is due to the presence of the ground plane. The presence of the ground plane also greatly reduces the amount of energy radiated by the transmission line as compared to that radiated by the antenna [1]. For example, the maximum of $|\mathcal{E}_\psi|$ (scaled) in Fig. 14(a) for $\psi = 90^\circ$ is $4.65 \cdot 10^{-3}$. For comparison, the maximum of $|\mathcal{E}_\psi|$ at $\psi = 90^\circ$ for a traveling- wave antenna in free space with the same excitation is approximately 0.16, about 34 times greater.

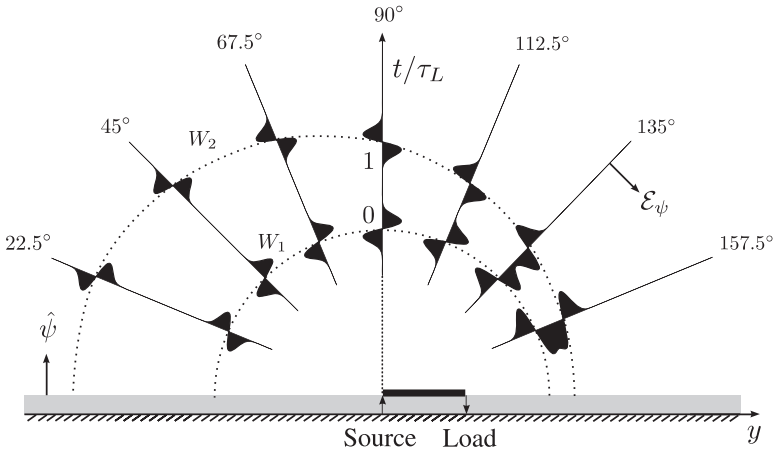

(a)

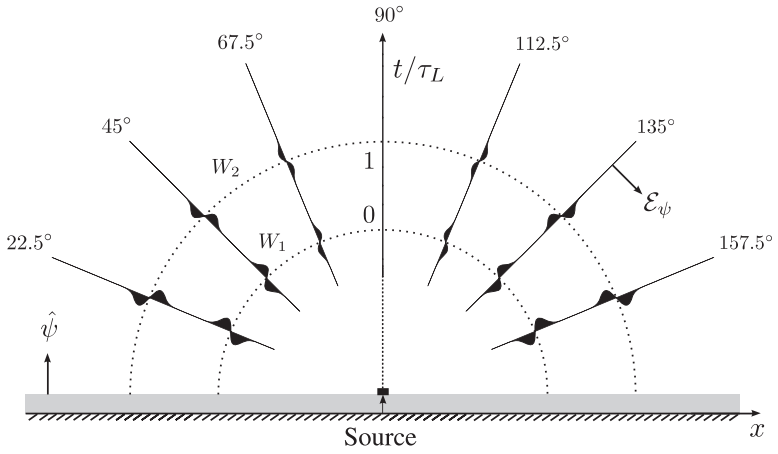

(b)

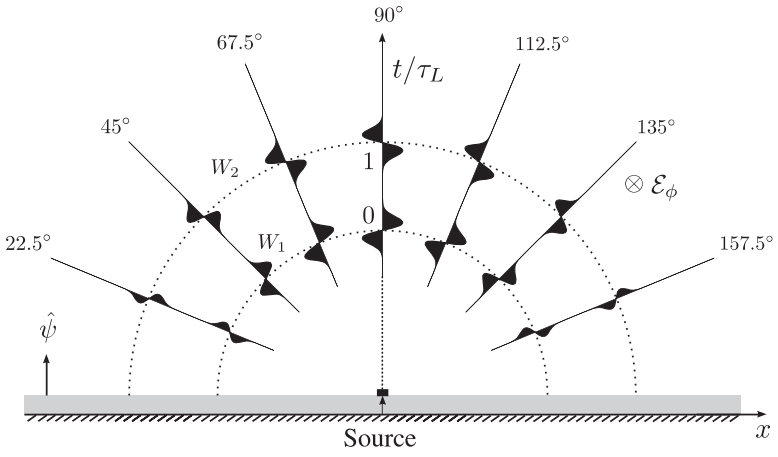

(c)

Figure 14: Time-domain radiation from a length of microstrip line. (a) The $\hat{\boldsymbol{\psi}}$ component of the the time-domain radiated electric field at different angles in the yz plane. (b) The $\hat{\boldsymbol{\psi}}$ component, and (c) the $\hat{\boldsymbol{\phi}}$ component of the time-domain radiated electric field at different angles in the xz plane.

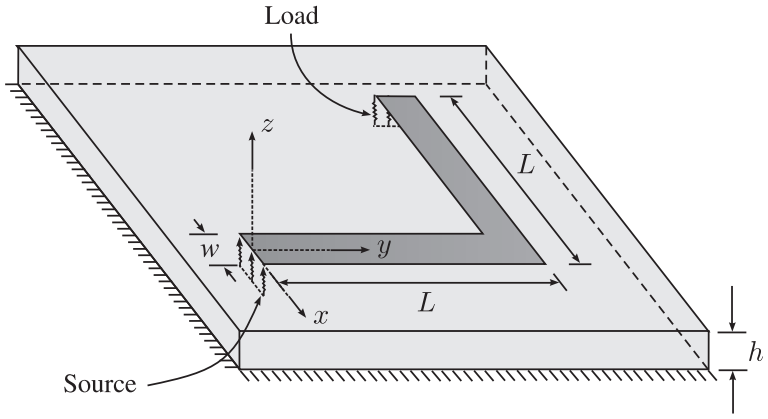

Figure 15: The geometry of the microstrip bend.

Next, we consider an extension of the straight microstrip line considered above; namely, the microstrip line with a right-angle bend shown in Fig. 15. The physical parameters for the bend are the same as those for the microstrip line. The radiation from the microstrip bend in the xz and yz plane is given in Fig. 16 and 17, respectively. In both figures, the first subfigure [16(a),17(a)] shows the $\hat{\boldsymbol{\psi}}$ component of the radiated electric field, and the second subfigure [16(b),17(b)] shows the $\hat{\boldsymbol{\phi}}$ component of the radiated electric field. The electric field in each graph is positive on the side of the time axis for which $\hat{\boldsymbol{\psi}}$ points away from the axis (clockwise direction). The dashed curves W_1, W_2 and W_3 represent spherical wavefronts centered at the source, bend, and termination, respectively. The new feature in this example is obviously wavefront W_2, which is due to the discontinuity at the bend. It will now be shown that the radiation from the structure in Fig. 15, including the radiation from the bend, can be explained in terms of the results already obtained for the simpler structure in Fig. 13, by the use of a simple model for the bent microstrip line.

As we did for the previous example, we have examined the fields on the surface of the bent microstrip line, and observed that there is very little reflection from the bend. This observation naturally leads us to a simple, conceptual model for the bent microstrip line. Specifically, we will assume that the microstrip bend consists of *two* microstrip line segments (as in Fig. 13) at a right angle to each other and joined together at the point of the bend. We will assume further that, at the bend, the currents in the load region of the first segment

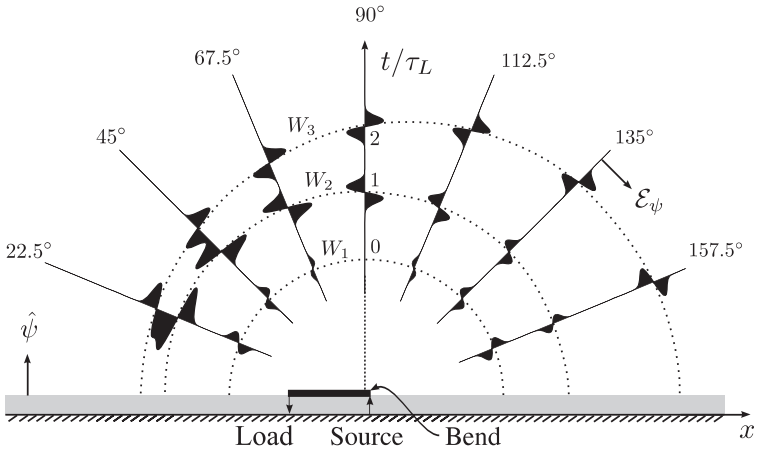

(a)

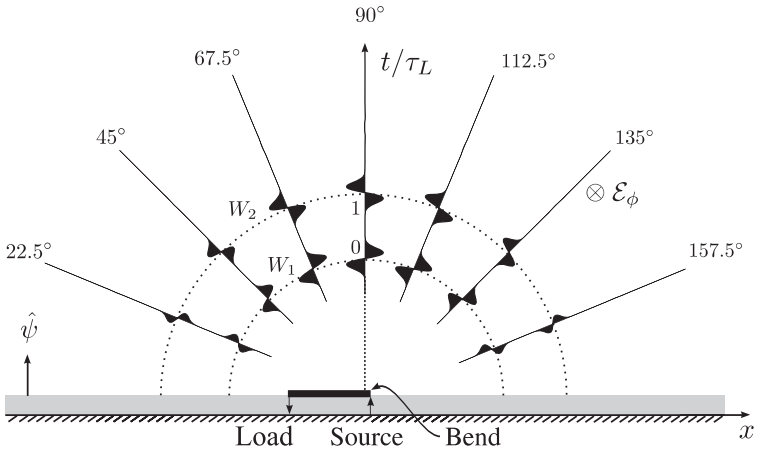

(b)

Figure 16: Time-domain radiation from a microstrip bend (xz plane). (a) The ψ-component, and (b) the ϕ-component of the time-domain radiated electric field at different angles in the xz plane.

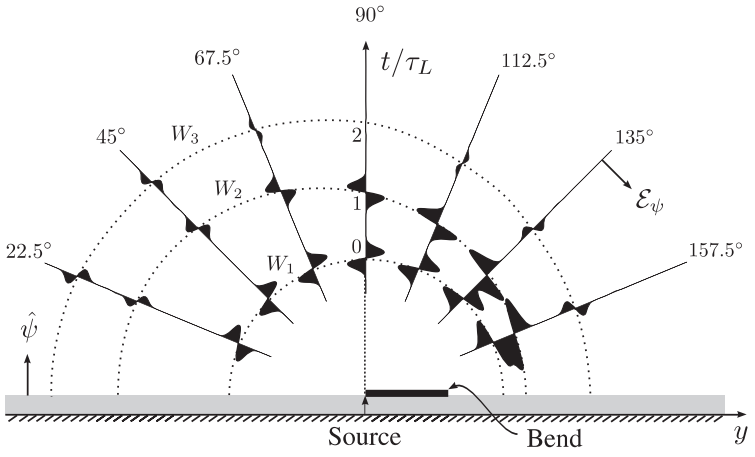

(a)

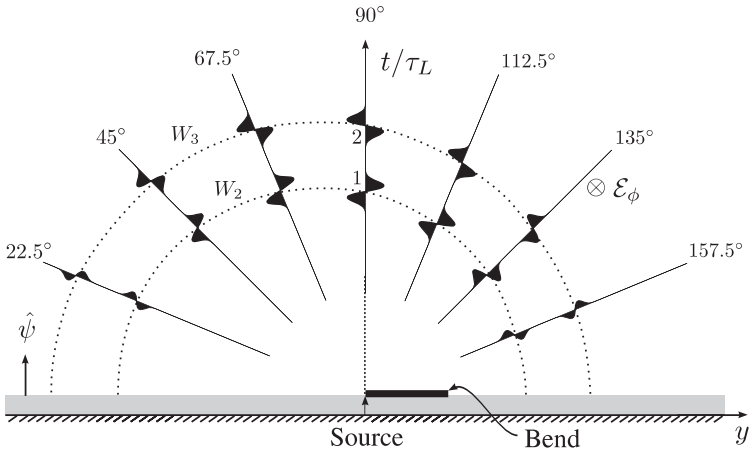

(b)

Figure 17: Time-domain radiation from a microstrip bend (yz plane). (a) The ψ-component, and (b) the ϕ-component of the time-domain radiated electric field at different angles in the yz plane.

cancels the currents in the source region of the second segment. This model implies that the radiation from a bent microstrip line (as in Fig. 15) is the sum of the contributions of two microstrip lines (as in Fig. 13), joined together at right angles at the point of the bend.

In light of this model, we can make meaningful comparisons between Figs. 16–17 and Fig. 14. For example, we readily observe that Fig. 16(b) is *exactly the same* as Fig. 14(c). This is simply because the $\hat{\boldsymbol{\phi}}$ component of the radiation is solely due to the first segment of the microstrip bend; and the $\hat{\boldsymbol{\phi}}$ response of this segment was already given in the previous example by Fig. 14(c). In a similar fashion, Fig. 14(b) can be interpreted as the $\hat{\boldsymbol{\psi}}$ component of the electric field radiated by the first segment in our microstrip bend model. Adding this contribution to the (spatially inverted and delayed) $\hat{\boldsymbol{\psi}}$ response of the second segment that is given by Fig. 14(a), we obtain Fig. 16(a).

Similar comparisons can be made between Fig. 17 and Fig. 14. As above, we observe that Fig. 17(b) is almost identical to Fig. 14(c). This is simply because the $\hat{\boldsymbol{\phi}}$ component of the radiation is due to the second segment of the microstrip bend; and the $\hat{\boldsymbol{\phi}}$ response of this segment was already given in the previous example by Fig. 14(c). The additional delays in Fig. 17(b) are simply due to the shifting of the origin from the beginning of the second segment to the beginning of the first segment. In a similar fashion, Fig. 14(b) can be interpreted as the $\hat{\boldsymbol{\psi}}$ component of the electric field radiated by the second segment in our microstrip bend model. Adding this contribution to the $\hat{\boldsymbol{\psi}}$ response of the first segment that is given by Fig. 14(a), we obtain Fig. 17(a). The extra delays in Fig. 17(a) are again due to the shifting of the origin.

In summary, it can be stated that the quasi-TEM wave turns the right-angle corner with little difficulty, radiating small amounts of energy (see the previous section for quantitative results) at the source, bend and termination regions.

CHAPTER III

TF/SF BOUNDARY FOR GENERAL MULTILAYERED MEDIA

The geometry for the TF/SF boundary (or the plane-wave injector) was presented previously in Section 1.5, Fig. 5, which is reproduced in Fig. 18 for convenience. It was stated in Section 1.5 that the TF/SF boundary technique relies entirely on the *a priori* knowledge of the incident wave (a plane wave in our case) in the presence of the multilayered medium. Therefore, the principal purpose of this chapter is to obtain the plane wave incident on the multilayered medium, along with all the reflections from the material interfaces.

3.1 Solving for the Incident Field

3.1.1 Formulation

The first step in solving for any electromagnetic field is to observe the symmetries inherent in the geometry and the excitation. The most obvious symmetry in the plane-wave injector setting in Fig. 18 is the invariance of both the geometry and the incident plane wave in a direction that is perpendicular to a plane called the *principal plane*, represented by the gray sheet G in Fig. 19. Without loss of generality, we assume that G coincides with the xz plane, so there is no variation in the y direction. This plane contains both the direction of propagation $\hat{\boldsymbol{k}}_i$ for the incident wave and the axis of symmetry z for the multilayered medium. From the aforementioned symmetry, it follows that the incident plane wave at any point in space can be obtained by projection onto G. In the following analysis, we will therefore be concerned with the solution of the incident field on the two-dimensional plane G.

The preceding simplification to two dimensions is by no means unique to the plane wave. In fact, it is valid for any two-dimensional source, an example of which is an infinite current filament with uniform current perpendicular to the principal plane G in Fig. 19. Owing to its relative simplicity, it is possible to find much deeper symmetries for the plane wave, which allows further simplification to one dimension. This reduction is explained next.

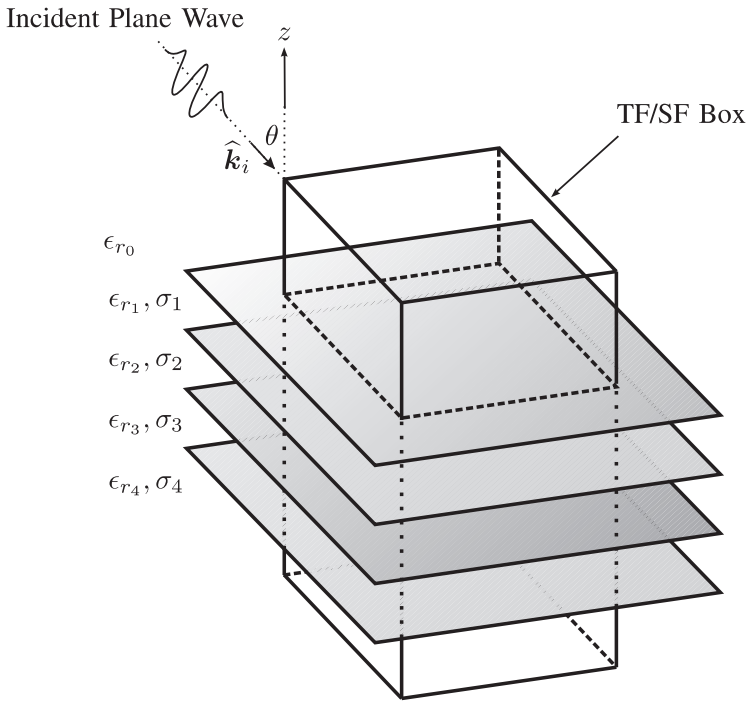

Figure 18: Geometry of the plane-wave injector for general lossy multilayered media.

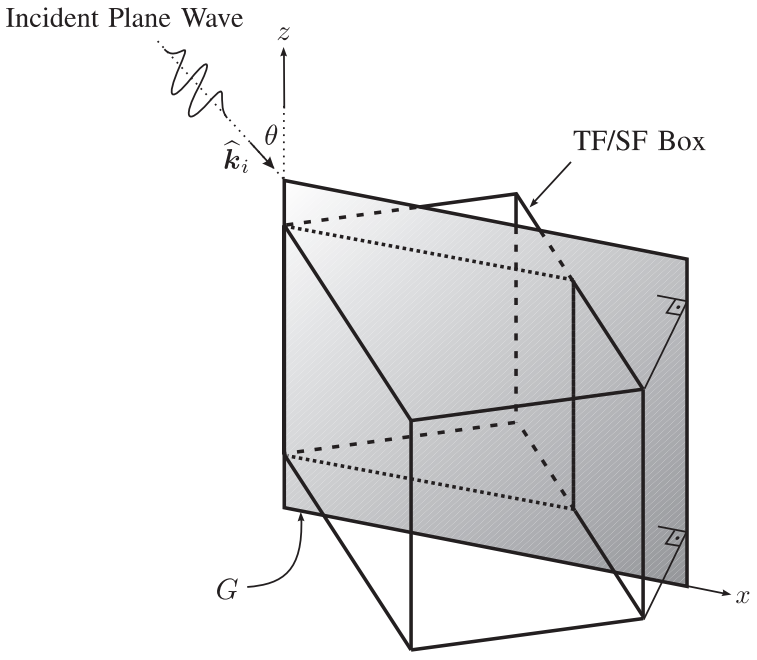

Figure 19: Principal plane G for the incident plane wave.

At every interface in the multilayered structure, the component of the phase velocity tangential to the interface (x component) must be the same. If c_0 is the speed of light in the lossless uppermost medium ($n = 0$), then $v_x = c_0/\sin\theta$ in all layers, where θ is the angle between $\hat{\boldsymbol{k}}_i$ and $\hat{\boldsymbol{z}}$, see Fig. 19. This statement is equivalent to what is called *phase matching* in frequency domain. Now any component of the electromagnetic field in any layer can be written as a function of only two variables: z and $t - x/v_x = t - x\sin\theta/c_0$. Thus the partial derivatives with respect to time and with respect to the spatial variable x are simply related. After using this relationship for derivatives and the invariance with respect to y, Maxwell's equations can be split into two independent sets. [1] The first set of equations has only one component to the electric field, $\mathcal{E}_y$, and this component is perpendicular to the plane G, so this set of equations is referred to as *transverse electric* (TE). After introducing the notation $\mathcal{E}^h = \mathcal{E}_y$, $\mathcal{H}^h = -\mathcal{H}_x$, this set of equations becomes

$$\begin{aligned} \frac{\partial \mathcal{E}^h}{\partial z} &= -\Big[\mu_0\Big]\frac{\partial \mathcal{H}^h}{\partial t} \\ \frac{\partial \mathcal{H}^h}{\partial z} &= -\Big[\epsilon_0(\epsilon_r - \epsilon_{r_0}\sin^2\theta)\Big]\frac{\partial \mathcal{E}^h}{\partial t} \qquad \text{(TE)} \\ \mathcal{H}_z &= Y_0\sqrt{\epsilon_{r_0}}\sin\theta\,\mathcal{E}^h\ . \end{aligned} \tag{101}$$

The second set of equations has only one component to the magnetic field, $\mathcal{H}_y$, and this component is perpendicular to the plane G, so this set of equations is referred to as *transverse magnetic* (TM). After introducing the notation $\mathcal{E}^e = \mathcal{E}_x$, $\mathcal{H}^e = \mathcal{H}_y$, this set of equations becomes

$$\begin{aligned} \frac{\partial \mathcal{E}^e}{\partial z} &= -\left[\frac{\mu_0(\epsilon_r - \epsilon_{r_0}\sin^2\theta)}{\epsilon_r}\right]\frac{\partial \mathcal{H}^e}{\partial t} \\ \frac{\partial \mathcal{H}^e}{\partial z} &= -\Big[\epsilon_0\epsilon_r\Big]\frac{\partial \mathcal{E}^e}{\partial t} \qquad \text{(TM)} \\ \mathcal{E}_z &= -\frac{Z_0\sqrt{\epsilon_{r_0}}\sin\theta}{\epsilon_r}\,\mathcal{H}^e \end{aligned} \tag{102}$$

In (101) and (102), ϵ_r and ϵ_{r_0} denote the relative permittivities at the field position and the uppermost layer, respectively, and $Z_0 = 1/Y_0 = (\mu_0/\epsilon_0)^{1/2}$. For simplicity, it is assumed that there is no loss, i.e., the relative permittivity ϵ_r is real. The results will be generalized

[1] This procedure is described comprehensively in [17], but their results are given in frequency domain. Although our time-domain results can be obtained directly from [17] using inverse Fourier transformation, we have also provided a pure time-domain derivation in Appendix C.

to lossy media in the following section.

The behavior of the incident field, which consists of the initial plane wave incident from the uppermost layer and all of the reflections at the interfaces, is completely described by the first two equations in each set, (101) and (102). Notice that they are the familiar transmission-line (TL) equations for propagation in the direction z, and that they only involve components of the field that are transverse to z: $\mathcal{E}^h, \mathcal{H}^h$ for TE and $\mathcal{E}^e, \mathcal{H}^e$ for TM. These equations must be discretized for use in the FDTD method. As will be seen shortly, the discretized field components are placed on a 1-*D auxiliary grid*, similar to the one used in the free-space TF/SF method [2]. Unlike the free-space auxiliary grid, our grid always aligns with the z axis, since the equations (101)–(102) describe the evolution of the fields in the z direction.

The first two equations in (101) closely resemble the equations for a 1-D TEM wave [2], which suggests the staggered temporal-spatial positioning of $\{\mathcal{E}^h, \mathcal{H}^h\}$, along with leap-frog time updating. The third equation in (101) suggests placing $\mathcal{H}_z$ at the same spatial positions as $\mathcal{E}^h$. However, since all the components of the electric field in the main simulation grid are usually discretized identically in time, we choose to evaluate $\mathcal{H}_z$ at the same time points as $\{\mathcal{H}^e, \mathcal{H}^h\}$. This has the slight disadvantage of having to interpolate $\mathcal{H}_z$ in time for the discretization of the third equation in (101). The preceding arguments apply similarly to the equations in (102). The resulting placement of the field components $\{\mathcal{E}^h, \mathcal{E}^e, \mathcal{E}_z, \mathcal{H}^h, \mathcal{H}^e, \mathcal{H}_z\}$ on the temporal-spatial 1-D auxiliary grid is shown in Fig. 20(a). The update equations are given by the discretization of (101) and (102):

$$\mathcal{H}^h\Big|_{k+1/2}^{n+1/2} = \mathcal{H}^h\Big|_{k+1/2}^{n-1/2} - \frac{\Delta t}{\mu_0 \Delta z}\left[\mathcal{E}^h\Big|_{k+1}^{n} - \mathcal{E}^h\Big|_{k}^{n}\right] \tag{103}$$

$$\begin{aligned}\mathcal{E}^h\Big|_{k}^{n+1} = \mathcal{E}^h\Big|_{k}^{n} &- \frac{\Delta t}{\epsilon_0(\,\epsilon_r|_k - \epsilon_{r_0}\sin^2\theta)\Delta z} \\ &\cdot\left[\mathcal{H}^h\Big|_{k+1/2}^{n+1/2} - \mathcal{H}^h\Big|_{k-1/2}^{n+1/2}\right]\end{aligned} \tag{104}$$

$$\mathcal{H}_z|_k^{n+1/2} = -\,\mathcal{H}_z|_k^{n-1/2} + 2Y_0\sqrt{\epsilon_{r_0}}\sin\theta\;\mathcal{E}^h\Big|_k^n \tag{105}$$

and

$$\mathcal{H}^e|_{k+1/2}^{n+1/2} = \mathcal{H}^e|_{k+1/2}^{n-1/2} - \frac{\epsilon_r|_{k+1/2}\,\Delta t}{\mu_0(\,\epsilon_r|_{k+1/2} - \epsilon_{r_0}\sin^2\theta)\Delta z} \cdot \left[\mathcal{E}^e|_{k+1}^{n} - \mathcal{E}^e|_{k}^{n}\right] \tag{106}$$

$$\mathcal{E}^e|_{k}^{n+1} = \mathcal{E}^e|_{k}^{n} - \frac{\Delta t}{\epsilon_0\;\epsilon_r|_k\,\Delta z}\left[\mathcal{H}^e|_{k+1/2}^{n+1/2} - \mathcal{H}^e|_{k-1/2}^{n+1/2}\right] \tag{107}$$

$$\mathcal{E}_z|_{k+1/2}^{n+1} = -\,\mathcal{E}_z|_{k+1/2}^{n} - \frac{2Z_0\sqrt{\epsilon_{r_0}}\sin\theta}{\epsilon_r|_{k+1/2}}\,\mathcal{H}^e|_{k+1/2}^{n+1/2}\;. \tag{108}$$

Note that the field components $\{\mathcal{E}^h, \mathcal{E}^e, \mathcal{H}_z\}$ are evaluated at integer spatial positions $(k, k+1, \ldots)$ and the field components $\{\mathcal{H}^h, \mathcal{H}^e, \mathcal{E}_z\}$ are evaluated at half-integer spatial positions $(k-1/2, k+1/2, \ldots)$, consistent with the placement in Fig. 20(a). The relative permittivity ϵ_r is evaluated at either integer (k) or half-integer $(k+1/2)$ positions. At the integer positions (k), the permittivity values at the locations of $\mathcal{E}_x, \mathcal{E}_y$ are used, whereas for the half-integer positions $(k+1/2)$, the permittivity values at the locations of $\mathcal{E}_z$ are used. Near the dielectric interfaces, equivalent permittivities [10, 11] are used to preserve second-order accuracy. Changes in the relative permittivity $\epsilon_r|_k$ resulting from material discontinuities create reflections, which represent the reflections of the incident plane wave from the dielectric interfaces.

Now, the evolution of the incident electric and magnetic field components are completely described in the z direction by the TE and TM equation sets (101)–(102), given the incident field is a plane wave. This evolution is approximated by central differences in the 1-D auxiliary grid in Fig. 20(a). We have seen that the phase velocity in the x direction is constant $(c_0/\sin\theta)$ in all layers; therefore, fields at different x values can be easily derived from those at any other x value by introducing a time delay. This property can be used to obtain the field values on the *two-dimensional* principal plane G, as shown in Fig. 20(b). A 1-D auxiliary grid as in Fig. 20(a) is placed at $x = 0$; this is shown magnified in the figure. Because only the spatial placement is shown, the field components $\{\mathcal{E}^h, \mathcal{E}^e, \mathcal{H}_z\}$ and $\{\mathcal{H}^h, \mathcal{H}^e, \mathcal{E}_z\}$ are collated at the same position (index k) on the z axis. Once the time history of the 1-D auxiliary grid at $x = 0$ is determined using the update equations (103)–(108), the field values at other x values can be simply obtained by introducing a time delay. For example, the TE electric field component $\mathcal{E}^h$ at $x = x_0$ is given by the value of $\mathcal{E}^h$ at $x = 0$

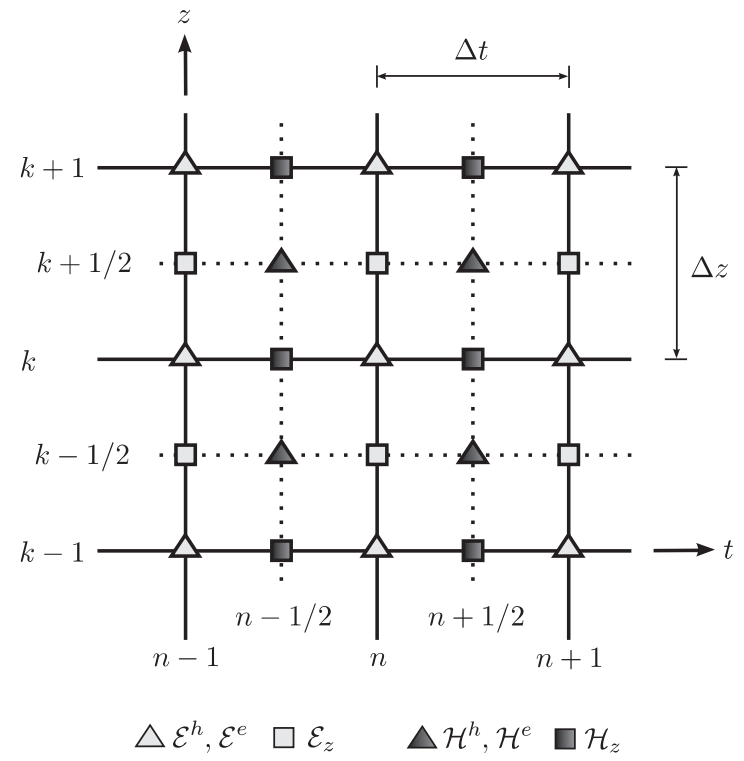

(a)

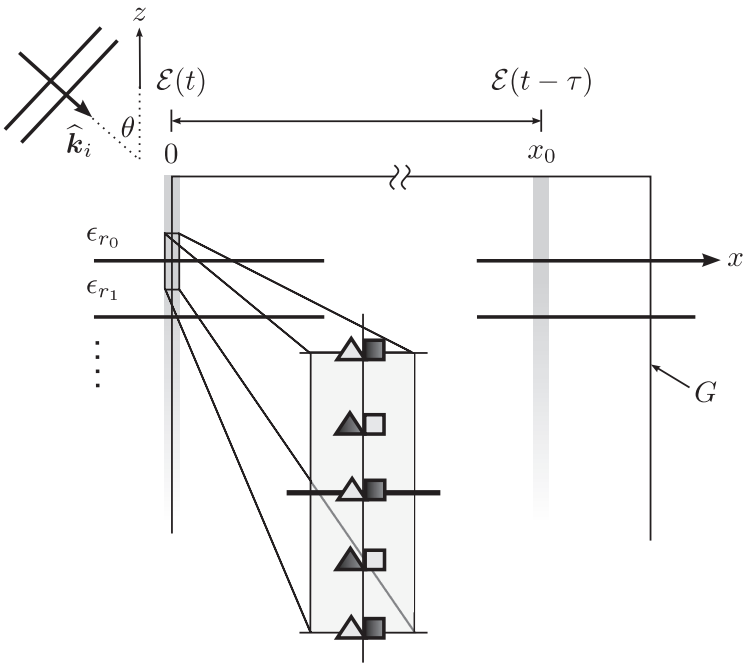

(b)

Figure 20: The usage of the 1-D auxiliary grid for obtaining the incident field on the principal plane G. (a) The temporal-spatial 1-D auxiliary grid. (b) The 2-D principal plane G, with a 1-D auxiliary grid at $x = 0$.

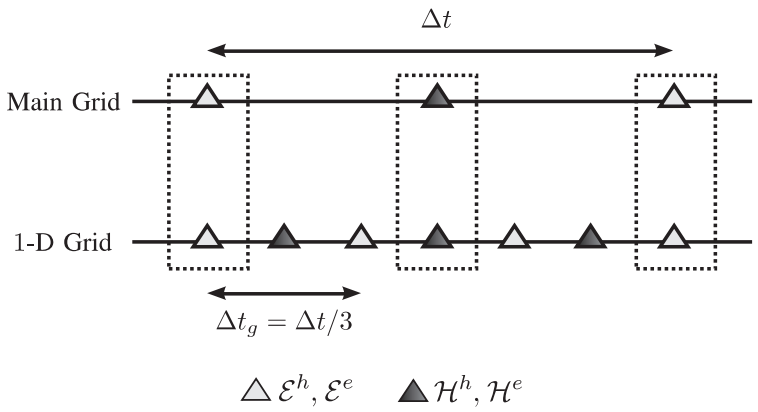

Figure 21: The reduction of the time step in the 1-D auxiliary grid for stability.

at an earlier time [see Fig. 20(b)]:

$$\mathcal{E}^h(x_0, z, t) = \mathcal{E}^h(0, z, t - \tau) = \mathcal{E}^h(0, z, t - \frac{x_0 \sin\theta}{c_0}) \ . \tag{109}$$

In light of the above discussion, the method of obtaining the incident field values on the TF/SF box in Fig. 18 can be summarized as follows. The time history of a single 1-D auxiliary grid at $x = 0$ is computed using the update equations (103)–(108), and stored off-line. When an incident field value is required at any point on the TF/SF box within the main simulation, the point is projected onto the principal plane G and the field value at the projected point on G is calculated using the available information on the time history at $x = 0$, along with the time delay relation (109). Because the time history consists of a discrete set of time values, interpolation in time is usually necessary while using (109).

3.1.2 Stability, Excitation and Dispersion

We now have the necessary tools to compute the incident field on the principal plane G, which consists of the initial plane wave incident from the uppermost layer and all of the reflections from the dielectric interfaces. There are, however, several aspects of the 1-D auxiliary grid in Fig. 20(a) that require further elaboration. First, we need to investigate the important issue of *stability* in the 1-D auxiliary grid. The stability requirement for (103)–(104) and (106)–(107) is given by the Courant stability criterion:

$$\Delta t \leq \frac{\Delta z}{c'} \ , \tag{110}$$

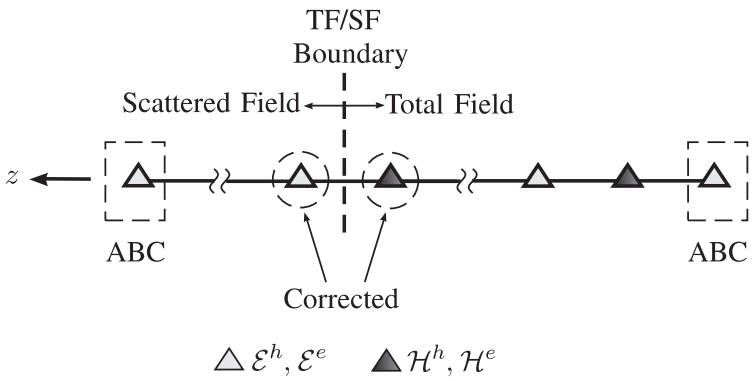

Figure 22: Grid termination and incident wave conditions for the 1-D auxiliary grid.

in which $c' = (\epsilon_0\mu_0(\epsilon_r - \epsilon_{r_0}\sin^2\theta))^{-1/2}$ is the velocity of propagation in the 1-D auxiliary grid in Fig. 20(a). Because it is possible to have $c' > c = (\epsilon_0\mu_0)^{-1/2}$, the use of the same values $\Delta t, \Delta z$ in the 1-D auxiliary grid as in the main grid might lead to instability. In this case, it is necessary to use either a larger Δz or a smaller Δt for the 1-D auxiliary grid. The former is undesirable because it results in poor spatial accuracy. Hence, a smaller time step, $\Delta t_g = \Delta t/k$ $(k > 1)$, is used in the 1-D auxiliary grid to maintain stability. Because it is still necessary to conform to the main-grid time spacing, Δt is divided by increasing *odd* integer values $(k = 3, 5, \ldots)$, as θ is increased further beyond the stability limit. In these cases, k 1-D-auxiliary-grid updates are done in a single main grid update cycle. An example with $k = 3$ is shown in Fig. 21, in which the upper line denotes the time axis for the main grid and the lower line denotes the time axis for the 1-D auxiliary grid. It is seen that the choice of odd k guarantees that every field component in the main grid has a corresponding field component in the 1-D auxiliary grid at the same instant of time. This correspondence is shown by the dashed rectangles in Fig. 21.

The second issue to consider is the *excitation* of the 1-D auxiliary grid, which consists of two parts: the introduction of the initial plane wave (shown in the top left corner in Fig. 20(b)), and the absorption of the scattered and transmitted plane waves at the two ends of the grid, namely, the proper termination of the grid. These two parts are shown schematically in Fig. 22. For introducing the initial plane wave, a one-dimensional TF/SF boundary (or a *one-way injector*) [2] is constructed. Corrections are applied to the update equations (103)–(108) for two field components (one $\mathcal{E}$ and one $\mathcal{H}$) situated at opposite

sides of the TF/SF boundary. The correction terms are directly proportional to the h- or e-polarized components of the initial plane wave. Exact expressions for these terms can be found in [2]. At the lower and upper ends of the grid, absorbing boundary conditions (ABC) are applied to efficiently absorb the waves that reach these points. A simple first-order ABC is sufficient for most practical purposes:

$$\mathcal{F}_0^{n+1} = \mathcal{F}_0^n + \frac{S-1}{S+1}\left(\mathcal{F}_1^{n+1} - \mathcal{F}_0^n\right) \tag{111}$$

$$\mathcal{F}_{N+1}^{n+1} = \mathcal{F}_N^n + \frac{S-1}{S+1}\left(\mathcal{F}_N^{n+1} - \mathcal{F}_{N+1}^n\right) \ , \tag{112}$$

in which $\mathcal{F}$ is $\mathcal{E}^e$ or $\mathcal{E}^h$, $S = c'\Delta t/\Delta z$ is the Courant number and N is the number of grid cells in the 1-D auxiliary grid.

Finally, we will quantify the effects of *grid dispersion* on the performance of the plane-wave injector. Grid dispersion is a numerical artifact encountered in discrete approximation methods like FDTD, which causes different spatial frequencies to propagate in the grid with different velocities [2]. The single most important criterion in building a plane-wave injector is the accuracy of the incident field assumed on the TF/SF boundary, including the dispersion effects inherent in the 3-D grid. In our plane-wave injector, the incident wave is obtained through the use of a 1-D auxiliary grid, which brings its own dispersion effects into the picture. Surprisingly, this turns out to be an advantage, since the dispersion effects in the 3-D grid can be emulated by the dispersion in the 1-D auxiliary grid, resulting in a more accurate incident field [25]. By the same token, the incident field obtained through a 1-D auxiliary grid is more "accurate" than the exact analytical incident field on the TF/SF boundary, since the latter does not account for dispersion. Here, accuracy refers to the degree of containment of the incident field inside the TF/SF boundary, rather than the similarity to exact analytical values.

The dispersion analysis in [25] is for a 2-D main grid. For our purposes, this analysis has to be extended into a 3-D main grid, since the principal plane in Fig. 19 need not be parallel to one of the principal axes. However, the analysis follows along the same lines as that of [25]. Here, we need to consider the difference between the dispersion factors in the 3-D main grid and the 1-D auxiliary grid. The dispersion equation for the 3-D grid is given

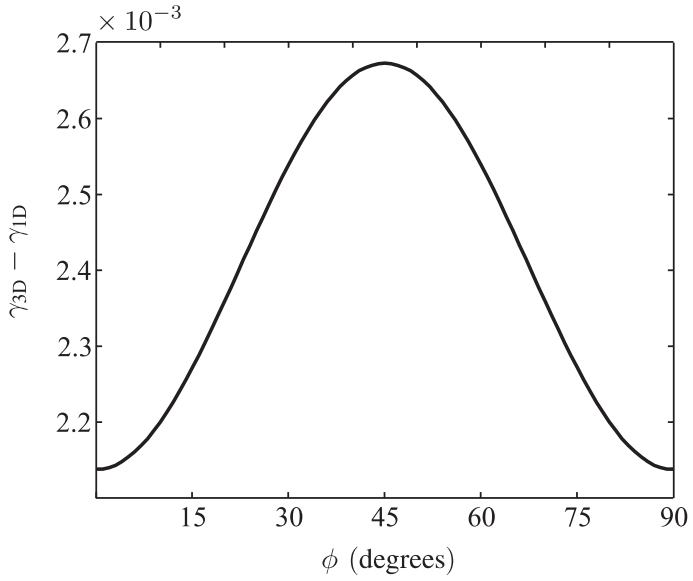

Figure 23: The difference between the dispersion factors $\gamma_{3D} - \gamma_{1D}$ in the 3-D main grid and the 1-D auxiliary grid.

by [2]

$$\sin^2\left(\frac{\pi S}{(\lambda/\Delta)}\right) = S^2\left[\sin^2\left(\frac{\pi \sin\theta\cos\phi}{(\lambda/\Delta)\gamma}\right) + \sin^2\left(\frac{\pi \sin\theta\sin\phi}{(\lambda/\Delta)\gamma}\right) + \sin^2\left(\frac{\pi\cos\theta}{(\lambda/\Delta)\gamma}\right)\right] , \tag{113}$$

in which $S = c\Delta t/\Delta$ is the Courant factor, λ/Δ is the number of grid cells per free-space wavelength, and $\gamma = v_p/c$ is the velocity of propagation in the 3-D grid normalized by c. This equation has to be solved numerically for γ. On the other hand, the dispersion equation for the 1-D auxiliary grid can be solved for γ in closed form, yielding [2]

$$\gamma = \frac{\pi\cos\theta}{(\lambda/\Delta)\sin^{-1}\left(\frac{\cos\theta}{S}\sin\left(\frac{\pi S}{(\lambda/\Delta)}\right)\right)} . \tag{114}$$

As we mentioned above, it is the *difference* between the 3-D dispersion factor γ_{3D} in (113) and the 1-D dispersion factor γ_{1D} in (114) that plays a role in the performance of the injector. The results in [25] can be obtained directly by substituting $\phi = 0$ into (113). Therefore, it is sufficient to analyze the effects of a nonzero ϕ, namely, the effects of deviations from perpendicular incidence toward oblique incidence. To this end, we will assume $\theta = 30°$, which is the angle that yields the maximum discrepancy $\gamma_{3D} - \gamma_{1D}$ for $\phi = 0$ [25], and use (113)–(114) to investigate the impact of nonzero ϕ on this discrepancy. In Fig. 23, we show the difference $\gamma_{3D} - \gamma_{1D}$ for different ϕ values, and $\lambda/\Delta = 10$, which is a common

value in many simulations. The Courant factor S does not have an appreciable effect on the difference $\gamma_{3D} - \gamma_{1D}$. The results in Fig. 23 show that the difference $\gamma_{3D} - \gamma_{1D}$ is maximum for $\phi = 45°$, and this maximum is 25% greater than the value for $\phi = 0$.

3.1.3 Example

We will now present an example that illustrates the use of the plane-wave injector described in the previous subsections. The geometry for the example is shown in Fig. 24(a): two parallel infinite dielectric slabs with relative permittivity $\epsilon_r = 2.5$, thickness 5 cm, and spacing 5 cm are in free space. They are illuminated by an incident plane wave with direction of propagation $\hat{\boldsymbol{k}}_i$ lying in the xz plane at an angle of $\theta = 70°$ to the z axis. The electric field of this wave is transverse to $\hat{\boldsymbol{k}}_i$ at an angle of 45° to the y axis, and it is a unit-amplitude Gaussian pulse in time: $\mathcal{E}^i(t) = \exp(-(t/\tau)^2/2)$ with $\tau = 40$ ps.

The parameters for the FDTD simulation are grid size 50 cm×1 cm×50 cm, grid spacing $\Delta x = \Delta y = \Delta z = \Delta = 1$ mm, and time step $\Delta t = (0.98/\sqrt{3})\Delta/c$. The solution space is surrounded by convolutional PML [6] of thickness 0.5 cm, with the slabs penetrating into the PML. The TF/SF boundary, represented by the dashed rectangle in Fig. 24(b), is 2.5 cm from the PML boundaries. To satisfy the stability requirement discussed earlier, the time step for the 1-D auxiliary grid is chosen to be one third of that for the main grid: $\Delta t_g = \Delta t/3$.

In Fig. 24(b), the magnitude of the electric field on the xz plane is displayed in dB on a gray scale, with black representing 0 dB and white representing −60 dB. To help with interpretation, the directions of propagation for the initial plane wave, $\hat{\boldsymbol{k}}_i$, and the first reflection and transmission at the upper surface of the top slab, $\hat{\boldsymbol{k}}_r$ and $\hat{\boldsymbol{k}}_t$, are shown on the plot. The multiple reflections from and transmissions through the two slabs are evident in the plot. Notice that, as expected, there is no field in the region between the TF/SF box and the PML. If an additional object were to be placed in the solution space, for example in one of the slabs, the scattered field from this object would appear in this region. If the scattered far field from the object were desired, it could be obtained by applying a near-field-to-far-field transformer for multilayered media to the field in this region (such a

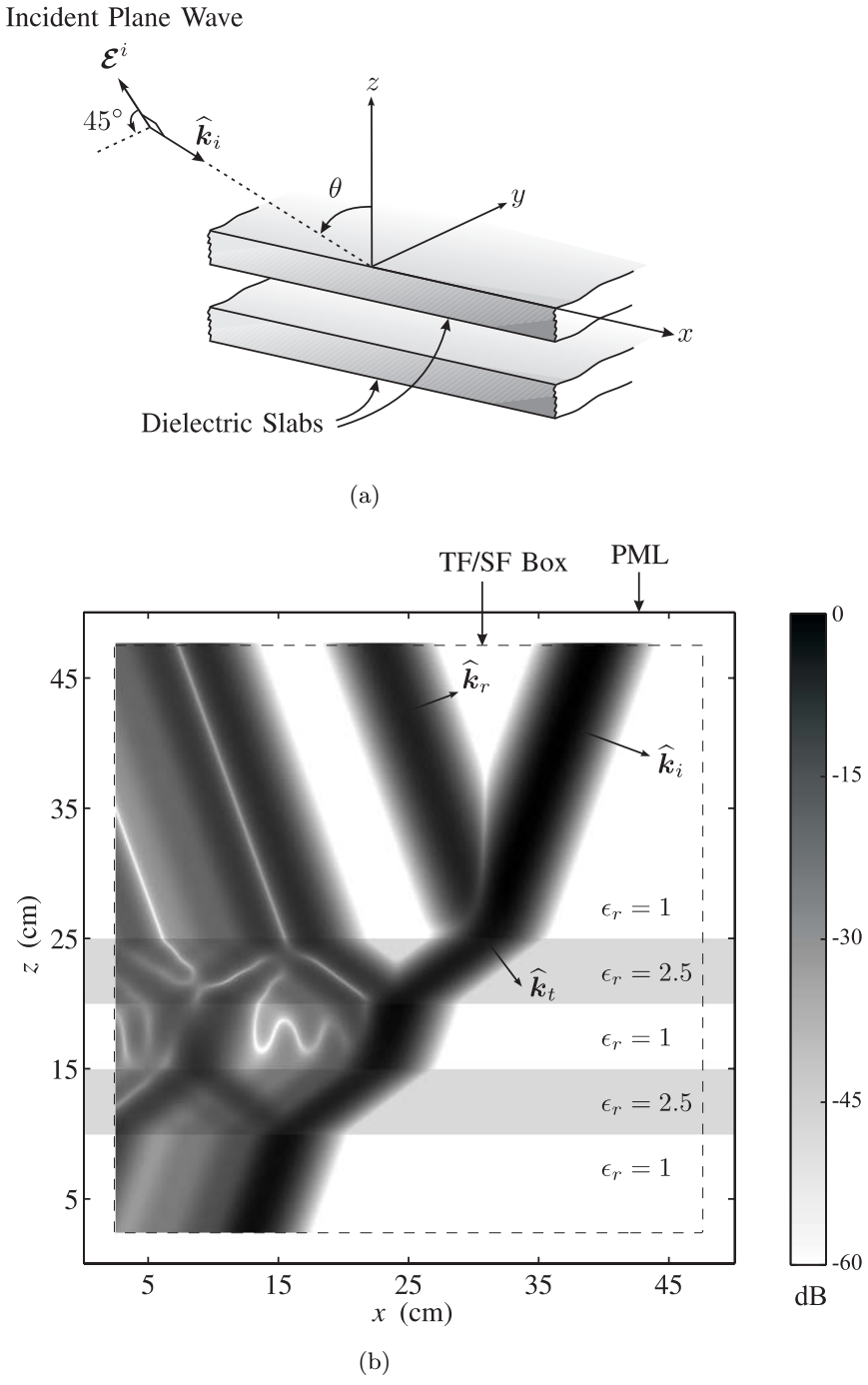

Figure 24: An example of plane-wave injection into a multilayered FDTD grid. (a) Geometry. (b) Grayscale plot of the dB–magnitude of the electric field in the xz plane.

transformer is presented in [32]). Note that this far field would only be due to the object in the presence of the slabs; it would not include the plane-wave scattering from the slabs.

Before concluding this section, we will compare the results given in the above example to those obtained using frequency-domain analysis followed by inverse Fourier transformation. The frequency-domain analysis of plane waves obliquely incident on multilayered media is well-documented in the literature [12]. Computational routines are also available online [33]. In Fig. 25, the y and z components of the electric field at the center of the FDTD grid in Fig. 24(b) are compared with those obtained using frequency-domain analysis and inverse Fourier transformation. The two results are seen to be in very good agreement.

3.2 Generalization to Lossy Media

3.2.1 Formulation

The transmission-line equations (101)–(102) are derived in Appendix C for *lossless* multilayered media. Can we follow a similar procedure in the presence of *loss* in the multilayered medium? In other words, can we find time-domain transmission-line equations similar to (101)–(102) for lossy multilayered media? The answer is yes, but the direct time-domain route followed in Appendix C turns out to be inefficient. Instead, we will start with the frequency-domain versions of (101)–(102) given in [17], and try to invert these equations to time domain in the presence of loss. The advantage of this detour is the possibility of representing loss directly by using the *complex relative permittivity* ϵ_r^*:

$$\epsilon_r^* = \epsilon_r' - j\frac{\sigma}{\omega\epsilon_0} \ , \tag{115}$$

in which σ is the conductivity (S/m) of the material and ω is the angular frequency. The frequency-domain transmission-line equations in [17] are

$$\begin{aligned} \frac{\partial E^h}{\partial z} &= -j\omega\mu_0 H^h \\ \frac{\partial H^h}{\partial z} &= -j\omega\epsilon_0(\epsilon_r^* - \epsilon_{r_0}\sin^2\theta)E^h \qquad \text{(TE)} \\ H_z &= Y_0\sqrt{\epsilon_{r_0}}\sin\theta\, E^h \end{aligned} \tag{116}$$

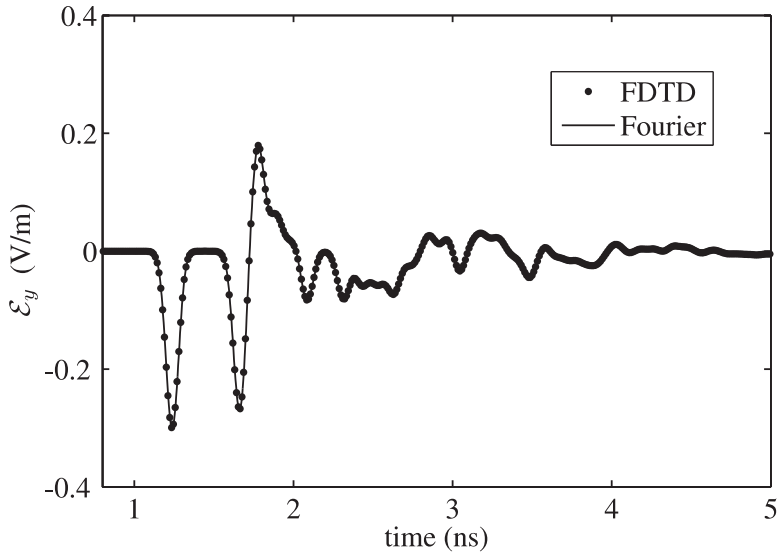

(a)

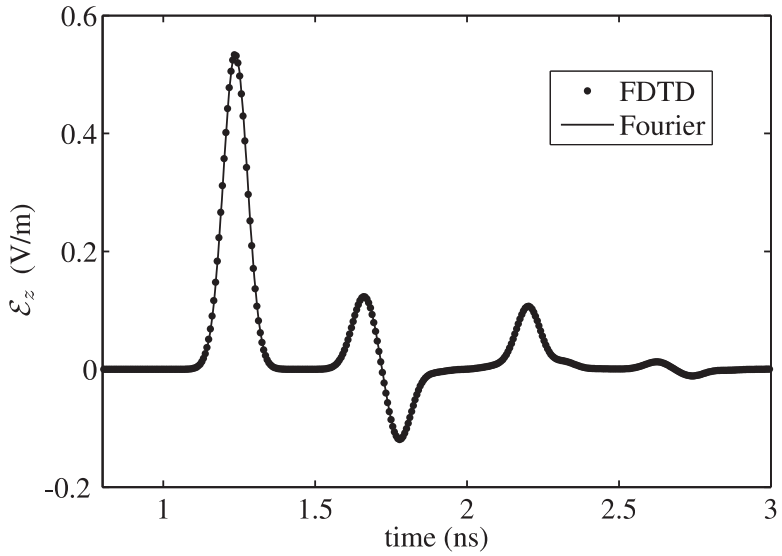

(b)

Figure 25: Comparison of the components of the electric field at the center of Fig. 24(b) obtained through the FDTD method (dots) and Fourier transformation (solid line): (a) y component, (b) z component.

and

$$\begin{aligned}
\frac{\partial E^e}{\partial z} &= -j\omega \frac{\mu_0(\epsilon_r^* - \epsilon_{r_0}\sin^2\theta)}{\epsilon_r^*} H^e \\
\frac{\partial H^e}{\partial z} &= -j\omega\epsilon_0\epsilon_r^* E^e \qquad\qquad \text{(TM)} \\
E_z &= -\frac{Z_0\sqrt{\epsilon_{r_0}}\sin\theta}{\epsilon_r^*}\, H^e \ ,
\end{aligned} \tag{117}$$

in which Roman font denotes frequency-domain variables. For no loss ($\sigma = 0$), these equations yield the time-domain transmission-line equations (101)–(102) upon inverse Fourier transformation ($j\omega \rightarrow \partial/\partial t$). However, if there is loss in the medium, the complex ϵ_r^* term in the denominator of the first TM equation in (117) complicates its direct inversion to the time domain. In [25], ϵ_r^* is carried inside the partial derivative $\partial/\partial z$ in the left-hand side and another variable $E^{e'}$ is defined for $\epsilon_r^* E^e$. The accuracy of this step is questionable for the following reason: From the TM equations in (117), it can be shown that both E^e and H^e must be continuous throughout the medium. Therefore, $E^{e'} = \epsilon_r^* E^e$ must be *discontinuous* across a material boundary. This discontinuity poses a problem when we attempt to discretize $E^{e'}$ and approximate $\partial E^{e'}/\partial z$ by the resulting finite differences. Because the theoretical values for $E^{e'}$ are discontinuous, the finite difference approximation of $\partial E^{e'}/\partial z$ predicts unnatural spikes in the H-field, although the H-field is continuous in theory. To avoid this problem, we will use a different approach. We will let

$$H^{e'} = \frac{H^e}{\epsilon_r^*} \ , \tag{118}$$

and invert (116)–(117) to the time domain using this definition:

$$\begin{aligned}
\frac{\partial \mathcal{E}^h}{\partial z} &= -\mu_0 \frac{\partial \mathcal{H}^h}{\partial t} \\
\frac{\partial \mathcal{H}^h}{\partial z} &= -\sigma\mathcal{E}^h - \epsilon_0(\epsilon_r' - \epsilon_{r_0}\sin^2\theta)\frac{\partial \mathcal{E}^h}{\partial t} \qquad \text{(TE)} \\
\mathcal{H}_z &= Y_0\sqrt{\epsilon_{r_0}}\sin\theta\, \mathcal{E}^h
\end{aligned} \tag{119}$$

and

$$\begin{aligned}
\frac{\partial \mathcal{E}^e}{\partial z} &= -\frac{\sigma\mu_0}{\epsilon_0}\mathcal{H}^{e'} - \mu_0(\epsilon_r' - \epsilon_{r_0}\sin^2\theta)\frac{\partial \mathcal{H}^{e'}}{\partial t} \\
\frac{\partial \mathcal{H}^e}{\partial z} &= -\sigma\mathcal{E}^e - \epsilon_0\epsilon_r' \frac{\partial \mathcal{E}^e}{\partial t} \qquad\qquad \text{(TM)} \\
\mathcal{E}_z &= -Z_0\sqrt{\epsilon_{r_0}}\sin\theta\, \mathcal{H}^{e'} \ .
\end{aligned} \tag{120}$$

In addition to the above equations, (118) introduces another equation that defines the relation between the auxiliary variable $\mathcal{H}^{e'}$ and the magnetic field variable $\mathcal{H}^{e}$:

$$\frac{\partial \mathcal{H}^e}{\partial t} = \frac{\sigma}{\epsilon_0}\mathcal{H}^{e'} + \epsilon_r' \frac{\partial \mathcal{H}^{e'}}{\partial t} \ . \tag{121}$$

Now, the reason for defining $H^{e'} = H^e/\epsilon_r^*$ instead of $E^{e'} = \epsilon_r^* E^e$ is clear: The spatial derivative of $\mathcal{H}^{e'}$ never appears in the equations (120)–(121), so the discontinuity of $\mathcal{H}^{e'}$ across material boundaries does not affect the finite-difference approximation. The validity of this assertion will be demonstrated through an example in the next subsection.

The discretization of the TE and TM equations in (119)–(120) lead to familiar update equations, the common forms of which can be found in [2]. The update equation corresponding to the auxiliary equation (121) has the same form. This auxiliary update converts $\mathcal{H}^{e'}$ to $\mathcal{H}^{e}$ and must be performed together with the first update in (120).

The presence of loss introduces an additional memory requirement for storing the auxiliary variable $\mathcal{H}^{e'}$ and an additional computational requirement for converting $\mathcal{H}^{e'}$ to $\mathcal{H}^{e}$. Since the 1-D auxiliary grid in Fig. 20(a) is usually much smaller than the main grid, these additional requirements do not cause an appreciable reduction in performance.

Since the uppermost layer is always assumed lossless, the TF/SF boundary and the upper grid termination in Fig. 22 are unchanged when loss is introduced in the other media. However, the presence of loss in the lowermost layer requires a modification in the absorbing boundary condition in (112). Assuming an electric conductance σ in the lowermost layer, the TE and TM components of the incident electric field both satisfy the following dissipative wave equation (superscript p is either h or e):

$$\frac{\partial^2 \mathcal{E}^p}{\partial z^2} - \frac{1}{(c')^2}\left(\frac{\partial^2}{\partial t^2} + \frac{\sigma'}{\epsilon_0}\frac{\partial}{\partial t}\right)\mathcal{E}^p = 0 \ , \tag{122}$$

in which $c' = c/(\epsilon_r - \epsilon_{r_0}\sin^2\theta)^{1/2}$, and $\sigma' = \sigma/(\epsilon_r - \epsilon_{r_0}\sin^2\theta)$. A stable method for terminating the finite-difference grid for such a dissipative wave equation has been derived in [34].

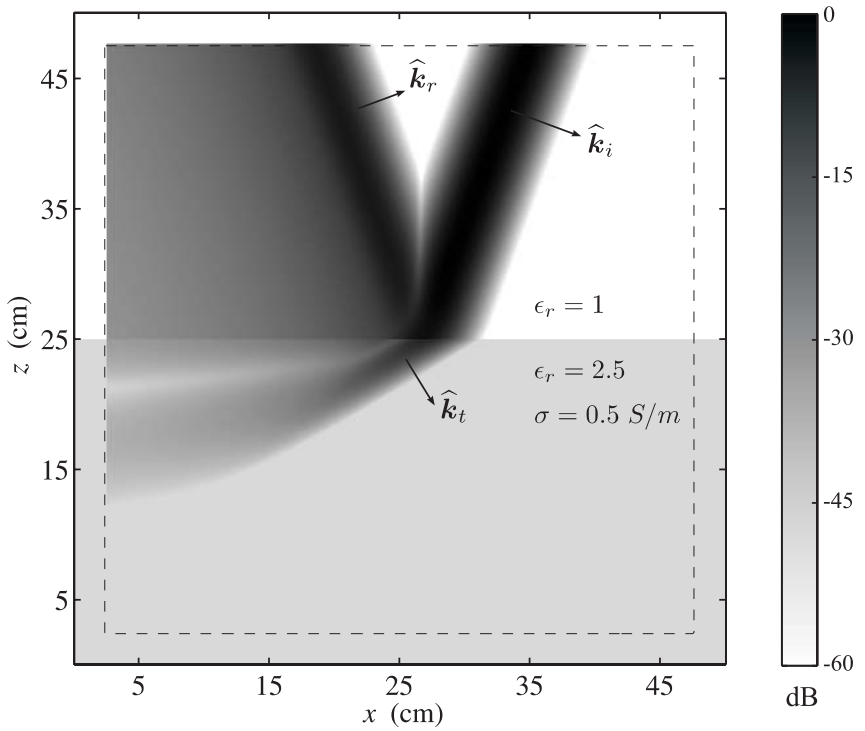

Figure 26: An example of plane-wave injection into a two-layered FDTD grid representing a lossy ground.

3.2.2 Example

To illustrate the use of the plane-wave injector in lossy multilayered media, we present a simple and practical example: a two-layered medium consisting of free space and lossy ground. Although the efficiency of the method described above is not affected by the number of layers present in the medium, a two-layered lossy ground is considered merely because of its common appearance in the FDTD literature. The geometry for this example is shown in Fig. 26. The electrical parameters for the ground represented by the gray half-space in Fig. 26 are $\epsilon_r = 2.5$ and $\sigma = 0.5$ S/m, and all of the other parameters for the FDTD simulation, including those for the incident plane wave, are the same as for the example in Fig. 24.

In Fig. 26, the magnitude of the electric field on the xz plane is displayed as before in dB on a gray scale, with black representing 0 dB and white representing -60 dB. Again, to help with interpretation, the directions of propagation for the incident, $\hat{\boldsymbol{k}}_i$, reflected, $\hat{\boldsymbol{k}}_r$, and transmitted, $\hat{\boldsymbol{k}}_t$, waves are shown on the plot. As expected, the transmitted wave is seen to rapidly decay in amplitude after entering the lossy ground. Notice that the shapes

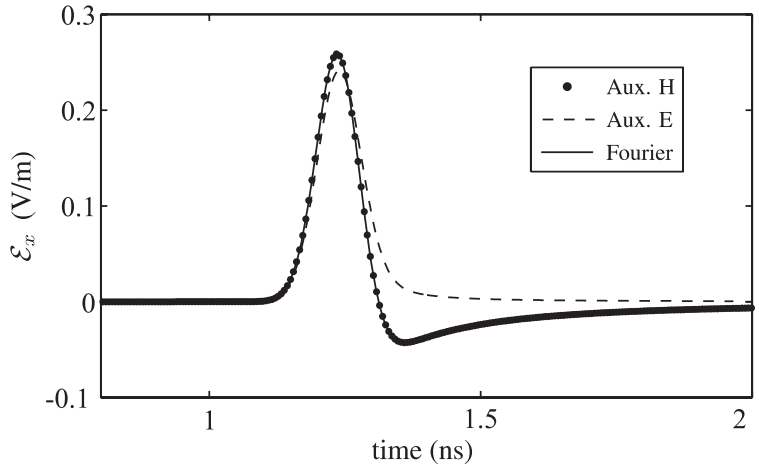

Figure 27: Comparison of the x components of the electric field at the center of the 1-D auxiliary grid for Fig. 26 obtained through different methods: the auxiliary $\mathcal{H}^{e'}$ method (dots), the auxiliary $\mathcal{E}^{e'}$ method (dashed line), and Fourier transformation (solid line).

of the reflected and transmitted pulses are quite different from the shape of the incident pulse. This is particularly evident for the reflected wave, which is spread out in space much more than the incident wave. This distortion is caused by the frequency dependence of the complex relative permittivity for the ground (115), which not only adds dispersion for the propagation in the ground but also to the reflection coefficient for the wave above the ground.

Finally, we will demonstrate the accuracy of the method introduced above for lossy media by comparing our results to those presented in [25], and those obtained using Fourier transformation [33]. In Fig. 27, we present the x component of the electric field at the center of the 1-D auxiliary grid for Fig. 26 obtained through the auxiliary $\mathcal{H}^{e'}$ method in (118) (dots), the auxiliary $\mathcal{E}^{e'}$ method given in [25] (dashed line), and Fourier transformation (solid line). It is seen that the auxiliary $\mathcal{H}^{e'}$ method predicts the electric field at the boundary with better accuracy.

3.3 Inhomogeneous Plane Waves

3.3.1 Formulation

Our treatment so far has excluded a special case, namely, the presence of inhomogeneous (or evanescent) plane waves [1] in certain layers. This type of plane wave is observed in

layer n when the incident plane wave is a slow wave for medium n. This means that the transverse phase velocity of the incident plane wave along the interfaces (which is constant throughout the multilayered medium) is smaller than the speed of light in layer n. In that case, a plane-wave front does not form in the wake of the disturbance at the interface between medium $n-1$ and medium n. For an incidence angle θ and lossless media, the above condition is expressed mathematically as

$$\sin\theta > \sqrt{\frac{\epsilon_{r_n}}{\epsilon_{r_0}}} \ , \tag{123}$$

and called the *total internal reflection* (TIR) condition [12].

Although it is usually considered to be a frequency-domain concept, the inhomogeneous plane wave has a number of distinctive properties in the time domain. Similar to its frequency-domain counterpart, it does not carry any energy in the direction normal to the layers and away from interface (unless there are other layers below for which the TIR condition does not apply), and it decays in amplitude in that direction. Unlike its frequency-domain counterpart, the decay is usually non-exponential. However, as the wave shape becomes more narrowband in frequency, the decay begins to assume the exponential behavior that would be expected from a single-frequency inhomogeneous plane wave.

Perhaps the most peculiar feature an inhomogeneous plane has in the time domain is apparent non-causality [35]. This phenomenon is most evident for signals of wide bandwidth, and is absent for practical narrowband signals in which the spectrum is concentrated about a single frequency. In this section, we adapt the previously described plane-wave injector the include the latter – inhomogeneous plane waves of narrow bandwidth.

The governing transmission-line equations for an inhomogeneous plane wave are the same as the TE and TM equations in (101)–(102) for a homogeneous plane wave; however, the TIR condition in (123) changes the nature of these equations considerably. With the TIR condition, they become

$$\begin{aligned} \frac{\partial \mathcal{E}^h}{\partial z} &= -\Big[\mu_0\Big]\frac{\partial \mathcal{H}^h}{\partial t} \\ \frac{\partial \mathcal{H}^h}{\partial z} &= \Big[\epsilon_0(\epsilon_{r_0}\sin^2\theta - \epsilon_{r_n})\Big]\frac{\partial \mathcal{E}^h}{\partial t} \\ \mathcal{H}_z &= Y_0\sqrt{\epsilon_{r_0}}\sin\theta\,\mathcal{E}^h \ , \end{aligned} \tag{124}$$

and

$$\begin{aligned} \frac{\partial \mathcal{E}^e}{\partial z} &= \left[\frac{\mu_0(\epsilon_{r_0}\sin^2\theta - \epsilon_{r_n})}{\epsilon_{r_n}}\right]\frac{\partial \mathcal{H}^e}{\partial t} \\ \frac{\partial \mathcal{H}^e}{\partial z} &= -\Big[\epsilon_0\epsilon_{r_n}\Big]\frac{\partial \mathcal{E}^e}{\partial t} \\ \mathcal{E}_z &= -\frac{Z_0\sqrt{\epsilon_{r_0}}\sin\theta}{\epsilon_r}\,\mathcal{H}^e \end{aligned} \tag{125}$$

in which the coefficients in square brackets are positive.

If we proceed as we did for the homogeneous plane waves in Sec. 3.1 and discretize (124)–(125) to obtain update equations similar to (103)–(108), we encounter a serious problem: The resulting update equations corresponding to (124)–(125) are *unstable*. In contrast to the TE and TM update equations (103)–(108) for homogeneous plane waves, this instability does not depend on the choice of the time step Δt or the grid spacing Δz. Since the equations (124)–(125) can be written as second-order elliptic equations for $\mathcal{E}^h$ and $\mathcal{E}^e$, the leap-frog algorithm is inherently unstable [36, 37]. If we wish to inject an inhomogeneous plane wave into medium n, we must modify the traditional time-stepping in (103)–(108) to obtain stable solutions of (124)–(125).

Our method relies on the assumption that the system is narrowband; consequently, we shall find it extremely useful to employ the *analytic representation* (or complex representation) [38] of the narrowband electromagnetic field. This representation is commonly used in the analysis of narrowband disturbances in optics, and is related to the phasor concept used for single-frequency (or monochromatic) systems. In this representation, we regard the field variables as the real parts of *complex* field variables that are *analytic* in the complex time plane $\widetilde{t} = t_r + j\,t_i$. For example, the TE electric field variable is written as

$$\mathcal{E}^h(t) = \mathcal{A}(t)\cos(\phi(t) + \omega_0 t) = \Re\left\{\widetilde{\mathcal{E}}^h(t)\right\}\ , \tag{126}$$

in which ω_0 is the center frequency of the narrowband excitation, and the *analytic TE electric field* is defined as

$$\widetilde{\mathcal{E}}^h(t) = \mathcal{E}^h(t) + j\,\widehat{\mathcal{E}}^h(t) = \mathcal{A}(t)e^{j\phi(t)}e^{j\omega_0 t}\ . \tag{127}$$

It can be shown that $\widetilde{\mathcal{E}}^h(t)$ is indeed an analytic function [39] in the upper complex half

plane $t_i > 0$, and its real and imaginary parts form a Hilbert transform pair [38, 40]:

$$\begin{aligned} \mathcal{E}^h &= -\mathscr{H}\{\widehat{\mathcal{E}}^h\} \\ \widehat{\mathcal{E}}^h &= \mathscr{H}\{\mathcal{E}^h\} \ . \end{aligned} \tag{128}$$

Note that the system of PDEs (124)–(125) is linear and purely real, so the imaginary parts of the analytic field variables can be discarded at the end of the analysis.

The following analysis will be presented for the TE equation set (124); the results are similar for the TM case. The main idea in the analytic representation of narrowband systems is that the functions $\mathcal{A}(t)$, $\phi(t)$ vary slowly compared to $\omega_0 t$, and the derivative of the analytic TE electric variable can be approximated as

$$\frac{\partial \widetilde{\mathcal{E}}^h(t)}{\partial t} \approx (j\omega_0)\mathcal{A}(t)e^{j\phi(t)}e^{j\omega_0 t} \ . \tag{129}$$

Applying the narrowband assumption (129) to (124), we obtain

$$\mathcal{E}^h = j\,\frac{C}{\omega_0}\,\frac{\partial \mathcal{H}^h}{\partial z} \tag{130}$$

$$\mathcal{H}^h = j\,\frac{D}{\omega_0}\,\frac{\partial \mathcal{E}^h}{\partial z} \ , \tag{131}$$

in which $C = 1/(\epsilon_0(\epsilon_{r_n} - \epsilon_{r_0}\sin^2\theta)) < 0$, and $D = 1/\mu_0 > 0$. For clarity, we have omitted the tilde ($\sim$) on the field variables; however, it must be understood that the analytic field variables are used throughout the 1-D auxiliary grid whenever there are inhomogeneous waves present in the system. To illustrate the discretization and the updating method for the above equations, we assume a 3-cell thick layer supporting inhomogeneous waves, as shown in Fig. 28. The interfaces between the layer and the neighboring layers are shown by thick solid lines at spatial positions $z = (k+2)\Delta z$ and $z = (k-1)\Delta z$. The plane wave is assumed to be propagating at $z \geq (k+2)\Delta z$ and $z \leq (k-1)\Delta z$. The region in which the plane wave is assumed to be inhomogeneous is enclosed by the gray rectangle in Fig. 28. For the sake of illustration, the rectangle covers only the time values $t = (n-1/2)\Delta t$, $n\Delta t$ and $(n+1/2)\Delta t$, which will appear in our update equations.

In the shaded region in Fig. 28, the TE equations in (130)–(131) can be discretized as

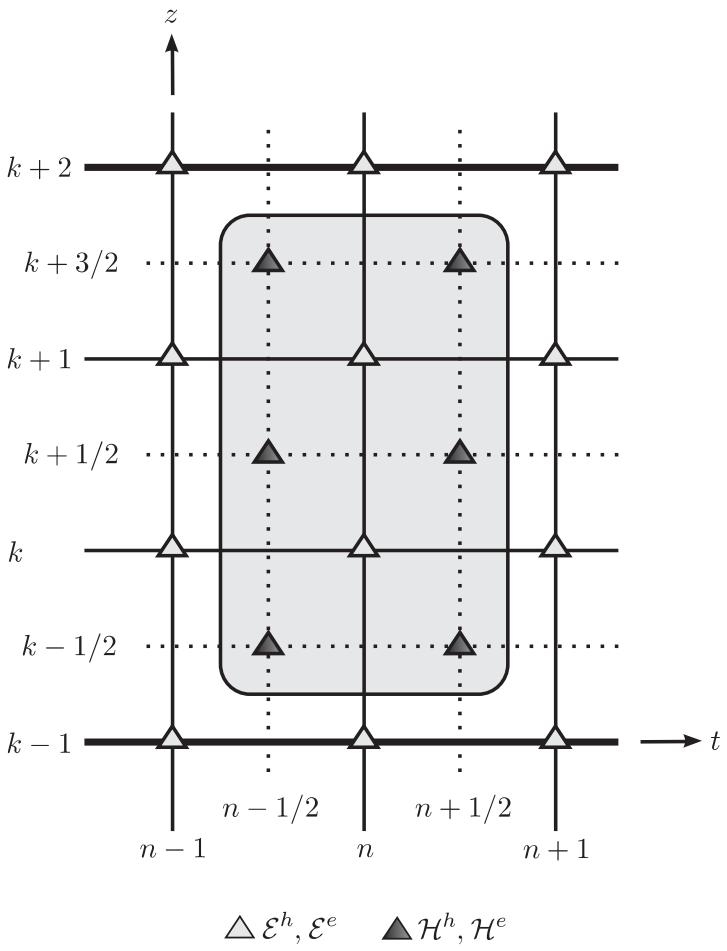

Figure 28: Grid showing a 3-cell thick layer that supports inhomogeneous plane waves.

follows:

$$\mathcal{E}^h\Big|_k^n = j\frac{C_k}{\omega_0\Delta z}\cdot\left[\frac{\mathcal{H}^h\big|_{k+1/2}^{n+1/2}+\mathcal{H}^h\big|_{k+1/2}^{n-1/2}}{2}-\frac{\mathcal{H}^h\big|_{k-1/2}^{n+1/2}+\mathcal{H}^h\big|_{k-1/2}^{n-1/2}}{2}\right] \tag{132}$$

$$\frac{\mathcal{H}^h\big|_{k+1/2}^{n+1/2}+\mathcal{H}^h\big|_{k+1/2}^{n-1/2}}{2} = j\frac{D_{k+1/2}}{\omega_0\Delta z}\left[\mathcal{E}^h\Big|_{k+1}^n-\mathcal{E}^h\Big|_k^n\right]. \tag{133}$$

Combining (132) and (133), we obtain the following *implicit* equation for the TE electric field $\mathcal{E}^h$:

$$\mathcal{E}^h\Big|_k^n = \frac{-C_k}{(\omega_0\Delta z)^2}\left[D_{k+1/2}\,\mathcal{E}^h\Big|_{k+1}^n-(D_{k+1/2}+D_{k-1/2})\,\mathcal{E}^h\Big|_k^n+D_{k-1/2}\,\mathcal{E}^h\Big|_{k-1}^n\right]. \tag{134}$$

The implicit equation in (134) can be written as a linear tridiagonal system $Ax = b$, for which efficient solution algorithms such as LU decomposition exist [41]. In reference to Fig. 28, the update coefficients $\{D_{k-1/2}, C_k, D_{k+1/2}, C_{k+1}, D_{k+3/2}\}$ are used to fill the 2×2

tridiagonal matrix A, and the update coefficients $\{D_{k-1/2}, C_k, C_{k+1}, D_{k+3/2}\}$ along with $\mathcal{E}^e_{k+2}$, $\mathcal{E}^e_{k-1}$ are used to fill the vector b. After solving for the electric field, the magnetic field can be directly obtained from (133).

It is apparent from (134) that the electric field components in the region with inhomogeneous waves depend on the electric field values at the interfaces, specifically, $\mathcal{E}^h_{k+2}$, $\mathcal{E}^h_{k-1}$ in Fig. 28. This suggests a straightforward update cycle for the entire 1-D auxiliary grid, which can be summarized as follows. Assuming that the initial values for the electric and magnetic fields are known everywhere in the grid, we start by applying a single leap-frog update to the electric and magnetic field components in the regions with homogeneous waves. Then, we solve for the electric field values in the regions with inhomogeneous waves using the implicit equation (134). Finally, we update the magnetic field values in the same regions using (133).

As a side note, we simply state without detail that if the plane wave is inhomogeneous at the interfaces ($z = (k+2)\Delta z, (k-1)\Delta z$ in Fig. 28), an implicit equation similar to (134) is constructed for the *magnetic field* $\mathcal{H}^h$, and solved in a similar manner.

3.3.2 Stability and Excitation

The updating scheme explained above is unconditionally stable for regions with pure inhomogeneous waves, but the real stability issue arises at the *interfaces*, where a transition from homogeneous plane waves to inhomogeneous plane waves occurs. Some insight can be obtained into this problem by investigating the case shown in Fig. 29, where the 1-D auxiliary grid consists of an isolated interface at $z = k_0\Delta z$ between two regions with homogeneous and inhomogeneous plane waves. At the interface denoted by the thick solid line ($z = k_0\Delta z$), the plane wave is homogeneous; and right below the interface ($z = (k_0 - 1/2)\Delta z$), the plane wave is inhomogeneous. All field components except those at $z = k_0\Delta z, (k_0 - 1/2)\Delta z$ are assumed to be zero. Denoting the temporal z-transforms [42] of $\{\mathcal{E}^h|^n_{k_0}, \mathcal{H}^h|^{n-1/2}_{k_0-1/2}\}$ by $\{\widetilde{E}, \widetilde{H}\}$ respectively, the update equations for the field variables can be written as

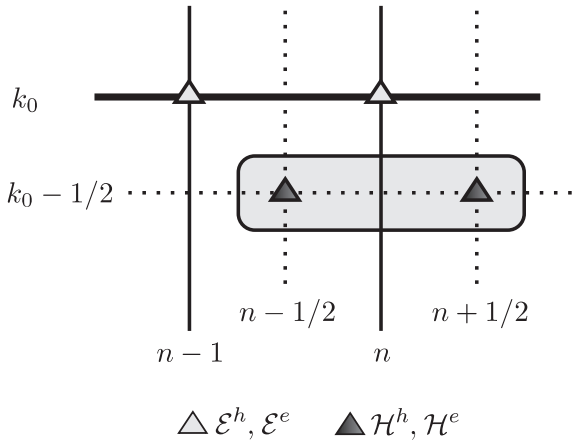

Figure 29: A simple grid that consists of an isolated interface between two regions with homogeneous (upper) and inhomogeneous (lower) plane waves.

$$(z-1)\,\widetilde{E} = -\frac{C_{k_0}\Delta t}{\Delta z}\,\widetilde{H} \tag{135}$$

$$(z+1)\,\widetilde{H} = j\,\frac{2\,D_{k_0-1/2}}{\omega_0 \Delta z}\,\widetilde{E}\ . \tag{136}$$

Note that (135) follows from (104), and (136) follows from (133). This is a mixture of the usual leap-frog scheme used for the homogeneous waves in (103)–(104), and the implicit scheme used for the inhomogeneous waves in (133)–(134). The stability of this mixed update scheme is determined by the roots $z_{1,2}$ of the determinant of the system (135)–(136):

$$z_{1,2} = \pm\sqrt{1-\xi^2} + j\,\xi \tag{137}$$

in which

$$\xi = \frac{C_{k_0} D_{k_0-1/2} \Delta t/\omega_0}{\Delta z^2}\ . \tag{138}$$

It is readily seen that the roots $z_{1,2}$ stay on the unit circle and the update scheme is stable if and only if

$$\frac{\sqrt{|C_{k_0} D_{k_0-1/2}|}\sqrt{\Delta t/\omega_0}}{\Delta z} < 1\ . \tag{139}$$

Note that this condition only applies for the simple case for which the 1-D auxiliary grid consists of the close proximity of an interface between two regions with homogeneous and inhomogeneous waves, as shown in Fig. 29. Numerous computer experiments suggest that the stability condition for a more general grid with an arbitrary multilayered structure has

the same form as (139), only with a tighter bound:

$$\frac{\sqrt{|C_{k_0} D_{k_0-1/2}|}\sqrt{\Delta t/\omega_0}}{\Delta z} < 0.5 \ . \tag{140}$$

The final stability condition (140) for inhomogeneous plane waves is partly empirical, and presents further challenges for its analytical verification and/or improvement.

Another vital issue that requires attention is the excitation of the 1-D auxiliary grid in the presence of analytic field variables. At this point, we must answer an important question: How do we ensure the analyticity of the field variables throughout the 1-D auxiliary grid? The answer lies in a fundamental result from the theory of partial differential equations (PDEs): The Cauchy-Kowalewski theorem [37] guarantees the analyticity of the field variables if the excitation of the PDEs (124)–(125) governing them is analytic. Remember from the discussion regarding the excitation of the 1-D auxiliary grid in Sec. 3.1.2 (specifically, Fig. 22 and the related discussion) that the corrections applied to the 1-D auxiliary grid are proportional to the initial plane wave, and they play the role of the excitation of the PDEs (124)–(125). Consequently, the critical step in the generalization to analytic field variables is the generalization to an *analytic initial plane wave*. This generalization requires a minor additional computation, i.e., the Hilbert transformation of the real initial plane-wave waveform according to (128). This operation is usually done off-line, since the initial plane wave is usually fixed before the simulation.

It should be noted that the generalization to complex field variables doubles the storage and computation requirement in the 1-D auxiliary grid, but this overhead is usually negligible compared to the total computational load of the main simulation.

3.3.3 Example

Finally, we present an example illustrating the creation of narrowband inhomogeneous plane waves using the plane-wave injector. Specifically, we will demonstrate the *frustrated total internal reflection* (FTIR) phenomenon [1], which is inherently associated with inhomogeneous plane waves. The configurations to be used in this discussion are shown in Fig. 30. In Fig. 30(a), a plane wave is incident from a medium with relative permittivity $\epsilon_r = 2.5$

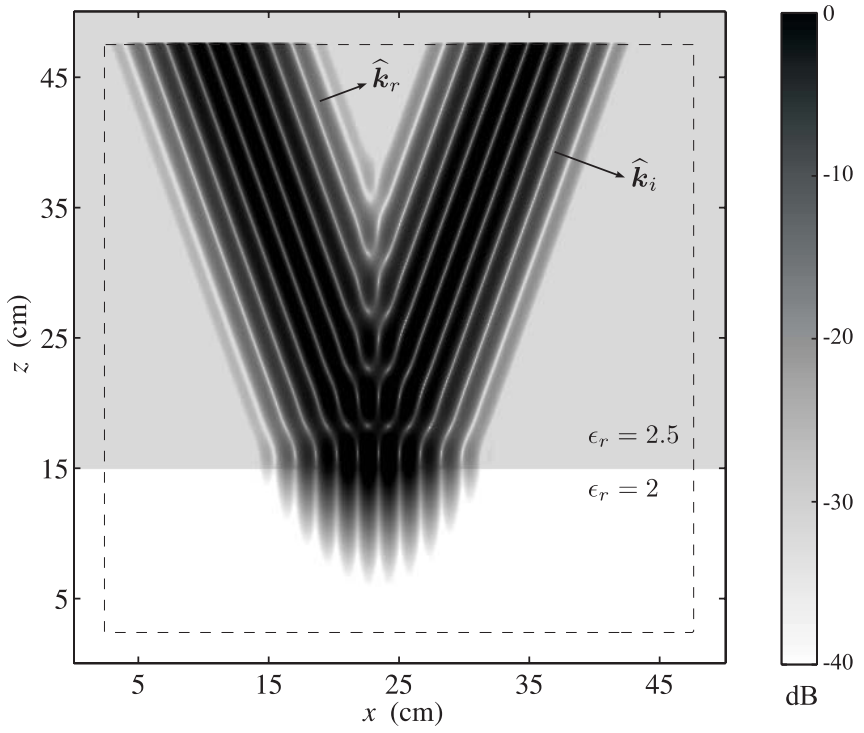

(a)

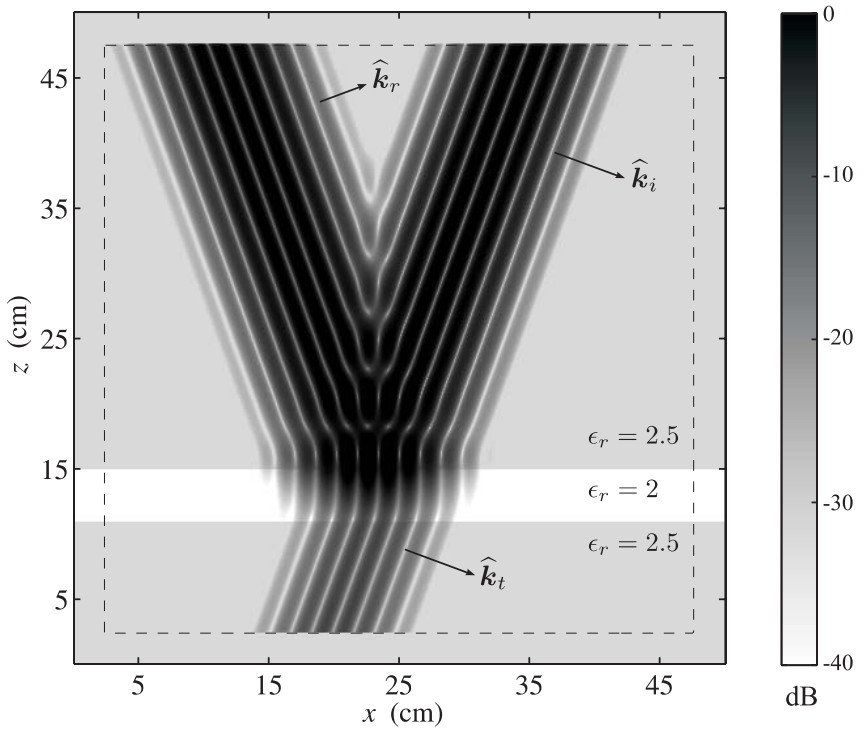

(b)

Figure 30: An example of the injection of narrowband inhomogeneous plane waves into multilayered media. (a) Total internal reflection. (b) Frustrated total internal reflection. Grayscale plots (dB) are for the magnitude of the electric field in the xz plane.

onto a half space with lower permittivity $\epsilon_r = 2$. In Fig. 30(b), the lower half space has been replaced by a slab with $\epsilon_r = 2$ and thickness 4 cm. In both figures, the magnitude of the electric field in the xz plane is displayed as before in dB on a gray scale, with black representing 0 dB and white representing -40 dB.

The electric field of the incident plane wave is a sinusoid of frequency $f_0 = 6.32$ GHz modulated by a unit-amplitude Gaussian pulse: $\mathcal{E}^i(t) = \exp(-(t/\tau)^2/2)\sin(2\pi f_0 t)$ with $\tau = 135$ ps. This type of waveform is typical for optical signals. As in the other examples, the direction of propagation $\hat{\boldsymbol{k}}_i$ is at the angle $\theta = 70^\circ$ to the z axis. Thus, according to (123), total internal reflection occurs at the interface of the half space: $\sin(\theta) = 0.940 > \sqrt{\epsilon_{r_1}/\epsilon_{r_0}} = \sqrt{2/2.5} = 0.894$. This is evident in the plot for Fig. 30(a). The incident plane wave is completely reflected at the interface, and an inhomogeneous plane wave, which decays in the direction normal to the interface, forms in the lower half space.

The results in Fig. 30(b) are more interesting. Some of the energy in the incident plane wave has been transmitted through the slab and is propagating away from the slab as a plane wave at direction $\hat{\boldsymbol{k}}_t$. The amount of the transmitted energy depends on the thickness of the slab relative to the decay rate for an inhomogeneous plane wave in the slab. This is an example of the FTIR phenomenon mentioned earlier. The transfer of energy from the uppermost layer to the lowermost layer is seemingly in contradiction with the fact that inhomogeneous waves do not carry any energy in the direction normal to the interfaces. However, a thorough analysis shows that this is true for an inhomogeneous wave that forms in a half space and decays in one direction, but not for the sum of two inhomogeneous waves that decay in opposite directions [1].

The FTIR phenomenon summarized in this example is the basis for any technological method that utilizes evanescent waves, such as near-field photolithography [43–46], and subwavelength imaging [47–49]. Evanescent waves are also frequently used in the FDTD simulations of left-handed metamaterials [46, 47, 50–52], which manifest interesting theoretical behavior such as amplification of inhomogeneous plane waves [53]. Since any evanescent field can be expressed as a spectrum of inhomogeneous plane waves, this plane-wave injector has the potential to contribute further toward the better understanding and improvement

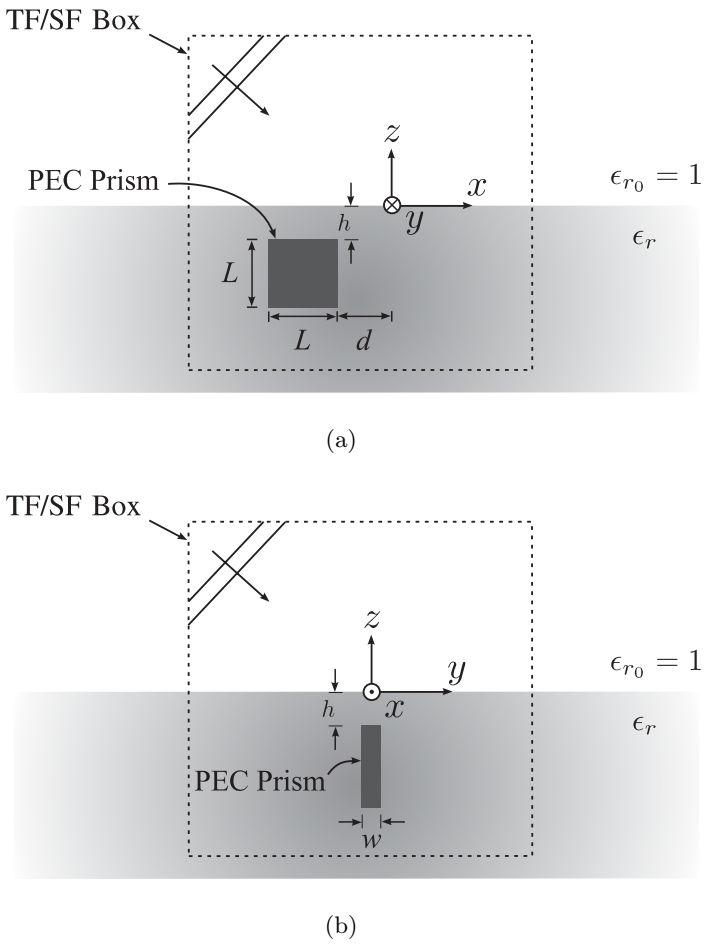

Figure 31: The geometry of the plane-wave scattering example. (a) Cross section in the xz plane. (b) Cross section in the yz plane.

of such techniques.

3.4 Transparency to Scattered Field

The examples considered so far have been for perfect multilayered media, namely, multilayered media that do not contain any imperfections that disturb the planar-layered structure of the geometry. The TF/SF boundary technique is also suited for applications in which there is a scattering imperfection within the TF/SF boundary. Indeed, the TF/SF boundary method is usually used for analyzing the electromagnetic field scattered from these scatterers. This is made possible by the complete transparency of the TF/SF boundary to any scattered field coming from inside [2].

An example geometry for a scattering problem is shown in Fig. 31. The cross sections of the geometry in the xz plane and yz plane are depicted in Fig. 31(a) and Fig. 31(b), respectively. A perfectly-conducting (PEC) rectangular prism of size $(L, w, L) =$ 5cm$\times$0.4cm$\times$5cm is placed $h = 1$ cm deep into a dielectric ground of relative permittivity $\epsilon_r = 1.5$. The PEC prism is $d = 4$ cm away from the origin.

In Fig. 32, we present field snapshots from the FDTD simulation of the above geometry. The FDTD parameters are the same as the ones used for Fig. 24 and Fig. 26, except the following differences: The grid size is 30 cm$\times$1 cm$\times$30 cm, and the TF/SF boundary is 5 cm away from the absorbing boundaries. A plane wave with the same parameters as those used for Fig. 24 and Fig. 26 is injected into the grid using the TF/SF boundary. In Fig. 32(a), the PEC prism is absent, and the plane wave propagates in the presence of an undisturbed two-layered medium. The magnitude of the electric field in the xz plane is shown in the figure, with black representing 0 dB and white representing -40 dB. It is observed that the plane wave is fully contained within the TF/SF boundary. Fig. 32(b) shows the magnitude of the electric field in the xz plane at the same time instant as Fig. 32(a), with the PEC prism placed into the dielectric ground, as in Fig. 31. The plane wave is scattered from the PEC prism, and the scattered wave exits the TF/SF boundary without any reflection or attenuation. The electric field outside the TF/SF boundary consists only of the scattered field, and the field inside the TF/SF boundary consists of the total field, which is defined as the sum of the incident plane wave and the scattered field. Indeed, this contrast is the motivation behind the name "total-field/scattered-field boundary".

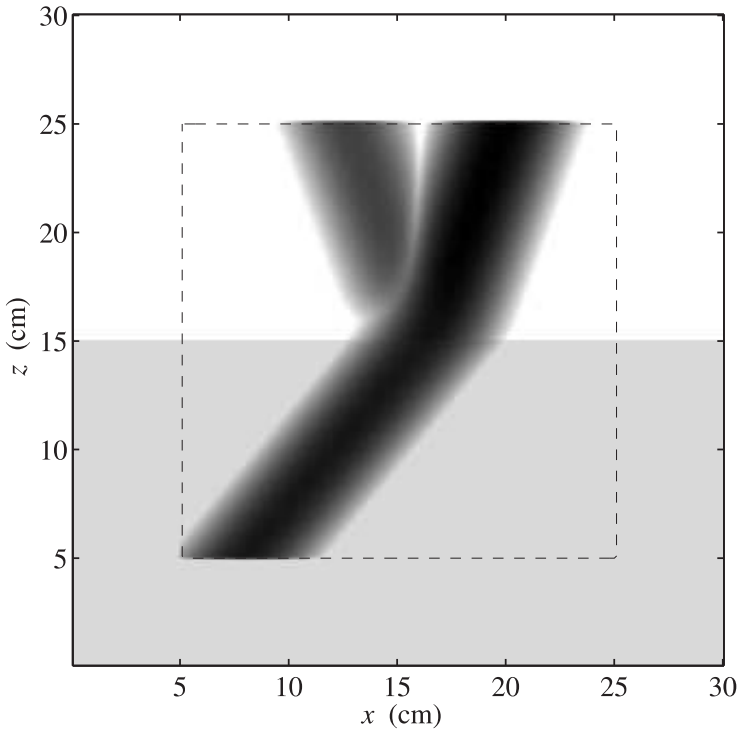

(a)

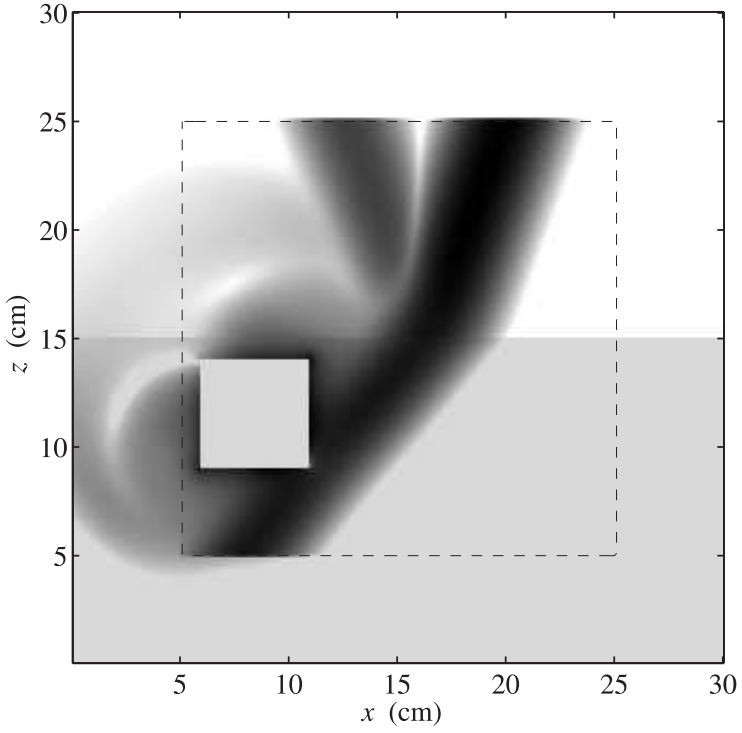

(b)

Figure 32: An example of plane-wave scattering in multilayered media. (a) Incident field without any scatterer inside the TF/SF boundary. (b) Total field with a PEC prism inside the TF/SF boundary.

CHAPTER IV

APPLICATION EXAMPLES

In this chapter, we present practical examples that demonstrate the use of the techniques developed in Chapter 2 (NFFFT) and Chapter 3 (TF/SF boundary) in the FDTD analysis of multilayered media. In the previous chapters, we considered examples that involved the method that is the subject of the respective chapter. For example, we only considered the far-field radiation from structures placed on half spaces and grounded slabs in Chapter 2. Similarly, we only investigated the performance of the TF/SF boundary (namely, containment of the incident plane wave, and transparency to the scattered wave) in Chapter 3. In this chapter, we bring into use both of the methods developed in Chapter 2–3; that is, the examples utilize both the TF/SF boundary, and the near-field-to far-field transform.

4.1 Scattering in Multilayered Media

In this section, we consider two problems that involve the scattering from perfectly conducting objects placed in a multilayered medium, when the incident field is a plane wave. The process of introducing the incident plane wave into the FDTD grid necessitates the use of the TF/SF boundary for multilayered media, while the calculation of the far-zone field scattered from the scattering object is done by the NFFFT. For this approach to be successful, the fields on the NFFFT box in Fig. 6 must comprise only the *scattered field*. This is indeed the basic premise of the TF/SF boundary technique: allowing only the scattered field to exit the boundary. The mentioned transparency of the TF/SF boundary to the scattered wave was demonstrated in Section 3.4. The general configuration used for scattering problems in multilayered media is shown in Fig. 33. The TF/SF boundary contains the imperfections (or the scatterers) in the multilayered medium, denoted collectively as A. Field corrections are applied on the TF/SF boundary to create a contained plane wave, denoted by the arrow in the upper-left corner of the TF/SF boundary. The scattering structure creates a scattered wave, denoted by the arrow in the upper-right corner of the

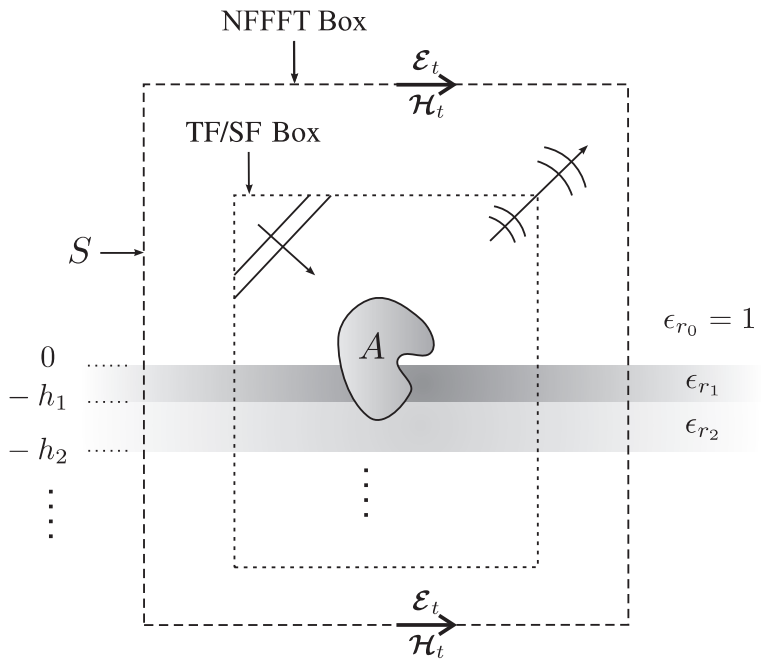

Figure 33: The configuration used for problems involving plane-wave scattering in multi-layered media.

TF/SF boundary. This wave exits the boundary with complete transparency, and reaches the near-field-to-far-field transformer, denoted by S in Fig. 33. The tangential electric and magnetic fields $\boldsymbol{\mathcal{E}}_t$, $\boldsymbol{\mathcal{H}}_t$ on S therefore belong to the scattered wave due to the scattering structure A in the multilayered medium. The important point here is the following: The fields that reach the NFFFT box S in Fig. 33 *do not* include the incident plane wave. This is because the incident plane wave is almost entirely contained within the TF/SF boundary, which is inside the NFFFT box S.

As our first example, we revisit the case considered in Section 3.4. The geometry for this example was shown in Fig. 31. In this example, a PEC rectangular prism of size 5cm×0.4cm×5cm was placed 1 cm deep in a dielectric half space (or ground), and a plane wave with a Gaussian envelope was incident on the half space. The wave scattered from the PEC prism was visible in Fig. 32(b), but radiated electric field was not discussed. We now quantify the radiated electric field for this geometry using the NFFFT developed in Chapter 2. In Fig. 34 and Fig. 35, the radiated electric field (normalized by $1/r$) scattered from the PEC prism is shown for different angles in the xz plane and yz plane, respectively.

In both figures, the first subfigure represents the ψ component, and the second subfigure represents the ϕ component of the radiated electric field. The time axis is normalized by $\tau_L = L/v$, in which $L = 5$ cm is the maximum dimension of the PEC prism, and $v = c/\sqrt{\epsilon_r}$ is the velocity of propagation in the dielectric ground. The radiated electric field waveforms are positive on the side of the time axis for which $\hat{\boldsymbol{\psi}}$ points away from the axis (counter-clockwise direction). The waveforms in Fig. 34(a), Fig. 35(a), and Fig. 35(b) are drawn in the same scale; whereas Fig. 34(b) is amplified by a factor of 10. The Gaussian waveform of the incident plane wave is referenced to the origin.

The relative differences in the amplitudes of the ψ and ϕ components of the radiated electric field in Fig. 34(a)–Fig. 35(b) can be explained qualitatively using simple arguments. For example, we observe that the ϕ component of the radiated electric field in the xz plane in Fig. 34(b) has the smallest average amplitude. This is simply because the surface currents on the PEC prism mostly reside on faces that are parallel to the xz plane, which is also a null plane for the ϕ component of the electric field radiated by these electric currents. The ϕ component of the radiated electric field in the xz plane is created by the currents on the faces that are parallel to the yz and xy planes. These faces have smaller areas compared to the two faces that are parallel to the xz plane. Note also that in Fig. 35(a), the ψ component of the radiated electric field decreases in amplitude as ψ gets closer to 90°. This is because the z axis is a null axis for the ψ component of the electric currents on the faces that are parallel to the xz plane.

As our second example, we consider the geometry shown in Fig. 36. In this geometry, a PEC rectangular prism is again placed in a two-layered medium, similar to the previous example shown in Fig. 31. The dimensions of the PEC prism are the same as before: $L = 5$ cm, $w = 0.4$ cm, $d = 4$ cm. Here, the upper half space has a *higher* relative permittivity than the lower half space: $\epsilon_{r_0} = 2.5 > \epsilon_{r_1} = 2$. This will allow the creation of an *inhomogeneous plane wave* as was done for the example in Section 3.3.3. As in Fig. 24, 26, and 30, the direction of propagation of the incident plane wave $\hat{\boldsymbol{k}}_i$ lies in the xz plane, and is at the angle $\theta = 70°$ to the z axis. The polarization of the incident plane wave is as shown in Fig. 24(a). The parameters of the FDTD simulation and the electric field waveform of the

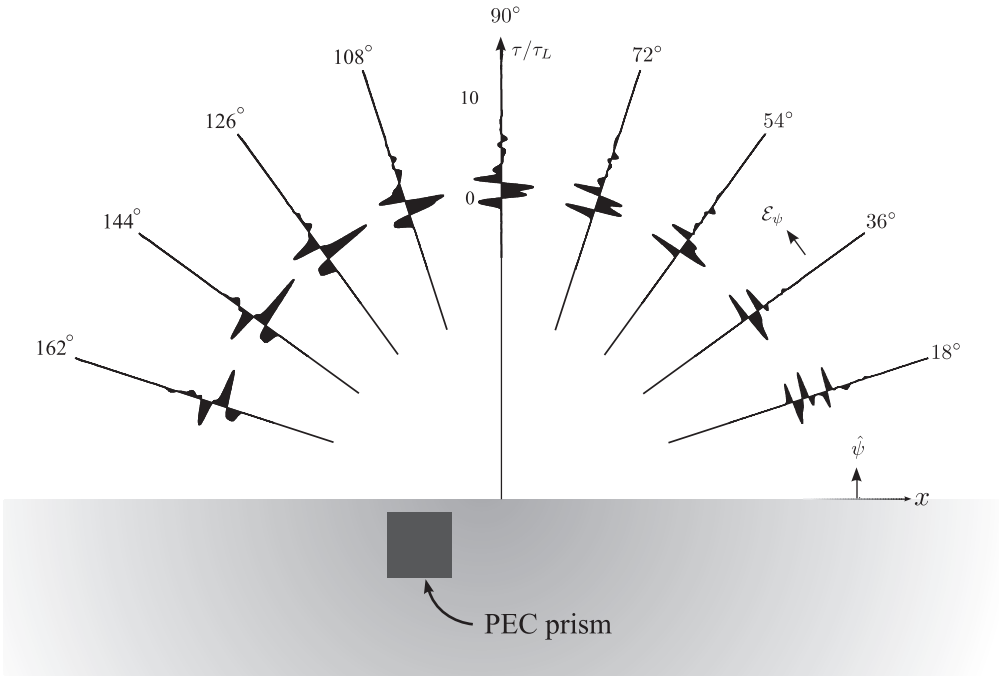

(a)

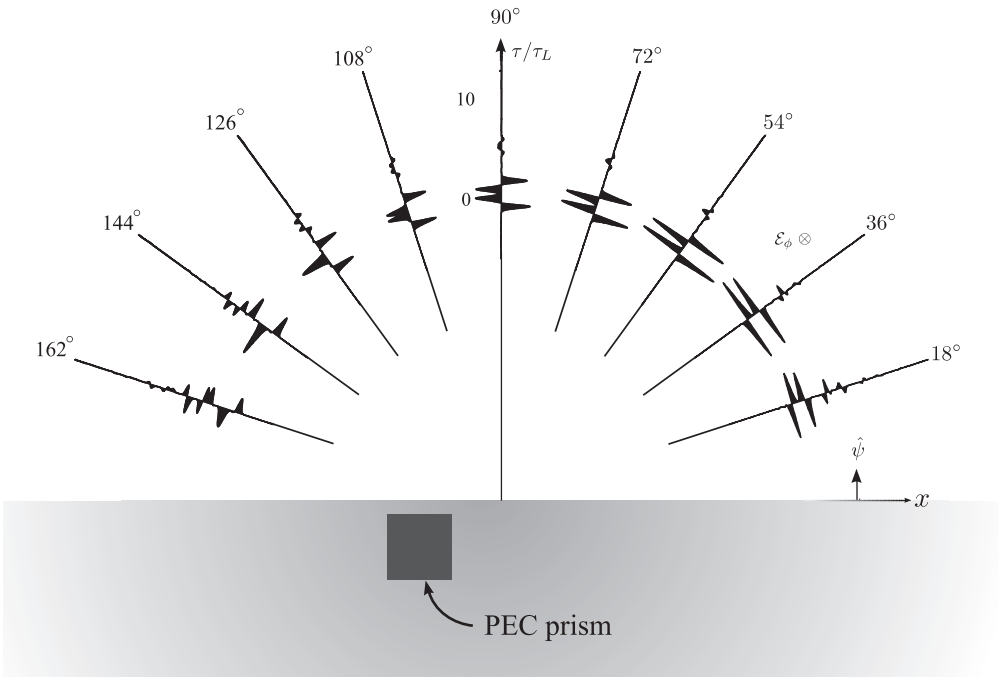

(b)

Figure 34: Plane-wave scattering from a PEC rectangular prism buried in a dielectric ground. (a) The ψ component, and (b) the ϕ component (amplified by 10) of the scattered electric field in the xz plane.

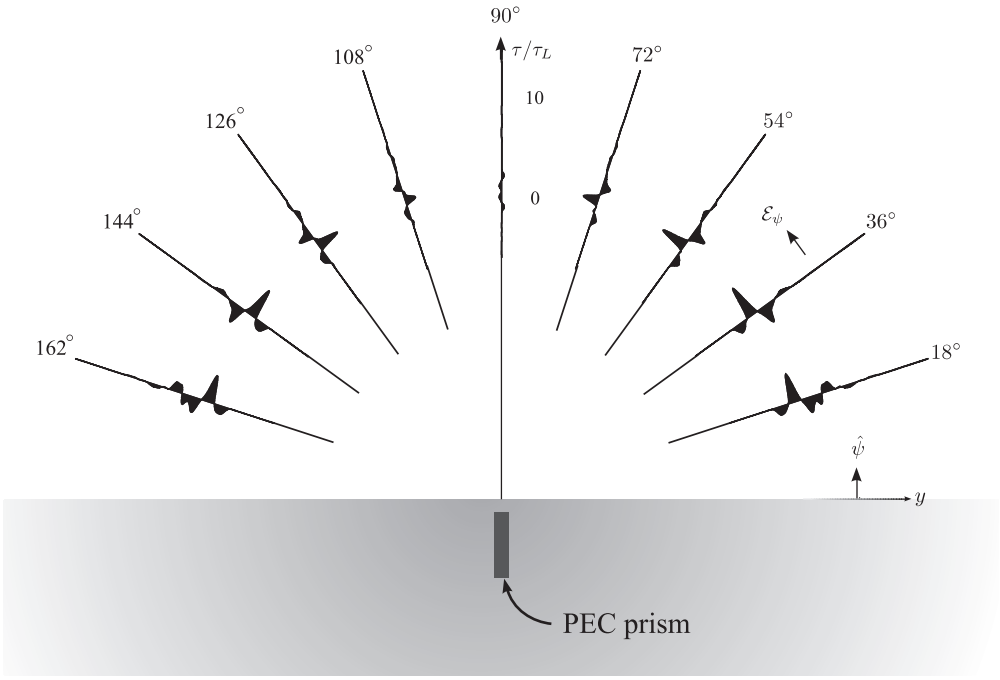

(a)

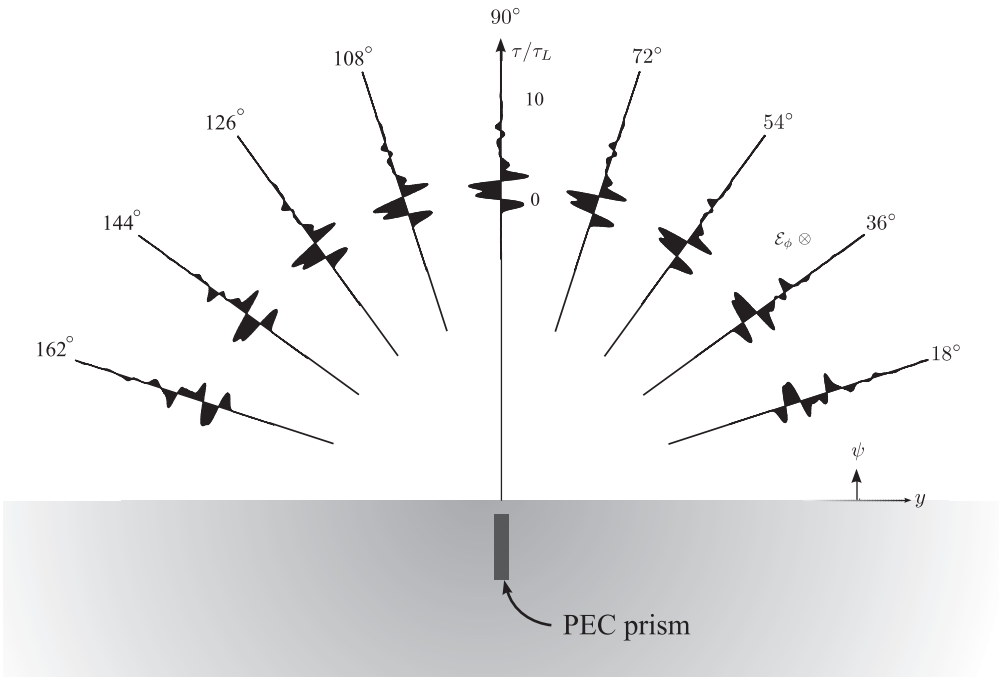

(b)

Figure 35: Plane-wave scattering from a PEC rectangular prism buried in a dielectric ground. (a) The ψ component, and (b) the ϕ component of the scattered electric field in the yz plane.

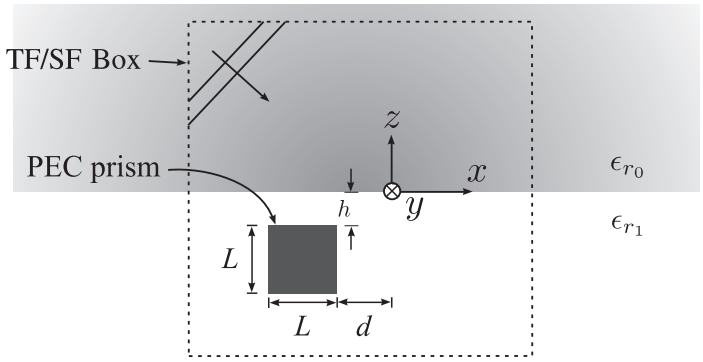

(a)

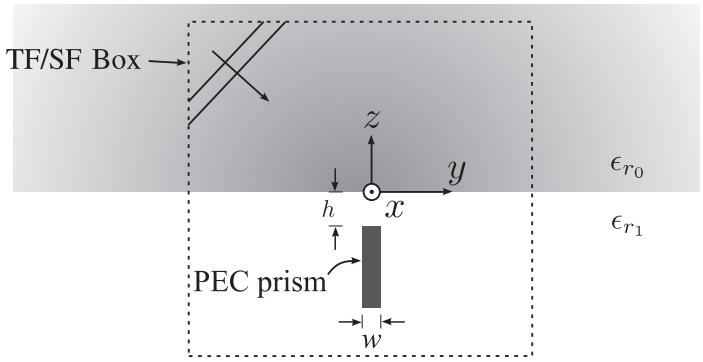

(b)

Figure 36: The geometry of the inhomogeneous-plane-wave scattering problem. (a) Cross section in the xz plane. (b) Cross section in the yz plane.

incident plane wave are the same as those used for Fig. 30. The reference point for the sine-modulated Gaussian waveform is the origin.

Without the PEC scatterer, the incident plane wave is completely reflected at the interface, and an inhomogeneous plane wave, which decays in the direction normal to the interface, is formed in the lower half space. This case was shown previously in Section 3.3.3, Fig. 30(a). Here, we investigate the effects of a PEC scatterer placed in the lower half space, as in Fig. 36. In Fig. 37, the scattering process is illustrated by a progression of field snapshots from the FDTD simulation of this geometry. In Fig. 37(a), the inhomogeneous plane wave has not yet made contact with the PEC prism below the interface. In Fig. 37(b), the inhomogeneous plane wave is passing over the PEC prism, and the scattered wave is

beginning to appear. In Fig. 37(c), the inhomogeneous plane wave has passed the PEC prism, and the spherical scattered wave is clearly visible both above and below the interface. In Fig. 37(d), the scattered wave has traveled away from the PEC prism, and most of the scattered energy propagates downward as an extension to the inhomogeneous plane wave in the lower half space. The area between the scattered wave and the inhomogeneous plane wave indeed looks similar to the interface between the propagating plane wave and the inhomogeneous plane wave in Fig. 30(b).

The scattering process shown in Fig. 37 and summarized above is essentially the conversion of the inhomogeneous plane wave to a propagating wave. This was also observed in Section 3.3.3 in the context of frustrated total internal reflection (FTIR), in which an inhomogeneous plane wave in a layer gives rise to a propagating wave in a lower layer. This phenomenon was demonstrated in Fig. 30(b). As in the FTIR example, the creation of an energy-carrying wave from an inhomogeneous plane wave that carries no energy away from the interface poses an apparent contradiction. The answer to this problem was given in Section 3.3.3: Two inhomogeneous waves that decay in opposite directions *do* carry net energy in one direction [1].

Using the NFFFT developed in Chapter 2, we can quantify the radiated electric field, as was done in the previous example. In Fig. 38, the ψ component of the radiated electric field is shown at different angles in the xz plane. The radiated electric field in the lower half space ($\pi < \psi < 2\pi$) is obtained using the extension for the NFFFT explained in Section 2.3. The time axis is normalized by $\tau_L = L/v$, in which $L = 5$ cm is the maximum dimension of the PEC prism, and $v = c/\sqrt{\epsilon_{r_1}}$ is the velocity of propagation in the lower half space. The radiated electric field waveforms are positive on the side of the time axis for which $\hat{\boldsymbol{\psi}}$ points away from the axis (counter-clockwise direction). The dashed lines in the upper half space at $\psi = 26.56^\circ$ and $\psi = 153.43^\circ$ denote the boundaries of the range of angles in which the radiated electric field is defined in the upper half space. This range contains all possible directions that a plane wave refracting from the lower half space to the upper half space can propagate.

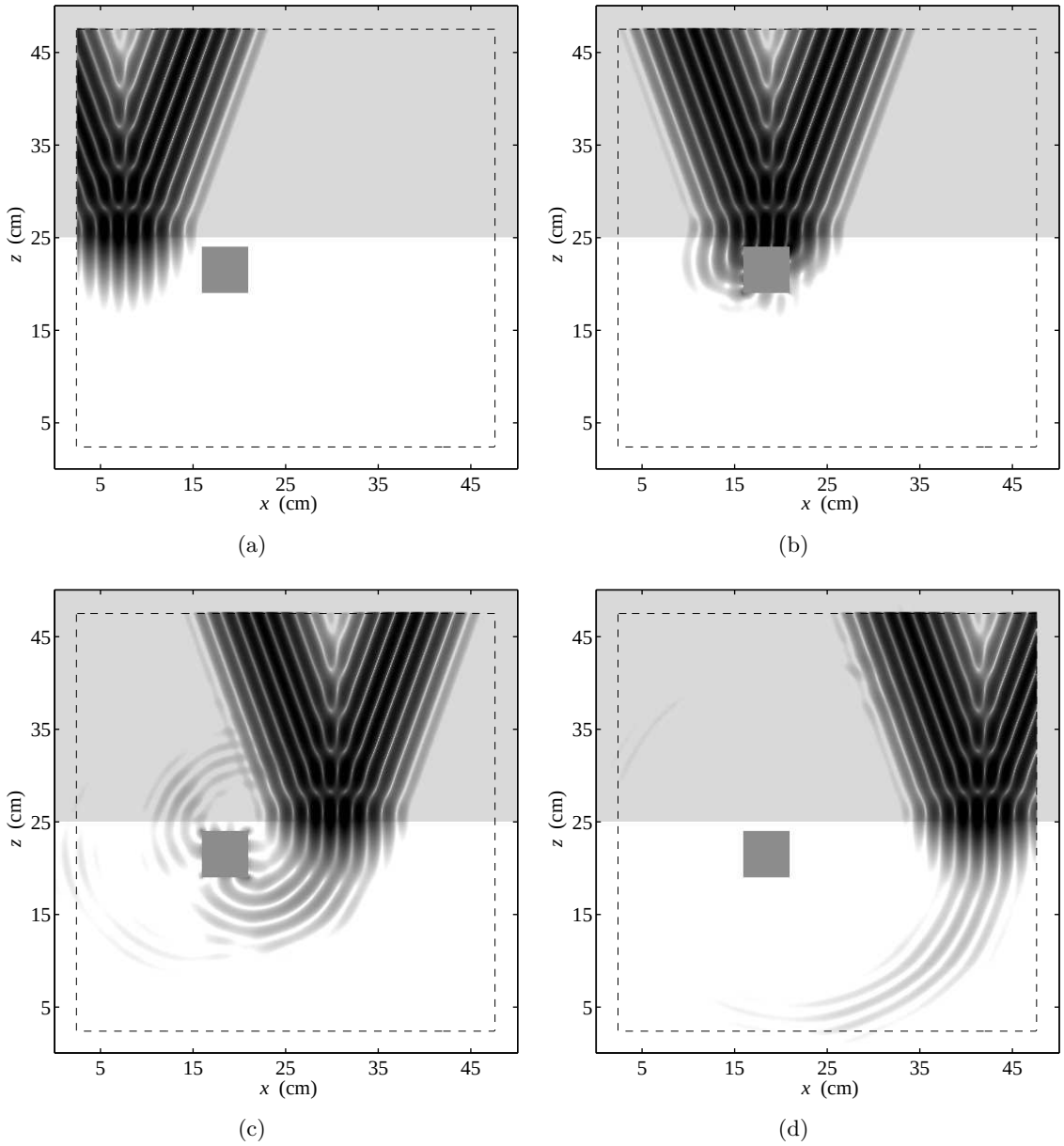

Figure 37: Conversion of an inhomogeneous plane wave to a propagating wave on scattering from a PEC rectangular prism. The magnitude of the electric field in the xz plane is shown at different time instants in (a)-(d).

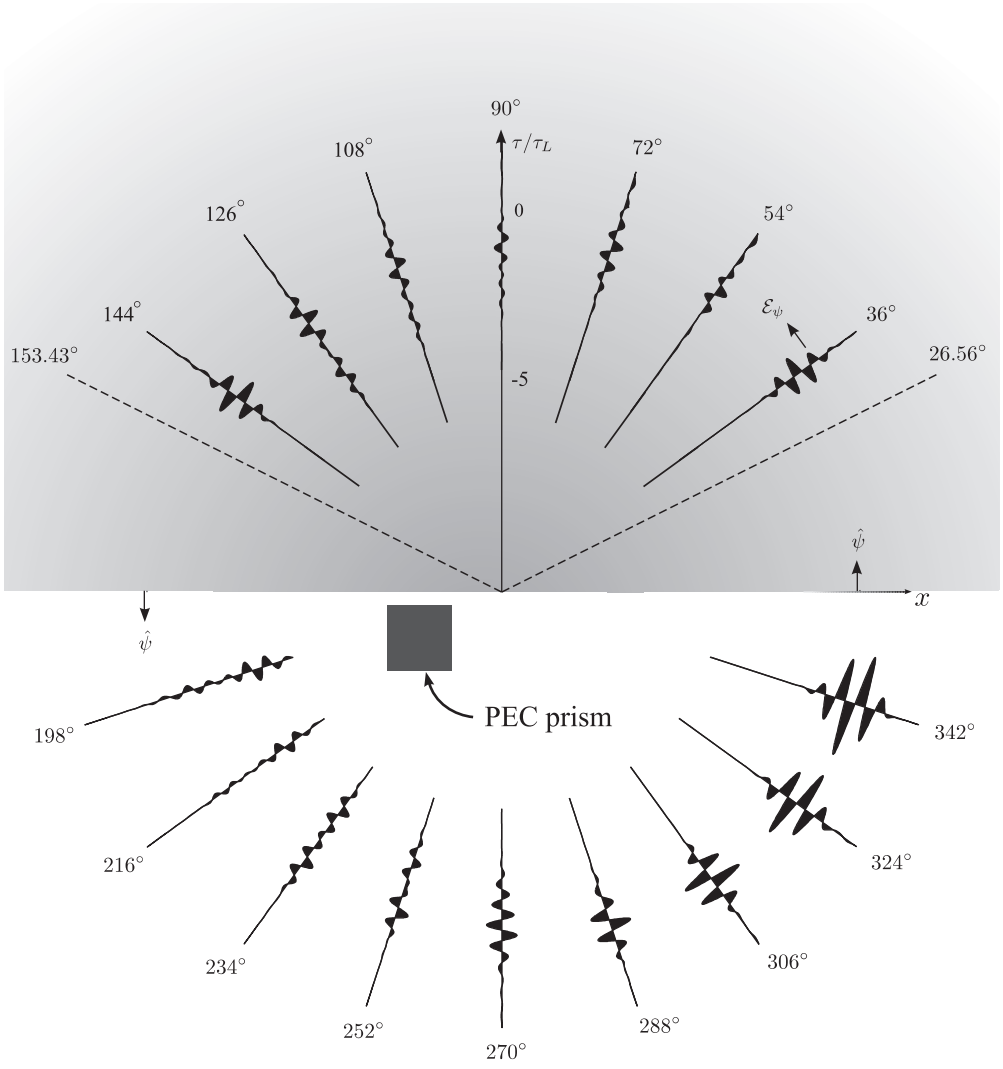

Figure 38: Inhomogeneous-plane-wave scattering from a PEC rectangular prism in a two-layered medium. The ψ component of the scattered electric field is shown at different angles in the xz plane.

4.2 Radiating Structures in Multilayered Media

In this section, we continue our series of examples utilizing both the NFFFT from Chapter 2 and the TF/SF boundary from Chapter 3. In the previous section, we considered scattering problems in which the TF/SF boundary was used to inject a plane wave into the grid, and the scattered wave was evaluated in the far-zone using the NFFFT. In this section, we bring the NFFFT and the TF/SF boundary together in a different fashion. Our analysis is centered on a *reciprocity theorem*, which relates the radiated field of an antenna caused by an excitation voltage at its terminals to the received voltage at its terminals caused by an incident plane wave. We consider different antennas in multilayered media, and demonstrate their reciprocity. To this end, we use two different configurations, and perform FDTD simulations for these configurations separately. The first one is the *transmitting* configuration, in which the antenna is excited at its terminals, and radiates into the multilayered medium. The second configuration is the *receiving* configuration, in which a plane wave is incident on the antenna, and the voltage at its terminals is observed. If the excitation voltage in the transmitting case and the incident plane-wave waveform in the receiving case are related, then the reciprocity theorem states that the radiated field in the transmitting case and the received voltage in the receiving case are also related. We will use the NFFFT for the transmitting case and the TF/SF boundary for the receiving case, and bring the results together to validate this reciprocity relation.

The common geometry of the examples considered in this section is shown in Fig. 39. In Fig. 39(a), an arbitrary antenna is radiating in a multilayered medium. The antenna is excited at its input terminal by a transmission line supporting a TEM wave. The transmission line is connected in one end to the network analyzer, which is perfectly matched to the line, and provides the excitation. The network analyzer should be considered merely as an ideal matching termination and a perfect signal generation/signal measurement device. The incident current wave that travels toward the antenna is denoted by $\mathcal{I}_t^+(t)$, measured in reference to the position in the transmission line denoted by the horizontal dashed line at $z = 0$ in Fig. 39(a). The NFFFT surface S encloses the antenna, the transmission line, and the network analyzer. The far-zone electric field created by this combined system is

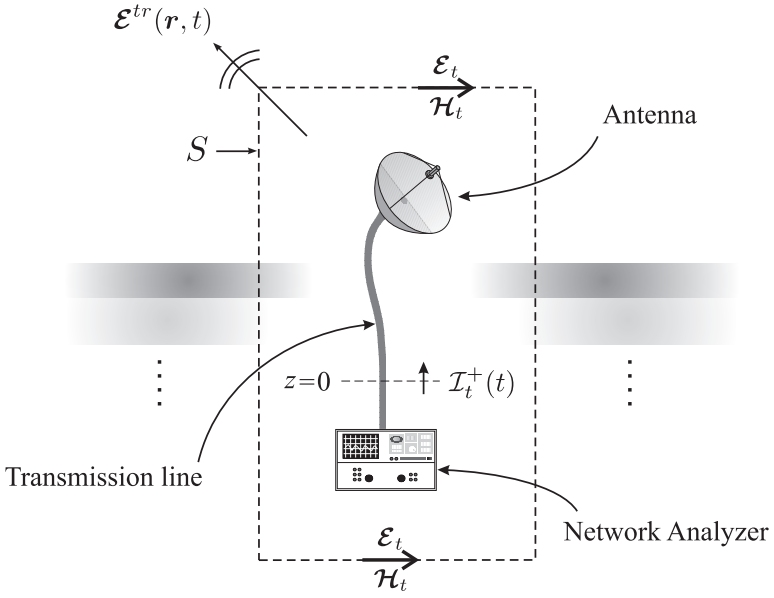

(a)

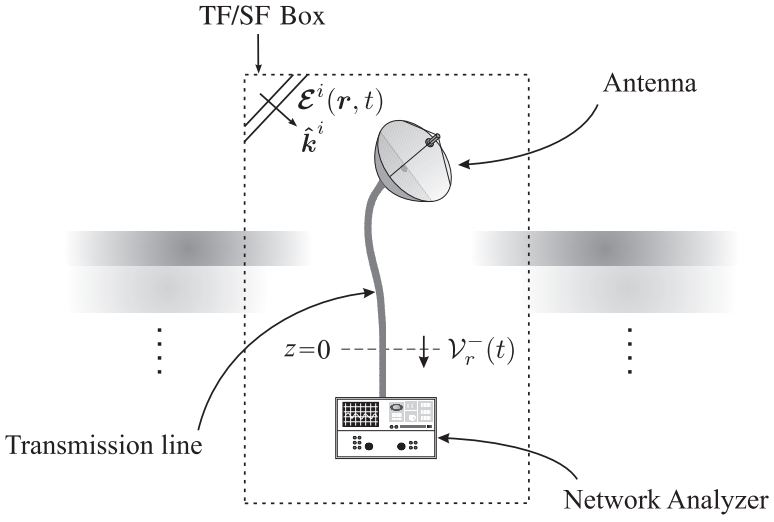

(b)

Figure 39: The general geometry for the reciprocity relation. (a) The transmitting case. (b) The receiving case.

denoted by $\boldsymbol{\mathcal{E}}^{tr}(\boldsymbol{r},t)$. The reference point of this waveform is the same as that of $\mathcal{I}_t^+(t)$, namely, $z=0$ in Fig. 39(a). If the antenna is not matched exactly to the transmission line, a portion of the incident energy in the line is reflected from the terminals of the antenna. The important point to note is that $\mathcal{I}_t^+(t)$ does *not* include this reflection. However, it is crucial for the validity of the reciprocity theorem that this reflection be completely absorbed by the matched termination at the network analyzer.

In Fig. 39(b), the antenna is in the receiving configuration. A plane wave with direction of propagation is $\hat{\boldsymbol{k}}^i$ is incident on the combined system consisting of the antenna, the transmission line, and the network analyzer. With reference to $z=0$ in the transmission line, the incident plane wave has the waveform $\boldsymbol{\mathcal{E}}^i(\boldsymbol{r},t)$. The plane wave creates a voltage waveform in the transmission line, and this waveform travels toward the matched termination at the network analyzer. At the reference point $z=0$, this received voltage waveform is given by $\mathcal{V}_r^-(t)$.

Now, we are in a position to state the reciprocity theorem that we mentioned in the beginning of this section. This theorem links four time-dependent functions in two different configurations shown in Fig. 39(a) and Fig. 39(b): $\mathcal{I}_t^+(t)$, $\boldsymbol{\mathcal{E}}^{tr}(\boldsymbol{r},t)$, $\mathcal{V}_r^-(t)$, and $\boldsymbol{\mathcal{E}}^i(\boldsymbol{r},t)$. This theorem is a useful time-domain variation of the well-known frequency-domain reciprocity theorem. It was derived in [54], and is given in its simplest form by

$$\mathcal{V}_r^-(t) \star \frac{d\mathcal{I}_t^+(t)}{dt} = \frac{2\pi}{\mu_0}\boldsymbol{\mathcal{E}}^i(0,t) \odot r\boldsymbol{\mathcal{E}}^{tr}(-r\hat{\boldsymbol{k}}^i, t+r/c) \ , \tag{141}$$

in which $\star$ denotes time convolution, and $\odot$ denotes convolutional dot product, defined previously in (25). In (141), $\boldsymbol{\mathcal{E}}^i(0,t)$ is the incident plane wave at $\boldsymbol{r}=0$, or equivalently, $z=0$ in the transmission line. The vector waveform $\boldsymbol{\mathcal{E}}^{tr}(-r\hat{\boldsymbol{k}}^i, t+r/c)$ is the radiated electric field at the direction that the plane wave is incident from, advanced by r/c. Note that the distance r is measured from the reference point $z=0$ in the transmission line.

The reciprocity theorem (141) has many implications, but we will make use of the following one in our examples [54]: In the transmitting case in Fig. 39(a), let the incident current $\mathcal{I}_t^+(t)$ be the pulse $p(t)$, and in the receiving case in Fig. 39(b), let the j^{th} component ($j=x,y,z$) of the incident electric field vector, $\mathcal{E}_j^i(0,t)$, be proportional to the derivative

of the same pulse, $dp(t)/dt$:

$$\mathcal{E}_j^i(0,t) = \frac{\mu_0}{2\pi}\frac{d\mathcal{I}_t^+(t)}{dt} \ . \tag{142}$$

Then, (141) states that the j^{th} component of the radiated electric field vector in the transmitting case, $r\mathcal{E}_j^{tr}(-r\hat{\boldsymbol{k}}^i, t + r/c)$, is equal to the voltage in the receiving case, $\mathcal{V}_r^-(t)$:

$$r\mathcal{E}_j^{tr}(-r\hat{\boldsymbol{k}}^i, t + r/c) = \mathcal{V}_r^-(t) \ . \tag{143}$$

In each example given later in this section, we analyze two different configurations shown schematically in Fig. 39(a) and Fig. 39(b), which are arranged to satisfy the relation (142). Then, we observe the radiated field $\boldsymbol{\mathcal{E}}^{tr}(\boldsymbol{r}, t)$ and the received voltage $\mathcal{V}_r^-(t)$, and demonstrate the validity of the reciprocity relation (143).

An important practical problem regarding the network analyzer in Fig. 39 must be handled before presenting the examples. It is apparent that both the transmitting and receiving configurations in Fig. 39(a) and Fig. 39(b) utilize an idealized network analyzer. In the transmitting case, the ideal network analyzer creates a desired current waveform $\mathcal{I}_t^+(t)$ in the transmission line, and absorbs the reflections coming from the terminals of the antenna. In the receiving case, the network analyzer makes a perfect measurement of the received voltage $\mathcal{V}_r^-(t)$. For simulating these tasks, we use the *simple feed model* [55, 56]. The geometry of the simple feed model is shown in Fig. 40. In this model, a virtual transmission line is connected to the feed gap of the antenna. This transmission line simulates the transmission line in Fig. 39, and is modeled by a separate 1-D FDTD grid. The voltages and currents in the transmission line are represented by two discrete sets of values placed at staggered positions both in space and time. In Fig. 40, the 1-D FDTD grid is shown below the feed gap of the antenna. The voltage V^n and current $I^{n+1/2}$ values on the 1-D grid are represented by black squares and white triangles, respectively. The transmission line supports the TEM wave (encountered previously in Section 1.2), which is completely described by the following equations for the voltage and current in the

transmission line:

$$\frac{\partial \mathcal{V}}{\partial t} = -(cZ_c)\frac{\partial \mathcal{I}}{\partial z} \tag{144}$$

$$\frac{\partial \mathcal{I}}{\partial t} = -(c/Z_c)\frac{\partial \mathcal{V}}{\partial z} \ , \tag{145}$$

in which c and Z_c are the velocity of propagation and the characteristic impedance of the transmission line, respectively. In our simulations, we fix the value of c at $c = (\epsilon_0\mu_0)^{-1/2}$, and vary the characteristic impedance Z_c. For the 1-D FDTD grid representing the transmission line in Fig. 40, the TEM equations for the voltage and the current in (144)–(145) are discretized as follows:

$$\mathcal{V}_k^{n+1} = \mathcal{V}_k^n - Z_c\frac{c\Delta t}{\Delta z}\left[\mathcal{I}_{k+1/2}^{n+1/2} - \mathcal{I}_{k-1/2}^{n+1/2}\right] \tag{146}$$

$$\mathcal{I}_{k+1/2}^{n+1/2} = \mathcal{I}_{k+1/2}^{n-1/2} - \frac{1}{Z_c}\frac{c\Delta t}{\Delta z}\left[\mathcal{V}_{k+1}^n - \mathcal{V}_k^n\right] \ . \tag{147}$$

The 1-D FDTD grid is terminated by a matched load at $z = -L$, and connected to the feed gap of the antenna at $z = z_g$. At this point, some information is exchanged between the 1-D grid and the 3-D simulation grid. This exchange is done at every time step in the main simulation, and constitutes an approximation to the real connection between the transmission line and the terminals of the antenna. During this exchange, the voltage value $\mathcal{V}^n(z = z_g)$ in the 1-D grid is translated to electric field values in the feed gap, and used in the 3-D grid:

$$\mathcal{E}^n = \mathcal{V}^n(z = z_g)/\Delta z \ . \tag{148}$$

This operation is denoted by the solid upward arrow below the feed gap in Fig. 40. The current value $\mathcal{I}^{n+1/2}(z = z_g + \Delta z/2)$ in the 1-D grid is obtained from the 3-D grid by applying Ampère's law on the contour $\mathcal{C}$:

$$\mathcal{I}^{n+1/2} = \int_C \boldsymbol{\mathcal{H}}^{n+1/2} \cdot \boldsymbol{dl} \ . \tag{149}$$

This operation is denoted by the solid downward arrow below the feed gap in Fig. 40.

In summary, the TEM equations (146)–(147) describe the evolution of the voltage and current in the virtual transmission line, and the exchange equations (148) and (149) simulate the connection between the 1-D FDTD grid representing the transmission line and the

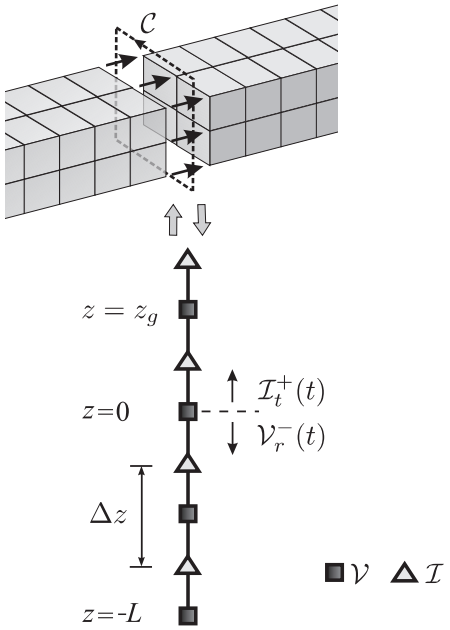

Figure 40: The geometry of the simple feed model.

feed gap of the antenna in the 3-D simulation grid. Remember that the incident current waveform $\mathcal{I}_t^+(t)$ in Fig. 39(a) and the received voltage waveform $\mathcal{V}_r^-(t)$ in Fig. 39(b) are both referenced to the reference point $z = 0$ in the transmission line, which is also shown in Fig. 40. In the transmitting case, the one-way injector [2] (shown previously in Section 3.1.2, see description of Fig. 22) is used to launch the incident current wave $\mathcal{I}_t^+(t)$. In the receiving case, the voltage $\mathcal{V}_r^-(t)$ at $z = 0$ is observed and recorded.

Now, we are ready to present some examples of the two configurations shown in Fig. 39. In the next two subsections, we will consider two different radiating structures placed on an ungrounded dielectric slab. The first is a simple dipole, while the second is a more complex and practical antenna: a resistively-loaded bowtie. Both of these structures will be analyzed in the reciprocity context described in this section, and the relation (143) will be confirmed.

4.2.1 Dipole on an Ungrounded Dielectric Slab

In this subsection, we analyze a simple antenna radiating in the presence of an ungrounded dielectric slab. The antenna considered is a *center-fed dipole* placed at the interface between the ungrounded dielectric slab and the uppermost half space. The geometry for this example

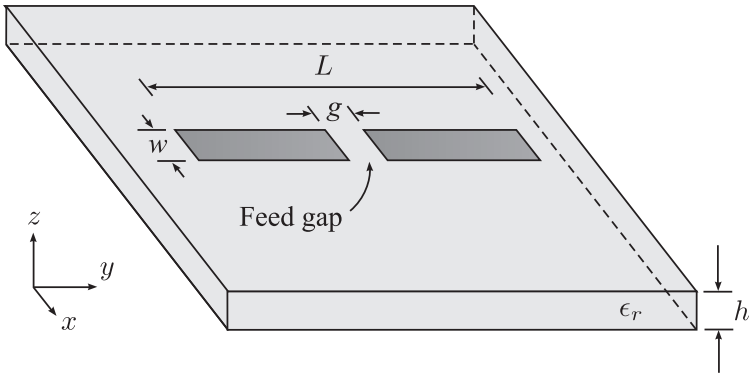

Figure 41: Center-fed dipole radiating on an ungrounded dielectric slab.

is shown in Fig. 41. The dipole is of length $L = 5$ cm, and width $w = 2$ mm. The dipole is fed from a feed gap of width $g = 1$ mm at its center, using the simple feed model described previously in this section. The origin of the geometry is at the center of the feed gap of the antenna. This point is also the reference point $z = 0$ for the configurations in Fig. 39. The dielectric substrate has relative permittivity $\epsilon_r = 2.5$, and is placed in air ($\epsilon_{r_0} = \epsilon_{r_2} = 1$). The thickness of the substrate is $h = 5$ mm.

In the transmitting case, the incident current waveform $\mathcal{I}_t^+(t)$ is a Gaussian pulse:

$$\mathcal{I}_t^+(t) = I_0 \exp(-(t/\tau)^2/2) \ , \tag{150}$$

in which $\tau = 80$ ps. The radiated electric field at a fixed direction $\hat{\boldsymbol{k}}$ is calculated using an NFFFT box surrounding the dipole:

$$r\boldsymbol{\mathcal{E}}^{tr}(r\hat{\boldsymbol{k}}, t + r/c) = \mathcal{E}_\theta(t)\hat{\boldsymbol{\theta}} + \mathcal{E}_\phi(t)\hat{\boldsymbol{\phi}} \ . \tag{151}$$

In the receiving case, the TF/SF boundary is used to introduce a plane wave from the direction of observation in the transmitting case, $\hat{\boldsymbol{k}}$, and, according to (142), the waveform of the incident electric field $\boldsymbol{\mathcal{E}}^i(0,t)$ is made proportional to the derivative of the incident current pulse $\mathcal{I}_t^+(t)$ in the transmitting case:

$$\boldsymbol{\mathcal{E}}^i(0,t) = \hat{\boldsymbol{e}}^i \left[\frac{\mu_0}{2\pi}\frac{d\mathcal{I}_t^+(t)}{dt}\right] = \hat{\boldsymbol{e}}^i \left[\frac{\mu_0}{2\pi} I_0 \left(\frac{-t}{\tau^2}\right) \exp(-(t/\tau)^2/2)\right] \ , \tag{152}$$

in which $\hat{\boldsymbol{e}}^i$ denotes the polarization of the incident plane wave. If (152) is satisfied, the reciprocity theorem (141) states that the following relation must hold between the radiated

field $r\boldsymbol{\mathcal{E}}^{tr}(r\hat{\boldsymbol{k}}, t+r/c)$ in the transmitting case and the received voltage $\mathcal{V}_r^-(t)$ in the receiving case:

$$\hat{\boldsymbol{e}}^i \cdot \left(\mathcal{E}_\theta(t)\hat{\boldsymbol{\theta}} + \mathcal{E}_\phi(t)\hat{\boldsymbol{\phi}}\right) = \mathcal{V}_r^-(t) \ . \tag{153}$$

The parameters for the FDTD grid used to simulate the geometry shown in Fig. 41 are grid dimensions 2cm × 7.5cm ×1.5cm and cell size $\Delta x = \Delta y = \Delta z = 1$ mm. The solution space is surrounded by convolutional PML (CPML) blocks of thickness 1 cm, with the ungrounded dielectric slab penetrating into the PML. The characteristic impedance Z_c of the transmission line is 50 Ω. The transmitting and receiving configurations shown in Fig. 39 are constructed and simulated separately. These two configurations are made to satisfy the relation (152) between the incident current wave $\mathcal{I}_t^+(t)$ in the transmitting case and the incident plane wave $\hat{\boldsymbol{e}}^i \cdot \boldsymbol{\mathcal{E}}^i(0,t)$ in the receiving case. Then, the radiated electric field $\hat{\boldsymbol{e}}^i \cdot [r\boldsymbol{\mathcal{E}}^{tr}(r\hat{\boldsymbol{k}}, t+r/c)]$ in the transmitting case and the received voltage $\mathcal{V}_r^-(t)$ in the receiving case are tested for the reciprocity relation (153).

In Fig. 42(a) and Fig. 42(b), these two waveforms are compared at different angles of observation in the yz and xz plane, respectively. The time axis is normalized by $\tau_L = L/c$, which is the time for a plane wave in free space to travel the length of the dipole. In Fig. 42(a), the polarization $\hat{\boldsymbol{e}}^i$ of the electric field vector in the incident plane wave is equal to the unit vector $\hat{\boldsymbol{\psi}}$ at the observation angle ψ. Therefore, according to (153), the ψ component of the radiated electric field at angle ψ should be equal to the received voltage $\mathcal{V}_r^-(t)$ in the receiving case:

$$\mathcal{E}_\psi(t) = \mathcal{V}_r^-(t) \ . \tag{154}$$

In Fig. 42(a), the ψ component of the radiated electric field, $\mathcal{E}_\psi(t)$, and the received voltage $\mathcal{V}_r^-(t)$ are plotted together at different observation angles in the yz plane. The solid line denotes the radiated electric field, whereas the dotted line denotes the received voltage. The agreement is seen to be very good. In Fig. 42(b), the polarization $\hat{\boldsymbol{e}}^i$ of the electric field vector in the incident plane wave is equal to the unit vector $\hat{\boldsymbol{\phi}}$, which corresponds to $\hat{\boldsymbol{y}}$ in the xz plane. Therefore, according to (153), the ϕ component of the radiated electric

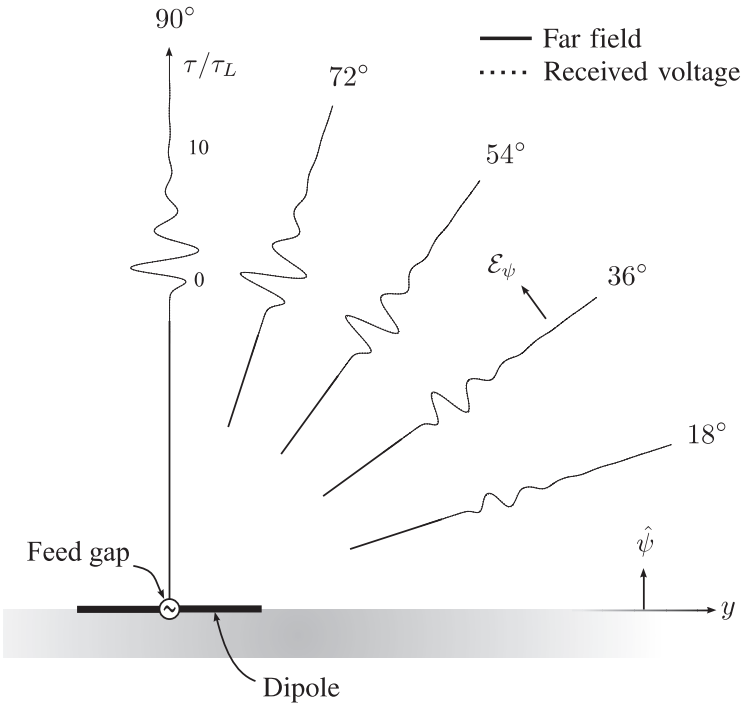

(a)

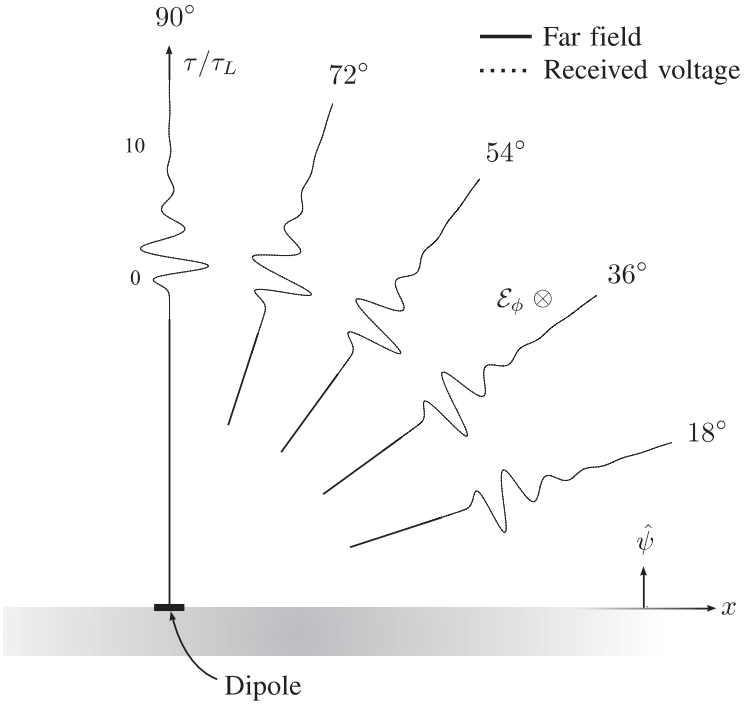

(b)

Figure 42: Demonstration of reciprocity for a dipole on an ungrounded substrate. The received voltage is compared to (a) the ψ component of the radiated electric field in the yz plane, and (b) the ϕ component of the radiated electric field in the xz plane.

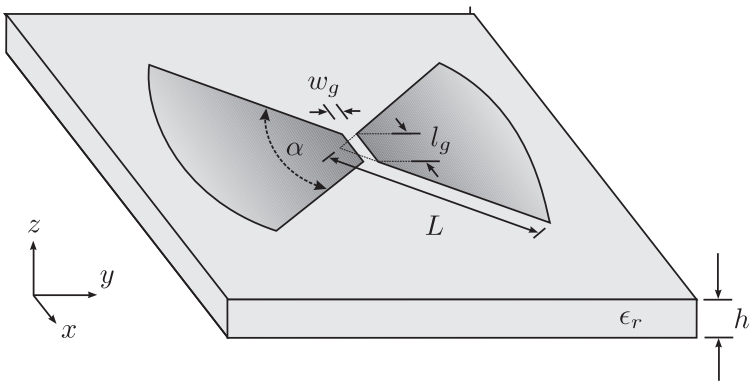

Figure 43: Resistively-loaded bowtie antenna placed on an ungrounded dielectric slab.

field should be equal to the received voltage $\mathcal{V}_r^-(t)$ in the receiving case:

$$\mathcal{E}_\phi(t) = \mathcal{V}_r^-(t) \ . \tag{155}$$

In Fig. 42(b), the ϕ component of the radiated electric field, $\mathcal{E}_\phi(t)$, and the received voltage $\mathcal{V}_r^-(t)$ are plotted together at different observation angles in the xz plane. The solid and dotted lines denote the radiated electric field and the received voltage, respectively. The agreement is again seen to be very good.

4.2.2 UWB Antenna on an Ungrounded Dielectric Slab

Next, we consider a more practical antenna: a *resistively-loaded bowtie antenna* on an ungrounded dielectric slab. The bowtie shape is encountered commonly in ultra-wideband (UWB) antenna applications [57–60]. The geometry of the bowtie antenna is shown in Fig. 43. The bowtie antenna shown in the figure is referred to as a "fan-top" [57], due to its rounded ends.

The antenna is mounted on a dielectric slab of thickness $h = 6$ mm and relative permittivity $\epsilon_r = 2.5$. The arms of the bowtie antenna are identical circular sections with flare angle $\alpha = 90^\circ$ and radius $L = 16$ cm. The antenna is excited through a narrow feed gap of width $w_g = 2$ mm and length $l_g = 1.6$ cm. The bowtie antenna is made of a resistive material with sheet resistance profile

$$R(\rho) = R_h \ \frac{\rho/L}{1 - \rho/L} \ , \tag{156}$$

in which ρ is the distance from the apex of the circular section, $R(\rho)$ is the sheet resistance (in $\Omega/\square$) at radius ρ, and R_h is the sheet resistance at $\rho = L/2$. With this profile, the resistance per unit length of the bowtie (resistance of an annular section with unit length in the ρ direction) has the dependence $r(\rho) \propto (1 - \rho/L)^{-1}$, similar to the one used for cylindrical antennas [61]. According to (156), the bowtie antenna behaves like an ideal PEC near the feed ($R(\rho) \to 0$), and blends into the dielectric slab ($R(\rho) \to \infty$) near the ends of the antenna. In our example, we assume $R_h = 1\,k\Omega/\square$.

The geometry shown in Fig. 43 is simulated using an FDTD grid with dimensions 25cm $\times$ 35cm $\times$2cm and cell size $\Delta x = \Delta y = \Delta z = 2$ mm. The solution space is surrounded by convolutional PML (CPML) blocks of thickness 1 cm, with the ungrounded dielectric slab penetrating into the PML. The characteristic impedance Z_c of the transmission line is $100\,\Omega$. The incident current waveform $\mathcal{I}_t^+(t)$ is a modulated Gaussian pulse, shown in Fig. 44(a):

$$\mathcal{I}_t^+(t) = I_0 \exp(-(t/\tau)^2/2) \sin(2\pi f_0 t) \ , \tag{157}$$

in which $f_0 = 6.85$ GHz, $\tau = 64.4$ ps. This waveform has a -10 dB bandwidth of 7.5 GHz, and occupies the UWB band between $3.1 - 10.6$ GHz assigned by FCC. The extent of this waveform in space can be compared to the length of the bowtie antenna by examining Fig. 44(b), in which a snapshot of the electric field is shown in the transmitting mode. The magnitude of the electric field in the xy plane is plotted on a grayscale, with white denoting -60 dB, and black denoting 0 dB. It is apparent from the figure that the incident current waveform (157) is a relatively short pulse on the antenna.

For the reciprocity analysis of the UWB bowtie antenna in Fig. 43, the transmitting and receiving configurations shown in Fig. 39 are constructed and simulated separately. These two configurations satisfy the relation (152) between the incident current wave $\mathcal{I}_t^+(t)$ in the transmitting case and the incident plane wave $\hat{\boldsymbol{e}}^i \cdot \boldsymbol{\mathcal{E}}^i(0,t)$ in the receiving case. Then, the radiated electric field $\hat{\boldsymbol{e}}^i \cdot [r\boldsymbol{\mathcal{E}}^{tr}(r\hat{\boldsymbol{k}}, t + r/c)]$ in the transmitting case and the received voltage $\mathcal{V}_r^-(t)$ in the receiving case are tested for the reciprocity relation (153). In Fig. 45(a) and Fig. 45(b), these two waveforms are compared at different angles of observation in the yz and xz planes, respectively. The time axis is normalized by $\tau_L = L/c$, which is the

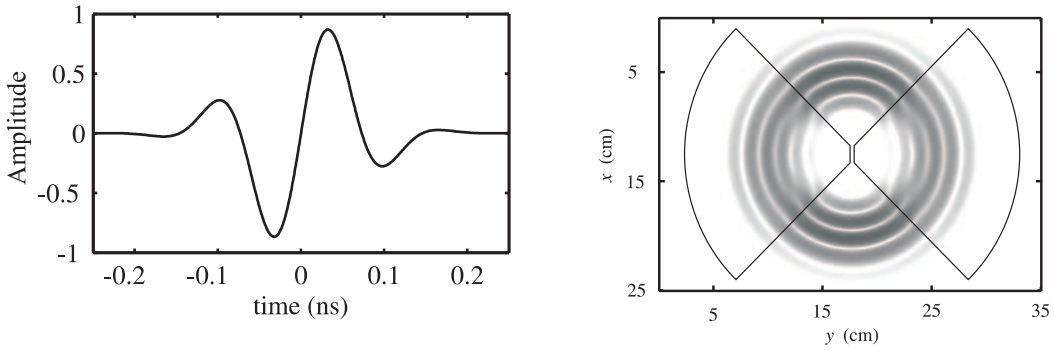

(a) (b)

Figure 44: Temporal and spatial graphs for the incident current waveform given by (157). (a) The time-domain graph of the waveform. (b) The spatial extent of the waveform on the antenna.

time for a plane wave in free space to travel the length of one of the arms of the antenna. In Fig. 45(a), the polarization $\hat{\boldsymbol{e}}^i$ of the electric field vector in the incident plane wave is equal to the unit vector $\hat{\boldsymbol{\psi}}$ at the observation angle ψ. Therefore, according to (153), the ψ component of the radiated electric field at angle ψ should be equal to the received voltage $\mathcal{V}_r^-(t)$ in the receiving case:

$$\mathcal{E}_\psi(t) = \mathcal{V}_r^-(t) \ . \tag{158}$$

In Fig. 45(a), the ψ component of the radiated electric field, $\mathcal{E}_\psi(t)$, and the received voltage, $\mathcal{V}_r^-(t)$, are plotted together at different observation angles in the yz plane. The solid line denotes the radiated electric field, whereas the dotted line denotes the received voltage. The agreement is seen to be very good. In Fig. 45(b), the polarization $\hat{\boldsymbol{e}}^i$ of the electric field vector in the incident plane wave is equal to the unit vector $\hat{\boldsymbol{\phi}}$, which corresponds to $\hat{\boldsymbol{y}}$ in the xz plane. Therefore, according to (153), the ϕ component of the radiated electric field should be equal to the received voltage $\mathcal{V}_r^-(t)$ in the receiving case:

$$\mathcal{E}_\phi(t) = \mathcal{V}_r^-(t) \ . \tag{159}$$

In Fig. 45(b), the ϕ component of the radiated electric field, $\mathcal{E}_\phi(t)$, and the received voltage, $\mathcal{V}_r^-(t)$, are plotted together at different observation angles in the xz plane. The solid and dotted lines denote the radiated electric field and the received voltage, respectively. The agreement is again seen to be very good.

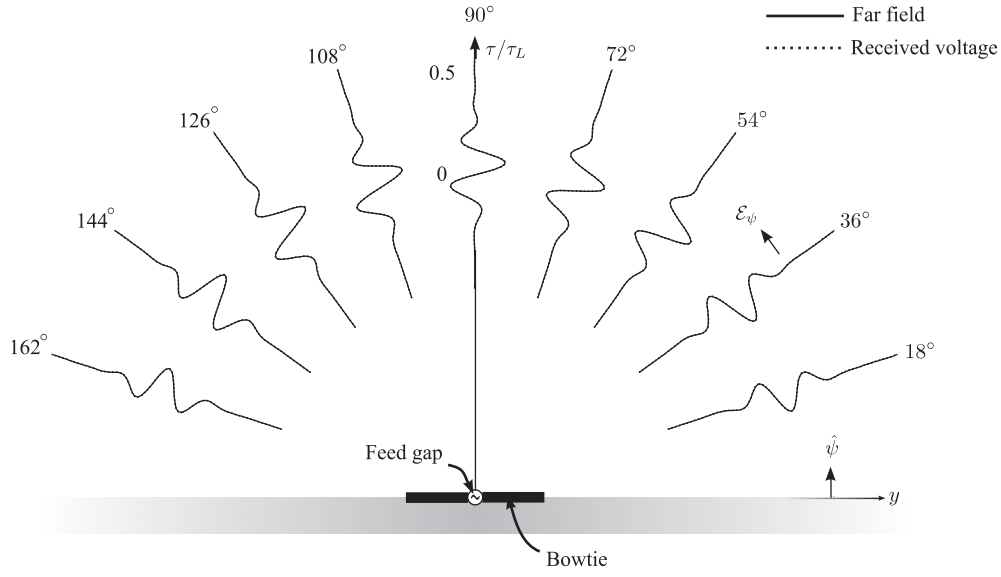

(a)

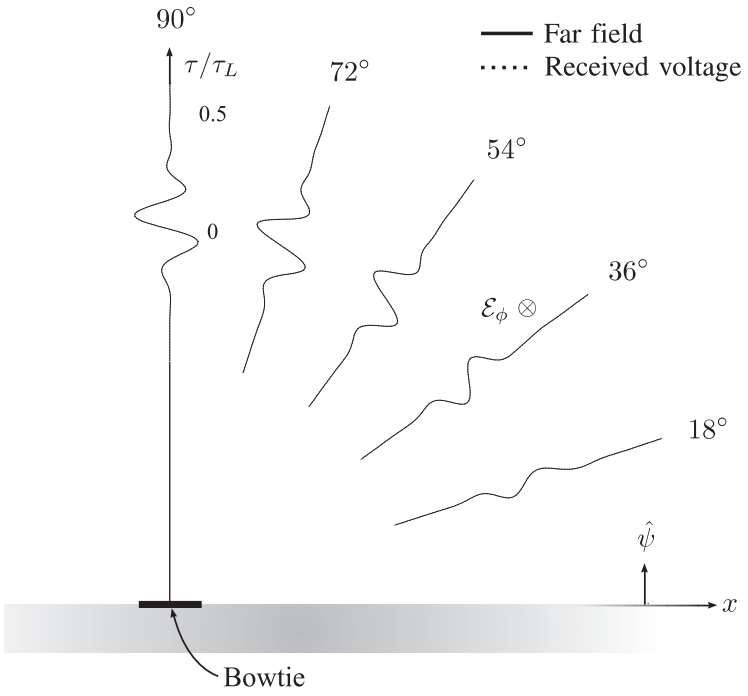

(b)

Figure 45: Demonstration of reciprocity for a resistively-loaded bowtie antenna on an ungrounded substrate. The received voltage is compared to (a) the ψ component of the radiated electric field in the yz plane, and (b) the ϕ component of the radiated electric field in the xz plane.

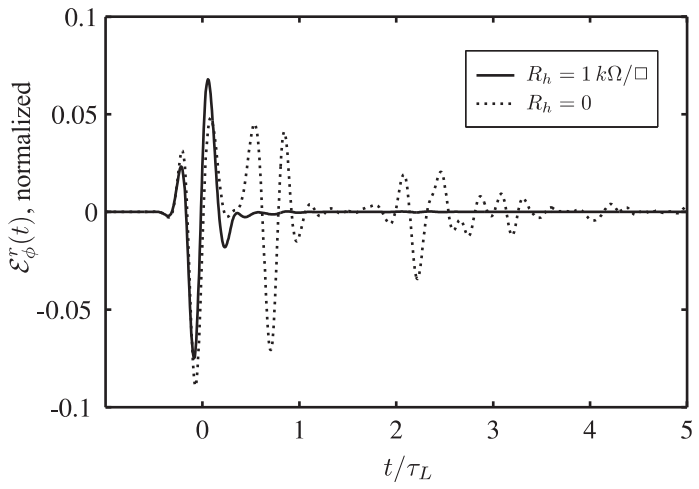

Figure 46: Effect of resistive loading on the radiated electric field of the UWB bowtie antenna.

The success of the bowtie antenna in the UWB realm lies in its ability to transmit short pulses. In both Fig. 45(a) and Fig. 45(b), the pulse shapes of the radiated electric field waveforms demonstrate this feature. For example, in the xz plane [Fig. 45(b)], the radiated pulses have roughly the same shape as the exciting current waveform, $\mathcal{I}_t^+(t)$, shown in Fig. 44(a). The resistive loading (156) is a vital design element that greatly affects the UWB performance of the antenna. Specifically, it minimizes the unwanted reflections from the ends, and causes the energy to be released gradually along the entire length of the circular arms of the antenna. The role of resistive loading in this context can be better understood by examining the case *without* resistive loading, namely, $R_h = 0$ in (156). In Fig. 46, the ϕ component of the radiated electric field at $\psi = 18^\circ$ in the xz plane is compared for two bowtie antennas: one with $R_h = 1\,k\Omega/\square$ (resistive loading) and the other with $R_h = 0$ (no resistive loading.) The solid line denotes the radiated electric field for $R_h = 1\,k\Omega/\square$, and the dotted line denotes the radiated electric field for $R_h = 0$. The radiated field is normalized by $Z_c\,I_0/r$, with the incident current amplitude I_0 given in (157). From Fig. 46, it is clear that the resistive loading has a significant effect on the duration of the pulse radiated from the antenna. With resistive loading, the radiated electric field consists of a single pulse with the shape of the incident current waveform in Fig. 44(a). Without resistive loading, the current on the arms of the bowtie bounces back and forth between

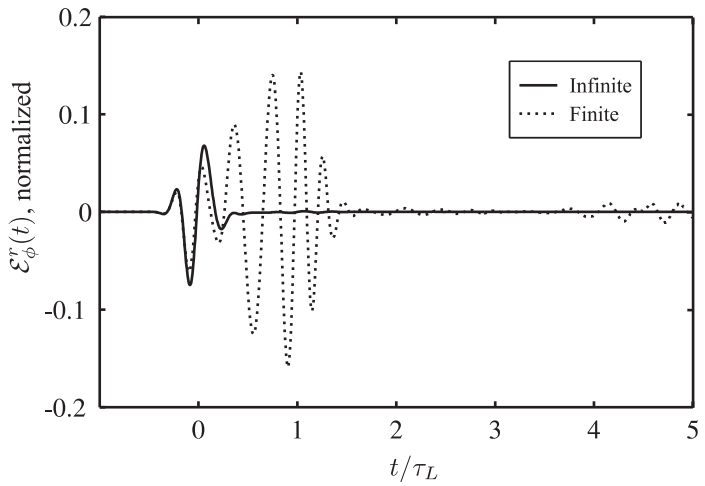

Figure 47: Effect of a finite substrate on the radiated electric field of the resistively-loaded UWB bowtie antenna.

the ends of the antenna and the feed region, which creates the extra pulses in the radiated field. This type of radiation is undesirable for UWB applications, since it occupies a large time interval.

An important assumption in the analysis of the bowtie antenna is that the dielectric substrate on which the antenna is mounted is of *infinite* extent. Using the NFFFT for free space, we can also investigate the effects of a *finite substrate* on the performance of the bowtie antenna. In Fig. 47, the ϕ component of the radiated electric field at $\psi = 18^\circ$ in the xz plane is compared for two cases: one with an infinite substrate (the same as Fig. 46), and the other with a finite substrate of size 60cm $\times$ 80cm $\times$2cm. The finite substrate is enclosed in an NFFFT box, and the radiated electric field is computed in free space. It is seen that the finite substrate has a considerable effect on the radiated electric field. The end effects become more pronounced for angles close to the grazing angle, $\psi = 0$. The NFFFT for the infinite dielectric substrate eliminates these effects, and allows us to evaluate the unperturbed radiation from the UWB antenna.

CHAPTER V

THE INPUT ADMITTANCE OF A PROLATE-SPHEROIDAL MONOPOLE ANTENNA FED BY A MAGNETIC FRILL

In this chapter, we include our previous work on an entirely different subject, namely, the analysis of *prolate spheroidal monopoles*, which was completed between June 2004 and January 2005 [62]. At that time, this research subject was considered as a possible thesis topic. Although the focus of our research has changed since then, the originality of the work and the amount of effort spent on creating it prompted us to include it in our thesis.

5.1 Introduction

Electromagnetic problems involving spheroidal structures have been studied for many years. The analyses of prolate-spheroidal antennas and forced oscillations of prolate-spheroidal structures include the well-known treatments of Stratton and Chu, Schelkunoff, Page and Adams, and Ryder [63–67] from the period 1939–1952. A comprehensive review of the approaches to the prolate-spheroidal antenna problem from that period can be found in [68].

The common assumption in the early analyses is that the antenna is fed through a *feed-gap* on the surface of the spheroid, with the gap containing various field distributions. Relatively recent treatments (e.g. [69, 70]) have further contributed to the theory of the spheroidal antenna built on the feed-gap assumption. However, as first stated in [63], the feed-gap model tends to produce a diverging series for the input susceptance of the antenna for vanishingly small widths of the feed-gap. In fact, this effect is not limited to spheroidal antennas; it has been observed in various types of antenna problems involving infinitely narrow feed-gaps [71–75]. Furthermore, despite its inherent simplicity, it is difficult to relate the feed-gap model directly to any practical method for feeding the antenna. This constitutes a problem in deriving data for practical use and in verifying the analytical results by any sort of measurement.

The *frill source* feed [76–78], which has been used for modelling wire antennas fed through an image plane by a coaxial line, is a suitable choice for overcoming the aforementioned problems. For example, the frill source feed model was used successfully in the theory for the thin-wire loop antenna to obtain a convergent series for the susceptance [79]. However, to the best of the authors' knowledge, the only interest in applying the frill source feed model to spheroidal antennas occurred in two early reports [80, 81]. In both of these works, the field of the TEM mode in the coaxial line was used in a variational formulation to obtain an approximation for the input admittance. The numerical results obtained were necessarily limited by the computational resources available at the time.

In this chapter, an analytical description is provided for a prolate-spheroidal monopole antenna fed through an image plane by a coaxial transmission line, subject to the TEM mode approximation for the field in the coaxial aperture of the transmission line. This is accomplished through the use of the aforementioned frill source feed.

5.2 Theory

5.2.1 Spheroidal Wave Functions

In the prolate-spheroidal coordinate system shown in Fig. 48 [82], each point is characterized by a triplet of numbers (η, ξ, ϕ), where $-1 \leq \eta \leq 1$ is the prolate angle variable corresponding to hyperboloidal surfaces with foci $\pm F$ on the z-axis, $1 \leq \xi < \infty$ is the radial variable corresponding to ellipsoidal surfaces with the same foci, and $0 \leq \phi < 2\pi$ is the azimuthal angle variable corresponding to planes perpendicular to the plane $z = 0$ and passing through the origin.

Assuming harmonic time dependence, $e^{j\omega t}$, the scalar wave equation becomes

$$(\nabla^2 + \beta^2)\psi = 0 \ , \tag{160}$$

where $\beta = \omega/c$ is the wavenumber in the free space. When separation of variables is applied to this equation in spheroidal coordinates, solutions are obtained in the following form [83]:

$$\psi_{mn} = S_{mn}(\gamma, \eta) R^{(i)}_{mn}(\gamma, \xi) e^{\pm jm\phi} \ , \tag{161}$$

in which $\gamma = \beta F$ (corresponding to the parameter c in [83]), $S_{mn}(\gamma, \eta)$ is the spheroidal angle

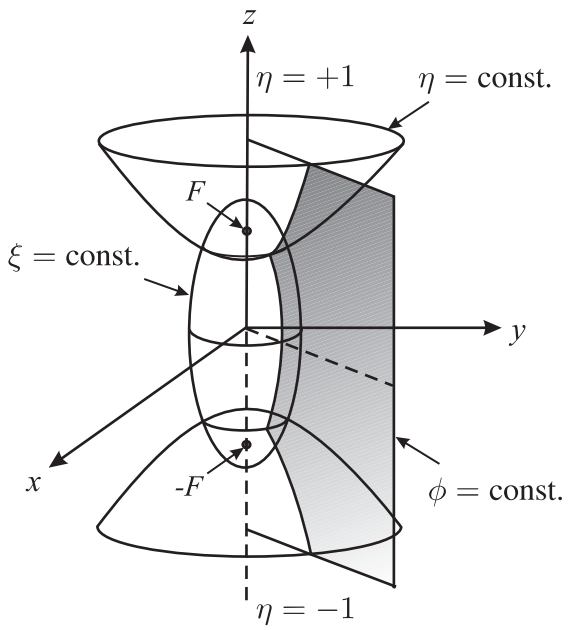

Figure 48: The prolate-spheroidal coordinate system.

function of the first kind, and $R_{mn}^{(i)}(\gamma,\xi)$ is the spheroidal radial function of the first ($i=1$) or second ($i=2$) kind. In most antenna problems, only these functions are encountered. They can be expanded in terms of associated Legendre functions of the first and second kind, $P_n^m(z)$ and $Q_n^m(z)$ [40, 84, 85], of order m and degree n as follows [83][1]:

$$S_{mn}(\gamma,\eta) = \sum_{r=0,1}^{\infty}{}' \, (-1)^m d_r^{mn}(\gamma) P_{m+r}^m(\eta) \tag{162a}$$

$$R_{mn}^{(1)}(\gamma,\xi) = \frac{1}{\kappa_{mn}^{(1)}(\gamma)} \sum_{r=0,1}^{\infty}{}' \, d_r^{mn}(\gamma) P_{m+r}^m(\xi) \tag{162b}$$

$$\begin{aligned} R_{mn}^{(2)}(\gamma,\xi) = \frac{1}{\kappa_{mn}^{(2)}(\gamma)} \Bigg[& \sum_{r=-2m,-2m+1}^{\infty}{}' \, d_r^{mn}(\gamma) Q_{m+r}^m(\xi) \\ & + \sum_{r=2m+2,2m+1}^{\infty}{}' \, d_{\rho|r}^{mn}(\gamma) P_{r-m-1}^m(\xi) \Bigg] \; . \end{aligned} \tag{162c}$$

The spheroidal radial function of the fourth kind is defined as

$$R_{mn}^{(4)}(\gamma,\xi) = R_{mn}^{(1)}(\gamma,\xi) - j\, R_{mn}^{(2)}(\gamma,\xi) \; . \tag{163}$$

[1]The term $(-1)^m$ is included in (162a) to account for Flammer's non-standard definition of the Legendre function $P_n^m(x)$ for $|x| \leq 1$. In our study, Legendre functions are defined according to [84].

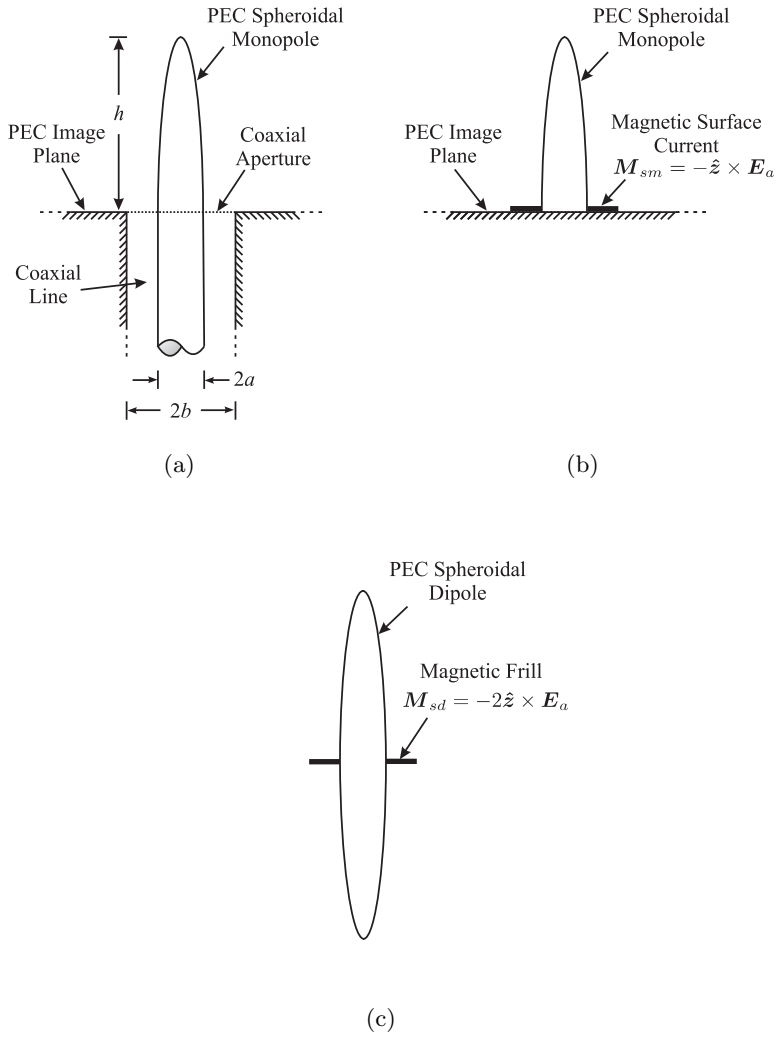

Figure 49: Development of the model for the spheroidal monopole antenna. (a) Spheroidal monopole fed through an image plane by a coaxial transmission line. (b) Geometry equivalent to that of (a) for calculating the field for $\eta \geq 0$. (c) Image equivalent of (b).

In the above equations, the prime over the summation sign indicates that the summations extend over only even values of r if $n-m$ is even, and over only odd values of r if $n-m$ is odd. The expansion coefficients $d_r^{mn}(\gamma)$ and $d_{\rho|r}^{mn}(\gamma)$ satisfy certain recurrence relations, and the joining factors $\kappa_{mn}^{(1)}(\gamma)$ and $\kappa_{mn}^{(2)}(\gamma)$ are functions of $d_r^{mn}(\gamma)$ and $d_{\rho|r}^{mn}(\gamma)$ [83, 86]. The normalization constant $N_{mn}(\gamma)$ is defined via the orthogonality property of the spheroidal angle function,

$$\int_{-1}^{1} S_{mn}(\gamma,\eta)S_{mp}(\gamma,\eta)d\eta = N_{mn}(\gamma)\delta_{np} \ , \tag{164}$$

in which

$$\delta_{np} = \begin{cases} 1, & n=p \\ 0, & n\neq p \ . \end{cases} \tag{165}$$

The normalization constant is related to the coefficients $d_r^{mn}(\gamma)$ as follows:

$$N_{mn}(\gamma) = 2\sum_{r=0,1}^{\infty\prime} \frac{(r+2m)!\ (d_r^{mn}(\gamma))^2}{(2r+2m+1)\ r!} \ . \tag{166}$$

In the remainder of the chapter, the dependence of $d_r^{mn}(\gamma)$, $d_{\rho|r}^{mn}(\gamma)$, $\kappa_{mn}^{(1)}(\gamma)$, $\kappa_{mn}^{(2)}(\gamma)$, and $N_{mn}(\gamma)$ on γ will usually not be shown explicitly.

5.2.2 Equivalent Model for the Monopole Antenna

Fig. 49(a) shows a spheroidal monopole antenna of height h, radius a, and semi-focal length $F = (h^2-a^2)^{1/2}$ fed through an infinite, perfectly-conducting (PEC) image plane by a coaxial transmission line. If we assume that the tangential electric field in the coaxial aperture of the transmission line is $\boldsymbol{E}_a$, then the geometry shown in Fig. 49(b) is equivalent to that shown in Fig. 49(a) for calculating the electromagnetic field for $\eta \geq 0$ [87]. Here the magnetic surface current placed on the PEC image plane is

$$\boldsymbol{M}_{sm} = -\hat{\boldsymbol{z}} \times \boldsymbol{E}_a. \tag{167}$$

Now using the method of images, the geometry in Fig. 49(b) can be replaced by the image equivalent shown in Fig. 49(c). Here, the current of the magnetic frill source is

$$\boldsymbol{M}_{sd} = -2\hat{\boldsymbol{z}} \times \boldsymbol{E}_a \ . \tag{168}$$

At this point, the following approximation will be used: The electric field in the aperture of the coaxial transmission line will be taken to be that of the TEM mode:

$$\boldsymbol{E}_a = \frac{V_0}{\rho' \ln(b/a)} \hat{\boldsymbol{\rho}}', \tag{169}$$

in which V_0 is the voltage, ρ' is the radial coordinate in the cylindrical coordinate system, and a and b are the inner and outer conductor radii, respectively. This approximation has been shown to be a useful and fairly accurate one for wire antennas fed through an image plane by a coaxial line. For example, the actual input admittance of the antenna has been shown to be equal to that of the antenna fed by the TEM magnetic frill source plus a small correction added to the input susceptance [79, 88].

On the surface of the PEC spheroidal dipole in Fig. 49(c), the tangential component of the electric field (E_η) must vanish. This constitutes a boundary condition that is central to the problem at hand. The tangential electric field is created by two sources: the magnetic current of the frill source, and the induced electric current on the surface of the dipole. The field of the former is the *incident* field, and the field of the latter is the *scattered* field. In the following two subsections, these two fields will be analyzed.

5.2.3 Tangential Component of the Incident Electric Field on the Surface of the Spheroid

The surface of the dipole shown in Fig. 49(c) corresponds to the coordinate surface $\xi = \xi_a = (1-(a/h)^2)^{-1/2}$, and the frill source resides on the surface $S : \{\eta = 0, \xi_a \leq \xi \leq \xi_b, 0 \leq \phi < 2\pi\}$. After using (169) with (168), in spheroidal coordinates, the magnetic surface current of the frill becomes

$$\boldsymbol{M}_{sd}(\xi') = \frac{-2V_0}{F\sqrt{\xi'^2 - 1}\ln(b/a)} \hat{\boldsymbol{\phi}}'. \tag{170}$$

In the following, the primed variables will be used for the source point, and the unprimed variables will be used for the observation point. The incident electric field resulting from the current (170) is [89]

$$\boldsymbol{E}^i = -\frac{1}{4\pi} \iint_S \boldsymbol{M}_{sd} \times \nabla' \Psi dS', \tag{171}$$

in which the free-space scalar Green function is

$$\Psi = \frac{e^{-j\beta r}}{r} \ . \tag{172}$$

After inserting (170), the integrand of (171) becomes [40]

$$\boldsymbol{M}_{sd} \times \nabla' \Psi = \frac{-2V_0}{F\sqrt{\xi'^2 - 1}\ln(b/a)} \hat{\boldsymbol{\phi}}' \times \left(\hat{\boldsymbol{\eta}}' \frac{1}{h_{\eta'}} \frac{\partial \Psi}{\partial \eta'} + \hat{\boldsymbol{\xi}}' \frac{1}{h_{\xi'}} \frac{\partial \Psi}{\partial \xi'} + \hat{\boldsymbol{\phi}}' \frac{1}{h_{\phi'}} \frac{\partial \Psi}{\partial \phi'} \right), \tag{173}$$

in which $h_{\eta'}$, $h_{\xi'}$, and $h_{\phi'}$ are the metric coefficients for the prolate-spheroidal coordinates [86]:

$$h_{\eta'} = F\sqrt{\frac{\xi'^2 - \eta'^2}{1 - \eta'^2}} \tag{174a}$$

$$h_{\xi'} = F\sqrt{\frac{\xi'^2 - \eta'^2}{\xi'^2 - 1}} \tag{174b}$$

$$h_{\phi'} = F\sqrt{(\xi'^2 - 1)(1 - \eta'^2)} \ . \tag{174c}$$

Because the geometry and the source are rotationally symmetric about the z-axis, there is no dependence on ϕ', i. e. , $\partial/\partial\phi' = 0$. After noting that $\eta' = 0$ on the frill, (173) becomes

$$\boldsymbol{M}_{sd} \times \nabla' \Psi = \frac{2V_0}{F^2 \ln(b/a)} \left(\frac{1}{\xi'\sqrt{\xi'^2 - 1}} \right) \left[\hat{\boldsymbol{\eta}}' \sqrt{\xi'^2 - 1} \frac{\partial \Psi}{\partial \xi'} - \hat{\boldsymbol{\xi}}' \frac{\partial \Psi}{\partial \eta'} \right]. \tag{175}$$

On the surface of the dipole ($\xi = \xi_a$), the tangential component of the electric field must vanish. Hence, only the η-component of (175) is necessary for the analysis. Using Table 1, and again noting that $\eta' = 0$ on the surface of the frill, it follows that

$$\hat{\boldsymbol{\eta}} \cdot \hat{\boldsymbol{\xi}}' = \hat{\boldsymbol{\eta}} \cdot (\hat{\boldsymbol{x}} \cos\phi' + \hat{\boldsymbol{y}} \sin\phi') = -\eta \sqrt{\frac{\xi^2 - 1}{\xi^2 - \eta^2}} \cos(\phi - \phi') \tag{176a}$$

$$\hat{\boldsymbol{\eta}} \cdot \hat{\boldsymbol{\eta}}' = \hat{\boldsymbol{\eta}} \cdot \hat{\boldsymbol{z}} = \xi \sqrt{\frac{1 - \eta^2}{\xi^2 - \eta^2}} \ . \tag{176b}$$

Now after using (176), the η-component of (175) becomes

$$\begin{aligned} \hat{\boldsymbol{\eta}} \cdot (\boldsymbol{M}_{sd} \times \nabla' \Psi) = & \frac{2V_0}{F^2 \ln(b/a)} \\ & \cdot \left[\xi \sqrt{\frac{1 - \eta^2}{\xi^2 - \eta^2}} \left(\frac{1}{\xi'} \frac{\partial \Psi}{\partial \xi'} \right) + \eta \sqrt{\frac{\xi^2 - 1}{\xi^2 - \eta^2}} \left(\frac{1}{\xi'\sqrt{\xi'^2 - 1}} \cos(\phi - \phi') \frac{\partial \Psi}{\partial \eta'} \right) \right]. \end{aligned} \tag{177}$$

Table 1: Dot products of unit vectors of prolate-spheroidal coordinates and rectangular coordinates.

	$\hat{\boldsymbol{x}}$	$\hat{\boldsymbol{y}}$	$\hat{\boldsymbol{z}}$
$\hat{\boldsymbol{\xi}}$	$\xi\sqrt{\frac{1-\eta^2}{\xi^2-\eta^2}}\cos\phi$	$\xi\sqrt{\frac{1-\eta^2}{\xi^2-\eta^2}}\sin\phi$	$\eta\sqrt{\frac{\xi^2-1}{\xi^2-\eta^2}}$
$\hat{\boldsymbol{\eta}}$	$-\eta\sqrt{\frac{\xi^2-1}{\xi^2-\eta^2}}\cos\phi$	$-\eta\sqrt{\frac{\xi^2-1}{\xi^2-\eta^2}}\sin\phi$	$\xi\sqrt{\frac{1-\eta^2}{\xi^2-\eta^2}}$
$\hat{\boldsymbol{\phi}}$	$-\sin\phi$	$\cos\phi$	0

Inserting (177) into (171), the η-component of the incident electric field at $\xi = \xi_a$ can be written as follows:

$$\begin{aligned} E^i_\eta(\eta,\xi_a) &= -\frac{1}{4\pi}\int_{\xi_a}^{\xi_b}\int_0^{2\pi} \hat{\boldsymbol{\eta}}\cdot(\boldsymbol{M}_{sd}\times\nabla'\Psi)\mid_{\xi=\xi_a} h_{\phi'}h_{\xi'}d\phi'd\xi' \\ &= \frac{-V_0}{2\pi\ln(b/a)}\left[\xi_a\sqrt{\frac{1-\eta^2}{\xi_a^2-\eta^2}}\,\Im_1+\eta\sqrt{\frac{\xi_a^2-1}{\xi_a^2-\eta^2}}\,\Im_2\right], \end{aligned} \tag{178}$$

in which the two definite integrals $\Im_1$ and $\Im_2$ are

$$\Im_1 = \left\{\int_0^{2\pi}(\Psi\mid_{\xi'=\xi_b}-\Psi\mid_{\xi'=\xi_a})d\phi'\right\}_{\eta'=0} \tag{179}$$

$$\Im_2 = \int_{\xi_a}^{\xi_b}\frac{d\xi'}{\sqrt{\xi'^2-1}}\left\{\int_0^{2\pi}\cos(\phi'-\phi)\frac{\partial\Psi}{\partial\eta'}d\phi'\right\}_{\eta'=0}. \tag{180}$$

Before elaborating further on the integrals (179) and (180), the following expansion of the Green function Ψ in (172) in spheroidal coordinates is introduced [83, pg.47]:

$$\Psi = -j2\beta\sum_{m=0}^{\infty}\sum_{n=m}^{\infty}\frac{2-\delta_{0m}}{N_{mn}}S_{mn}(\gamma,\eta)S_{mn}(\gamma,\eta')\cdot\cos(m(\phi-\phi'))R^{(1)}_{mn}(\gamma,\xi_<)R^{(4)}_{mn}(\gamma,\xi_>)\ , \tag{181}$$

in which,

$$\begin{aligned} &\xi_< : \text{smaller of } \xi \text{ and } \xi' \\ &\xi_> : \text{larger of } \xi \text{ and } \xi'\ . \end{aligned} \tag{182}$$

5.2.3.1 Integral $\Im_1$

Using (181), the integral $\Im_1$ in (179) becomes

$$\Im_1 = -j2\beta \sum_{m=0}^{\infty} \sum_{n=m}^{\infty} \frac{2-\delta_{0m}}{N_{mn}} S_{mn}(\gamma,\eta) S_{mn}(\gamma,0) \cdot \int_0^{2\pi} \cos(m(\phi'-\phi)) d\phi' R_{mn}^{(1)}(\gamma,\xi_a) \left[R_{mn}^{(4)}(\gamma,\xi_b) - R_{mn}^{(4)}(\gamma,\xi_a) \right] , \quad (183)$$

where now in (182), $\xi_< = \xi_a$ and $\xi_> = \xi'$, because $\xi = \xi_a$ and $\xi_a \leq \xi' \leq \xi_b$. The trigonometric integral in (183) is simply

$$\int_0^{2\pi} \cos(m(\phi'-\phi)) d\phi' = 2\pi\delta_{0m} , \quad (184)$$

and [83, pg.21]

$$S_{0n}(\gamma,0) = \begin{cases} \frac{(-1)^{n/2} n!}{2^n (n/2)!(n/2)!} & \text{if } n \text{ is even} \\ 0 & \text{if } n \text{ is odd} . \end{cases} \quad (185)$$

With (184) and (185), (183) simplifies to

$$\Im_1 = -j4\pi\beta \sum_{k=0}^{\infty} \frac{1}{N_{0,2k}} \frac{(-1)^k (2k)!}{2^{2k} k! k!} S_{0,2k}(\gamma,\eta) R_{0,2k}^{(1)}(\gamma,\xi_a) \left[R_{0,2k}^{(4)}(\gamma,\xi_b) - R_{0,2k}^{(4)}(\gamma,\xi_a) \right] . \quad (186)$$

5.2.3.2 Integral $\Im_2$

After inserting (181), the ϕ' integral in (180) becomes

$$\left\{ \int_0^{2\pi} \cos(\phi'-\phi) \frac{\partial \Psi}{\partial \eta'} d\phi' \right\}_{\eta'=0} = -j2\beta \sum_{m=0}^{\infty} \sum_{n=m}^{\infty} \frac{2-\delta_{0m}}{N_{mn}} S_{mn}(\gamma,\eta) S'_{mn}(\gamma,0) \cdot \int_0^{2\pi} \cos(\phi'-\phi) \cos(m(\phi'-\phi)) d\phi' R_{mn}^{(1)}(\gamma,\xi_a) R_{mn}^{(4)}(\gamma,\xi') . \quad (187)$$

The trigonometric integral in (187) is easily evaluated,

$$\int_0^{2\pi} \cos(\phi'-\phi) \cos(m(\phi'-\phi)) d\phi' = \pi\delta_{1m} , \quad (188)$$

so only $S'_{1n}(\gamma,0)$ is needed in (187), which is given by [83, pg. 21]

$$S'_{1n}(\gamma,0) = \begin{cases} \frac{(-1)^{n/2-1}(n+2)!}{2^n (n/2-1)!(n/2+1)!} & \text{if } n \text{ is even} \\ 0 & \text{if } n \text{ is odd} . \end{cases} \quad (189)$$

With these results, (187) becomes

$$\left\{\int_0^{2\pi}\cos(\phi'-\phi)\frac{\partial\Psi}{\partial\eta'}d\phi'\right\}_{\eta'=0} = -j2\pi\beta\sum_{k=1}^{\infty}\frac{2}{N_{1,2k}}\frac{(-1)^{k-1}(2k+2)!}{2^{2k}(k-1)!(k+1)!} \cdot S_{1,2k}(\gamma,\eta)R^{(1)}_{1,2k}(\gamma,\xi_a)R^{(4)}_{1,2k}(\gamma,\xi') \ . \quad (190)$$

With (190), $\Im_2$ in (180) becomes

$$\Im_2 \quad = \quad -j4\pi\beta\sum_{k=1}^{\infty}\frac{1}{N_{1,2k}}\frac{(-1)^{k-1}(2k+2)!}{2^{2k}(k-1)!(k+1)!}S_{1,2k}(\gamma,\eta)R^{(1)}_{1,2k}(\gamma,\xi_a)I_{2k}(\gamma,\xi_a,\xi_b) \quad , \quad (191)$$

in which the following definition is introduced:

$$I_{2k}(\gamma,\xi_a,\xi_b) = \int_{\xi_a}^{\xi_b}\frac{d\xi'}{\sqrt{\xi'^2-1}}R^{(4)}_{1,2k}(\gamma,\xi') \ . \quad (192)$$

After substituting (163) into (192), the following expression is obtained for the function $I_{2k}(\gamma,\xi_a,\xi_b)$:

$$I_{2k}(\gamma,\xi_a,\xi_b) = \int_{\xi_a}^{\xi_b}\frac{d\xi'}{\sqrt{\xi'^2-1}}\left[\frac{1}{\kappa^{(1)}_{1,2k}}\sum_{r=0,1}^{\infty\,\prime} d_r^{1,2k}P^1_{1+r}(\xi') - j\frac{1}{\kappa^{(2)}_{1,2k}}\Big(\sum_{r=-2,-1}^{\infty\,\prime} d_r^{1,2k}Q^1_{1+r}(\xi') + \sum_{r=4,3}^{\infty\,\prime} d_{\rho|r}^{1,2k}P^1_{r-2}(\xi')\Big)\right]. \quad (193)$$

Since $2k-1$ is odd for any k, the summations in (193) extend only over odd values of r. After exchanging the order of the sums and integrals, (193) becomes

$$I_{2k}(\gamma,\xi_a,\xi_b) = \frac{1}{\kappa^{(1)}_{1,2k}}\sum_{r=0}^{\infty} d_{2r+1}^{1,2k}\int_{\xi_a}^{\xi_b}\frac{P^1_{2r+2}(\xi')}{\sqrt{\xi'^2-1}}d\xi' - j\frac{1}{\kappa^{(2)}_{1,2k}}\Big(\sum_{r=-1}^{\infty} d_{2r+1}^{1,2k}\int_{\xi_a}^{\xi_b}\frac{Q^1_{2r+2}(\xi')}{\sqrt{\xi'^2-1}}d\xi' + \sum_{r=2}^{\infty} d_{\rho|2r-1}^{1,2k}\int_{\xi_a}^{\xi_b}\frac{P^1_{2r-3}(\xi')}{\sqrt{\xi'^2-1}}d\xi'\Big). \quad (194)$$

Substituting $m=1$ into the functional identities [84, 8.6.6-7]

$$\begin{aligned} P_n^m(z) &= (z^2-1)^{m/2}\,\frac{d^mP_n(z)}{dz^m} \\ Q_n^m(z) &= (z^2-1)^{m/2}\,\frac{d^mQ_n(z)}{dz^m} \end{aligned} \quad , \quad \text{for} \quad z>1 \ , \quad (195)$$

and inserting the resulting expressions into (194) yields the following result for $I_{2k}(\gamma,\xi_a,\xi_b)$:

$$I_{2k}(\gamma,\xi_a,\xi_b) = \frac{1}{\kappa^{(1)}_{1,2k}}\sum_{r=0}^{\infty} d_{2r+1}^{1,2k}\left[P_{2r+2}(\xi_b)-P_{2r+2}(\xi_a)\right] - j\frac{1}{\kappa^{(2)}_{1,2k}}\Big(\sum_{r=-1}^{\infty} d_{2r+1}^{1,2k}\left[Q_{2r+2}(\xi_b)-Q_{2r+2}(\xi_a)\right] + \sum_{r=2}^{\infty} d_{\rho|2r-1}^{1,2k}\left[P_{2r-3}(\xi_b)-P_{2r-3}(\xi_a)\right]\Big). \quad (196)$$

Upon substitution of the series representations for the integrals (186) and (191) with (196) into (178), the tangential component of the incident electric field on the surface of the dipole is obtained entirely in terms of known special functions and parameters.

5.2.4 Tangential Component of the Scattered Electric Field on the Surface of the Spheroid

The next step is to obtain the tangential component of the scattered electric field on the surface of the dipole. Following the discussions in [64] and [69], the various components of the scattered field *outside* the dipole can be expanded in spheroidal coordinates as follows:

$$H_{\phi}^{s}(\eta,\xi) = \frac{1}{h_{\phi}} A(\eta,\xi) \tag{197}$$

$$E_{\eta}^{s}(\eta,\xi) = \frac{1}{j\omega\epsilon_0 h_{\xi} h_{\phi}} \frac{\partial A(\eta,\xi)}{\partial \xi} \tag{198}$$

$$E_{\xi}^{s}(\eta,\xi) = -\frac{1}{j\omega\epsilon_0 h_{\eta} h_{\phi}} \frac{\partial A(\eta,\xi)}{\partial \eta} \ , \tag{199}$$

where

$$A(\eta,\xi) = \frac{h_{\phi}}{F} \sum_{n=1,3,5,\ldots}^{\infty} a_n \ S_{1n}(\gamma,\eta) R_{1n}^{(4)}(\gamma,\xi) \ . \tag{200}$$

Due to the symmetry of the geometry with respect to the plane $z = 0$, $S_{1n}(\gamma,\eta)$ must be an even function of η. Hence, the summation in (200) only includes odd n. In (200), the required behavior of the fields at infinity is accounted for via the spheroidal radial function of the fourth kind, which has the asymptotic behavior

$$R_{mn}^{(4)}(\gamma,\xi) \xrightarrow{\gamma\xi\to\infty} \frac{1}{\gamma\xi} e^{-j(\gamma\xi - \frac{1}{2}(n+1)\pi)} \ . \tag{201}$$

The coefficients a_n in (200) are arbitrary complex constants; therefore, they may be chosen to satisfy the boundary condition for the total electric field on the surface of the PEC spheroid:

$$E_{\eta}(\eta,\xi_a) = E_{\eta}^{s}(\eta,\xi_a) + E_{\eta}^{i}(\eta,\xi_a) = 0 \ , \quad -1 \le \eta \le 1 \ . \tag{202}$$

Mathematically, the completeness property of the spheroidal angle function set $\{S_{mn}(\gamma,\eta), n = m, m+1, \ldots\}$ over the function space $L^2[-1,1]$ ensures that such an arrangement for $\{a_n\}$ is not only possible, but also unique [90]. Furthermore, the orthogonality of this set

offers a practical method to evaluate the coefficients a_n. Now, after substituting (198) with (200) in (202) the following constraint for the coefficients a_n is obtained:

$$\sum_{n=0}^{\infty} a_{2n+1} S_{1,2n+1}(\gamma,\eta) \left[\frac{\partial}{\partial\xi}\left(\sqrt{\xi^2-1}\, R^{(4)}_{1,2n+1}(\gamma,\xi)\right)\right]_{\xi=\xi_a} = -j\omega\epsilon_0 F^2 \sqrt{\xi_i^2-\eta^2} E^i_\eta(\eta,\xi_a) \ . \tag{203}$$

Multiplying both sides of (203) by $S_{1m}(\gamma,\eta)$, integrating over $-1 \le \eta \le 1$, and using (164), the coefficients a_{2n+1} are obtained in closed form:

$$a_{2n+1} = -\frac{jY_0V_0\gamma}{N_{1,2n+1}\left[\frac{\partial}{\partial\xi}\left(\sqrt{\xi^2-1}\, R^{(4)}_{1,2n+1}(\gamma,\xi)\right)\right]_{\xi=\xi_a}} V_n(\gamma,\xi_a,\xi_b) \ , \tag{204}$$

in which $Y_0 = (\epsilon_0/\mu_0)^{1/2}$ is the wave admittance of free space, and the following definition is introduced, as in [69]:

$$V_n(\gamma,\xi_a,\xi_b) = \frac{F}{V_0}\int_{-1}^{1} E^i_\eta(\eta,\xi_a)\sqrt{\xi_a^2-\eta^2} S_{1,2n+1}(\gamma,\eta) d\eta \ . \tag{205}$$

The dimensionless function $V_n(\gamma,\xi_a,\xi_b)$ will be called the *source parameter*. It encapsulates the effect of the source on the current distribution, and it only depends on the incident electric field created by the source. Using the results of subsection 5.2.3, (205) becomes:

$$\begin{aligned} V_n(\gamma,\xi_a,\xi_b) = {} & \frac{-F}{2\pi\ln(b/a)} \\ & \cdot\left[\xi_a\int_{-1}^{1}\sqrt{1-\eta^2}\,\Im_1\, S_{1,2n+1}(\gamma,\eta)d\eta + \sqrt{\xi_a^2-1}\int_{-1}^{1}\eta\,\Im_2\, S_{1,2n+1}(\gamma,\eta)d\eta\right]. \end{aligned} \tag{206}$$

For simplification, the source parameter is divided into two components:

$$V_n(\gamma,\xi_a,\xi_b) = \sum_{k=0}^{\infty} V^{(1)}_{n,k}(\gamma,\xi_a,\xi_b) + \sum_{k=1}^{\infty} V^{(2)}_{n,k}(\gamma,\xi_a,\xi_b) \ , \tag{207}$$

where

$$V^{(1)}_{n,k}(\gamma,\xi_a,\xi_b) \ = \ \frac{j2\gamma}{\ln(b/a)}\frac{(-1)^k(2k)!}{2^{2k}k!k!}(\xi_a)R^{(1)}_{0,2k}(\gamma,\xi_a)\left[R^{(4)}_{0,2k}(\gamma,\xi_b) - R^{(4)}_{0,2k}(\gamma,\xi_a)\right]J_{kn}(\gamma) \tag{208}$$

$$V^{(2)}_{n,k}(\gamma,\xi_a,\xi_b) \ = \ \frac{j2\gamma}{\ln(b/a)}\frac{(-1)^{k-1}(2k+2)!}{2^{2k}(k-1)!(k+1)!}(\xi_a^2-1)^{1/2}R^{(1)}_{1,2k}(\gamma,\xi_a)I_{2k}(\gamma,\xi_a,\xi_b)K_{kn}(\gamma) \ , \tag{209}$$

with

$$J_{kn}(\gamma) = \frac{1}{N_{0,2k}} \int_{-1}^{1} \sqrt{1-\eta^2} S_{0,2k}(\gamma,\eta) S_{1,2n+1}(\gamma,\eta) d\eta \tag{210}$$

$$K_{kn}(\gamma) = \frac{1}{N_{1,2k}} \int_{-1}^{1} \eta S_{1,2k}(\gamma,\eta) S_{1,2n+1}(\gamma,\eta) d\eta \ . \tag{211}$$

We will now obtain analytical expressions for the two definite integrals in (210) and (211). The integral in (210) is expanded using (162a):

$$J_{kn}(\gamma) = \frac{1}{N_{0,2k}} \int_{-1}^{1} \sqrt{1-\eta^2} \Big(\sum_{r=0}^{\infty} (-1)^0 d_{2r}^{0,2k} P_{2r}(\eta) \Big) \Big(\sum_{s=0}^{\infty} (-1)^1 d_{2s}^{1,2n+1} P_{2s+1}^1(\eta) \Big) d\eta \tag{212}$$

$$= -\frac{1}{N_{0,2k}} \sum_{r=0}^{\infty} \sum_{s=0}^{\infty} d_{2r}^{0,2k} d_{2s}^{1,2n+1} \int_{-1}^{1} \sqrt{1-\eta^2} P_{2r}(\eta) P_{2s+1}^1(\eta) d\eta \ . \tag{213}$$

From the functional identity [91, 8.733-4]

$$\sqrt{1-\eta^2} P_{2r}(\eta) = \frac{1}{4r+1} \left[P_{2r-1}^1(\eta) - P_{2r+1}^1(\eta) \right] \tag{214}$$

and [91, 7.112-1]

$$\int_{-1}^{1} P_n^m(\eta) P_k^m(\eta) d\eta = \frac{2}{2n+1} \frac{(n+m)!}{(n-m)!} \delta_{nk} \ , \tag{215}$$

it follows that

$$\int_{-1}^{1} \sqrt{1-\eta^2} P_{2r}(\eta) P_{2s+1}^1(\eta) d\eta = \frac{4r(2r-1)}{(4r-1)(4r+1)} \delta_{s,r-1} - \frac{4(r+1)(2r+1)}{(4r+1)(4r+3)} \delta_{s,r} \ . \tag{216}$$

Then, (210) becomes

$$J_{kn}(\gamma) \ = \ \frac{1}{N_{0,2k}} \sum_{r=0}^{\infty} d_{2r}^{0,2k} \left[-\frac{4r(2r-1)}{(4r-1)(4r+1)} d_{2r-2}^{1,2n+1} \ + \ \frac{4(r+1)(2r+1)}{(4r+1)(4r+3)} d_{2r}^{1,2n+1} \right]. \tag{217}$$

The integral in (211) is similarly expanded using (162a):

$$K_{kn}(\gamma) = \frac{1}{N_{1,2k}} \int_{-1}^{1} \eta \Big(\sum_{r=0}^{\infty} (-1)^1 d_{2r+1}^{1,2k} P_{2r+2}^1(\eta) \Big) \Big(\sum_{s=0}^{\infty} (-1)^1 d_{2s}^{1,2n+1} P_{2s+1}^1(\eta) \Big) d\eta \tag{218}$$

$$= \frac{1}{N_{1,2k}} \sum_{r=0}^{\infty} \sum_{s=0}^{\infty} d_{2r+1}^{1,2k} d_{2s}^{1,2n+1} \int_{-1}^{1} \eta P_{2r+2}^1(\eta) P_{2s+1}^1(\eta) d\eta \ . \tag{219}$$

From [91, 8.733-2]

$$\eta P_{2r+2}^1(\eta) = \frac{1}{4r+5} \left[(2r+2) P_{2r+3}^1(\eta) + (2r+3) P_{2r+1}^1(\eta) \right], \tag{220}$$

and (215), it follows that

$$\int_{-1}^{1} \eta P_{2r+2}^{1}(\eta) P_{2s+1}^{1}(\eta) d\eta = \frac{2(2r+2)(2r+3)(2r+4)}{(4r+5)(4r+7)} \delta_{s,r+1} + \frac{2(2r+1)(2r+2)(2r+3)}{(4r+3)(4r+5)} \delta_{s,r} \ . \quad (221)$$

Then, (211) becomes

$$K_{kn}(\gamma) = \frac{1}{N_{1,2k}} \sum_{r=0}^{\infty} d_{2r+1}^{1,2k} \cdot \left[\frac{2(2r+2)(2r+3)(2r+4)}{(4r+5)(4r+7)} d_{2r+2}^{1,2n+1} + \frac{2(2r+1)(2r+2)(2r+3)}{(4r+3)(4r+5)} d_{2r}^{1,2n+1} \right]. \quad (222)$$

Finally, the tangential component of the scattered electric field on the surface of the dipole is obtained using (198) with (200) and (204):

$$E_{\eta}^{s}(\eta, \xi_a) = \frac{-V_0}{F\sqrt{\xi_a^2 - \eta^2}} \sum_{n=0}^{\infty} \frac{V_n(\gamma, \xi_a, \xi_b)}{N_{1,2n+1}} S_{1,2n+1}(\gamma, \eta) \ . \quad (223)$$

5.2.5 Current Distribution

Using the equivalence principle [87], the geometry shown in Fig. 49(c) can be replaced by an equivalent one in which the PEC spheroid is replaced by the following surface current density in free space:

$$\boldsymbol{J}_s(\eta, \xi_a) = \hat{\boldsymbol{\eta}} \Big\{ I(\eta) / \big[2\pi h_{\phi}(\eta, \xi_a) \big] \Big\} \ , \quad (224)$$

in which $I(\eta)$ is the current distribution on the dipole. The scattered electromagnetic field within the spheroid bounded by this current is given by (197)–(199) with the function $A(\eta, \xi)$ replaced by $B(\eta, \xi)$:

$$B(\eta, \xi) = \frac{h_{\phi}}{F} \sum_{n=1,3,5,\ldots}^{\infty} b_n \ S_{1n}(\gamma, \eta) R_{1n}^{(1)}(\gamma, \xi) \ . \quad (225)$$

In (225), the spheroidal radial function of the first kind $R_{1n}^{(1)}(\gamma, \xi)$ is used to make the field regular on the axis $\xi = 1$. The tangential component of the scattered electric field must be continuous at the surface current; that is, $E_{\eta}^{s}(\eta, \xi_a^{+}) = E_{\eta}^{s}(\eta, \xi_a^{-})$, in which ξ_a^{+} and ξ_a^{-} approach ξ_a from above and below, respectively. Therefore, it follows from (198) with (200)

and (225) that the coefficients b_n and a_n are related by

$$b_{2n+1} = a_{2n+1} \left[\frac{\frac{\partial}{\partial \xi}\left(\sqrt{\xi^2-1}\, R^{(4)}_{1,2n+1}(\gamma,\xi)\right)}{\frac{\partial}{\partial \xi}\left(\sqrt{\xi^2-1}\, R^{(1)}_{1,2n+1}(\gamma,\xi)\right)} \right]_{\xi=\xi_a} . \tag{226}$$

Now the current distribution can be determined from the boundary condition for the tangential component of the magnetic field:

$$\begin{aligned} I(\eta) &= 2\pi h_\phi (H^s_\phi(\eta,\xi_a^+) - H^s_\phi(\eta,\xi_a^-)) \\ &= 2\pi (A(\eta,\xi_a) - B(\eta,\xi_a)) \ , \end{aligned} \tag{227}$$

which, after substituting (200) with (204) and (225) with (226), becomes

$$\begin{aligned} I(\eta) = \frac{2\pi h_\phi}{F} \sum_{n=0}^{\infty} S_{1,2n+1}(\gamma,\eta) \frac{-jY_0V_0\gamma}{N_{1,2n+1}}\ V_n(\gamma,\xi_a,\xi_b) \\ \cdot \left[\frac{R^{(4)}_{1,2n+1}(\gamma,\xi_a)}{\left[\frac{\partial}{\partial \xi}\left(\sqrt{\xi^2-1}\, R^{(4)}_{1,2n+1}(\gamma,\xi)\right)\right]_{\xi=\xi_a}} - \frac{R^{(1)}_{1,2n+1}(\gamma,\xi_a)}{\left[\frac{\partial}{\partial \xi}\left(\sqrt{\xi^2-1}\, R^{(1)}_{1,2n+1}(\gamma,\xi)\right)\right]_{\xi=\xi_a}} \right] . \end{aligned} \tag{228}$$

In order to simplify (228), the following definition is introduced:

$$r_n(\gamma,\xi_a) \ = \ \frac{\sqrt{\xi_a^2-1} R^{(4)}_{1,2n+1}(\gamma,\xi_a)}{\left[\frac{\partial}{\partial \xi}\left(\sqrt{\xi^2-1}\, R^{(4)}_{1,2n+1}(\gamma,\xi)\right)\right]_{\xi=\xi_a}} - \frac{\sqrt{\xi_a^2-1} R^{(1)}_{1,2n+1}(\gamma,\xi_a)}{\left[\frac{\partial}{\partial \xi}\left(\sqrt{\xi^2-1}\, R^{(1)}_{1,2n+1}(\gamma,\xi)\right)\right]_{\xi=\xi_a}} \ . \tag{229}$$

With this definition, the current distribution in (228) becomes

$$I(\eta) = -j2\pi Y_0 V_0 \gamma \sum_{n=0}^{\infty} S_{1,2n+1}(\gamma,\eta) \frac{r_n(\gamma,\xi_a)}{N_{1,2n+1}} \sqrt{1-\eta^2} V_n(\gamma,\xi_a,\xi_b) \ . \tag{230}$$

The function $r_n(\gamma,\xi_a)$ in (229) is a minor variant of the Infeld's function ζ_{2n}, as defined in [71]. Its definition comprises only known functions and parameters.

We now have the desired result, an analytical expression for the current distribution on the spheroidal monopole that only involves known special functions and parameters, that is, (230) with (229), (207), (217) and (222).

5.2.6 Input Admittance

The current distribution $I(\eta)$ is valid for all the points on the monopole. Specifically, knowledge of the current at the source, i. e. , $\eta = 0$, can be used to determine the *input*

admittance of the monopole:

$$Y_{\text{TEM}} = G_{\text{TEM}} + jB_{\text{TEM}} = \frac{I(0)}{V_0} \ . \tag{231}$$

After setting $\eta = 0$ in (230), and introducing the identity [83, pg. 21]

$$S_{1,2n+1}(\gamma, 0) = \frac{(-1)^n (2n+2)!}{2^{2n+1} n!(n+1)!} \ , \tag{232}$$

we obtain

$$Y_{\text{TEM}} = \sum_{n=0}^{\infty} Y_n = -j2\pi Y_0 \gamma \sum_{n=0}^{\infty} \frac{(-1)^n (2n+2)!}{2^{2n+1} n!(n+1)!} \frac{r_n(\gamma, \xi_a)}{N_{1,2n+1}} V_n(\gamma, \xi_a, \xi_b) \ . \tag{233}$$

In the remaining analysis, the dependence of Y_n on γ, ξ_a, and ξ_b will not be shown explicitly.

Using (229) and (207)–(209) in the series (233), the input admittance can be calculated. In the next section, a computational technique will be introduced for this purpose.

5.3 Numerical Evaluation of the Series for the Input Admittance

The theoretical properties of the spheroidal wave functions $S_{mn}(\gamma, \eta)$, $R^{(1)}_{mn}(\gamma, \xi)$, and $R^{(4)}_{mn}(\gamma, \xi)$ have been thoroughly investigated [40, 83, 86, 92], but their computation is still considered difficult. Efficient numerical procedures for computing these functions with unrestricted complex parameters have been absent until recently [93–95]. For their computation, the expansion in (162) is the most commonly used one in the literature, and is theoretically valid for an unlimited range of γ. However, since the expansion is in terms of Legendre functions, to which the spheroidal functions reduce when $\gamma = 0$, the expansions in (162) are practically useful for values of γ from zero up to about ten [83]. Various computational methods for the expansion coefficients $d^{mn}_r(\gamma)$ and $d^{mn}_{\rho|r}(\gamma)$ and the joining factors $\kappa^{(1)}_{mn}(\gamma)$ and $\kappa^{(2)}_{mn}(\gamma)$ in (162) are given in [83] and [86].

The computation of the input admittance in (233) requires the total current passing upward through the circle $\{\eta = 0, \xi = \xi_a, \, 0 \le \phi < 2\pi\}$. This circle coincides with the inner edge of the magnetic frill, at which a logarithmic singularity exists in the η-component of the incident electric field [78]. From (171) and (172), it follows that the singularity is only in the real part of the field, since $\sin(\beta r)/r$ has a finite limit as $r \to 0$, as opposed to $\cos(\beta r)/r$. The PEC boundary condition dictates that the total tangential electric field must be zero

on the perfectly conducting surface of the dipole in Fig. 49(c), including the neighborhood of the singularity. Therefore, the scattered electric field should exhibit the same kind of singularity. Nevertheless, the series for the scattered electric field in (223) consists of terms that are finite on the surface of the dipole, including the inner edge of the frill. Therefore, it can be anticipated that a small number of terms in (223) will poorly represent the electric field near the source. In Fig. 50(a), the incident tangential electric field is compared to the series for the scattered tangential electric field (223) truncated at 100, 500, and 1000 terms. The difficulty of accurately representing the singularity with the series (223) (even with 1000 terms) is evident.

In contrast to the electric field, the incident magnetic field is finite everywhere in space, including the source region [78]. In addition, it can be proven that the total magnetic field is also finite everywhere in space, including the inner edge of the frill. Consequently, the current is finite in the feed region; and the series in (233) is *convergent*. This fact is clearly demonstrated in Fig. 50(b), which shows that the series for the total magnetic field (and current) converges everywhere on the surface of the monopole. However, as can be seen in this figure, a large number of terms ($\sim$1000) in the series is required to accurately represent the total magnetic field or current near the feed region. Hence, it can be stated qualitatively that the series for the input admittance (233) is *slowly convergent*.

At this point, it should be noted that series for the conductance (G_{TEM}) rapidly converges, typically to 10–15 digits after 5–6 terms. This is because the conductance represents the power lost via the *radiated* field, which can be accurately described using a few fundamental current modes. Higher current modes having more variation along the monopole surface contribute less to the radiated field. However, these higher modes have a significant effect on the near-field and the local energy distribution. This makes the susceptance (B_{TEM}) dependent on these modes. For this reason, the slowly convergent part of the input admittance (233) is the susceptance.

The slow convergence of the series in (233) requires us to employ an approximate method that will increase the computation efficiency, and still retain a specified accuracy. The need for approximation arises mainly from the increasing complexity of computing the terms of

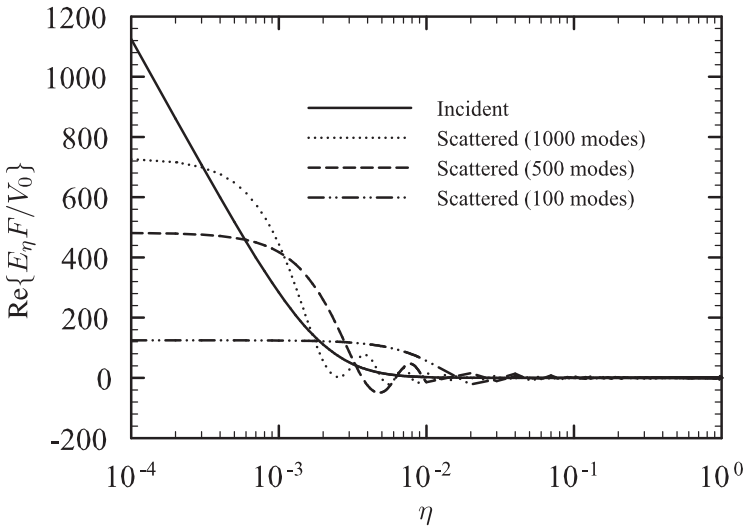

(a)

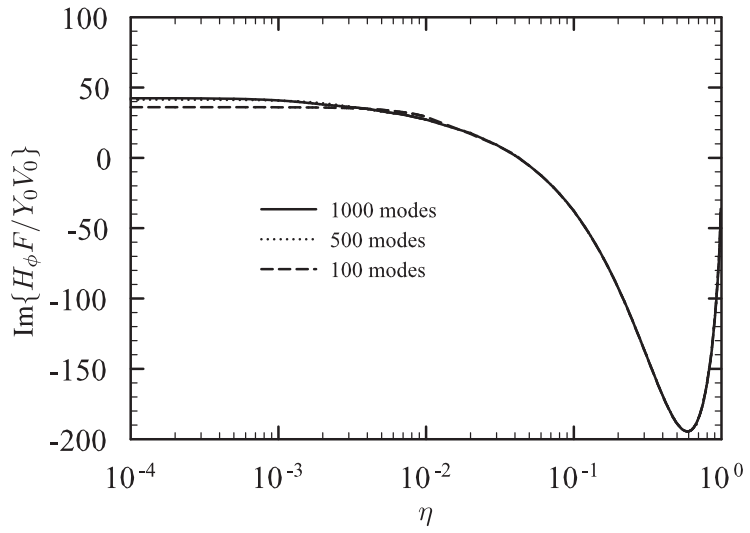

(b)

Figure 50: (a) The real part of the tangential component of the electric field at the surface of the monopole (normalized by V_0/F). Results for the truncated series for the scattered field (223) (with inverted sign) are compared to the incident field (178). (b) The imaginary part of the ϕ-component of the total magnetic field at the surface of the monopole (normalized by Y_0V_0/F). Results for the truncated series (derived from (230)) are compared. $h/\lambda = 0.5$, $h/a = 10^3$, $Z_c = 50\ \Omega$ ($b/a = 2.30...$).

(233) for large n. This is a consequence of the computation of spheroidal wave functions for each n, which becomes a formidable task for a large number of values. It must be remembered that there are no recurrence relations between spheroidal wave functions of different order n, unlike Legendre and Bessel functions [83].

Our method of approximation can be simply summarized as follows: We represent the spheroidal wave functions by Legendre functions at large n, and utilize the recurrence relations to obtain a large number of terms. For sufficiently large n values (the criterion for which is given later), the Legendre functions are approximated by simpler functions, which allow the analytical summation of the rest of the series. This analytical summation embodies the slowly-convergent part in the series (233), which is due to the singularity in the tangential electric field, thus resolving the practical problem of summing (233) up to inaccessibly large terms. In the subsequent paragraphs and Appendix D, the aforementioned approximation process is explained in detail.

We divide the series in (233) into four partial sums:

$$Y_{\mathrm{TEM}} = \sum_{n=0}^{n_{\mathrm{max1}}} Y_n + \sum_{n=n_{\mathrm{max1}+1}}^{n_{\mathrm{max2}}} Y_n^a + \sum_{n=n_{\mathrm{max2}+1}}^{n_{\mathrm{max3}}} Y_n^b + \sum_{n=n_{\mathrm{max3}+1}}^{\infty} Y_n^c \,. \tag{234}$$

The derivation of Y_n^a, Y_n^b, Y_n^c, guidelines for choosing n_{max1}, n_{max2}, n_{max3}, and the assessment of the accuracy of (234) are detailed in Appendix D.

The term Y_n^a is obtained by replacing the spheroidal wave functions in Y_n with their asymptotic forms in n, i. e. , Legendre functions; which are considerably easier to calculate than spheroidal wave functions. The term Y_n^b is obtained by substituting into Y_n^a the asymptotic forms of the Legendre functions for large n, which only include algebraic operations on known parameters. The term Y_n^c is a simplified form of Y_n^b for large n, chosen such that analytical methods can be used for reducing the infinite partial sum $\sum_{n=n_{\mathrm{max3}+1}}^{\infty} Y_n^c$ to a finite sum.

An important point is that the full partition in (234) may not be necessary in certain cases. Specifically, for thick monopoles with moderate electrical length, the partition

$$Y_{\mathrm{TEM}} = \sum_{n=0}^{n_{\mathrm{max1}}} Y_n + \sum_{n=n_{\mathrm{max1}+1}}^{\infty} Y_n^c \tag{235}$$

can yield high accuracy with an appropriate value of $n_{\max 1}$. For example, for the monopole used for the measurements in Section 5.5, the input susceptance B_{TEM} converges to 4 digits with $n_{\max 1} = 100$.

The partition in (234) has another important advantage: It is shown in Appendix D that the last three partial sums in (234) are proportional to the frequency ω. Hence, for a fixed geometry, only the first partial sum in (234) has to be recalculated for different frequencies.

In Fig. 51 and Fig. 52, the input admittance and input impedance of the prolate-spheroidal monopole antenna are graphed, respectively, for a practical range of the electrical length: $0 < h/\lambda \leq 0.65$. Notice that the vertical scale is logarithmic, and that "+" and "−" signs are used to indicate where the susceptance is positive and negative, respectively. The dimensions of the TEM magnetic frill feeding the antenna correspond to a coaxial line with $Z_c = 50\ \Omega$ ($b/a = 2.30...$). In all figures, a family of curves is shown; each curve is for a different thickness of the monopole. Here, the logarithmic parameter $\Omega = 2\ln(2h/a)$, customarily used with cylindrical antennas, indicates the thickness for the range $\Omega = 6.0$ ($h/a = 10.0$) to $\Omega = 15.0$ ($h/a = 904$). These graphs should be useful for design purposes.

It is instructive to compare the results in Fig. 51 for the prolate-spheroidal antenna with those for a similar cylindrical antenna. Such results can be found in the work of R. W. P. King [96], in particular, the King-Middleton second-order results for the input admittance of the cylindrical dipole antenna. While the results for the two antennas are qualitatively the same, there are noticeable differences around the first resonant length. For very thin prolate-spheroidal antennas, the resonant length is near $h/\lambda \approx 0.25$, and it moves to *higher* values of h/λ for thicker antennas. Whereas, for very thin cylindrical antennas, the resonant length is near $h/\lambda \approx 0.25$, and it moves to *lower* values of h/λ for thicker antennas. In addition, for the prolate-spheroidal antenna, the maximum in the input conductance, which occurs near resonance, is approximately the same for all of the thicknesses displayed: $G_{\mathrm{TEM}} \approx 27.5$ mS. For the cylindrical antenna, there is more variation in the maximum value of the conductance for comparable changes in thickness.

To complete the discussion of the spheroidal monopole antenna, we will describe the

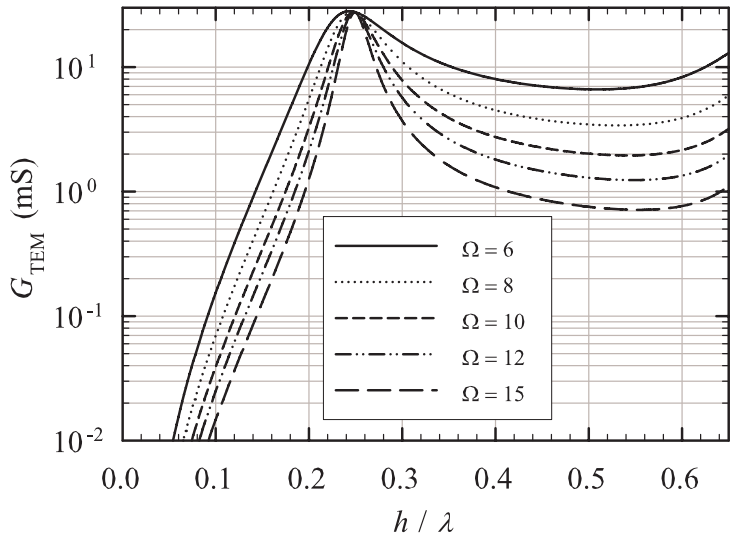

(a)

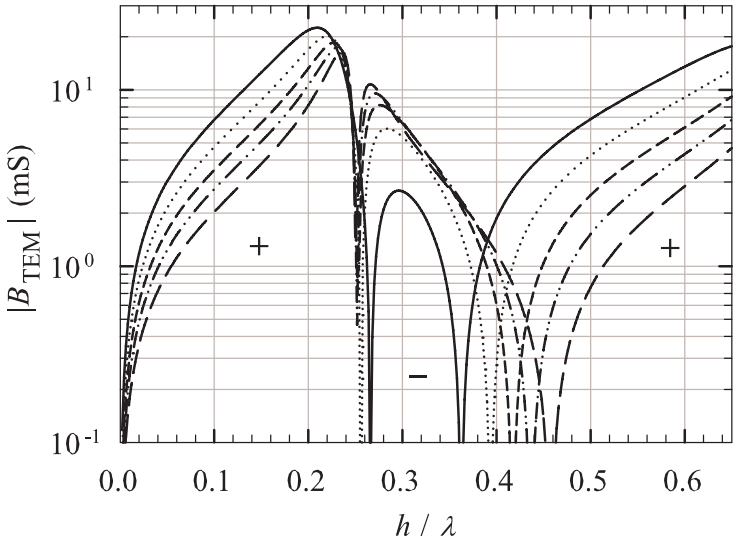

(b)

Figure 51: The input admittance of the prolate-spheroidal monopole antenna as a function of the electrical length. $Z_c = 50\ \Omega$ ($b/a = 2.30...$). (a) Input conductance G_{TEM}. (b) Absolute input susceptance $|B_{\mathrm{TEM}}|$.

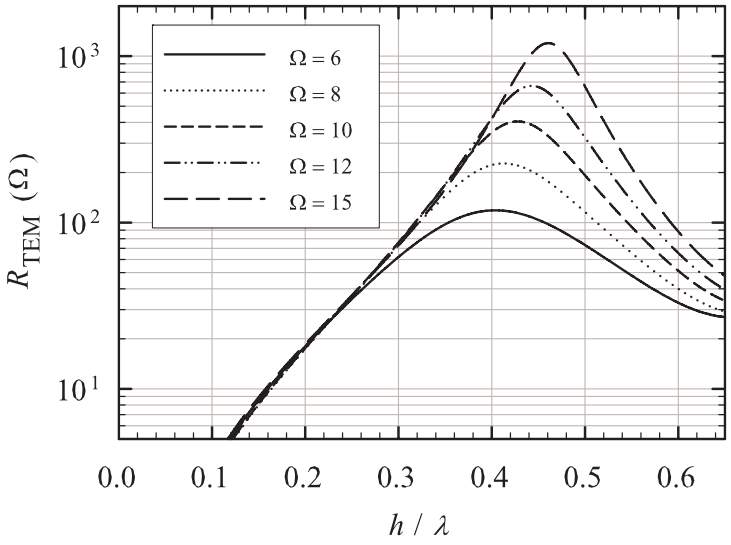

(a)

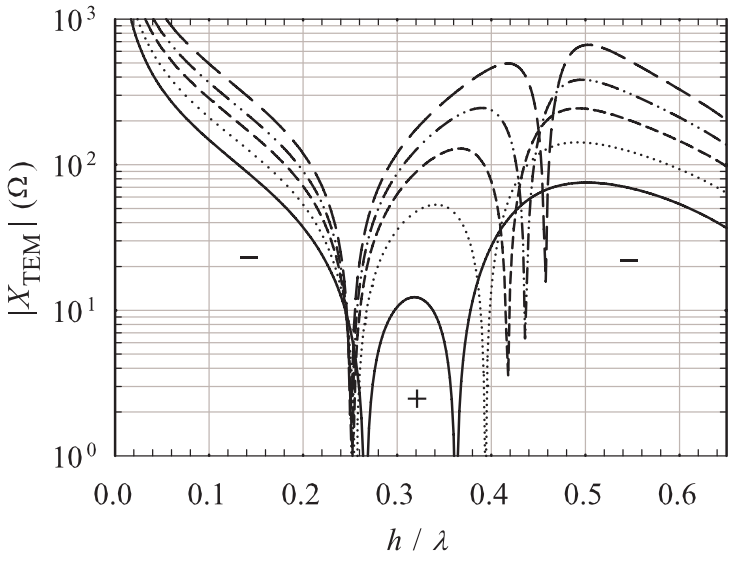

(b)

Figure 52: The input impedance of the prolate-spheroidal monopole antenna as a function of the electrical length. $Z_c = 50\ \Omega$ ($b/a = 2.30...$). (a) Input resistance R_{TEM}. (b) Absolute input reactance $|X_{\mathrm{TEM}}|$.

radiated or far-zone field, viz., the asymptotic field for $r \to \infty$. In the spherical coordinate system (r, θ, ϕ), the radiated field has only two components E_θ^r and $H_\phi^r = Y_0 E_\theta^r$, and they can be obtained analytically by methods quite similar to those already presented. The radiated electric field consists of two terms: the incident field, which is due to the magnetic current of the frill source, and the scattered field, which is due the induced electric current on the monopole. Numerical calculations show that the latter is much greater than the former, typically greater by at least three orders of magnitude. Hence, we only need to consider the scattered electric field, which is given by the series

$$E_\theta^r(r,\theta) = j\,V_0 \frac{e^{-j\beta r}}{r} \sum_{n=0}^{\infty} (-1)^n \frac{V_n(\gamma,\xi_a,\xi_b)\,S_{1,2n+1}(\gamma,\cos\theta)}{N_{1,2n+1}\left[\frac{\partial}{\partial\xi}\left(\sqrt{\xi^2-1}\,R_{1,2n+1}^{(4)}(\gamma,\xi)\right)\right]_{\xi=\xi_a}} \,. \tag{236}$$

For monopoles of moderate electrical length, this series converges very quickly.

The radiated electric field (236) was used to calculate the directivity of the monopole,

$$D(\theta) = \frac{4\pi r^2 Y_0 |E_\theta^r(r,\theta)|^2}{G_{\mathrm{TEM}}|V_0|^2} \,, \tag{237}$$

for which numerical results are presented in Fig. 53. Here the maximum directivity, $D_{\max}$ (Fig. 53(a)), and the angle at which it occurs, $\theta_{\max}$ (Fig. 53(b)) are shown as functions of the electrical length h/λ for three values of the thickness, $\Omega = 6$, 10, and 15. The three small insets in Fig. 53(a) show power patterns for the three lengths $h/\lambda = 0.5$, 0.7, and 1.0, and two thicknesses $\Omega = 6$ (solid line) and 15 (dashed line).

For an electrically short monopole, the maximum directivity occurs at broadside ($\theta_{\max} = 90°$) and $D_{\max} \approx 3$ ($D_{\max} \approx 3/2$ for the dipole). The maximum directivity stays at broadside and increases with electrical length until $h/\lambda \approx 0.6$. After this point, a multi-lobed field pattern forms (see pattern for $h/\lambda = 0.7$), and the maximum directivity decreases. When $h/\lambda \approx 1.0$, the field pattern has a single, well-defined, elevated lobe at $\theta_{\max} \approx 60°$, and $D_{\max} \approx 4.6$. As the electrical length is increased further, this behavior is repeated. For monopoles of practical length (those with maximum directivity at broadside, $h/\lambda < 0.6$), the maximum directivity is higher the thinner the monopole, the larger Ω. When the spheroidal monopole is very thin, e.g. $\Omega = 15$, the behavior for the maximum directivity is very similar to that for the infinitesimally-thin, cylindrical dipole antenna with a sinusoidal distribution of current [1, Sec. 8.5.3].

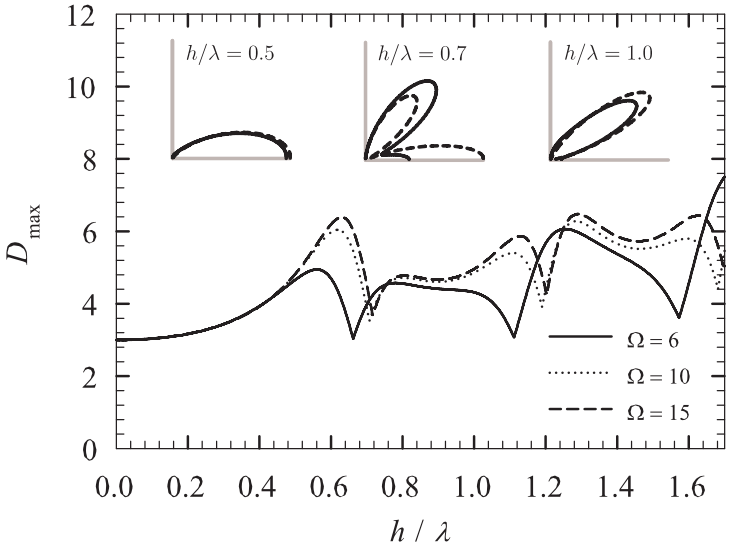

(a)

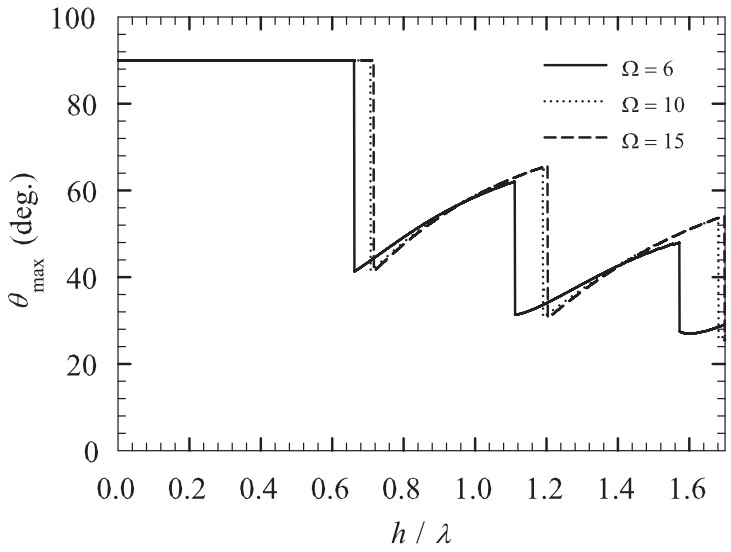

(b)

Figure 53: Directivity of the prolate-spheroidal monopole antenna as a function of the electrical length: (a) maximum directivity, and (b) angle at which it occurs. The insets show power patterns for the lengths $h/\lambda = 0.5$, 0.7, and 1.0. $Z_c = 50\ \Omega$ ($b/a = 2.30...$).

Table 2: Comparison of the theoretical and numerical results for the input admittance of the prolate spheroidal monopole. $a = 0.01\lambda$, $b/a = 1.20$.

$2h/\lambda$	Admittance at feed point (mS)			
	Theoretical		MoM (Bibby)	
	Real	Imag.	Real	Imag.
0.25	0.19479	4.8959	0.19479	4.896
0.375	1.98679	8.6748	1.9868	8.675
0.5	13.7015	2.7583	13.701	2.758
0.75	2.18848	0.0546	2.1885	0.0546
1.0	1.23152	2.1963	1.2315	2.196

5.4 Comparison of Theory with Previous Results

The input admittance of a prolate-spheroidal monopole fed by a magnetic frill has been investigated by Bibby and Peterson [97] using the method of moments [98]. Their results are compared with ours in Table 2. The parameters for the monopole are: $a = 0.01\lambda$, $b/a = 1.20$. In Table 2, the length of the equivalent dipole [see Fig. 49(c)] normalized by the free-space wavelength λ is given in first column. The second and third columns show the real and imaginary parts of the input admittances of the equivalent dipole obtained using the theoretical formulas derived in this chapter. The fourth and fifth columns are taken from the numerical results in [97, Table II]. It is seen that there is excellent agreement between the two results.

5.5 Comparison of Theory with Measurements

An experimental model was constructed for the prolate-spheroidal monopole antenna, and measurements made with this model were used to verify the theoretical calculations. The experimental setting is shown in Fig. 54. The monopole was fed through an aluminum image plane by a precision coaxial line (7 mm line with an APC-7 connector). The image plane was large enough (6.1 m $\times$ 6.1 m) to make reflections from its rolled edges negligible.

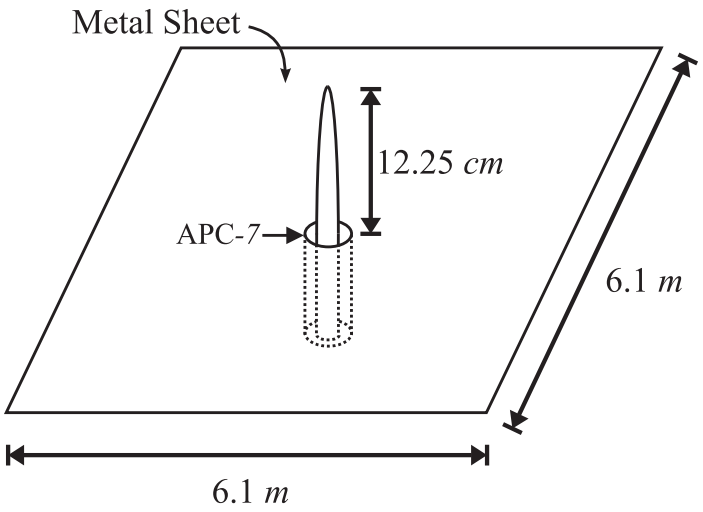

(a)

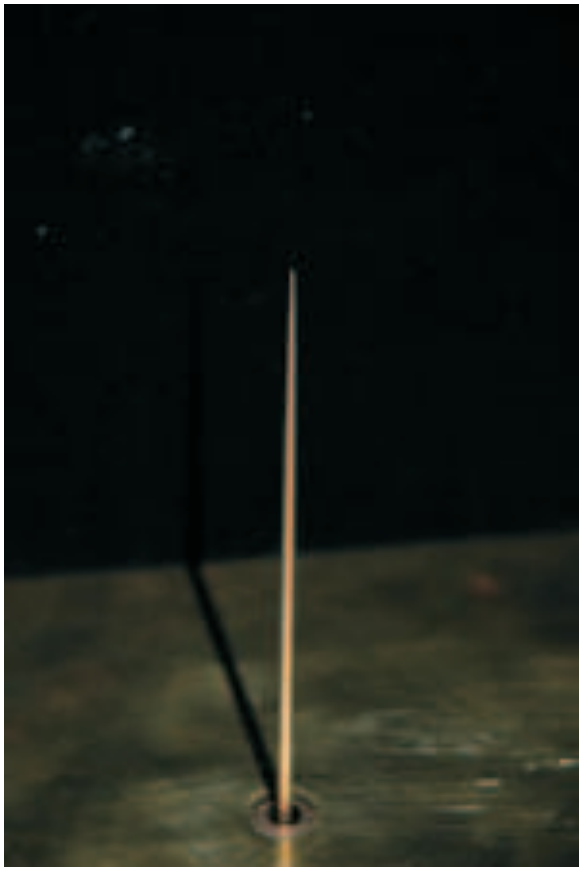

(b)

Figure 54: The experimental setup used in the measurement of the input admittance of the prolate-spheroidal monopole antenna. (a) Schematic drawing. (b) Picture.

For the measurements to be described, the dimensions of the coaxial line and monopole were such that $Z_c = 50\ \Omega$ ($b/a = 2.30...$) and $h/a = 80.5$ ($\Omega = 10.16$). The input admittance of the antenna was measured with an Agilent Model 8720D Network Analyzer.

The theoretical results for the input admittance (solid line) are compared with the measured results (dashed line) in Fig. 55 for a range of electrical lengths: Fig. 55(a) for $0 < h/\lambda \leq 1.0$, and Fig. 55(b) for $1.0 \leq h/\lambda \leq 2.0$. This range of electrical lengths includes the first four resonances of the antenna and the first three antiresonances. There is generally very good agreement between the theory and the measurements, and this agreement attests the value of the theoretical model for practical applications. However, there are noticeable, small differences, particularly in the input susceptance (B), once the electrical length is greater than about $h/\lambda = 1.25$. These differences are most likely due to two effects. The first effect is the fact that a perfect prolate-spheroidal shape could not be obtained for the experimental model. This can alter the effective electrical length of the spheroid. The second effect is the TEM field approximation that is used in the theoretical model. It is well known that the correction for this approximation is the addition of a small negative capacitive admittance [79, 88], and as can be seen in Fig. 55(b), a small negative susceptance added to the theory would improve the comparison. Morris has presented results that can be used to estimate this correction, and for our length of antenna ($h = 11.995$ cm) and transmission line ($b/a = 2.30...$), the correction is [88]

$$\delta Y \approx -j0.23(h/\lambda)\ . \tag{238}$$

In Fig. 56, for the longer values of h/λ, three input susceptances for the spheroidal monopole antenna are compared: Y_{TEM} (solid line), $Y_{\mathrm{TEM}} + \delta Y$ (dashed line), and measured Y (dotted line). Notice that the vertical scale is logarithmic for this graph. Clearly, the small correction ($|\delta Y| < 0.5$ mS) brings the theory and measurements into better agreement.

In Fig. 57, the measured input admittance of the prolate-spheroidal monopole antenna is compared with that for a cylindrical monopole antenna (right circular cylinder) of similar size: the same values of b/a and h/a. The results for the two antennas are similar; however, there is a distinct difference: From the location of the resonant points, the prolate-spheroidal

monopole appears to be shorter than the cylindrical monopole by about 8%. This difference has been noted in the past by other investigators, and is qualitatively described by the "equivalent length" concept [65, 69].

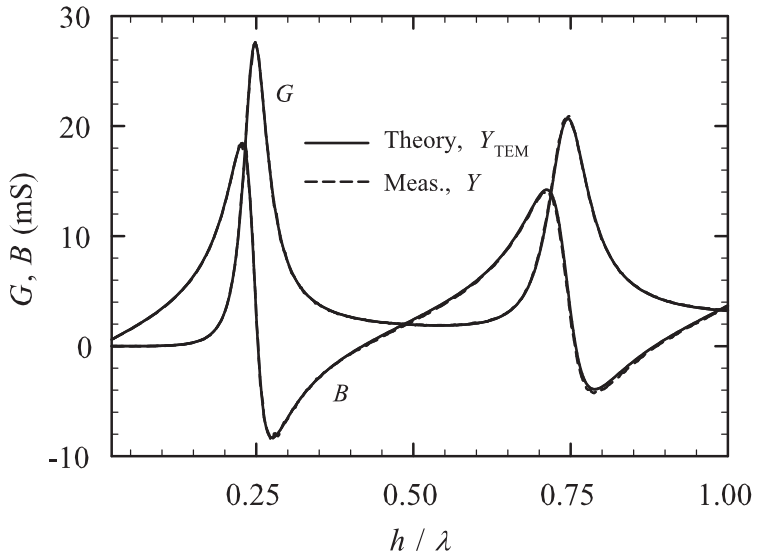

(a)

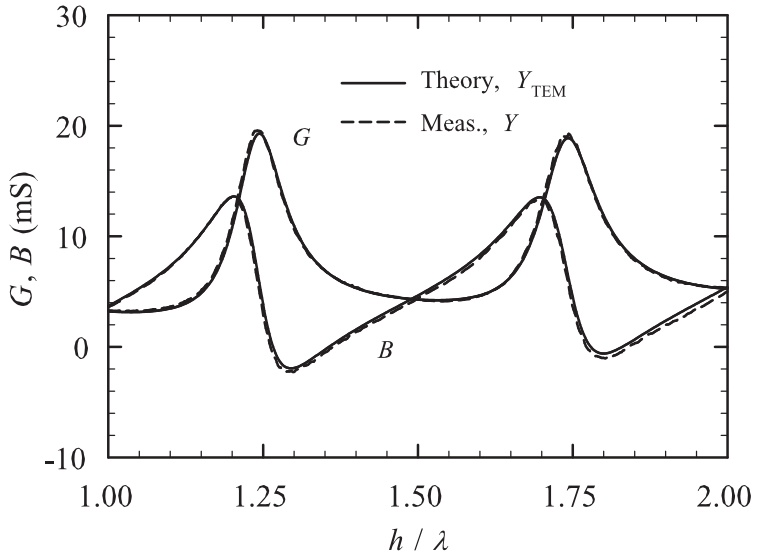

(b)

Figure 55: Comparison of the theoretical and measured input admittances for the prolate-spheroidal monopole antenna. $Z_c = 50\ \Omega$ ($b/a = 2.30...$), $h/a = 80.5$.

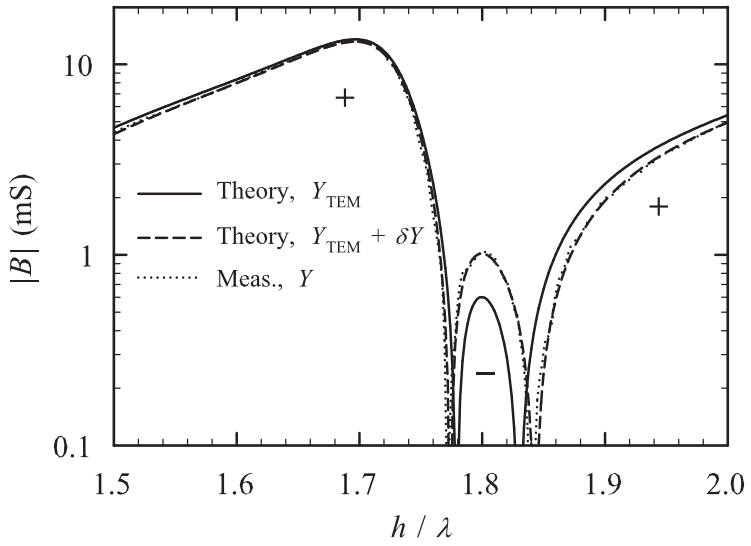

Figure 56: Comparison of input susceptances for the prolate-spheroidal monopole antenna. $Z_c = 50\ \Omega$ ($b/a = 2.30...$), $h/a = 80.5$.

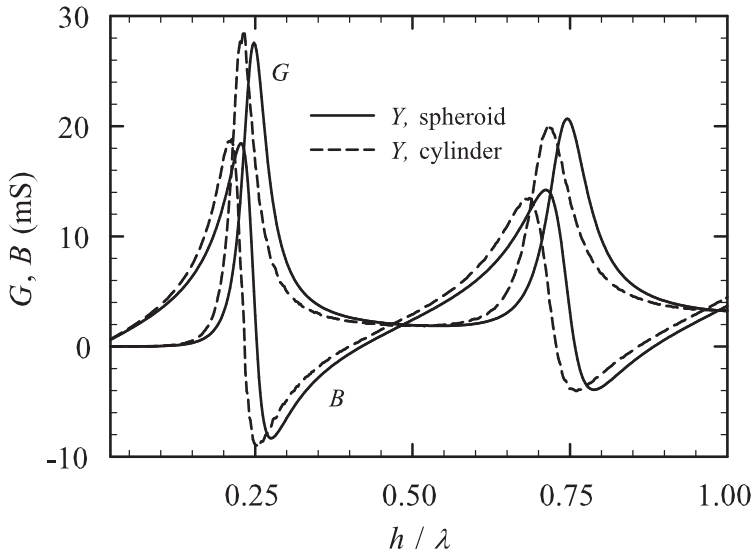

Figure 57: Comparison of measured input admittances for the prolate-spheroidal monopole antenna and the cylindrical monopole antenna. $Z_c = 50\ \Omega$ ($b/a = 2.30...$), $h/a = 80.5$.

CHAPTER VI

CONCLUSIONS

In this thesis, supplemental techniques were developed for the FDTD analysis of multilayered media. The first of these techniques is the near-field-to far-field transform (NFFFT), which is applicable to non-dispersive multilayered media. The second technique is the TF/SF boundary, or the plane-wave injector, which is applicable for general (possibly lossy) multilayered media.

In Chapter 2, a direct time-domain near-field-to-far-field transform was presented for the FDTD analysis of structures radiating in a lossless multilayered medium. An "on-the-fly" method similar to the one used in the free-space NFFFT was introduced, which involves keeping track of ten far-field storage arrays instead of six, as is the case for the NFFFT in free space. It was observed that the computational overhead increases with the number of delayed impulses in the functions $\mathcal{V}_v^p(t|\, z'), \mathcal{V}_i^p(t|\, z')$, and that the overhead is greatest when the observation point is close to the interface. The derivation of the NFFFT was given in a manner that relies heavily on the *transmission-line* analog associated with the multilayered medium. This allowed the step-by-step generalization of the NFFFT from a simple medium such as the dielectric half space in Section 2.2.1 to a general multilayered medium in Section 2.2.4. In Section 2.3, the applicability of the NFFFT was extended to the radiated electric field in the lowermost half space.

After the formulation for the NFFFT in general multilayered media was presented, illustrative examples were given to demonstrate the use of the NFFFT. First, a thin cylindrical dipole on a dielectric half space was analyzed using the developed NFFFT. Then, the NFFFT was applied to the FDTD analysis of the radiation from two microstrip line configurations: a length of matched microstrip line, and a matched microstrip bend. The results for the first configuration agreed with simple traveling-wave antenna theory, which asserts that the radiation occurs at the feed and the termination, and predicts the radiated

pulses to be approximately proportional to the derivative of the driving voltage waveform. The results for the second configuration were shown to be direct consequences of those for the first configuration, by the use of a simple conceptual model for the bend that consists of two microstrip line segments joined together at a right angle to each other.

In Chapter 3, a TF/SF boundary (or a plane-wave injector) was presented for a general lossy multilayered medium. The independence of both the geometry and the incident plane wave in a certain direction (perpendicular to the principal plane G in Fig. 19) was exploited to reduce Maxwell's equations to two sets (TE and TM) of 1-D transmission-line (TL) equations on the axis of symmetry. A 1-D auxiliary FDTD grid was used to solve for these equations. Implementation issues such as field placement, stability and excitation were discussed. It was noted that the issue of stability becomes important when the angle of incidence θ is large (close to $\pi/2$). In these cases, the time step in the 1-D auxiliary grid was reduced by an odd factor to maintain stability. Next, the plane-wave injector was generalized to lossy media. Problems with earlier attempts for this generalization in the literature were discussed. Afterwards, the plane-wave injector was generalized to handle narrowband inhomogeneous waves. The physical reasons for assuming a narrowband incident plane wave were discussed. It was noted that these waves required implicit field updates in their respective regions. Finally, the transparency of the TF/SF boundary to the scattered field was demonstrated using a simple example.

In Chapter 4, the NFFFT and TF/SF boundary were applied together to a series of practical examples. In the first set of problems, the TF/SF boundary was used to introduce a plane wave into a multilayered medium containing a perfectly-conducting scatterer. The scattered field in the far zone was calculated using the NFFFT. In the second set of examples, radiation problems were considered. Two different antennas were investigated in transmission and reception modes, and a time-domain reciprocity relation was confirmed between the results obtained from these cases. In the transmission mode, the NFFFT was used to calculate the radiated electric field, while the TF/SF boundary was used to introduce the plane wave incident on the antenna in the reception mode. The antenna considered in the second example was a practical antenna: a resistively-loaded UWB bowtie.

For demonstrating the use of the developed methods, the antenna was placed on an infinite ungrounded dielectric slab. The antenna was investigated in the transmission and reception modes, and the UWB performance of the antenna was evaluated. It was shown that the methods introduced in our study are promising tools for analyzing UWB structures mounted on multilayered substrates.

In Chapter 5, previous work on a different subject was presented for completeness. Specifically, the input admittance of the prolate-spheroidal monopole antenna fed by a coaxial transmission line through an image plane was derived using the TEM approximation on the coaxial aperture. The resulting series for the input admittance was seen to be slowly convergent, so a special numerical procedure for calculating the series was introduced to achieve high accuracy and computational efficiency. The input admittance of a prolate-spheroidal monopole with practical dimensions was measured and compared to the theory. Comparisons were also made between the theory and previous MoM results. Both comparisons showed very good agreement.

APPENDIX A

TIME-DOMAIN RADIATED ELECTRIC FIELD IN A MULTILAYERED MEDIUM

In this Appendix, we will derive the relations in Sec. 2.2 between the radiated electric field in the upper half space and the time-domain surface currents $\boldsymbol{\mathcal{J}}_t, \boldsymbol{\mathcal{M}}_t$ in Fig. 6. The results will be presented for a more general setting, where an arbitrary volumetric current distribution $\boldsymbol{\mathcal{J}}, \boldsymbol{\mathcal{M}}$ is present. The specialization to surface currents $\boldsymbol{\mathcal{J}}_t, \boldsymbol{\mathcal{M}}_t$ is then trivial.

Let us first consider the frequency-domain counterpart of Fig. 6, in which localized sources $\boldsymbol{J}(\boldsymbol{r}'), \boldsymbol{M}(\boldsymbol{r}')$ radiate in a lossless multilayered medium. Let $z = z_0$ be any plane above the localized sources. In the subsequent analysis, we will use the *plane-wave spectrum* on this plane to derive the radiated electric field. The 2-D Fourier transform $\boldsymbol{\rho} = (x, y) \rightarrow \boldsymbol{k}_{\boldsymbol{\rho}} = (k_x, k_y)$ (or the *spectral decomposition*) of the electric field in the $z = z_0$ plane is denoted as

$$\widetilde{\boldsymbol{E}}(k_x, k_y, z_0) = \widetilde{E}_x(k_x, k_y, z_0)\hat{\boldsymbol{x}} + \widetilde{E}_y(k_x, k_y, z_0)\hat{\boldsymbol{y}} + \widetilde{E}_z(k_x, k_y, z_0)\hat{\boldsymbol{z}} \ . \tag{239}$$

Without the $\hat{\boldsymbol{z}}$ component, (239) is commonly known as the *plane-wave spectrum* of the field. Using the invariance of the geometry in Fig. 6 in the xy plane, (239) can be expressed in terms of the *spectral superposition integral* [17]:

$$\widetilde{\boldsymbol{E}}(\boldsymbol{k}_{\boldsymbol{\rho}}, z_0) = \int_{-\infty}^{\infty} \widetilde{\overline{\boldsymbol{G}}}^{EJ}(\boldsymbol{k}_{\boldsymbol{\rho}}, z_0|\, z') \cdot \widetilde{\boldsymbol{J}}(\boldsymbol{k}_{\boldsymbol{\rho}}, z')dz' + \int_{-\infty}^{\infty} \widetilde{\overline{\boldsymbol{G}}}^{EM}(\boldsymbol{k}_{\boldsymbol{\rho}}, z_0|\, z') \cdot \widetilde{\boldsymbol{M}}(\boldsymbol{k}_{\boldsymbol{\rho}}, z')dz' \ , \tag{240}$$

in which $\widetilde{\boldsymbol{J}}(\boldsymbol{k}_{\boldsymbol{\rho}}, z')$, $\widetilde{\boldsymbol{M}}(\boldsymbol{k}_{\boldsymbol{\rho}}, z')$ are the spectral decompositions of the source currents $\boldsymbol{J}(\boldsymbol{r}')$, $\boldsymbol{M}(\boldsymbol{r}')$. In (240), $\widetilde{\overline{\boldsymbol{G}}}^{EJ,EM}(\boldsymbol{k}_{\boldsymbol{\rho}}, z|\, z')$ denote the *spectral dyadic Green functions*, given in Appendix B, (308)–(309). Substituting the 2-D Fourier integrals for $\widetilde{\boldsymbol{J}}(\boldsymbol{k}_{\boldsymbol{\rho}}, z')$ and $\widetilde{\boldsymbol{M}}(\boldsymbol{k}_{\boldsymbol{\rho}}, z')$ into

(240), we obtain

$$\begin{aligned}\widetilde{\boldsymbol{E}}(\boldsymbol{k_\rho}, z_0) = &\iiint_V \widetilde{\widetilde{\boldsymbol{G}}}^{EJ}(\boldsymbol{k_\rho}, z_0|\, z') \cdot \boldsymbol{J}(\boldsymbol{r'}) e^{j\boldsymbol{k_\rho}\cdot\boldsymbol{\rho'}} dV' \\ &+ \iiint_V \widetilde{\widetilde{\boldsymbol{G}}}^{EM}(\boldsymbol{k_\rho}, z_0|\, z') \cdot \boldsymbol{M}(\boldsymbol{r'}) e^{j\boldsymbol{k_\rho}\cdot\boldsymbol{\rho'}} dV' \ ,\end{aligned} \tag{241}$$

in which the volume V encloses all sources.

The key point in the derivation is that the electric field above the plane $z = z_0$ can be expressed *directly* in terms of the plane-wave spectrum (239) [1]. To this end, the plane-wave spectrum in (239) is inserted into the Fourier superposition integral [1, eq. (3.83a)]:

$$\begin{aligned}\boldsymbol{E}(\boldsymbol{r}) = \frac{1}{(2\pi)^2} \int_0^\infty \int_0^{2\pi} \Bigg\{ &\widetilde{E}_x(\boldsymbol{k_\rho}, z_0)\hat{\boldsymbol{x}} + \widetilde{E}_y(\boldsymbol{k_\rho}, z_0)\hat{\boldsymbol{y}} \\ - \left(\frac{k_\rho}{k_z}\right) &\left[\widetilde{E}_x(\boldsymbol{k_\rho}, z_0)\cos v + \widetilde{E}_y(\boldsymbol{k_\rho}, z_0)\sin v\right]\hat{\boldsymbol{z}} \Bigg\} \cdot e^{-j(k_\rho \rho \cos(v-\phi) + k_z(z-z_0))} dv\, dk_\rho \ ,\end{aligned} \tag{242}$$

in which $\rho = (x^2 + y^2)^{1/2}$, and $k_z = (k_0^2 - k_\rho^2)^{1/2}$, $\mathrm{Im}(k_z) < 0$. The resulting field in (242) satisfies Maxwell's equations in the region $z > z_0$ and the boundary condition on the plane $z = z_0$, hence is the unique solution for the electric field. There are, however, several analytical details that require attention in this formulation. Since the entire space is lossless, the multilayered medium may support eigenmodes that are *not* absolutely integrable (e.g. surface waves decaying as $\rho^{-1/2}$, plane waves decaying as r^{-1}), hence, the conventional 2-D Fourier transform for real k_x, k_y does not exist. For this reason, the integration along the real k_ρ axis in (242) is not valid. To circumvent this problem without abandoning the conventional 2-D Fourier transform, it usually assumed that there is a vanishingly small loss in the uppermost half space, so that all the eigenmodes of the multilayered medium decay exponentially in all directions. This ensures absolute integrability, and the existence of the conventional 2-D Fourier transform pair [99].

The radiated electric field in the uppermost half space can be obtained by asymptotic evaluation of the integral in (242) for $r \to \infty$. Substituting (241) into (242) and evaluating the v integral, we obtain Bessel functions with varying order n. The remaining semi-infinite integral for k_ρ is then converted to an infinite integral by the use of Hankel functions [99]. The steepest-descent method [13, 99] can then be applied to the infinite k_ρ integral by deforming the path of integration to the steepest-descent path passing from the saddle

point $k_\rho = k_0 \sin\theta$. For large enough $k_0 r$, the contribution from the vicinity of the saddle-point dominates the field in every direction [13]. We therefore neglect the contributions from the singularities in the k_ρ plane (which result in surface waves), and consider only the saddle-point contribution. In this case, it is unnecessary to carry out the cumbersome procedure detailed above; we instead apply the simple *stationary-phase* argument directly to the double integral (242) [1, Sec. 3.6.2]. The radiated electric field obtained by this method is given by

$$\begin{aligned} \boldsymbol{E}^{\boldsymbol{r}}(\boldsymbol{r}) &= \frac{jk_0}{2\pi}\frac{e^{-jk_0 r}}{r} e^{jk_0 z_0 \cos\theta} \boldsymbol{F}(\theta,\phi) \\ &= \frac{jk_0}{2\pi}\frac{e^{-jk_0 r}}{r} e^{jk_0 z_0 \cos\theta} \left[F_\theta(\theta,\phi)\hat{\boldsymbol{\theta}} + F_\phi(\theta,\phi)\hat{\boldsymbol{\phi}} \right] \ , \end{aligned} \tag{243}$$

with

$$F_\theta(\theta,\phi) = (\hat{\boldsymbol{x}}\cos\phi + \hat{\boldsymbol{y}}\sin\phi)\cdot \widetilde{\boldsymbol{E}}(\alpha,\beta,z_0) \tag{244}$$

$$F_\phi(\theta,\phi) = (-\hat{\boldsymbol{x}}\sin\phi\cos\theta + \hat{\boldsymbol{y}}\cos\phi\cos\theta)\cdot \widetilde{\boldsymbol{E}}(\alpha,\beta,z_0) \ , \tag{245}$$

in which $k_0 = \omega/c$, $\alpha = k_0\cos\phi\sin\theta$, and $\beta = k_0\sin\phi\sin\theta$.

Taking the inverse temporal Fourier transform of (243) with (244)–(245) and (241), we obtain

$$\boldsymbol{\mathcal{E}}^r(\boldsymbol{r},t) = \frac{1}{2\pi c r}\frac{\partial}{\partial t}\left[\mathcal{F}_\theta\left(\theta,\phi,t-r/c\right)\hat{\boldsymbol{\theta}} + \mathcal{F}_\phi\left(\theta,\phi,t-r/c\right)\hat{\boldsymbol{\phi}} \right] \ , \tag{246}$$

with

$$\mathcal{F}_{\theta,\phi}(\theta,\phi) = \iiint_V \left[\boldsymbol{\mathcal{G}}^{EJ}_{\theta,\phi}(\theta,\phi,t|z') \odot \boldsymbol{\mathcal{J}}(\boldsymbol{r}',t) + \boldsymbol{\mathcal{G}}^{EM}_{\theta,\phi}(\theta,\phi,t|z') \odot \boldsymbol{\mathcal{M}}(\boldsymbol{r}',t) \right]_{t_r} dV' \ , \tag{247}$$

in which $t_r = t + (x'\cos\phi\sin\theta + y'\sin\phi\sin\theta)/c$ is the lateral retarded time, $\boldsymbol{\mathcal{J}}(\boldsymbol{r}',t)$, $\boldsymbol{\mathcal{M}}(\boldsymbol{r}',t)$ are the time domain source currents, and $\boldsymbol{\mathcal{G}}^{EJ,EM}_{\theta,\phi}(\theta,\phi,t|z')$ are the inverse temporal Fourier transforms of

$$e^{jk_0 z_0\cos\theta}\left(\hat{\boldsymbol{x}}\cos\phi + \hat{\boldsymbol{y}}\sin\phi\right)\cdot \widetilde{\overline{\boldsymbol{G}}}^{EJ,EM}(\alpha,\beta,z_0|\,z') \tag{248}$$

and

$$e^{jk_0 z_0\cos\theta}\left(-\hat{\boldsymbol{x}}\sin\phi\cos\theta + \hat{\boldsymbol{y}}\cos\phi\cos\theta\right)\cdot \widetilde{\overline{\boldsymbol{G}}}^{EJ,EM}(\alpha,\beta,z_0|\,z') \ , \tag{249}$$

respectively. Substituting $\boldsymbol{k_\rho} = (k_x, k_y) = (\alpha, \beta)$ into (308)–(309) in Appendix B, applying the dot product in (248)–(249), and finally taking the inverse temporal Fourier transform, we obtain the following expressions for $\boldsymbol{\mathcal{G}}_{\theta,\phi}^{EJ,EM}(\theta, \phi, t|z')$:

$$\boldsymbol{\mathcal{G}}_{\theta}^{EJ} = -\hat{\boldsymbol{x}}\mathcal{V}_i^e \cos\phi - \hat{\boldsymbol{y}}\mathcal{V}_i^e \sin\phi + \hat{\boldsymbol{z}} Z_0 \mathcal{V}_v^e \sin\theta/\epsilon_r' \tag{250}$$

$$\boldsymbol{\mathcal{G}}_{\theta}^{EM} = \hat{\boldsymbol{x}}\mathcal{V}_v^e \sin\phi - \hat{\boldsymbol{y}}\mathcal{V}_v^e \cos\phi \tag{251}$$

$$\boldsymbol{\mathcal{G}}_{\phi}^{EJ} = \hat{\boldsymbol{x}}\mathcal{V}_i^h \sin\phi\cos\theta - \hat{\boldsymbol{y}}\mathcal{V}_i^h \cos\phi\cos\theta \tag{252}$$

$$\boldsymbol{\mathcal{G}}_{\phi}^{EM} = \hat{\boldsymbol{x}}\mathcal{V}_v^h \cos\phi\cos\theta + \hat{\boldsymbol{y}}\mathcal{V}_v^h \sin\phi\cos\theta - \hat{\boldsymbol{z}} Y_0 \mathcal{V}_i^h \sin\theta\cos\theta \ . \tag{253}$$

Here, ϵ_r' denotes the relative permittivity at the source point, $Z_0 = 1/Y_0 = \sqrt{\mu_0/\epsilon_0}$ is the wave impedance of free space. The functions $\mathcal{V}_v^p(t|\,z')$, $\mathcal{V}_i^p(t|\,z')$ in (250)–(253) are given by

$$\mathcal{V}_v^p(t|\,z') = \mathcal{V}_v^p(z_0, t + z_0\cos\theta/c|\,z') \tag{254}$$

$$\mathcal{V}_i^p(t|\,z') = \mathcal{V}_i^p(z_0, t + z_0\cos\theta/c|\,z') \ , \tag{255}$$

in which $\mathcal{V}_v^p(z_0, t|\,z')$, $\mathcal{V}_i^p(z_0, t|\,z')$ are the *time-domain TL Green functions* for the source coordinates $(z, t) = (z', 0)$ and observation coordinates $(z, t) = (z_0, t)$. These TL Green functions are the basic solutions of the transmission-line equations in Appendix B, (285)–(288), after substitution of $\boldsymbol{k_\rho} = (k_x, k_y) = (\alpha, \beta)$ and inversion to time domain:

$$\begin{aligned} \frac{\partial \mathcal{V}^e}{\partial z} &= -\left[\frac{\mu_0(\epsilon_r - \sin^2\theta)}{\epsilon_r}\right]\frac{\partial \mathcal{I}^e}{\partial t} \\ \frac{\partial \mathcal{I}^e}{\partial z} &= -\Big[\epsilon_0\epsilon_r\Big]\frac{\partial \mathcal{V}^e}{\partial t} \end{aligned} \qquad \text{(TM)} \tag{256}$$

$$\begin{aligned} \frac{\partial \mathcal{V}^h}{\partial z} &= -\Big[\mu_0\Big]\frac{\partial \mathcal{I}^h}{\partial t} \\ \frac{\partial \mathcal{I}^h}{\partial z} &= -\Big[\epsilon_0(\epsilon_r - \sin^2\theta)\Big]\frac{\partial \mathcal{V}^h}{\partial t} \end{aligned} \qquad \text{(TE)} \ . \tag{257}$$

The propagation constants k^p and the characteristic impedances Z^p of these transmission lines are given by Appendix B, (289)–(291) with the same changes as above:

$$k^p = k_0\sqrt{\epsilon_r - \sin^2\theta} \tag{258}$$

$$Z^e = \frac{1}{Y^e} = Z_0\sqrt{\epsilon_r - \sin^2\theta}/\epsilon_r \tag{259}$$

$$Z^h = \frac{1}{Y^h} = Z_0/\sqrt{\epsilon_r - \sin^2\theta} \ . \tag{260}$$

The transmission-line Green function $\mathcal{V}_v^p(z_0,t|\,z')/\mathcal{V}_i^p(z_0,t|\,z')$ is defined as the voltage induced in the transmission line defined by (256) or (257) at the observation point z_0 at time t, created by an impulsive voltage/current at source point z' at time $t=0$. Since the propagation constant k^p in (258) is seen to be proportional to the frequency ω, the transmission line is *non-dispersive*. Therefore, the impulsive voltage/current waves preserve their shape while propagating in the transmission line. In a general multilayered medium, these impulsive traveling waves eventually encounter one or more *material interfaces* between different media. At these interfaces, the incoming impulsive waves will split into *transmitted* and *reflected* waves, which also have the shape of an impulse due to the frequency-independence of the characteristic impedances Z^p in (259)–(260). The propagation and reflection/transmission mechanism of impulsive waves lies at the heart of the near-field-to-far-field transform described in Chapter 2, and is explained more detail in Section 2.2.

If the TL Green functions $\mathcal{V}_v^p(z_0,t|\,z')$,$\mathcal{V}_i^p(z_0,t|\,z')$ pertinent to the geometry are known, the functions $\mathcal{V}_v^p(t|\,z')$, $\mathcal{V}_i^p(t|\,z')$ in (250)–(253) are obtained by a simple delaying operation as in (254)–(255). Note the cancelation of the z_0-dependence of $\mathcal{V}_v^p(z_0,t|\,z')$, $\mathcal{V}_i^p(z_0,t|\,z')$ by the time-advance $z_0\cos\theta/c$, which is expected since the choice of z_0 is practically arbitrary. It is seen from the detailed analysis in Section 2.2 that this is indeed the case for general multilayered media.

APPENDIX B

SPECTRAL DYADIC GREEN FUNCTIONS FOR PLANAR MULTILAYERED MEDIA

In this Appendix, we will derive the frequency-domain spectral dyadic Green functions for planar multilayered media. These functions constitute the basis of the near-field-to-far-field transformer (NFFFT) for general multilayered media.

First, we define the 2-D Fourier transform pair $f(x,y) \longleftrightarrow \widetilde{f}(k_x,k_y)$ as follows:

$$\widetilde{f}(k_x,k_y) = \iint_{-\infty}^{\infty} f(x,y) e^{j(k_x x + k_y y)} dxdy \tag{261}$$

$$f(x,y) = \frac{1}{(2\pi)^2} \iint_{-\infty}^{\infty} \widetilde{f}(k_x,k_y) e^{-j(k_x x + k_y y)} dk_x dk_y \ . \tag{262}$$

Let $f(x,y,z)$ denote a scalar field, or a component of a vector field. The *spectral decomposition* of the field in the x-y plane is defined by the following 2-D Fourier transform:

$$\begin{aligned} \widetilde{f}(k_x,k_y,z) = \widetilde{f}(\boldsymbol{k}_\rho,z) &= \iint_{-\infty}^{\infty} f(x,y,z) e^{j(k_x x + k_y y)} dxdy \\ &= \iint_{-\infty}^{\infty} f(\boldsymbol{\rho},z) e^{j\boldsymbol{k}_\rho \cdot \boldsymbol{\rho}} dxdy \ , \end{aligned} \tag{263}$$

in which

$$\boldsymbol{\rho} = x\,\hat{\boldsymbol{x}} + y\,\hat{\boldsymbol{y}} \tag{264}$$

$$\boldsymbol{k_\rho} = k_x\,\hat{\boldsymbol{x}} + k_y\,\hat{\boldsymbol{y}} \ . \tag{265}$$

The Maxwell curl equations for $e^{j\omega t}$ dependence are

$$\nabla \times \boldsymbol{E} = -j\omega\mu\boldsymbol{H} - \boldsymbol{M} \tag{266}$$

$$\nabla \times \boldsymbol{H} = j\omega\epsilon\boldsymbol{E} + \boldsymbol{J} \ . \tag{267}$$

The electric and magnetic fields can be written as superposition integrals involving the

electric and magnetic source currents:

$$\begin{aligned}\boldsymbol{E}(\boldsymbol{r}) &= \iiint_{-\infty}^{\infty} \bar{\boldsymbol{G}}^{EJ}(\boldsymbol{r}|\,\boldsymbol{r}') \cdot \boldsymbol{J}(\boldsymbol{r}')dV \\ &\quad + \iiint_{-\infty}^{\infty} \bar{\boldsymbol{G}}^{EM}(\boldsymbol{r}|\,\boldsymbol{r}') \cdot \boldsymbol{M}(\boldsymbol{r}')dV \end{aligned} \tag{268}$$

$$\begin{aligned}\boldsymbol{H}(\boldsymbol{r}) &= \iiint_{-\infty}^{\infty} \bar{\boldsymbol{G}}^{HJ}(\boldsymbol{r}|\,\boldsymbol{r}') \cdot \boldsymbol{J}(\boldsymbol{r}')dV \\ &\quad + \iiint_{-\infty}^{\infty} \bar{\boldsymbol{G}}^{HM}(\boldsymbol{r}|\,\boldsymbol{r}') \cdot \boldsymbol{M}(\boldsymbol{r}')dV \ , \end{aligned} \tag{269}$$

in which $\bar{\boldsymbol{G}}^{EJ,EM,HJ,HM}(\boldsymbol{r}|\,\boldsymbol{r}')$ are the *dyadic Green functions* [13]. Since the planar multilayered geometry is invariant in the x-y plane, i.e., the material properties depend only on z, the dyadic Green functions assume a $\boldsymbol{\rho} - \boldsymbol{\rho}'$ dependence:

$$\begin{aligned}\boldsymbol{E}(\boldsymbol{r}) &= \iiint_{-\infty}^{\infty} \bar{\boldsymbol{G}}^{EJ}(\boldsymbol{\rho} - \boldsymbol{\rho}', z|\,z') \cdot \boldsymbol{J}(\boldsymbol{\rho}', z')dV \\ &\quad + \iiint_{-\infty}^{\infty} \bar{\boldsymbol{G}}^{EM}(\boldsymbol{\rho} - \boldsymbol{\rho}', z|\,z') \cdot \boldsymbol{M}(\boldsymbol{\rho}', z')dV \end{aligned} \tag{270}$$

$$\begin{aligned}\boldsymbol{H}(\boldsymbol{r}) &= \iiint_{-\infty}^{\infty} \bar{\boldsymbol{G}}^{HJ}(\boldsymbol{\rho} - \boldsymbol{\rho}', z|\,z') \cdot \boldsymbol{J}(\boldsymbol{\rho}', z')dV \\ &\quad + \iiint_{-\infty}^{\infty} \bar{\boldsymbol{G}}^{HM}(\boldsymbol{\rho} - \boldsymbol{\rho}', z|\,z') \cdot \boldsymbol{M}(\boldsymbol{\rho}', z')dV. \end{aligned} \tag{271}$$

Applying the spectral decomposition in (263) to both sides of (270) and (271) and using the spatial convolution property of the 2-D Fourier transform, the following spectral superposition integral is obtained:

$$\begin{aligned}\widetilde{\boldsymbol{E}}(\boldsymbol{k}_{\boldsymbol{\rho}}, z) &= \int_{-\infty}^{\infty} \widetilde{\bar{\boldsymbol{G}}}^{EJ}(\boldsymbol{k}_{\boldsymbol{\rho}}, z|\,z') \cdot \widetilde{\boldsymbol{J}}(\boldsymbol{k}_{\boldsymbol{\rho}}, z')dz' \\ &\quad + \int_{-\infty}^{\infty} \widetilde{\bar{\boldsymbol{G}}}^{EM}(\boldsymbol{k}_{\boldsymbol{\rho}}, z|\,z') \cdot \widetilde{\boldsymbol{M}}(\boldsymbol{k}_{\boldsymbol{\rho}}, z')dz' \end{aligned} \tag{272}$$

$$\begin{aligned}\widetilde{\boldsymbol{H}}(\boldsymbol{k}_{\boldsymbol{\rho}}, z) &= \int_{-\infty}^{\infty} \widetilde{\bar{\boldsymbol{G}}}^{HJ}(\boldsymbol{k}_{\boldsymbol{\rho}}, z|\,z') \cdot \widetilde{\boldsymbol{J}}(\boldsymbol{k}_{\boldsymbol{\rho}}, z')dz' \\ &\quad + \int_{-\infty}^{\infty} \widetilde{\bar{\boldsymbol{G}}}^{HM}(\boldsymbol{k}_{\boldsymbol{\rho}}, z|\,z') \cdot \widetilde{\boldsymbol{M}}(\boldsymbol{k}_{\boldsymbol{\rho}}, z')dz' \ , \end{aligned} \tag{273}$$

in which $\widetilde{\bar{\boldsymbol{G}}}^{EJ,EM,HJ,HM}(\boldsymbol{k}_{\boldsymbol{\rho}}, z|\,z')$ are the *spectral dyadic Green functions*, which are the spectral decompositions of the dyadic Green functions in (268) and (269). Similarly, $\widetilde{\boldsymbol{J}}(\boldsymbol{k}_{\boldsymbol{\rho}}, z')$ and $\widetilde{\boldsymbol{M}}(\boldsymbol{k}_{\boldsymbol{\rho}}, z')$ are the spectral decompositions of the source currents $\boldsymbol{J}(\boldsymbol{r}')$ and $\boldsymbol{M}(\boldsymbol{r}')$. In this Appendix, we derive the spectral dyadic Green functions in (272) and (273),

following the steps in [17] and using identical notation. Although the spectral Green functions obtained in [17] are later inverse transformed back to spatial domain for use in integral transforms, we will find that the radiated fields in a multilayered medium can be obtained *directly* from the spectral dyadic Green functions, without any need for inversion to spatial domain.

We first apply the spectral decomposition in (263) to both sides of (266) and (267) to obtain the following equations [17]:

$$\frac{\partial \widetilde{\boldsymbol{E}}_t}{\partial z} = \frac{1}{j\omega\epsilon}(k^2 - \boldsymbol{k_\rho k_\rho}\cdot)(\widetilde{\boldsymbol{H}}_t \times \hat{\boldsymbol{z}}) + \boldsymbol{k_\rho}\frac{\widetilde{J}_z}{\omega\epsilon} - (\widetilde{\boldsymbol{M}}_t \times \hat{\boldsymbol{z}}) \tag{274}$$

$$\frac{\partial \widetilde{\boldsymbol{H}}_t}{\partial z} = \frac{1}{j\omega\mu}(k^2 - \boldsymbol{k_\rho k_\rho}\cdot)(\hat{\boldsymbol{z}} \times \widetilde{\boldsymbol{E}}_t) + \boldsymbol{k_\rho}\frac{\widetilde{M}_z}{\omega\mu} - (\hat{\boldsymbol{z}} \times \widetilde{\boldsymbol{J}}_t) \tag{275}$$

$$-j\omega\epsilon\widetilde{E}_z = j\boldsymbol{k_\rho}\cdot(\widetilde{\boldsymbol{H}}_t \times \hat{\boldsymbol{z}}) + \widetilde{J}_z \tag{276}$$

$$-j\omega\mu\widetilde{H}_z = j\boldsymbol{k_\rho}\cdot(\hat{\boldsymbol{z}} \times \widetilde{\boldsymbol{E}}_t) + \widetilde{M}_z \ , \tag{277}$$

in which the "$\sim$" sign above a field or source variable denotes the spectral decomposition of that variable, and the tangential and axial components of a field or source vector is defined as

$$\widetilde{\boldsymbol{F}} = \widetilde{\boldsymbol{F}}_t + \widetilde{F}_z\hat{\boldsymbol{z}} \ . \tag{278}$$

We will find it more convenient to switch from cartesian coordinates (k_x, k_y) to radial coordinates (u, v), where

$$k_x = u\cos v \tag{279}$$

$$k_y = u\sin v \tag{280}$$

$$\hat{\boldsymbol{u}} = \cos v\,\hat{\boldsymbol{x}} + \sin v\,\hat{\boldsymbol{y}} = \boldsymbol{k_\rho}/u \tag{281}$$

$$\hat{\boldsymbol{v}} = -\sin v\,\hat{\boldsymbol{x}} + \cos v\,\hat{\boldsymbol{y}} = \hat{\boldsymbol{z}} \times \hat{\boldsymbol{u}} \ . \tag{282}$$

If we let

$$\widetilde{\boldsymbol{E}}_t = \hat{\boldsymbol{u}}\,V^e + \hat{\boldsymbol{v}}\,V^h \tag{283}$$

$$\widetilde{\boldsymbol{H}}_t \times \hat{\boldsymbol{z}} = \hat{\boldsymbol{u}}\,I^e + \hat{\boldsymbol{v}}\,I^h \ , \tag{284}$$

and project (274) and (275) on $\hat{\boldsymbol{u}}$ and $\hat{\boldsymbol{v}}$, we obtain

$$\frac{\partial V^e}{\partial z} = -jk^e Z^e I^e + v^e \tag{285}$$

$$\frac{\partial I^e}{\partial z} = -jk^e Y^e V^e + i^e \ , \tag{286}$$

and

$$\frac{\partial V^h}{\partial z} = -jk^h Z^h I^h + v^h \tag{287}$$

$$\frac{\partial I^h}{\partial z} = -jk^h Y^h V^h + i^h \ , \tag{288}$$

in which the wavenumbers k^p and the TL impedances Z^p are given by (superscript p denoting e or h)

$$k^p = \sqrt{k_0^2 - k_\rho^2} \tag{289}$$

$$Z^e = \frac{1}{Y^e} = \frac{k^e}{\omega\epsilon_0\epsilon_r} \tag{290}$$

$$Z^h = \frac{1}{Y^h} = \frac{\omega\mu_0}{k^h} \ , \tag{291}$$

and the source terms are

$$v^e = \frac{k_\rho}{\omega\epsilon}\widetilde{J}_z - \widetilde{M}_v \qquad\qquad i^e = -\widetilde{J}_u \tag{292}$$

$$v^h = \widetilde{M}_u \qquad\qquad i^h = -\frac{k_\rho}{\omega\mu}\widetilde{M}_z - \widetilde{J}_v \ . \tag{293}$$

Now, from (283)–(284) and (276)–(277), the spectral fields can be expressed as

$$\widetilde{\boldsymbol{E}} = \widetilde{\boldsymbol{E}}_t + \widetilde{E}_z\hat{\boldsymbol{z}} = \hat{\boldsymbol{u}}\, V^e + \hat{\boldsymbol{v}}\, V^h - \hat{\boldsymbol{z}}\frac{1}{j\omega\epsilon}(jk_\rho I^e + \widetilde{J}_z) \tag{294}$$

$$\widetilde{\boldsymbol{H}} = \widetilde{\boldsymbol{H}}_t + \widetilde{H}_z\hat{\boldsymbol{z}} = -\hat{\boldsymbol{u}}\, I^h + \hat{\boldsymbol{v}}\, I^e + \hat{\boldsymbol{z}}\frac{1}{j\omega\mu}(jk_\rho V^h - \widetilde{M}_z) \ . \tag{295}$$

As is evident from (294) and (295), the superscripts e and h denote the TM and TE variables (with respect to z), respectively. The equations (285)–(288) are *transmission line* (TL) equations for voltage-current pairs (V^e, I^e) and (V^h, I^h) , with distributed voltage and current sources v^e, i^e, v^h, i^h, which are expressed in terms of electric and magnetic currents in (292) and (293). The TL voltage and currents V^e, I^e, V^h, I^h are linked to the spectral tangential field quantities $\widetilde{\boldsymbol{E}}_t, \widetilde{\boldsymbol{H}}_t$ via (283) and (284). Since the spectral axial field

quantities $\widetilde{E}_z, \widetilde{H}_z$ can be derived from the spectral tangential field quantities $\widetilde{\boldsymbol{E}}_t, \widetilde{\boldsymbol{H}}_t$ via (276) and (277), the TL equations (285)–(288) completely specify the relation between the spectral field quantities $\widetilde{\boldsymbol{E}}, \widetilde{\boldsymbol{H}}$ and the spectral sources $\widetilde{\boldsymbol{J}}, \widetilde{\boldsymbol{M}}$.

Thus, the vector problem in (274) and (275) has been reduced to the scalar TL problems in (285)–(288), the solutions of which are well documented in the literature. The Green functions associated with these TL problems are the voltages and currents at z due to unit impulsive voltages and currents at z'. Since there are 4 combinations involved, and two different TL's corresponding to the TM and TE pairs (V^e, I^e) and (V^h, I^h), we have a total of 8 TL Green functions (superscript p denoting e or h):

$$V_v^p(z|\, z') : \text{voltage at } z \text{ due to unit series voltage at } z' \tag{296}$$

$$V_i^p(z|\, z') : \text{voltage at } z \text{ due to unit shunt current at } z' \tag{297}$$

$$I_v^p(z|\, z') : \text{current at } z \text{ due to unit series voltage at } z' \tag{298}$$

$$I_i^p(z|\, z') : \text{current at } z \text{ due to unit shunt current at } z' \ . \tag{299}$$

The $\boldsymbol{k_\rho}$ dependence of the TL Green functions $V_v^p, I_v^p, V_i^p, I_i^p$ are not shown explicitly. From the linearity of the TL equations (285)–(288), the TL voltages and currents are obtained from superposition:

$$V^p = < V_v^p; v^p > + < V_i^p; i^p > \tag{300}$$

$$I^p = < I_v^p; v^p > + < I_i^p; i^p > \ , \tag{301}$$

in which the angle bracket denotes integration of the product of its parameters with respect to z'. Substituting (300) and (301) into (294) and (295), we obtain

$$\begin{aligned}\widetilde{\boldsymbol{E}} = \hat{\boldsymbol{u}} \left(< V_i^e; -\widetilde{J}_u > + < V_v^e; \frac{k_\rho}{\omega\epsilon'} \widetilde{J}_z - \widetilde{M}_v > \right) \\ + \hat{\boldsymbol{v}} \left(< V_i^h; \frac{-k_\rho}{\omega\mu'} \widetilde{M}_z - \widetilde{J}_v > + < V_v^h; \widetilde{M}_u > \right) - \hat{\boldsymbol{z}} \frac{1}{j\omega\epsilon} \\ \cdot \left(jk_\rho \left(< I_i^e; -\widetilde{J}_u > + < I_v^e; \frac{k_\rho}{\omega\epsilon'} \widetilde{J}_z - \widetilde{M}_v > \right) + \widetilde{J}_z \right)\end{aligned} \tag{302}$$

$$\widetilde{\boldsymbol{H}} = -\hat{\boldsymbol{u}}\left(< I_i^h; \frac{-k_\rho}{\omega\mu'}\widetilde{M}_z - \widetilde{J}_v > + < I_v^h; \widetilde{M}_u >\right) + \hat{\boldsymbol{v}}\left(< I_i^e; -\widetilde{J}_u > + < I_v^e; \frac{k_\rho}{\omega\epsilon'}\widetilde{J}_z - \widetilde{M}_v >\right) + \hat{\boldsymbol{z}}\frac{1}{j\omega\mu} \cdot \left(jk_\rho\left(< V_i^h; \frac{-k_\rho}{\omega\mu'}\widetilde{M}_z - \widetilde{J}_v > + < V_v^h; \widetilde{M}_u >\right) - \widetilde{M}_z\right) . \quad (303)$$

Comparing (272)–(273) and (302)–(303), the spectral dyadic Green functions can be written as [17]

$$\begin{aligned}\widetilde{\bar{\boldsymbol{G}}}^{EJ} &= -\hat{\boldsymbol{u}}\hat{\boldsymbol{u}}V_i^e - \hat{\boldsymbol{v}}\hat{\boldsymbol{v}}V_i^h + \hat{\boldsymbol{z}}\hat{\boldsymbol{u}}\frac{k_\rho}{\omega\epsilon}I_i^e \\ &\quad + \hat{\boldsymbol{u}}\hat{\boldsymbol{z}}\frac{k_\rho}{\omega\epsilon'}V_v^e + \hat{\boldsymbol{z}}\hat{\boldsymbol{z}}\frac{1}{j\omega\epsilon}\left[\frac{k_\rho^2}{j\omega\epsilon'}I_v^e - \delta(z-z')\right] \end{aligned} \quad (304)$$

$$\widetilde{\bar{\boldsymbol{G}}}^{EM} = -\hat{\boldsymbol{u}}\hat{\boldsymbol{v}}V_v^e + \hat{\boldsymbol{v}}\hat{\boldsymbol{u}}V_v^h + \hat{\boldsymbol{z}}\hat{\boldsymbol{v}}\frac{k_\rho}{\omega\epsilon}I_v^e - \hat{\boldsymbol{v}}\hat{\boldsymbol{z}}\frac{k_\rho}{\omega\mu'}V_i^h \quad (305)$$

$$\widetilde{\bar{\boldsymbol{G}}}^{HJ} = \hat{\boldsymbol{u}}\hat{\boldsymbol{v}}I_i^h - \hat{\boldsymbol{v}}\hat{\boldsymbol{u}}I_i^e - \hat{\boldsymbol{z}}\hat{\boldsymbol{v}}\frac{k_\rho}{\omega\mu}V_i^h + \hat{\boldsymbol{v}}\hat{\boldsymbol{z}}\frac{k_\rho}{\omega\epsilon'}I_v^e \quad (306)$$

$$\begin{aligned}\widetilde{\bar{\boldsymbol{G}}}^{HM} &= -\hat{\boldsymbol{u}}\hat{\boldsymbol{u}}I_v^h - \hat{\boldsymbol{v}}\hat{\boldsymbol{v}}I_v^e + \hat{\boldsymbol{z}}\hat{\boldsymbol{u}}\frac{k_\rho}{\omega\mu}V_v^h \\ &\quad + \hat{\boldsymbol{u}}\hat{\boldsymbol{z}}\frac{k_\rho}{\omega\mu'}I_i^h + \hat{\boldsymbol{z}}\hat{\boldsymbol{z}}\frac{1}{j\omega\mu}\left[\frac{k_\rho^2}{j\omega\mu'}V_i^h - \delta(z-z')\right] . \end{aligned} \quad (307)$$

Converting from radial unit vectors $(\hat{\boldsymbol{u}}, \hat{\boldsymbol{v}})$ to cartesian unit vectors $(\hat{\boldsymbol{x}}, \hat{\boldsymbol{y}})$ using (281) and (282), the spectral dyadic functions in (304)–(307) become

$$\begin{aligned}\widetilde{\bar{\boldsymbol{G}}}^{EJ} &= \hat{\boldsymbol{x}}\hat{\boldsymbol{x}}\left(-V_i^e\cos^2 v - V_i^h\sin^2 v\right) + \hat{\boldsymbol{y}}\hat{\boldsymbol{y}}\left(-V_i^e\sin^2 v - V_i^h\cos^2 v\right) \\ &\quad + \hat{\boldsymbol{x}}\hat{\boldsymbol{y}}\left(-V_i^e + V_i^h\right)\sin v\cos v + \hat{\boldsymbol{y}}\hat{\boldsymbol{x}}\left(-V_i^e + V_i^h\right)\sin v\cos v \\ &\quad + \hat{\boldsymbol{z}}\hat{\boldsymbol{z}}\frac{1}{j\omega\epsilon}\left[\frac{k_\rho^2}{j\omega\epsilon'}I_v^e - \delta(z-z')\right] + \hat{\boldsymbol{z}}\hat{\boldsymbol{x}}\left(\frac{k_\rho}{\omega\epsilon}I_i^e\cos v\right) \\ &\quad + \hat{\boldsymbol{z}}\hat{\boldsymbol{y}}\left(\frac{k_\rho}{\omega\epsilon}I_i^e\sin v\right) + \hat{\boldsymbol{x}}\hat{\boldsymbol{z}}\left(\frac{k_\rho}{\omega\epsilon'}V_v^e\cos v\right) + \hat{\boldsymbol{y}}\hat{\boldsymbol{z}}\left(\frac{k_\rho}{\omega\epsilon'}V_v^e\sin v\right) \end{aligned} \quad (308)$$

$$\begin{aligned}\widetilde{\bar{\boldsymbol{G}}}^{EM} &= \hat{\boldsymbol{x}}\hat{\boldsymbol{x}}\left(V_v^e - V_v^h\right)\sin v\cos v + \hat{\boldsymbol{y}}\hat{\boldsymbol{y}}\left(-V_v^e + V_v^h\right)\sin v\cos v \\ &\quad + \hat{\boldsymbol{x}}\hat{\boldsymbol{y}}\left(-V_v^e\cos^2 v - V_v^h\sin^2 v\right) + \hat{\boldsymbol{y}}\hat{\boldsymbol{x}}\left(V_v^e\sin^2 v + V_v^h\cos^2 v\right) \\ &\quad + \hat{\boldsymbol{z}}\hat{\boldsymbol{x}}\left(\frac{-k_\rho}{\omega\epsilon}I_v^e\sin v\right) + \hat{\boldsymbol{z}}\hat{\boldsymbol{y}}\left(\frac{k_\rho}{\omega\epsilon}I_v^e\cos v\right) \\ &\quad + \hat{\boldsymbol{x}}\hat{\boldsymbol{z}}\left(\frac{k_\rho}{\omega\mu'}V_i^h\sin v\right) + \hat{\boldsymbol{y}}\hat{\boldsymbol{z}}\left(\frac{-k_\rho}{\omega\mu'}V_i^h\cos v\right) \end{aligned} \quad (309)$$

$$\widetilde{\widetilde{\boldsymbol{G}}}^{HJ} = \hat{\boldsymbol{x}}\hat{\boldsymbol{x}}\left(-I_i^h + I_i^e\right)\sin v\cos v + \hat{\boldsymbol{y}}\hat{\boldsymbol{y}}\left(I_i^h - I_i^e\right)\sin v\cos v$$
$$+ \hat{\boldsymbol{x}}\hat{\boldsymbol{y}}\left(I_i^h\cos^2 v + I_i^e\sin^2 v\right) + \hat{\boldsymbol{y}}\hat{\boldsymbol{x}}\left(-I_i^h\sin^2 v - I_i^e\cos^2 v\right)$$
$$+ \hat{\boldsymbol{z}}\hat{\boldsymbol{x}}\left(\frac{k_\rho}{\omega\mu}V_i^h\sin v\right) + \hat{\boldsymbol{z}}\hat{\boldsymbol{y}}\left(\frac{-k_\rho}{\omega\mu}V_i^h\cos v\right)$$
$$+ \hat{\boldsymbol{x}}\hat{\boldsymbol{z}}\left(\frac{-k_\rho}{\omega\epsilon'}I_v^e\sin v\right) + \hat{\boldsymbol{y}}\hat{\boldsymbol{z}}\left(\frac{k_\rho}{\omega\epsilon'}I_v^e\cos v\right) \quad (310)$$

$$\widetilde{\widetilde{\boldsymbol{G}}}^{HM} = \hat{\boldsymbol{x}}\hat{\boldsymbol{x}}\left(-I_v^h\cos^2 v - I_v^e\sin^2 v\right)$$
$$+ \hat{\boldsymbol{y}}\hat{\boldsymbol{y}}\left(-I_v^h\sin^2 v - I_v^e\cos^2 v\right) + \hat{\boldsymbol{x}}\hat{\boldsymbol{y}}\left(-I_v^h + I_v^e\right)\sin v\cos v$$
$$+ \hat{\boldsymbol{y}}\hat{\boldsymbol{x}}\left(-I_v^h + I_v^e\right)\sin v\cos v + \hat{\boldsymbol{z}}\hat{\boldsymbol{z}}\frac{1}{j\omega\mu}\left[\frac{k_\rho^2}{j\omega\mu'}V_i^h - \delta(z-z')\right]$$
$$+ \hat{\boldsymbol{z}}\hat{\boldsymbol{x}}\left(\frac{k_\rho}{\omega\mu}V_v^h\cos v\right) + \hat{\boldsymbol{z}}\hat{\boldsymbol{y}}\left(\frac{k_\rho}{\omega\mu}V_v^h\sin v\right)$$
$$+ \hat{\boldsymbol{x}}\hat{\boldsymbol{z}}\left(\frac{k_\rho}{\omega\mu'}I_i^h\cos v\right) + \hat{\boldsymbol{y}}\hat{\boldsymbol{z}}\left(\frac{k_\rho}{\omega\mu'}I_i^h\sin v\right) \quad (311)$$

We now have the desired result; the spectral dyadic Green functions $\widetilde{\widetilde{\boldsymbol{G}}}^{EJ,EM,HJ,HM}(\boldsymbol{k_\rho}, z|\, z')$ are given by equations (308)–(311).

APPENDIX C

TRANSMISSION-LINE EQUATIONS FOR PLANE-WAVE INCIDENCE ON A LOSSLESS MULTILAYERED MEDIUM

In this Appendix, we present a direct time-domain derivation of the transmission-line equations (101)–(102) arising in the plane-wave incidence on a lossless multilayered medium.

We start with the observation made in the discussion preceding (101)–(102), namely, that the component of the phase velocity tangential to the interface (x component) must be the same at every interface in the multilayered structure. This velocity is equal to $v_x = c_0/\sin\theta$, where c_0 is the speed of light in the lossless uppermost medium ($n = 0$) and θ is the angle between $\hat{\boldsymbol{k}}_i$ and $\hat{\boldsymbol{z}}$ in Fig. 19. This is actually the defining property of a plane wave, which is nothing more than a radiating mode of a multilayered structure in free space. With this relation, any component of the field can be expressed as

$$\begin{aligned} \mathcal{E}(z,\xi) \qquad \text{with} \qquad \xi &= t - \frac{x}{c_0/\sin\theta} \\ &= t - \frac{x\sin\theta}{c_0} \ . \end{aligned} \tag{312}$$

Therefore

$$\frac{\partial \mathcal{E}(z,\xi)}{\partial t} = \frac{\partial \mathcal{E}}{\partial \xi}\frac{\partial \xi}{\partial t} = \frac{\partial \mathcal{E}}{\partial \xi} \tag{313}$$

$$\frac{\partial \mathcal{E}(z,\xi)}{\partial x} = \frac{\partial \mathcal{E}}{\partial \xi}\frac{\partial \xi}{\partial x} = -\frac{\sin\theta}{c_0}\frac{\partial \mathcal{E}}{\partial \xi} \ . \tag{314}$$

So the spatial and temporal derivatives of any field component are related as

$$\frac{\partial \mathcal{E}}{\partial x} = -\frac{\sin\theta}{c_0}\frac{\partial \mathcal{E}}{\partial t} \ . \tag{315}$$

Now let's examine the source-free Maxwell's equations in one of the layers using the relation (315). The electric-field curl equation

$$\nabla \times \boldsymbol{\mathcal{E}} = -\mu_0 \partial \boldsymbol{\mathcal{H}}/\partial t \tag{316}$$

with (315) can be expanded into three scalar equations:

$$\frac{\partial \mathcal{E}_y}{\partial z} = \mu_0 \frac{\partial \mathcal{H}_x}{\partial t} \tag{317}$$

$$\frac{\partial \mathcal{E}_x}{\partial z} + \frac{\sin\theta}{c_0}\frac{\partial \mathcal{E}_z}{\partial t} = -\mu_0 \frac{\partial \mathcal{H}_y}{\partial t} \tag{318}$$

$$-\frac{\sin\theta}{c_0}\frac{\partial \mathcal{E}_y}{\partial t} = -\mu_0 \frac{\partial \mathcal{H}_z}{\partial t} \tag{319}$$

Similarly, the magnetic-field curl equation

$$\nabla \times \boldsymbol{\mathcal{H}} = \epsilon\, \partial \boldsymbol{\mathcal{E}}/\partial t \tag{320}$$

with (315) can be expanded into three scalar equations:

$$\frac{\partial \mathcal{H}_y}{\partial z} = -\epsilon \frac{\partial \mathcal{E}_x}{\partial t} \tag{321}$$

$$\frac{\partial \mathcal{H}_x}{\partial z} + \frac{\sin\theta}{c_0}\frac{\partial \mathcal{H}_z}{\partial t} = \epsilon \frac{\partial \mathcal{E}_y}{\partial t} \tag{322}$$

$$-\frac{\sin\theta}{c_0}\frac{\partial \mathcal{H}_y}{\partial t} = \epsilon \frac{\partial \mathcal{E}_z}{\partial t} \tag{323}$$

We see that the equations (317),(319),(322) only involve the field components $(\mathcal{E}_y, \mathcal{H}_x, \mathcal{H}_z)$, and the equations (318),(321),(323) only involve the field components $(\mathcal{H}_y, \mathcal{E}_x, \mathcal{E}_z)$. We call the former and the latter equations *transverse-electric* (TE) and *transverse-magnetic* (TM) transmission-line equations, respectively, since the electric field is perpendicular to the principal plane G in the TE equations, and the magnetic field is perpendicular to the principal plane G in the TM equations. We integrate (319) in time and substitute into (322) to obtain the following final form of the TE equations:

$$\frac{\partial \mathcal{E}_y}{\partial z} = \mu_0 \frac{\partial \mathcal{H}_x}{\partial t} \tag{324}$$

$$\frac{\partial \mathcal{H}_x}{\partial z} = \epsilon_0(\epsilon_r - \epsilon_{r_0}\sin^2\theta)\frac{\partial \mathcal{E}_y}{\partial t} \tag{325}$$

$$\mathcal{H}_z = Y_0\sqrt{\epsilon_{r_0}}\sin\theta\, \mathcal{E}_y \tag{326}$$

Similarly, integrating (323) in time and substituting into (318), we obtain the following final form of the TM equations:

$$\frac{\partial \mathcal{E}_x}{\partial z} = -\frac{\mu_0(\epsilon_r - \epsilon_{r_0}\sin^2\theta)}{\epsilon_r}\frac{\partial \mathcal{H}_y}{\partial t} \tag{327}$$

$$\frac{\partial \mathcal{H}_y}{\partial z} = -\epsilon_0\epsilon_r \frac{\partial \mathcal{E}_x}{\partial t} \tag{328}$$

$$\mathcal{E}_z = -\frac{Z_0\sqrt{\epsilon_{r_0}}\sin\theta}{\epsilon_r}\mathcal{H}_y \tag{329}$$

Now, adopting the notation $\mathcal{E}^h = \mathcal{E}_y$, $\mathcal{H}^h = -\mathcal{H}_x$ for the TE equations and the notation $\mathcal{E}^e = \mathcal{E}_x$, $\mathcal{H}^e = \mathcal{H}_y$ for the TM equations, we obtain the time-domain equations (101)–(102).

APPENDIX D

DERIVATION OF THE PARTIAL SUMS IN THE SERIES FOR THE INPUT ADMITTANCE

In this Appendix, we present the details of the division of the series (233) into four partial sums given in (234).

In (234), we compute the exact terms Y_n of the series for the input admittance (233) up to $n = n_{\max 1}$. From $n = n_{\max 1} + 1$ to $n_{\max 2}$, we must find an accurate approximation for the spheroidal wave functions. For this purpose, it is necessary to look more closely at the differential equation satisfied by the spheroidal angle function $S_{mn}(\gamma, \eta)$:

$$\frac{d}{d\eta}\left[(1-\eta^2)\frac{dS_{mn}(\gamma,\eta)}{d\eta}\right] + \left[\lambda_{mn} - \gamma^2\eta^2 - \frac{m^2}{1-\eta^2}\right] S_{mn}(\gamma,\eta) = 0 \ . \tag{330}$$

From Sturm-Liouville theory [100], it is known that this differential equation has solutions with finite values at $\eta = \pm 1$ only for a countable infinity of real λ_{mn} values. The usual convention is to sort the eigenvalues in ascending order, and assign the labels $\lambda_{m,m}, \lambda_{m,m+1}, \cdots$. In this manner, it is guaranteed that the eigenvalues increase with increasing n. As a result, as $n \to \infty$, the term $\gamma^2\eta^2$ in (330) becomes negligible compared to the eigenvalue λ_{mn}. When the term $\gamma^2\eta^2$ is omitted ($\gamma = 0$), (330) reduces to the Legendre differential equation [40, 84, 85, 101]:

$$\frac{d}{dx}\left[(1-x^2)\frac{dF_n^m(x)}{dx}\right] + \left[\lambda_{mn} - \frac{m^2}{1-x^2}\right] F_n^m(x) = 0 \ , \tag{331}$$

in which the eigenvalues are chosen to be $\lambda_{mn} = n(n+1)$ with integer n for finiteness at $x = \pm 1$. For each eigenvalue, the two independent solutions of (331) are $P_n^m(x)$ and $Q_n^m(x)$. Therefore, it can be said that the spheroidal wave functions reduce to Legendre functions as $n \to \infty$. Motivated by this fact, in Y_n^a, all spheroidal functions will be replaced by appropriately normalized Legendre functions.

For computation of Y_n^a, the direct substitution of $\gamma = 0$ in the codes written for spheroidal functions is usually impractical. The most important reason for this is that

the terms Y_n^a are calculated up to some n that exceeds the applicable range of the codes written for the spheroidal functions. Another reason is that as $\gamma \to 0$, the codes for the spheroidal functions are very likely to encounter indeterminate forms such as ∞/∞, $0/0$, or $0 \cdot \infty$. It is therefore necessary to find the limiting forms of the spheroidal wave functions and parameters for $\gamma \to 0$, and write different codes for calculating the results. Using (162), (166), and the normalization scheme for the prolate coefficients $d_r^{mn}(\gamma)$ adopted by Flammer [83, pg. 21], the following expressions are obtained as $\gamma \to 0$:

$$d_r^{mn}(0) = \delta_{r,m-n} \tag{332a}$$

$$d_{\rho|r}^{mn}(0) = 0 \tag{332b}$$

$$N_{mn}(0) = \frac{2(n+m)!}{(2n+1)(n-m)!} \ . \tag{332c}$$

The normalization constant $N_{1,2n+1}(0)$ follows from (332c):

$$N_{1,2n+1}(0) = \frac{4(n+1)(2n+1)}{4n+3} \ . \tag{333}$$

As a first step in determining $V_n(0, \xi_a, \xi_b)$, (332a) is substituted into (217) and (222) to yield

$$J_{kn}(0) = \frac{2(n+1)(2n+1)}{4n+3} \left[-\delta_{k,n+1} + \delta_{k,n}\right] \tag{334a}$$

$$K_{kn}(0) = \frac{2n+1}{4n+3} \ \delta_{k,n+1} + \frac{2(n+1)}{4n+3} \ \delta_{k,n} \ . \tag{334b}$$

The second step is to evaluate the limits

$$\lim_{\gamma \to 0} \left\{ \gamma \, R_{0,2k}^{(1)}(\gamma, \xi_a) \left[R_{0,2k}^{(4)}(\gamma, \xi_b) - R_{0,2k}^{(4)}(\gamma, \xi_a) \right] \right\} \tag{335}$$

and

$$\lim_{\gamma \to 0} \left[\gamma \, R_{1,2k}^{(1)}(\gamma, \xi_a) \ I_{2k}(\gamma, \xi_a, \xi_b) \right] \tag{336}$$

to be used in (208) and (209), respectively. Using the limits [83]

$$\lim_{\gamma \to 0} \left[\frac{\gamma}{\kappa_{0,2k}^{(1)}(\gamma) \kappa_{0,2k}^{(2)}(\gamma)} \right] = -1 \tag{337a}$$

$$\lim_{\gamma \to 0} \left[\frac{\gamma}{\kappa_{1,2k}^{(1)}(\gamma) \kappa_{1,2k}^{(2)}(\gamma)} \right] = \frac{1}{2k(2k+1)} \tag{337b}$$

$$\lim_{\gamma\to 0}\left[\frac{\gamma}{\big(\kappa_{mn}^{(1)}(\gamma)\big)^2}\right]=0\ , \tag{337c}$$

along with (162b), (162c), and (332), the limits in (335) and (336) are found to be

$$jP_{2k}(\xi_a)\big(Q_{2k}(\xi_b)-Q_{2k}(\xi_a)\big) \tag{338}$$

and

$$-\,j\frac{1}{2k(2k+1)}P_{2k}^1(\xi_a)\big(Q_{2k}(\xi_b)-Q_{2k}(\xi_a)\big)\ , \tag{339}$$

respectively. Upon substitution of (334), (338), and (339) in (207), (208), and (209), the source parameter $V_n(0,\xi_a,\xi_b)$ becomes

$$V_n(0,\xi_a,\xi_b)=\frac{2(n+1)(2n+1)}{4n+3}\big(-\nu_{n+1}^{(1)}+\nu_n^{(1)}\big)+\frac{2n+1}{4n+3}\nu_{n+1}^{(2)}+\frac{2(n+1)}{4n+3}\nu_n^{(2)} \tag{340}$$

in which

$$\nu_k^{(1)}=\frac{j2}{\ln(b/a)}\frac{(-1)^k(2k)!}{2^{2k}k!k!}(\xi_a)jP_{2k}(\xi_a)\big(Q_{2k}(\xi_b)-Q_{2k}(\xi_a)\big)\ , \tag{341}$$

and

$$\nu_k^{(2)}=\frac{j2}{\ln(b/a)}\frac{(-1)^{k-1}(2k+2)!}{2^{2k}k!(k+1)!}(\xi_a^2-1)^{1/2}\frac{-j}{2(2k+1)}P_{2k}^1(\xi_a)\big(Q_{2k}(\xi_b)-Q_{2k}(\xi_a)\big)\ . \tag{342}$$

The Infeld function $r_n(0,\xi_a)$ is derived similarly using (163) with (162b), (162c), (332), and (337c):

$$r_n(0,\xi_a)=\frac{-(\xi_a^2-1)Q_{2n+1}^1(\xi_a)}{2(n+1)\big(Q_{2n}^1(\xi_a)-\xi_aQ_{2n+1}^1(\xi_a)\big)}-\frac{-(\xi_a^2-1)P_{2n+1}^1(\xi_a)}{2(n+1)\big(P_{2n}^1(\xi_a)-\xi_aP_{2n+1}^1(\xi_a)\big)}\ . \tag{343}$$

With (333), (340), and (343), Y_n^a is expressed entirely in terms of Legendre functions $P_n^m(z)$ and $Q_n^m(z)$. Note that the Legendre functions are easier to compute than the spheroidal wave functions, because there are recurrence relations between Legendre functions of different order and degree. Such relations do not exist for the spheroidal wave functions.

It is possible to obtain an estimate for $n_{\max 1}$ in (234) using the following fact: As the term $\gamma^2\eta^2$ gets smaller compared to λ_{mn}, the difference between the terms Y_n and Y_n^a approaches zero. Therefore, the truncation point $n_{\max 1}$ must satisfy the criterion $\lambda_{mn}\gg\gamma^2\eta^2$. Since the eigenvalues of (331) are $\lambda_{mn}=n(n+1)$, the following relation may be used for estimating $n_{\max 1}$:

$$n_{\max 1}(n_{\max 1}+1)\gg\gamma^2\eta^2\ , \tag{344}$$

or

$$n_{\max 1} \gg \gamma = \beta F \ . \tag{345}$$

Note that the approximation of spheroidal wave functions by Legendre functions makes them independent of frequency. Consequently, the dependence of Y_n^a on frequency becomes a linear one, through the term $-j2\pi Y_0 \gamma = -j2\pi\epsilon_0 \omega F$ in (233). This linear dependence is also present in Y_n^b and Y_n^c.

In Y_n^b, the Legendre functions are simplified even further for large n. The asymptotic forms used for the functions $P_n^m(\xi)$ and $Q_n^m(\xi)$ for large n are [84, 102] :

$$P_n^m(\xi) = (2\pi n)^{-1/2} \frac{\Gamma(n+1)}{\Gamma(n-m+1)} (\xi^2-1)^{-1/4} (\xi + \sqrt{\xi^2-1})^{n+1/2} \tag{346}$$

$$Q_n^m(\xi) = (\pi/2)^{1/2} e^{im\pi} \frac{\Gamma(n+m+1)}{\Gamma(n+3/2)} (\xi^2-1)^{-1/4} (\xi - \sqrt{\xi^2-1})^{n+1/2} \ . \tag{347}$$

Now an estimate for $n_{\max 2}$ in (234) will be obtained. First, it must be remembered that the accuracy of the asymptotic forms in (346) and (347) is a qualitative indicator of the similarity between Y_n^a and Y_n^b. Therefore, it is logical to require that, at the truncation point $n_{\max 2}$, the asymptotic forms in (346) and (347) are accurate. A suitable measure of similarity between the asymptotic forms in (346) and (347) and the original functions $P_n^m(\xi)$ and $Q_n^m(\xi)$ is the asymptotic condition [84]

$$n_{\max 2} > K_2 \frac{|m^2 - 1/4|}{2\sqrt{\xi_a^2 - 1}} \ , \tag{348}$$

where K_2 is the desired ratio of the the leading term to the first neglected term in the asymptotic expansions of the functions. This constraint is valid for both (346) and (347). It is interesting to note that the minimum number of terms needed to satisfy the asymptotic condition increases as $1/\sqrt{\xi_a - 1}$ as the spheroid gets thinner, i. e. , as $\xi_a \to 1$.

The definition of Y_n^c will involve some final simplifications of Y_n^b. Using (346) and (347) in (343), the form of the Infeld function used in Y_n^b is obtained:

$$r_n(0, \xi_a) = \frac{-\sqrt{\xi_a^2 - 1}}{n+1} \ . \tag{349}$$

For large n, this expression simplifies further to the form that will be used in Y_n^c:

$$r_n(0, \xi_a) = \frac{-\sqrt{\xi_a^2 - 1}}{n} \ . \tag{350}$$

Before seeking any simplification in $V_n(0,\xi_a,\xi_b)$, the following asymptotic results for $n,k\to\infty$ are noted:

$$\frac{(-1)^k(2k)!}{2^{2k}k!k!}\sim\frac{(-1)^k}{k\sqrt{\pi}}\frac{\Gamma(k+1/2)}{\Gamma(k)} \tag{351a}$$

$$\frac{(-1)^{k-1}(2k+2)!}{2^{2k}(k-1)!(k+1)!}\sim\frac{-4k(-1)^k}{\sqrt{\pi}}\frac{\Gamma(k+1/2)}{\Gamma(k)} \tag{351b}$$

$$\frac{(-1)^n(2n+2)!}{2^{2n+1}n!(n+1)!}\sim\frac{2(-1)^n}{\sqrt{\pi}}\frac{\Gamma(n+1/2)}{\Gamma(n)}\ , \tag{351c}$$

in which $\Gamma(z)$ is the Gamma function defined as [91, 8.31]

$$\Gamma(z)=\int_0^\infty e^{-t}t^{z-1}dt\ . \tag{352}$$

The main idea behind the simplification of $V_n(0,\xi_a,\xi_b)$ for large n originates from (347). A careful examination of (347) reveals that $Q_n(\xi_b)$ becomes negligible compared to $Q_n(\xi_a)$ for large enough n, since $\xi_b>\xi_a$. Using this approximation and neglecting the terms $Q_{2n}(\xi_b)$ and $Q_{2n+2}(\xi_b)$ in (340), the following expression for $V_n(0,\xi_a,\xi_b)$ is obtained:

$$V_n(0,\xi_a,\xi_b)\sim\frac{\xi_a}{\sqrt{\pi}\ln(b/a)\sqrt{\xi_a^2-1}}\frac{(-1)^n\,\Gamma(n+1/2)}{n\,\Gamma(n)}$$
$$\cdot\left[\frac{1}{2n(n+1)(4n+3)}\Big((2n+1)(4n^2+5n+2)+n(4n+3)(\xi_a^2-1)^{1/2}/\xi_a\Big)\right]\ . \tag{353}$$

The expression in square brackets in (353) is close to unity for $n\gg1$. Therefore, it is possible to simplify the form of $V_n(0,\xi_a,\xi_b)$ in (353) to

$$V_n(0,\xi_a,\xi_b)\sim\frac{\xi_a}{\sqrt{\pi}\ln(b/a)\sqrt{\xi_a^2-1}}\frac{(-1)^n\,\Gamma(n+1/2)}{n\,\Gamma(n)}\ , \tag{354}$$

which is the form of $V_n(0,\xi_a,\xi_b)$ that will be used in Y_n^c. A simpler form for the normalization constant $N_{mn}(0)$ is readily obtained using (333):

$$N_{1,2n+1}\sim 2n\ . \tag{355}$$

Using (350), (351c), (354), and (355), a suitable candidate for Y_n^c is obtained:

$$Y_n^c=\frac{j2Y_0\gamma\xi_a}{\ln(b/a)}\frac{1}{n^3}\left(\frac{\Gamma(n+1/2)}{\Gamma(n)}\right)^2\ . \tag{356}$$

Note that as $n\to\infty$, $\Gamma(n+1/2)/\Gamma(n)\sim n^{1/2}$ [102]. Therefore, Y_n^c behaves as $1/n^2$ at large n. Rewriting the the last partial sum in (234) as

$$\sum_{n=n_{\max3+1}}^{\infty}Y_n^c=\sum_{n=1}^{\infty}Y_n^c-\sum_{n=1}^{n_{\max3}}Y_n^c\ , \tag{357}$$

and making use of the numerical sum

$$\sum_{n=1}^{\infty} \frac{1}{n^3} \left(\frac{\Gamma(n+1/2)}{\Gamma(n)} \right)^2 = 4\pi \ln(2) - 8C \ , \tag{358}$$

where C is the Catalan constant, defined as

$$C = \sum_{n=0}^{\infty} \frac{(-1)^n}{(2n+1)^2} = 0.915966\ldots \ , \tag{359}$$

we obtain

$$\sum_{n=n_{\max 3+1}}^{\infty} Y_n^c = \frac{j2Y_0\gamma\xi_a}{\ln(b/a)}(4\pi\ln(2) - 8C) - \sum_{n=1}^{n_{\max 3}} Y_n^c \ , \tag{360}$$

which is a finite sum.

It is again necessary to obtain an estimate for the truncation point $n_{\max 3}$. Note that the accuracy of the aforementioned approximations of $V_n(0, \xi_a, \xi_b)$ depend on how large the ratio between $Q_{2n}(\xi_a)$ and $Q_{2n}(\xi_b)$ is. If the desired ratio is K_3, then the condition for $n_{\max 3}$ becomes

$$n_{\max 3} > \frac{1}{2} \frac{\ln(K_3) + \frac{1}{4}\ln\left(\frac{\xi_a^2-1}{\xi_b^2-1}\right)}{\ln\left(\frac{\xi_a - \sqrt{\xi_a^2-1}}{\xi_b - \sqrt{\xi_b^2-1}}\right)}. \tag{361}$$

Now, the accuracy of the approximations just described and used in (234) will be examined with a numerical example. For this purpose, the partition in (234) is rewritten as follows:

$$\begin{aligned} Y_{\text{TEM}} &= \sum_{n=0}^{n_{\max 1}} (Y_n - Y_n^a) + \sum_{n=0}^{n_{\max 2}} (Y_n^a - Y_n^b) + \sum_{n=0}^{n_{\max 3}} (Y_n^b - Y_n^c) + \sum_{n=0}^{\infty} Y_n^c \\ &= Y_{\text{TEM}}^{(1)} + Y_{\text{TEM}}^{(2)} + Y_{\text{TEM}}^{(3)} + Y_{\text{TEM}}^{c} \ , \end{aligned} \tag{362}$$

in which Y_n^b and Y_n^c at $n = 0$ are assigned the arbitrary value zero, as their behavior at large n is of only interest. The key point here is that the partition in (362) would reduce to the exact result in (233) if $n_{\max 1}$, $n_{\max 2}$, and $n_{\max 3}$ were all infinity. Therefore, the accuracy of the partition in (362), hence that of (234), depends entirely on the choice of these truncation points.

For the numerical example, we will choose a thin antenna, which is a computationally difficult case: $h/\lambda = 0.5$, $h/a = 10^3$, and $Z_c = 50\ \Omega$ ($b/a = 2.30...$). With these parameters,

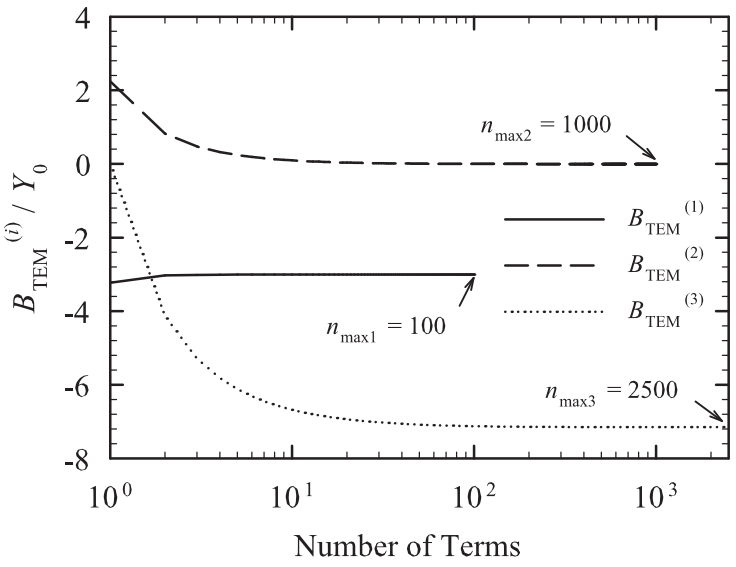

Figure 58: An example of the convergence rates of the series for $B_{\mathrm{TEM}}^{(i)}$ for the case $h/\lambda = 0.5$, $h/a = 10^3$, $Z_c = 50\ \Omega$ ($b/a = 2.30...$).

$\xi_a = 1 + 5 \cdot 10^{-7}$, $\xi_b = 1 + 2.645 \cdot 10^{-6}$, and the inequalities for the truncation points, (345), (348), and (361) become

$$\begin{aligned} n_{\mathrm{max1}} &\gg \pi \\ n_{\mathrm{max2}} &> 375 K_2 \\ n_{\mathrm{max3}} &> 385(\ln K_3 - 0.42)\ . \end{aligned} \tag{363}$$

Remembering the earlier discussion that the slowly convergent part of the input admittance is the susceptance, the imaginary parts of the truncated series $Y_{\mathrm{TEM}}^{(1)}$, $Y_{\mathrm{TEM}}^{(2)}$, and $Y_{\mathrm{TEM}}^{(3)}$ are plotted in Fig. 58 versus the number of terms. It can be clearly seen that the series converge, with truncation points chosen according to (363). In fact, an accuracy of five significant digits is obtained for Y_{TEM}, with the truncation points being $n_{\mathrm{max1}} = 100$, $n_{\mathrm{max2}} = 1000$, and $n_{\mathrm{max3}} = 2500$, respectively.

REFERENCES

[1] Smith, G. S., *An Introduction to Classical Electromagnetic Radiation*. New York, NY: Cambridge University Press, 1997. (Cited on pages 2, 7, 15, 45, 68, 75, 77, 87, 127, 139, and 140)

[2] Taflove, A. and Hagness, S. C., *Computational Electrodynamics: The Finite-Difference Time-Domain Method*. Boston: Artech House, 2nd ed., 2000. (Cited on pages 2, 3, 5, 7, 8, 12, 13, 20, 44, 54, 58, 59, 60, 66, 78, and 95)

[3] Yee, K. S., "Numerical solution of initial boundary value problems involving Maxwell's equations in isotropic media," *IEEE Trans. Antennas Propag.*, vol. AP-14, pp. 302 – 307, May 1966. (Cited on pages 2 and 6)

[4] Berenger, J.-P., "A perfectly matched layer for the absorption of electromagnetic waves," *J. Comput. Phys.*, vol. 114, pp. 185–200, Oct. 1994. (Cited on page 7)

[5] Gedney, S. D., "An anisotropic perfectly matched layer-absorbing medium for the truncation of FDTD lattices," *IEEE Trans. Antennas Propag.*, vol. 44, pp. 1630 – 9, Dec. 1996. (Cited on page 7)

[6] Roden, J. A. and Gedney, S. D., "Convolution PML (CPML): an efficient FDTD implementation of the CFD-PML for arbitrary media," *Microw. Opt. Technol. Lett.*, vol. 27, pp. 334–9, Dec. 2000. (Cited on pages 7 and 61)

[7] Luebbers, R., Kunz, K., Schneider, M., and Hunsberger, F., "A finite-difference time-domain near zone to far zone transformation," *IEEE Trans. Antennas Propag.*, vol. 39, pp. 429 – 33, Apr. 1991. (Cited on pages 7, 12, and 18)

[8] Oguz, U., Gurel, L., and Arikan, O., "An efficient and accurate technique for the incident-wave excitations in the FDTD method," *IEEE Trans. Microw. Theory Tech.*, vol. 46, pp. 869 – 82, June 1998. (Cited on page 7)

[9] Schneider, J. B., "Plane waves in FDTD simulations and a nearly perfect total-field/scattered-field boundary," *IEEE Trans. Antennas Propag.*, vol. 52, pp. 3280–7, Dec. 2004. (Cited on page 7)

[10] Hirono, T., Shibata, Y., Lui, W. W., Seki, S., and Yoshikuni, Y., "The second-order condition for the dielectric interface orthogonal to the Yee-lattice axis in the FDTD scheme," *IEEE Microw. Guided Wave Lett.*, vol. 10, pp. 359 – 61, Sept. 2000. (Cited on pages 9 and 55)

[11] Hwang, K.-P. and Cangellaris, A. C., "Effective permittivities for second-order accurate FDTD equations at dielectric interfaces," *IEEE Microw. Wireless Compon. Lett.*, vol. 11, pp. 158 – 60, Apr. 2001. (Cited on pages 9 and 55)

[12] Balanis, C. A., *Advanced Engineering Electromagnetics*. New York: Wiley, 1989. (Cited on pages 10, 24, 63, and 69)

[13] Felsen, L. B. and Marcuvitz, N., *Radiation and Scattering of Waves*. Piscataway, NJ: IEEE Press, 1994. (Cited on pages 12, 13, 139, 140, and 144)

[14] Demarest, K., Huang, Z., and Plumb, R., "An FDTD near-to-far-zone transformation for scatterers buried in stratified grounds," *IEEE Trans. Antennas Propag.*, vol. 44, pp. 1150 – 7, Aug. 1996. (Cited on page 12)

[15] Yu, W., Su, T., Huang, N.-T., and Mittra, R., "An improved approach to predict far field for infinite planar structure in FDTD simulations," in *2005 IEEE Antennas and Propagation Society International Symposium*, vol. 2A, (Washington DC, USA), pp. 86–9, July 2005. (Cited on page 12)

[16] Martin, T. and Pettersson, L., "FDTD time domain near-to-far-zone transformation above a lossy dielectric half-space," *Appl. Comput. Electromagn. Soc. J.*, vol. 16, pp. 45 – 52, Mar. 2001. (Cited on page 12)

[17] Michalski, K. A. and Mosig, J. R., "Multilayered media Green's functions in integral equation formulations," *IEEE Trans. Antennas Propag.*, vol. 45, pp. 508 – 19, Mar. 1997. (Cited on pages 12, 18, 53, 63, 138, 145, and 148)

[18] Vegni, L., Cicchetti, R., and Capece, P., "Spectral dyadic Green's function formulation for planar integrated structures," *IEEE Trans. Antennas Propag.*, vol. 36, pp. 1057 – 65, Aug. 1988. (Cited on page 12)

[19] Tai, C.-T., *Dyadic Green Functions in Electromagnetic Theory*. Scranton, PA: Intext Educational Publishers, 1971. (Cited on pages 12 and 22)

[20] Umashankar, K. and Taflove, A., "A novel method to analyze electromagnetic scattering of complex objects," *IEEE Trans. Electromagn. Compat.*, vol. EMC-24, pp. 397–405, Nov. 1982. (Cited on page 13)

[21] Mur, G., "Absorbing boundary conditions for the finite-difference approximation of the time-domain electromagnetic-field equations," *IEEE Trans. Electromagn. Compat.*, vol. EMC-23, pp. 377–82, Nov. 1981. (Cited on page 13)

[22] Wong, P., Tyler, G., Baron, J., Gurrola, E., and Simpson, R., "A three-wave FDTD approach to surface scattering with applications to remote sensing of geophysical surfaces," *IEEE Trans. Antennas Propag.*, vol. 44, pp. 504–14, Apr. 1996. (Cited on page 14)

[23] Hsu, T.-T. and Carin, L., "FDTD analysis of plane-wave diffraction from microwave devices on an infinite dielectric slab," *IEEE Microw. Guided Wave Lett.*, vol. 6, pp. 16–18, Jan. 1996. (Cited on page 14)

[24] Yi, Y., Chen, B., Fang, D.-G., and Zhou, B.-H., "A new 2-D FDTD method applied to scattering by infinite objects with oblique incidence," *IEEE Trans. Electromagn. Compat.*, vol. 47, pp. 756–62, Nov. 2005. (Cited on page 15)

[25] Winton, S. C., Kosmas, P., and Rappaport, C. M., "FDTD simulation of TE and TM plane waves at nonzero incidence in arbitrary layered media," *IEEE Trans. Antennas Propag.*, vol. 53, pp. 1721 – 8, May 2005. (Cited on pages 15, 59, 60, 65, and 68)

[26] Cicchetti, R., "Transient analysis of radiated field from electric dipoles and microstrip lines," *IEEE Trans. Antennas Propag.*, vol. 39, pp. 910 – 18, July 1991. (Cited on page 40)

[27] Cicchetti, R., "On the time-domain response of microstrip dipoles embedded in a low-loss grounded dielectric slab," *Microw. Opt. Technol. Lett.*, vol. 6, pp. 238 – 40, Mar. 1993. (Cited on pages 40 and 42)

[28] Cicchetti, R., "On the pulse radiation from a loaded microstrip line using a space-time dyadic Green's function approach," in *Ultra-Wideband, Short-Pulse Electromagnetics. Proceedings of an International Conference*, (Brooklyn, NY), pp. 321–7, Plenum, 1993. (Cited on page 40)

[29] Kominami, M., Pozar, D. M., and Schaubert, D. H., "Dipole and slot elements and arrays on semi-infinite substrates," *IEEE Trans. Antennas Propag.*, vol. AP-33, pp. 600–7, June 1985. (Cited on page 43)

[30] Pozar, D. M., *Microwave Engineering*. Hoboken, NJ: J. Wiley, 3rd ed., 2005. (Cited on pages 44 and 45)

[31] Collin, R. E., *Foundations for Microwave Engineering*. New York: IEEE Press, 2 ed., 2001. (Cited on page 44)

[32] Capoglu, I. R. and Smith, G. S., "A direct time-domain FDTD near-field-to-far-field transform in the presence of an infinite grounded dielectric slab," *IEEE Trans. Antennas Propag.*, vol. 54, pp. 3805–14, Dec. 2006. (Cited on page 63)

[33] Orfanidis, S. J., "MATLAB toolbox." Electromagnetic Waves and Antennas – Web Resource. http://www.ece.rutgers.edu/∼orfanidi/ewa/ (Date Accessed: 01/2007). (Cited on pages 63 and 68)

[34] Ramadan, O. and Niazi, A. Y., "One way wave equation type ABCs for terminating low loss media," *Electron. Lett.*, vol. 33, pp. 2052–4, Nov. 1997. (Cited on page 66)

[35] Kiwitt, J. E. and Reiss, K., "Total reflection in the time domain," *Electr. Eng.*, vol. 81, pp. 193–8, Nov. 1998. (Cited on page 69)

[36] Gustafsson, B., Kreiss, H., and Oliger, J., *Time Dependent Problems and Difference Methods*. New York: Wiley, 1995. (Cited on page 70)

[37] Garabedian, P., *Partial Differential Equations*. New York: Wiley, 1964. (Cited on pages 70 and 75)

[38] Born, M. and Wolf, E., *Principles of Optics : Electromagnetic Theory of Propagation, Interference and Diffraction of Light*. Cambridge: Cambridge University Press, 7th (expanded) ed., 1999. (Cited on pages 70 and 71)

[39] Brown, J. W. and Churchill, R. V., *Complex Variables and Applications*. McGraw-Hill, 7 ed., 2004. (Cited on page 70)

[40] Morse, P. M. and Feshbach, H., *Methods of Theoretical Physics*. New York: McGraw-Hill, 1953. (Cited on pages 71, 107, 111, 120, and 153)

[41] Press, W. H., Flannery, B. P., Teukolsky, S. A., and Vetterling, W. T., *Numerical Recipes: The Art of Scientific Computing*. Cambridge: Cambridge University Press, 1986. (Cited on page 72)

[42] Oppenheim, A. V., Schafer, R. W., and Buck, J. R., *Discrete-Time Signal Processing*. Upper Saddle River, N.J.: Prentice Hall, 2nd ed., 1999. (Cited on page 73)

[43] Tanaka, S., Nakao, M., Umeda, M., Ito, K., Nakamura, S., and Hatamura, Y., "Simulation of near-field photolithography using the finite-difference time-domain method," *J. Appl. Phys.*, vol. 89, pp. 3547–53, Apr. 2001. (Cited on page 77)

[44] Kik, P., Martin, A., Maier, S., and Atwater, H., "Metal nanoparticle arrays for near-field optical lithography," *Proc. SPIE - Int. Soc. Opt. Eng.*, vol. 4810, pp. 7–13, 2002. (Cited on page 77)

[45] Shirasaki, H. and Ueta, K., "Linewidth measurement simulations for semiconductor circuits by scatterometry using the FDTD and the time shortening calculation method," *Proc. SPIE - Int. Soc. Opt. Eng.*, vol. 5375, pp. 1331–8, May 2004. (Cited on page 77)

[46] Blaikie, R., Melville, D., and Alkaisi, M., "Super-resolution near-field lithography using planar silver lenses: A review of recent developments," *Microelectron. Eng.*, vol. 83, pp. 723–9, Apr. 2006. (Cited on page 77)

[47] Rao, X. S. and Ong, C. K., "Subwavelength imaging by a left-handed material superlens," *Phys. Rev. E (Stat. Nonlinear Soft Matter Phys.)*, vol. 68, pp. 67601–1, Dec. 2003. (Cited on page 77)

[48] Zhou, Q., Zhu, X., Dai, H., and Pan, E., "Three-dimensional modeling of near-field imaging in subwavelength periodic structures," *Proc. SPIE - Int. Soc. Opt. Eng.*, vol. 4923, pp. 7–11, 2002. (Cited on page 77)

[49] Ono, A., Kato, J., and Kawata, S., "Subwavelength optical imaging through a metallic nanorod array," *Phys. Rev. Lett.*, vol. 95, pp. 267407–1, Dec. 2005. (Cited on page 77)

[50] Kärkkäinen, M. K., "Numerical study of wave propagation in uniaxially anisotropic Lorentzian backward-wave slabs," *Phys. Rev. E (Stat. Nonlinear Soft Matter Phys.)*, vol. 68, p. 026602, Aug. 2003. (Cited on page 77)

[51] Rao, X. S. and Ong, C. K., "Amplification of evanescent waves in a lossy left-handed material slab," *Phys. Rev. B (Condens. Matter Mater. Phys.)*, vol. 68, pp. 113103–1, Sept. 2003. (Cited on page 77)

[52] Alu, A., Engheta, N., and Ziolkowski, R., "Finite-difference time-domain analysis of the tunneling and growing exponential in a pair of ϵ-negative and μ-negative slabs," *Phys. Rev. E (Stat. Nonlinear Soft Matter Phys.)*, vol. 74, pp. 16604–1, July 2006. (Cited on page 77)

[53] Ziolkowski, R. W. and Heyman, E., "Wave propagation in media having negative permittivity and permeability," *Phys. Rev. E (Stat. Nonlinear Soft Matter Phys.)*, vol. 64, pp. 056625–1, Nov. 2001. (Cited on page 77)

[54] Smith, G. S., "A direct derivation of a single-antenna reciprocity relation for the time domain," *IEEE Trans. Antennas Propag.*, vol. 52, pp. 1568–77, June 2004. (Cited on page 92)

[55] Bourgeois, J. M., *A Complete Three-Dimensional Electromagnetic Simulation of Ground-Penetrating Radars Using the Finite-Difference Time-Domain Method*. PhD thesis, Georgia Institute of Technology, Atlanta, GA, 1997. (Cited on page 93)

[56] Hertel, T., *Analysis and Design of Conical Spiral Antennas in Free Space and Over Ground*. PhD thesis, Georgia Institute of Technology, Atlanta, GA, 2001. (Cited on page 93)

[57] Shlager, K., Smith, G., and Maloney, J., "Optimization of bow-tie antennas for pulse radiation," *IEEE Trans. Antennas Propag.*, vol. 42, pp. 975–82, July 1994. (Cited on page 99)

[58] Hagness, S., Taflove, A., and Bridges, J., "Wideband ultralow reverberation antenna for biological sensing," *Electron. Lett.*, vol. 33, pp. 1594–5, Sept. 1997. (Cited on page 99)

[59] Hagness, S., Taflove, A., and Bridges, J., "Three-dimensional FDTD analysis of a pulsed microwave confocal system for breast cancer detection: design of an antenna-array element," *IEEE Trans. Antennas Propag.*, vol. 47, pp. 783–91, May 1999. (Cited on page 99)

[60] Ameya, M., Yamamoto, M., Nojima, T., and Ito, K., "Broadband printed dipole antenna employing self-complementary radiating element and microstrip line feed," *Electronics and Communications in Japan, Part 1 (Communications)*, vol. 89, no. 12, pp. 62–74, 2006. (Cited on page 99)

[61] Wu, T. and King, R., "The cylindrical antenna with nonreflecting resistive loading," *IEEE Trans. Antennas Propag.*, vol. AP-13, pp. 369–373, May 1965. (Cited on page 100)

[62] Capoglu, I. R. and Smith, G. S., "The input admittance of a prolate-spheroidal monopole antenna fed by a magnetic frill," *IEEE Trans. Antennas Propag.*, vol. 54, pp. 572–85, Feb. 2006. (Cited on page 105)

[63] Stratton, J. A. and Chu, L. J., "Steady-state solutions of electromagnetic problems: III. Forced oscillations of a prolate spheroid," *J. Appl. Phys.*, vol. 12, pp. 241–248, 1941. (Cited on page 105)

[64] Schelkunoff, S. A., *Advanced Antenna Theory*. New York: John Wiley & Sons, Inc., 1952. (Cited on pages 105 and 115)

[65] Page, L. and Adams, N. I., "The electrical oscillations of a prolate spheroid. Paper I," *Phys. Rev.*, vol. 53, pp. 819–831, May 1938. (Cited on pages 105 and 132)

[66] Ryder, R. M., "The electrical oscillations of a perfectly conducting prolate spheroid," *Phys. Rev.*, vol. 13, pp. 327–343, May 1942. (Cited on page 105)

[67] Page, L., "The electrical oscillations of a prolate spheroid. Paper II-III," *Phys. Rev.*, vol. 65, pp. 98–117, Feb. 1944. (Cited on page 105)

[68] Wait, J. R., "Theories of prolate spheroidal antennas," *Radio Science*, vol. 1, pp. 475–511, Apr. 1966. (Cited on page 105)

[69] Do-Nhat, T. and MacPhie, R. H., "The input admittance of thin prolate spheroidal dipole antennas with finite gap widths," *IEEE Trans. Antennas Propag.*, vol. 43, pp. 1243–1252, Nov. 1995. (Cited on pages 105, 115, 116, and 132)

[70] Jen, L. and Hu, C. S., "Spheroidal wave functions of large frequency parameters $c = kf$ and the radiation fields of a metallic prolate spheroid excited by any circumferential slot," *IEEE Trans. Antennas Propag.*, vol. AP-31, pp. 382–389, Mar. 1983. (Cited on page 105)

[71] Infeld, L., "The influence of the width of the gap upon the theory of antennas," *Quart. Appl. Math.*, vol. 5, pp. 113–132, July 1947. (Cited on pages 105 and 119)

[72] Wu, T. T., "Theory of the thin circular loop antenna," *J. Math, Phys.*, vol. 3, pp. 1301–1304, Nov.-Dec. 1962. (Cited on page 105)

[73] King, R. W. P. and Smith, G. S., *Antennas in Matter: Fundamentals, Theory, and Applications*. MIT Press, 1981. (Cited on page 105)

[74] Do-Nhat, T. and MacPhie, R. H., "The static electric field distribution between two semi-infinite circular cylinders: A model for the feed gap field of a dipole antenna," *IEEE Trans. Antennas Propag.*, vol. 35, pp. 1273–1280, Nov. 1987. (Cited on page 105)

[75] Do-Nhat, T. and MacPhie, R. H., "Effect of gap width on the admittance of solid circular cylindrical dipoles," *IEEE Trans. Antennas Propag.*, vol. 37, pp. 1545–1553, Dec. 1989. (Cited on page 105)

[76] Tsai, L. L., "A numerical solution for the near and far fields of an annular ring of magnetic current," *IEEE Trans. Antennas Propag.*, vol. AP-20, pp. 569–576, Sept. 1972. (Cited on page 106)

[77] Butler, C. M. and Tsai, L. L., "An alternate frill formulation," *IEEE Trans. Antennas Propag.*, vol. AP-21, pp. 115–116, Jan. 1973. (Cited on page 106)

[78] Sakitani, A. and Egashira, S., "Simplified expressions for the near fields of a magnetic frill current," *IEEE Trans. Antennas Propag.*, vol. AP-34, pp. 1059–1062, Aug. 1986. (Cited on pages 106, 120, and 121)

[79] Zhou, G. and Smith, G. S., "An accurate theoretical model for the thin-wire circular half-loop antenna," *IEEE Trans. Antennas Propag.*, vol. 39, pp. 1167–1177, Aug. 1991. (Cited on pages 106, 110, and 131)

[80] Flammer, C., "The prolate spheroidal monopole antenna," Tech. Rep. 22, Contract AF 19(604)-1296, 1954. (Cited on page 106)

[81] Gryaznova, T. A., Karplyuk, K. S., Filonenko, E. G., and Shashurin, I. P., "Input admittance of a spheroidal antenna excited by the open end of a coaxial line," *Radiotekhnika i Elektronika*, vol. 27, pp. 1719–26, Sept. 1982. (Cited on page 106)

[82] Weisstein, E. W., "Prolate spheroidal coordinates." From MathWorld – A Wolfram Web Resource. http://mathworld.wolfram.com/ProlateSpheroidalCoordinates.html (Date Accessed: 09/2004). (Cited on page 106)

[83] Flammer, C., *Spheroidal Wave Functions*. Stanford, California: Stanford University Press, 1957. (Cited on pages 106, 107, 109, 112, 113, 120, 123, and 154)

[84] Abramowitz, M. and Stegun, I. A., eds., *Handbook of Mathematical Functions with Formulas, Graphs, and Mathematical Tables*. U.S. Govt. Print. Off., 1964. (Cited on pages 107, 114, 153, and 156)

[85] Hobson, E. W., *The Theory of Spherical and Ellipsoidal Harmonics*. New York: Chelsea, 1955. (Cited on pages 107 and 153)

[86] Li, L.-W., Kang, X.-K., and Leong, M.-S., *Spheroidal Wave Functions in Electromagnetic Theory*. New York: Wiley, 2002. (Cited on pages 109, 111, and 120)

[87] Harrington, R. F., *Time-Harmonic Electromagnetic Fields*. New York: McGraw-Hill, 1961. (Cited on pages 109 and 118)

[88] Morris, M. E., "The admittance of an infinitely long monopole antenna driven by a coaxial line," Tech. Rep. SAND 78-1065, Sandia National Laboratories, Albuquerque, NM, May 1980. (Cited on pages 110 and 131)

[89] Stratton, J. A., *Electromagnetic Theory*. McGraw-Hill, 1941. (Cited on page 110)

[90] Debnath, L. and Mikusiński, P., *Introduction to Hilbert Spaces with Applications*. Academic Press, 1999. (Cited on page 115)

[91] Gradshteyn, I. and Ryzhik, I., *Table of Integrals, Series, and Products*. Academic Press, 1965. (Cited on pages 117 and 157)

[92] Stratton, J. A., Morse, P. M., Chu, L. J., and Hutner, R. A., *Elliptic Cylinder and Spheroidal Wave Functions, Including Tables of Separation Constants and Coefficients*. New York: Wiley, 1941. (Cited on page 120)

[93] Li, L. W., Yeo, T. S., Kooi, P. S., Leong, M. S., and Tan, K. Y., "Computations of spheroidal harmonics with complex arguments: A review with an algorithm," *Phys. Rev. E*, vol. 58, pp. 6792–6806, Nov. 1998. (Cited on page 120)

[94] Thompson, W. J., "Spheroidal wave functions," *IEEE Comput. Sci. Eng.*, vol. 1, pp. 84–87, May 1999. (Cited on page 120)

[95] Falloon, P. E., Abbott, P. C., and Wang, J. B., "Theory and computation of spheroidal wavefunctions," *J. Phys. A (Mathematical and General)*, vol. 36, pp. 5477–5495, May 2003. (Cited on page 120)

[96] King, R. W. P., *The Theory of Linear Antennas*. Cambridge, MA: Harvard University Press, 1956. (Cited on page 124)

[97] Bibby, M. M. and Peterson, A. F., "On the use of overdetermined systems in the adaptive numerical solution of integral equations," *IEEE Trans. Antennas Propag.*, vol. 53, pp. 2267–73, July 2005. (Cited on page 129)

[98] Peterson, A. F., Ray, S. L., and Mittra, R., *Computational Methods for Electromagnetics*. New York: IEEE Press, 1998. (Cited on page 129)

[99] Chew, W. C., *Waves and Fields in Inhomogeneous Media*. New York: Van Nostrand Reinhold, 1990. (Cited on page 139)

[100] Arfken, G., *Mathematical Methods for Physicists*. Orlando, FL: Academic Press, 3 ed., 1985. (Cited on page 153)

[101] Jackson, J. D., *Classical Electrodynamics*. John Wiley & Sons, Inc., 3 ed., 1999. (Cited on page 153)

[102] Virchenko, N. and Fedotova, I., *Generalized Associated Legendre Functions and Their Applications*. World Scientific, 2001. (Cited on pages 156 and 157)

VITA

İlker R. Çapoğlu was born in Rize, Turkey in 1981. He received his B.A. degree in electrical and electronics engineering from the Middle East Technical University (METU), Ankara, Turkey in 2002, and the M.S. degree in electrical and computer engineering from Georgia Institute of Technology, Atlanta, GA in 2003. From 2003 to 2007, he was employed as a graduate teaching and research assistant in the School of Electrical and Computer Engineering. His research interests include radiation and scattering from spheroidal structures, time-domain multilayered media Green's functions, and the FDTD analysis of multilayered media.

One of his greatest passions is performing authentic Turkish music; especially, playing the "bağlama" seen in the picture.